Twinning and the Dynamic Behavior of Magnesium and its Alloys

by

Vignesh Kannan

A dissertation submitted to The Johns Hopkins University in conformity with the requirements for the degree of Doctor of Philosophy.

Baltimore, Maryland

December, 2018

Abstract

With a density two-thirds that of aluminum, magnesium has great potential to become the most sought-after structural metal. Naturally, many applications for structural metals require them to remain resilient under extreme conditions of pressure, temperature and loading rates (some common scenarios being car crashes, high speed machining, ballistic impact and micrometeorite impact). Most materials behave very differently when subjected to these extreme conditions in comparison to conventional quasi-static isothermal loading. In the context of magnesium, its asymmetric hexagonal close packed crystal structure results in an anisotropy in plastic deformation which can be linked back to two major plastic deformation mechanisms at the crystal scale: dislocation slip and deformation twinning. In this thesis, we focus on a mechanism-based approach to understand plastic deformation in magnesium under high rates of loading. Special focus has been placed on understanding deformation twinning under these loading conditions.

We first investigate the macroscopic strength and ductility of a textured polycrystalline AZ31B magnesium alloy across 8 decades of strain rate ($10^{-4} - 10^{4}\, s^{-1}$) under

uniaxial compression along different loading orientations relative to the material texture. The macroscopic flow stress and strain hardening are found to be a function of both strain rate and loading orientation. Post-mortem microscopy reveals both dislocation slip and twin-dominant deformation, depending on the loading orientation relative to the sample texture. We find that deformation twinning is more active at high strain rates than at quasi-static rates. This tends to affect both material strength and ductility.

The next part of this thesis examines deformation twinning in greater detail. Using high strain rate experiments combined with in-situ high speed microscopy, we capture the dynamic evolution of deformation twins in single crystal magnesium. The measurements reveal the competition between twin nucleation and growth and its relation to macroscopic material response. A theoretical framework to predict twin propagation speeds is developed with significant potential to explain twin-twin and dislocation-twin interactions. Finally, we end with a discussion of the crystallographic nature of twins nucleated under both quasi-static and dynamic loading. The interplay between the mechanics of twinning (i.e. twin nucleation and growth kinetics) and the crystallography offers unique insights and may help improve predictive capabilities for the dynamic behavior of hcp crystals.

Thesis advisor and primary reader: Prof. K. T. Ramesh

Secondary Readers: Prof. Todd C. Hufnagel and Dr. Richard C. Becker

Acknowledgments

I remember the first time I walked into Prof. K. T. Ramesh's office, a nervous young graduate student who was in awe of everything around him and had no idea what scientific research was all about. When KT asked me what I wanted to do, I said, "I want to do non-linear mechanics!". The vast generality of that statement strikes me now (almost all of mechanics is non-linear!), but KT simply smiled and encouraged me to go on. Thinking back to that moment, I would like to thank him for patiently shaping me into the researcher I am today. His critical analysis of data, excruciating attention to minute detail and a boyish enthusiasm for new ideas, are lessons that I have imbibed over six years worth of interactions with him, both inside and outside the laboratory. In addition, KT has been a great teacher both of mechanics and the communication of mechanics. I would also like to thank Priti for being a genuine well-wisher in addition to being an incredible host when we were invited to their house during the holidays.

Next, I would like to thank my thesis committee, Dr. Richard Becker and Prof. Todd Hufnagel for their patient scrutiny of this thesis. I have known Todd over the years as a mentor and at times as a late night synchrotron 'lab buddy'. While I

have never taken a formal class with him, the lessons I have learned from him in the laboratory have been memorable. Rich has observed my work for a while now and I have particularly admired his attention to detail that would often question seemingly trivial assumptions. To the alumni from the Ramesh lab and collaborators from the Army Research Laboratory: Shailendra Joshi, Jamie Kimberley, Cyril Williams, Dan Casem, Jeff Lloyd, Emily Huskins and Leslie Lamberson, thank you for giving me timely guidance and encouragement during different phases of my doctoral research. A special thanks to Prof. Shailendra for hosting me at the University of Houston so I could learn the basics of crystal plasticity. I would also like to acknowledge Kavan Hazeli's role in collecting the microscopy data presented in chapter 6 of this thesis.

I owe a lot of my success and passion for research to my many teachers at Hopkins. To Prof. Vicky Nguyen, thank you for introducing me to the rigors of continuum mechanics, specifically tensor algebra and calculus. To Prof. Jafaar El-Awady, thank you for teaching me the basics of linear elasticity and plasticity. To Prof. Tim Weihs, I thank you for introducing me to the world of materials science. I came into the graduate program with a sentiment akin to fear for the materials sciences. My first graduate level materials science course with Tim not only got rid of the fear, but also introduced me to the wonders of the field. Since then, Tim has also been a keen observer of my research and his words of encouragement after my many conference presentations have greatly improved my confidence. To the late Prof. Bob Cammarata thank you for introducing me to the atomic structure of materials in

such an entertaining way. To Prof. Michael Falk, thank you for giving me a fresh perspective of thermodynamics in materials science. To Prof. Somnath Ghosh, thank you for introducing me to the rigors of the finite element method. Your course helped me appreciate the subject well beyond simply using a software.

My foray into graduate education would not have been possible without some amazing mentors during my undergraduate studies. To Prof. M. S. Sivakumar, thank you for being available any time to give me advice during and after my short stint at IIT Madras. To Prof. Sankaranarayanasamy, thank you for the advice you gave me when I was confused between going to graduate school and to work in the industry. At this juncture, I would also like to thank my high school teachers, especially Sampath sir and Shanthi Ashokan ma'am for passionately teaching me the sciences. A special shout-out to Visalakshi ma'am for her constant encouragement and support throughout middle and high school.

My friends have been my sources of support and inspiration through the years and graduate school was no exception. To the past members of the Ramesh group: Adam, Justin, Neha, Andy, Eswar, Ravi, Jamie and Lukasz, thank you for being great mentors. I would specifically like to thank Adam, Justin, Neha and Eswar for making me feel comfortable during my early years in the group. I still enjoy the memories of Adam always answering my nosy questions with a smile and Justin walking down to the lab to simply appreciate and answer doubts that I would have.

To the current members of the group: Matt, Meng, Andrew Leong, Debjoy, Amy,

ACKNOWLEDGMENTS

Andrew Robinson, Jason, Kimmie, Tracy, Minju, Alex, Sakshi, Gary, Fatma and Charles, your constant encouragement and critiques have played a very important role in shaping me as a researcher today. I enjoyed some very special friendships with you within the group. Matt was my first teacher of experimental mechanics. I owe the genesis and growth of my experimental skills to him. From a teacher to a great friend, Matt has played an important part during my journey in the Ramesh lab over the last six years. To Eswar Prasad, Jamie Hogan, Ravi Sastri and Andrew Leong, thank you for being my favourite post-doc mentors. In addition to science and data, I would always remember discussions with Eswar on philosophies of science, pragmatic advice and ensuing debates with Jamie and Ravi's life lessons on how I should decouple science and its associated politics among many more. To Tim Wright and Jim McCauley, thank you for the excellent discussions during group meeting. I have personally learned a lot from your experience and enthusiasm for knowledge.

Meng and I started working in the lab around the same time and we 'grew up' in the lab together. The endless hours we spent discussing optics, mechanics, experiments, history, geography, economics, politics and what not, have been memorable and I shall cherish those times. As gym coach, running partner and housemate (in addition to being synchrotron 'lab buddy') Andrew Leong and I have many memories to look back up on. To Debjoy and Amy, thank you for being pro-active in bringing the group together socially. The reputation that the Ramesh group has for being one of the few close-knit groups is primarily due to your efforts. In Debjoy I found a great

critic, coach, friend and a climbing teacher. Amy, our random discussions in the office and outside about running, Debjoy, paper reviews, travel and people who've suffered mild blows to the head have been fun and I will miss them. To Andrew Robinson, you have been an amazing and entertaining friend during the short time we overlapped at Hopkins. I particularly admired and learned from your brash outspoken attitude that very few people possess. Thank you for organizing the Montana trip that brought the entire group together and for leading us on a 'less-trodden' path during the Mt. Reynolds hike. The many conversations on kolsky bars, optics, helmets, philosophy and motorsports with Jason; on dogs, travel and swimming lessons with Kimmie; kung-fu, sport, food and bad puns with Tracy; and Alex's excellent cooking are memories I take with me as I leave Hopkins. To Sakshi, thank you for all those late night conversations on topics ranging from mathematics to society. To Minju, it has been great fun working alongside you these past few months. I would also like to thank my friends in the solid mechanics and materials science groups over the years: Suman, Ahmed, Shinu, Gianna, George, Harsh, Anindya, Max, Bunny, Luoning, Suhas, Xiaolong, Matt Vaughn, Kelvin, Barbara, Quan, Hao, Nick, Peng for their support and encouragement. The regular sports seasons, lab socials and many impromptu dinners and conversations have been great fun over these years.

To the staff at the mechanical engineering department and the Hopkins Extreme Materials Institute, thank you for keeping me shielded from administrative paperwork while I did my research. I would specifically like to thank Mike Bernard for being

ever so helpful and resourceful when I needed him, Katie Vaught for tolerating my frequent pestering and being a great friend and Bess, for always being ready to handle any administrative or multimedia hassle that we often could not solve. To the other staff at ME and HEMI: Kevin Adams, Scott McGhee, Jess Ader and Phylis Sevik, thank you. I would also like to take this moment to thank my friends at the JHU badminton club for the training sessions and friendship during those many nights on the court.

To my friends outside the Ramesh lab, I owe a lot of what I am today both personally and professionally. They have been as much family as friends. Kau has traveled this journey with me right from our times at NIT Trichy and I couldn't possibly do justice to describing his role as a close friend, brother, mentor and confidante. Prakruti 'Anni' taught me the beauty of revelling in simple things in life and she would always be around to cheer me up. Of course, her legendary bisi bele bath, rasam and puliogare leave out much to be spoken about. To little Keshu, the last eight months around you have been great fun and I am looking forward to seeing you grow over many more years to come. 'UA' Kiran and 'Geico' Kavitha have always been around during the times I needed to take a break from lab work and a connect back home, not to mention the amazing food they would cook during our periodic 'gang meet-ups'. To Kamal and Sugatri thank you for sharing this journey with me over the past years. Having been pampered by these three couples for as long as I can remember them, I seldom felt away from home in their presence. To Sayee, Nikhil,

ACKNOWLEDGMENTS

Pooja, Raghu and Aditya thank you for the great company during my early years at Hopkins.

The endless banter with Swathi on thamizh movies, food (especially Kiran's 'kola' balls), Chennai and many more leave me with many nostalgic memories and yet another lifelong friend. Preetham and I traveled to the US together and I shall forever relish memories of our early badminton games and carefree conversations. To Ghanesh, Aravinth, Purnima, Swetha, Sathish, Adarsh, Adi and Mohnish, the last few months we have spent together over potlucks, theater visits and game nights have been immense fun. While our friendships got strong over a short time, it is a pity I have had so little time to spend with you all and I hope our paths cross again.

To the 'suthurs' of NIT Trichy, I would not have reached this point if I hadn't met you all. Malar 'Paappa' has always been a trusted mentor, critic and wannabe bully. 'Bheem boy' Aashish taught me the value of controlled aggression and calmness. 'God' Roshan taught me the value of cold logic. My memories of college and the automobile lab with Kau, Paappa, Bheem, God, 'Suthur' MV, 'Daddy' Naga, 'Fruitwan' Jeet, 'Sleepy' Karthi, 'Ungle' Sathiya, 'Bullet' Ghanesh and 'Boose' Bhuvanesh have been the best of my life, and I have frequently looked back at them with fondness over the past six years. You were all responsible for me to pursue my graduate studies in the first place and continue to inspire me.

To my boys from school: Siddhu, Vivek, Arvind, Naga, Pranav, Hari and Bharath, our frequent conference calls and trips in the US will be cherished. I have known

many of you for over fifteen years now and our childhoods are intertwined. To the extended gang: Saro, thank you for being as important a friend as Siddhu himself has been; to Keerthana, you've been a great friend well before you became a part of this gang; thank you for the friendship and encouragement. To Bhargavi and Sushmita, welcome, and I hope to know you both better over the years to come.

To Deepi akka, thank you for being a personal inspiration and role model. I would also like to thank some of my 'older' friends: Mala aunty, Raju uncle, Ramesh uncle, Suju aunty, VR uncle, Meena aunty, Viji aunty and Guna uncle for being genuine well-wishers since well before my memory serves me.

To my grandparents, thank you for your care and support over the years. To Veena, from squabbling siblings to having conversations about life, you and I have both grown beyond recognition. Thank you for being understanding and trusting me for advice when you needed them. There will come a time when I will need yours too, and I trust you to give them to me. My father has been one of my greatest inspirations. From being a disciplinarian to a close companion, my memories of him have helped me make decisions and push the extra mile when I needed to. To my mother, you have been my strongest support system and a great friend. Thank you for teaching me discipline and strength, for always encouraging me to do what I wanted to do under any circumstance. Your role in this thesis is as important as mine.

Dedication

To Amma for being the boldest person I know, to Appa for being my role model to date, to my friends for being my mentors on life, to Veena for her trust & to nature for keeping us all enthralled!

Contents

List of Tables

List of Figures

Chapter 1

Introduction

The drive towards energy efficient technology is becoming more relevant in modern science and engineering. In addition to the more recent quest for renewable energy across disciplines, the study of lightweight structural metals has been a long standing effort in this direction. Traditionally, high strength steel is used for structural applications, but steel began to be replaced by aluminium around the turn of the 20th century. With a two-third reduction in density, magnesium has the potential to take steel's place as the most used structural metal (e.g., Pollock [6], Luo [7], Mordike and Ebert [8]) with applications in the automotive, aerospace, military and (by extension) manufacturing sectors. By the very nature of many of these application environments, the material is required to perform well under extreme conditions of pressure, temperature and loading rate. While significant strides are being made towards improving the alloying and processing capabilities of magnesium, it's behavior under extreme

loading conditions remains relatively less understood (Prasad et al. [9]).

This thesis embarks on a fundamental study of the behavior of magnesium under high loading rates.

1.1 The paradigm of mechanism-based multi-scale mechanics

At the smallest length scale relevant to this thesis, a material is an arrangement of atoms. In crystalline systems, this arrangement is periodic with the smallest repeating unit termed a unit cell. At a basic level, during small *elastic* deformations, the lattice arrangement and the shape of the material is preserved upon unloading. However, at large enough deformations, the material becomes permanently deformed and is said to have undergone plastic deformation. This occurs through the propagation of specific defects across the lattice at the atomic length scale (order of angstroms). The effects of these defects can be observed at different length scales all the way up to the macroscopic scales visible to the naked eye.

The macroscopic material response can be understood as a consequence of fundamental deformation mechanisms within the material. The rationale for this approach is simple in concept. The macroscopic rate of plastic deformation in a material is directly influenced by the rate of evolution of defects at various length scales and time scales. If we understand the evolution rate of these mechanisms as a function

of their driving forces, we should be able to build physically robust predictions for macroscopic strength and failure in these materials. The evolution rates as a function of their driving forces at the microscopic length scales are referred to as *kinetic laws* in this thesis and in literature.

However, this is a difficult problem. Direct measurements of the evolution of these defects at the small length and time scales are very difficult, and there is always a trade-off between the spatial and temporal resolutions. The instrumentation required to make measurements at small length scales typically lacks the time resolution, and vice versa. This often necessitates the use of simplifying assumptions that tend to obscure some of the physics involved. It is, hence, crucial to make decisions about the relevant physics that needs to be captured, which often requires the use of a mathematical model. Once we understand the kinetics to the desired level of detail, scaling this knowledge up to the macroscopic scale is yet another challenging task. We follow this paradigm of mechanism-based multi-scale mechanics throughout this thesis.

1.2 Hexagonal close packed metals: An overview of plasticity and failure

Magnesium has a hexagonal close packed (hcp) crystal structure. While our primary focus is on this metallic system, the understanding developed could be extended to

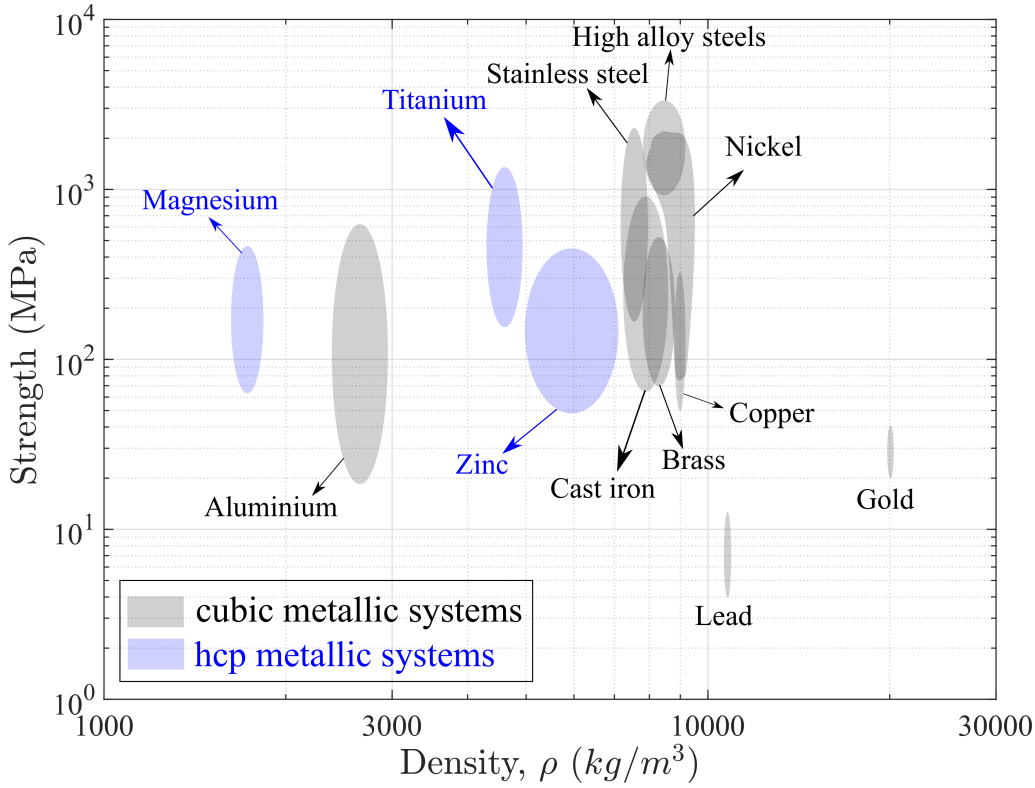

Figure 1.1: Ashby materials selection chart for metallic alloy systems plotting strength on the y-axis and density on the x-axis. Notice that most of the low density materials with the exception of aluminium are hcp with magnesium being the least dense.

other hcp metals as well. Figure 1.1 is a commonly used materials selection chart conceptualized by Ashby [10]. The x-axis is density and the y-axis is strength of the material. The regions marked show the range in this strength-density space where each material system resides. Data referred to in Figure 1.1 is a small subset (relevant only to metallic alloys) of the original series of charts. The cubic alloys are marked in gray while the hcp alloys are marked in blue. With the exception of aluminium, most of the low density metallic alloys have an hcp crystal structure. Hence, in

the general context of lightweight metallic systems for energy efficient technology, a deeper understanding of hcp metals and their alloys is desirable.

In face centered cubic (fcc) and body centered cubic (bcc) crystals, the most common mechanism of plastic deformation is dislocation slip. Dislocations are one-dimensional defects in the atomic lattice formed by the shearing of one portion of the crystal lattice with respect to another. The result of this shearing is an extra half plane of atoms that propagates through the crystal. The dislocation is defined at the edge of this extra half plane. Figure 1.2 is a two-dimensional schematic of a dislocation in a lattice. The spheres represent atoms and the extra half-plane is marked by the darker spheres. On the application of shear stresses in the direction of dislocation slip (red arrow in Figure 1.2), these defects glide on specific crystallographic planes (whose normal is marked by the blue arrow in Figure 1.2). The specific combination of slip plane and direction is used to define a specific dislocation type and is referred to as a dislocation slip system (or simply 'slip system'). The most common dislocation slip systems that are activated in a crystal are governed by the close packed directions, and hence vary for different lattice structures. The propagation is stress-driven and the dislocations begin to glide only when the resolved shear stresses on their slip planes exceed a critical value commonly known as the critical resolved shear stress (CRSS).

While dislocation slip systems are observed in hcp metals as well, they are more complex than these traditionally studied cubic metals, a fundamental reason being the

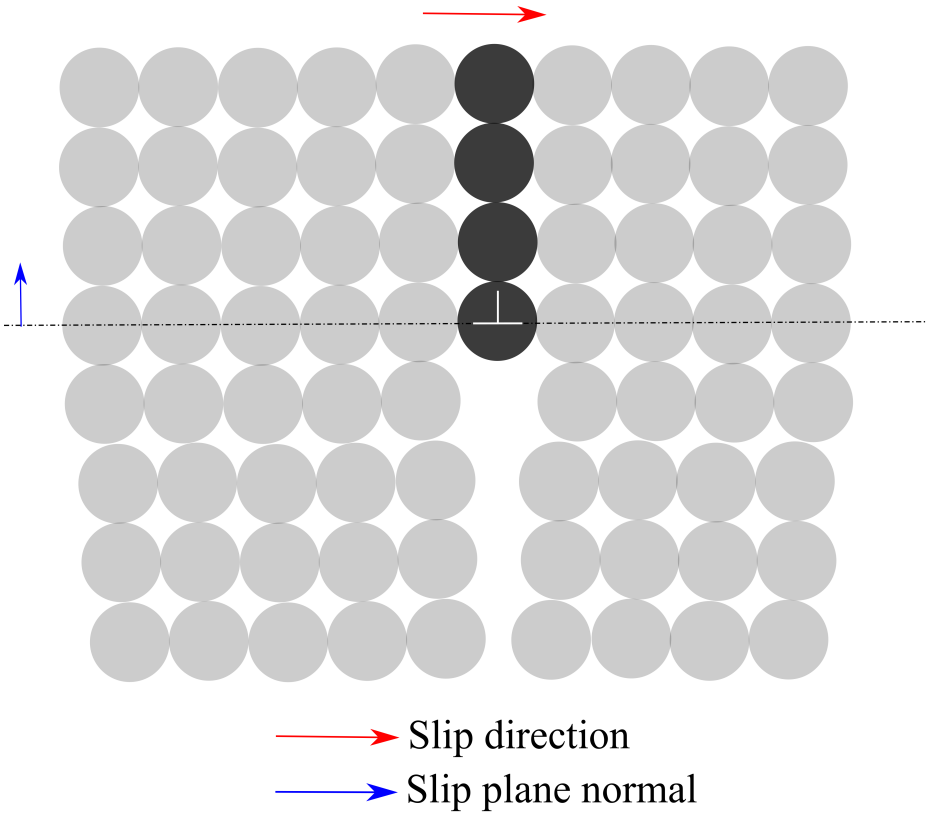

Figure 1.2: A schematic of a dislocation in a generic cubic crystal. The spheres represent atoms in the crystal. The extra plane of atoms is marked by the darker spheres.

greater asymmetry of the hcp lattice than the cubic lattices. Figure 1.3 is a schematic of the hcp lattice with the circles representing atomic positions in the lattice. The four commonly used axes are marked, along with the 'basal plane'.

The asymmetry of the crystal results in plastic *anisotropy* i.e. the shear strength of the crystal within the basal plane is different from that out of the basal plane. This implies that the CRSS for dislocations that cause shear within the basal plane is much lower than those that cause shear out of the basal plane. Under general loading conditions, 'deformation twinning' is an alternative mechanism that may cause easier

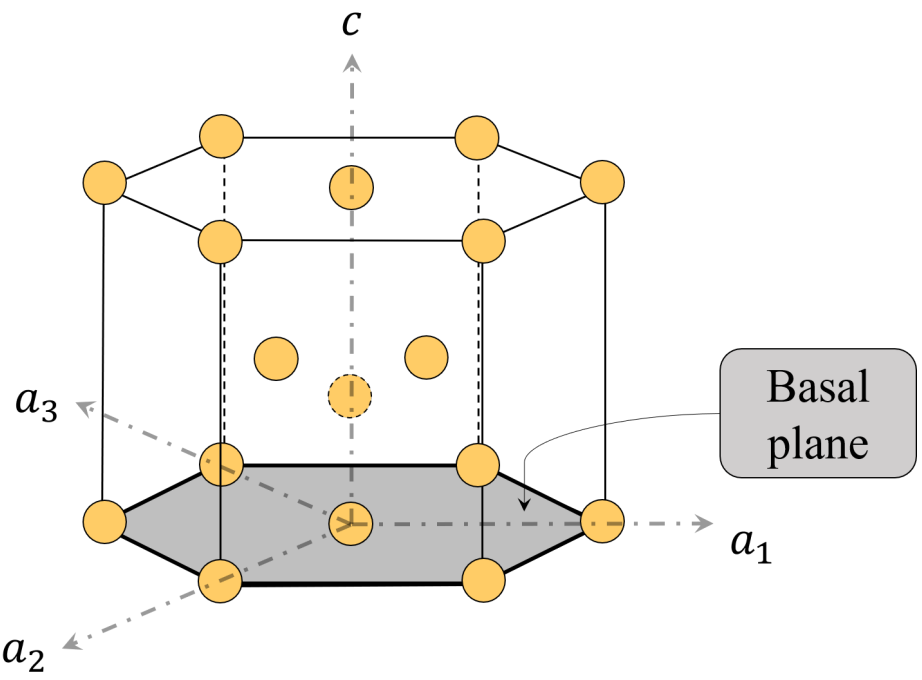

Figure 1.3: A schematic of hcp lattice. The circles represent positions of atoms in the lattice. Four commonly used axes and the basal plane are marked.

out-of-plane deformation than dislocation slip.

Deformation twins are volumes within the lattice which are re-oriented with respect to the parent lattice about a specific lattice direction. The re-oriented volume is bounded by surface defects commonly known as twin boundaries. Depending on the specific type of twin, the twin boundaries may or may not fall on a rational crystallographic plane (Christian and Mahajan [11]). As a deformation mechanism, twinning has been observed in fcc and bcc metals, particularly at very high strain rates involving shock loading or at cryogenic temperatures. In magnesium, twins are easily nucleated (for e.g. Barnett [12]).

Both dislocation slip and deformation twinning operate fundamentally at the sin-

gle crystal scale. A material system used for structural applications usually involves an aggregate of millions of small single crystals (also known as grains) mis-oriented with respect to each other. Such a material is referred to as being 'polycrystalline'. The orientation distribution of the grains is called 'texture' and is a crucial factor that controls material response. For some manufacturing and structural applications, a completely random texture is desirable such that every orientation of the block is equivalent and hence the material is isotropic. Many structural applications however, could take advantage of material anisotropy if it could be controlled. The inherent anisotropy of the hcp crystal often results in a directional texture, where most grains have a preferred orientation. Such a textured material would retain some of the plastic anisotropy of the hcp single crystal.

Anisotropy induced by texture also has important consequences in material failure. The differences in the strength of the material for different loading orientations may result in local heterogeneities in deformation (Needleman and Tvergaard [13]) and an onset of softening of the material. These local heterogeneities may grow, eventually resulting in material failure. Continuum plasticity shows that isotropic materials (at the macroscopic length scales) are often more resistant to these localization events than anisotropic materials (Needleman and Tvergaard [13]). High loading rates also have a significant effect on material strength, as discussed in section 1.3.

1.3 Dynamic behavior of materials: A background

The response of materials to high rates of deformation has been a subject of scientific research for nearly seven decades now. This focus is primarily because the response of many material systems at high loading rates is different from that at isothermal, quasi-static loading conditions. The time scales associated with dynamic phenomena (wave propagation being an example) span nanoseconds to milliseconds for typical structural length scales. Rapid increase in energy input at these short time scales tends to activate mechanisms in the material that would otherwise remain dormant at much longer time scales. Naturally, this changes the competition between different deformation mechanisms, eventually influencing material strength and failure.

In the context of plastic deformation of metals, dislocation slip at high rates of loading has been studied in considerable detail (Meyers [14]). The propagation of dislocations plays an important role at high strain rates (including shock loading conditions). With respect to twinning, we remain relatively ignorant of the kinetics of nucleation and growth. This thesis addresses some of the gaps in our understanding of twin nucleation and growth.

In the context of failure, common mechanisms of ductile failure at high strain rates include, adiabatic shear localization, ductile tearing and spall. Adiabatic shear

localization occurs due to the lack of sufficient time to conduct heat away from sites of localized deformation. Thermodynamically, this problem can be viewed as a competition between a material's ability to increase it's temperature locally (visco-plastic heating and specific heat capacity) and to conduct heat away from a site (thermal conductivity). Spall is a dynamic tensile failure process occurring in regions where large hydrostatic tensile stress states are developed. These high local stresses result in nucleation, growth and coalescence of voids in the material, eventually resulting in fracture. While the major focus of this thesis is on plastic deformation at high rates rather than failure, some observations and measurements of shear localization and fracture will be discussed. Spall, however is not studied in this thesis.

1.4 Plastic deformation mechanisms in magnesium

Figure 1.4a shows a schematic of the hcp lattice with four basis vectors marked as c, a_1, a_2 and a_3. The crystal lattice has the same dimensions (or lattice parameters) along the three a-axes, whereas it is longer along the c-axis (asymmetric). The aspect ratio of the crystal is defined by the ratio of the lattice parameters along the c-axis to the a-axes and is commonly called the c/a ratio in literature. While three basis vectors suffice to define directions and planes in the crystal, it is often convenient to use all four for hexagonal lattices. The notation hence used is called the four-index

notation and will be employed throughout this thesis.

Figure 1.4b and Figure 1.4c show the commonly observed dislocation slip systems that cause shear parallel to the basal plane of the hcp lattice. The arrows show slip directions and the shaded planes mark the slip planes. The c/a ratio controls the relative CRSS between different mechanisms. In magnesium (and in most hcp metals) basal ($\{0001\}\langle 11\bar{2}0\rangle$*) and prismatic ($\{10\bar{1}0\}\langle 11\bar{2}0\rangle$) slip are the most common mechanisms causing shear within the basal plane of the lattice (Figure 1.4b). Pyramidal $\langle a\rangle$ slip ($\{10\bar{1}1\}\langle 11\bar{2}0\rangle$) also causes shear within the basal plane (Figure 1.4c). Shear out of the basal plane is caused by pyramidal $\langle c+a\rangle$ slip ($\{11\bar{2}2\}\langle 11\bar{2}3\rangle$).

While there are multiple slip systems causing shear within the basal plane, there is only one common slip system that causes shear out of the plane. In addition, as discussed in section 1.2, the asymmetry of the crystal structure results in these different slip systems having very different CRSS. Table 1.1 shows the mean and standard deviation in CRSS values for different slip/ twin systems from literature compiled by Zhang and Joshi [2]. Figure 1.5 shows a bar plot for these CRSS values with the scatter from literature. Ignoring the last two data points corresponding to twinning for now, notice that the CRSS for pyramidal $\langle c+a\rangle$ slip is higher compared to the other slip systems that cause shear within the basal plane (marked by the blue bars). As noted in section 1.2, deformation twins help accommodate out-of-plane

*wherever applicable $\langle\,\rangle$ denotes a family of crystallographic directions along which dislocation glide/twinning shear occurs and $\{\,\}$ denotes a family of plane normals on which the glide/shear occurs. Specific directions and plane normals are denoted by [ ] and ( ) respectively.

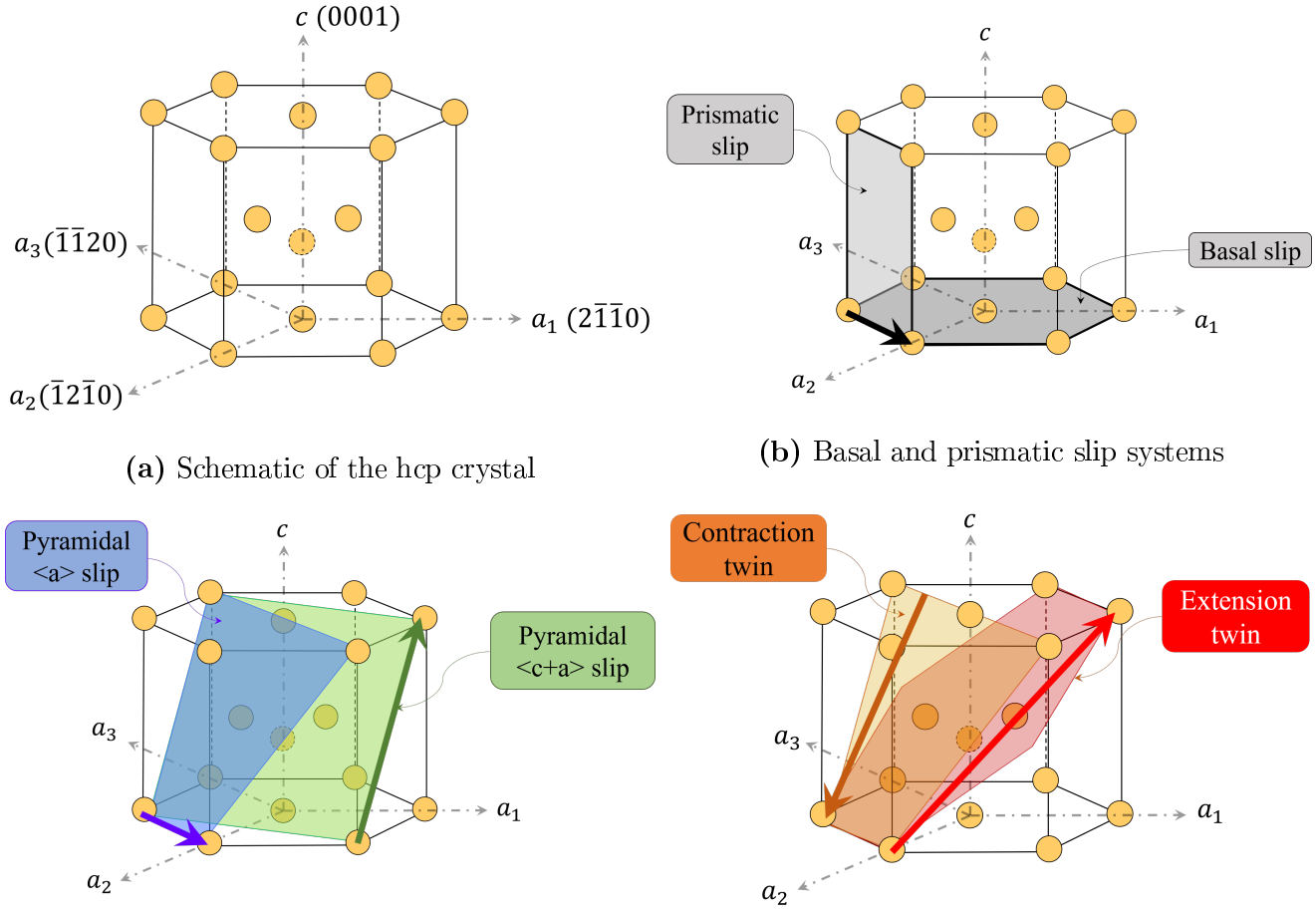

(a) Schematic of the hcp crystal

(b) Basal and prismatic slip systems

(c) Pyramidal slip systems

(d) Deformation twin systems

Figure 1.4: (a) Schematic of the hcp crystal with axes marked using the 4-index notation; (b)-(d) Scehmatic representation of slip and twin systems commonly observed in the magnesium single crystal.

Slip/ twin system	CRSS (MPa)	
	Mean	Standard deviation
Basal slip	0.8	N/A
Prismatic slip	32	16
Pyramidal slip	50.7	13.5
Extension twinning	2.3	1.1
Contraction twinning	64.8	27.8

Table 1.1: Critical resolved shear stresses for slip and twin systems in magnesium compiled by Zhang and Joshi [2].

deformations.

Like dislocations, twins may also have different crystallographic types. A specific twin type is described by the plane (denoted using {}) and direction (denoted using ⟨⟩) along which the twin is constrained to nucleate and grow. The planes are called 'twinning planes', the directions are called 'twinning directions' and the shear strain caused due to the lattice re-orientation within the twin is called 'twinning shear'. The specific twin types that are likely to nucleate depend on the c/a ratio of the hcp crystal (Yoo and Lee [15]). In magnesium, the extension twin ($\{10\bar{1}2\}\langle 10\bar{1}1\rangle$) that causes extension of the c-axis of the crystal is the most commonly observed twin type, whereas contraction twins ($\{10\bar{1}1\}$) that result in contraction of the c-axis are less commonly observed. While it is unclear if twins are driven solely by a resolved shear

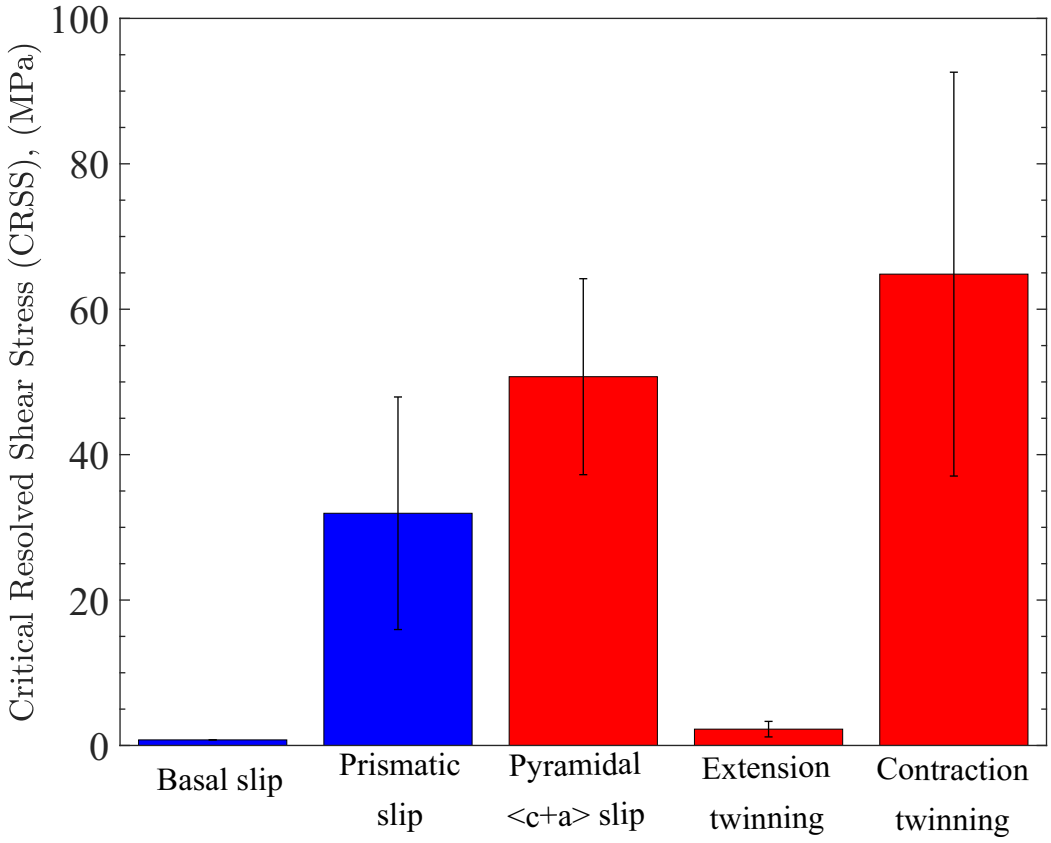

Figure 1.5: CRSS for different slip and twin systems in a magnesium single crystals from literature compiled in Zhang and Joshi [2].

stress, this is a simplifying assumption made in current computational models (for e.g. Zhang and Joshi [2], Lloyd and Becker [16]). Notice (from Figure 1.5) that the "CRSS" for extension twins appears to be a lot less than that for pyramidal slip or contraction twinning, making extension twinning the most preferred mechanism to cause out-of-plane deformation in this hcp crystal.

1.5 Organization of this thesis

In this thesis, we seek to understand plastic deformation as a function of strain rate in magnesium and its alloys using the micro-mechanical approach described in section 1.1. We use a range of experimental techniques to probe the material at different length and time scales. Wherever possible, we employ theoretical analyses to better understand the underlying deformation mechanisms.

We begin in chapter 2, by measuring the macroscopic mechanical response of a textured polycrystalline magnesium alloy (AZ31B) across eight decades of strain rate. The effects of strain rate and loading orientation on flow stress, hardening and failure are discussed along with the potential mechanisms involved. Chapter 3 takes this study forward by discussing fundamental deformation and failure mechanisms under high strain rate loading from the nano-meter up to the micro-meter length scales. The mechanisms at quasi-static and high strain rates are compared, to better understand the rate dependent macroscopic response. The relative activation and evolution of deformation twinning across strain rates is found to have a crucial role to play in the rate dependent response of these textured polycrystalline alloys.

Through the next part of this thesis, we explore deformation twinning as a fundamental mechanism in greater detail. Chapter 4 presents an experimental study on the dynamics and kinetics of twin nucleation and growth in single crystal magnesium at high strain rates. Analysis of the data reveals the competition between twin nu-

cleation and growth during different stages of deformation. In chapter 5, we seek to extend our understanding of twin growth by proposing a thermodynamically consistent multi-scale theoretical framework (inspired by Rosakis and Tsai [17] and Gurtin [18]) to study the growth dynamics of a twin boundary in an anisotropic elastic-plastic continuum.

Chapter 6 covers a different yet related aspect of deformation twinning. As an extension to chapter 4 and chapter 5, we study the crystallographic nature of twins nucleated at quasi-static and dynamic rates using microscopy on samples recovered after compression (we will refer to these studies as 'post-mortem'). The study concludes that the crystallographic twin types nucleated are similar across low and high strain rates within the strain rate range interrogated. We finally close in chapter 7 by summarizing the key findings in this thesis, their implications for material design, and potential avenues for future work.

Chapter 2

The effect of strain rate on plastic flow and failure in polycrystalline magnesium alloys

Preface: The following chapter is largely based on a manuscript submitted for publication. The co-authors are Xiaolong Ma, Nicholas M. Krywopusk, Laszlo J. Kecskes, Timothy P. Weihs and K. T. Ramesh. VK was the lead author in this study and performed the high strain rate experiments and related microscopy, data analysis, interpretation and manuscript preparation. XM performed the post-mortem transmission electron microscopy and analysis of the microscopy data. NMK was involved in the material processing and obtained the quasi-static dataset. LJK was involved in material processing and mentorship. TPW and KTR were PI's and involved in

mentorship, problem formulation and data interpretation. All authors contributed towards manuscript preparation and review.

2.1 Introduction and background

Polycrystalline wrought and rolled magnesium alloys suffer from low ductility and significant anisotropy. This is due in part to two coupled effects; (1) the anisotropy of the hexagonal close packed crystal structure and (2) the strong texture of such polycrystalline materials (discussed in section 1.2).

The inherent asymmetry of the hcp crystal results in the availability of limited easy slip systems. We showed (Figure 1.5) that slip mechanisms that cause deformation along the basal plane have a significantly lower critical resolved shear stress (CRSS) than out-of plane slip (prismatic and pyramidal slip) (Zhang and Joshi [2], E.W.Kelley [19]). This strong anisotropy in the CRSS of existing slip systems results in the activation of twinning as a common mode of deformation (Christian and Mahajan [11], Barnett [12], E.W.Kelley [19], Barnett [20], Prasad and Ramesh [21], Dixit et al. [22], Kannan et al. [23]). As a result of this complex set of deformation mechanisms with very different evolution rates, the magnesium crystal exhibits different flow stress and strain hardening trends along different loading orientations. When compressed along the c-axis it exhibits high flow stress, strong hardening and relatively low ductility (eg. Nave and Barnett [24], Agnew and Duygulu [25]). When loaded along a direction that is $\sim 45^{\circ}$ to the c-axis, it exhibits weaker hardening and greater ductility (eg.

Yi et al. [26]). However, when the crystal experiences extension along the c-axis, the stress-strain curve exhibits an initial weak slope followed by rapid hardening (eg. Dixit et al. [22], Kannan et al. [23]). The magnesium single crystal is hence said to have anisotropic strength, hardening and ductility.

In addition, most polycrystalline aggregates of magnesium tend to develop texture (section 1.2), an exception being AMX602 (Meredith et al. [27]). Rolled magnesium alloys possess significant mechanical anisotropy because of this texture (eg, Barnett [20], Ulacia et al. [28]). Similar anisotropy is observed in extruded bars as these also have basal textures, only slightly weaker than the rolled material (Dixit et al. [22], Yi et al. [29]). Hence, texture is a major variable that affects the mechanical response of a polycrystalline aggregate. At a micro-structural length scale, the relative activity of mechanisms changes with the dominant texture (relative to the loading orientation). In addition, under high strain rate loading conditions, understanding the evolution of dislocations and twins as a function of strain rate is critical in order to adequately model the effects of strain rate on macroscopic plastic flow characteristics such as strength and hardening, as well as subsequent material failure.

In this chapter, we study the effects of strain rate on the mechanical behavior of an AZ31B alloy processed by Equal Channel Angular Extrusion (ECAE) using fundamental experiments (i.e. imposing simple boundary conditions). We seek to develop detailed insight into the mechanical response of this ECAE AZ31B alloy across eight decades ($10^{-4} - 10^{4}\ s^{-1}$) of strain rate. Macroscopic flow stresses, hardening

and failure are characterized across this entire range of strain rates.

2.2 Material investigated

The material investigated was an AZ31B magnesium alloy processed by Equal Channel Angular Extrusion (ECAE) (e.g., Kim et al. [30], Agnew et al. [31], Figueiredo and Langdon [32]). ECAE is a severe plastic deformation approach that has been used to improve the ductility and reduce the anisotropy of wrought or rolled materials. Severe plastic deformation occurring at the intersection of the channels (shear zone) (Figure 2.1a) results in significant grain refinement (final grain sizes from sub-micron to a few microns) (eg. Agnew et al. [31], Figueiredo and Langdon [32], Yu et al. [33], Koike et al. [34], Li et al. [35]).

The ECAE alloy used in this study was obtained by extruding a warm-rolled H24 condition commercial alloy block (Magnesium Elektron) through a 90° ECAE die at 200°C at the rate of 0.38 mm/s and an applied backpressure of 8.5 MPa by the $4B_c$ route (Krywopusk et al. [36]). A schematic of the process is shown in Figure 2.1a. Orientations in the extruded block are identified by three directions (Figure 2.1b): the extrusion direction (ED), the transverse direction (TD) and the longitudinal direction (LD). The resulting texture of the material (Figure 2.1c) shows that the (0001) c-axis poles are oriented at $\sim 45°$ to the extrusion direction (Krywopusk et al. [36]). This texture is different from that of conventional rolled and extruded materials which have a predominant basal texture (Ulacia et al. [28]). The average grain size was

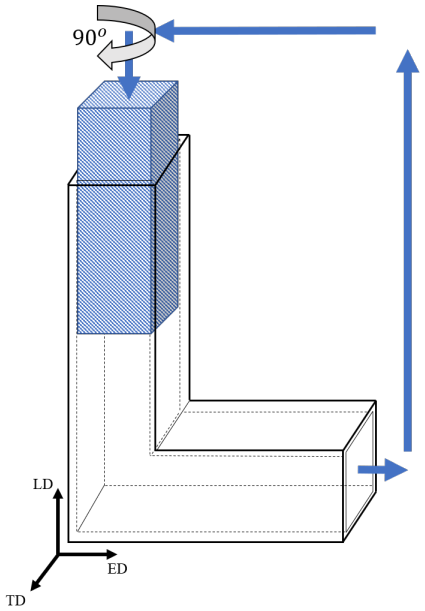

(a) Equal Channel Angular Extrusion

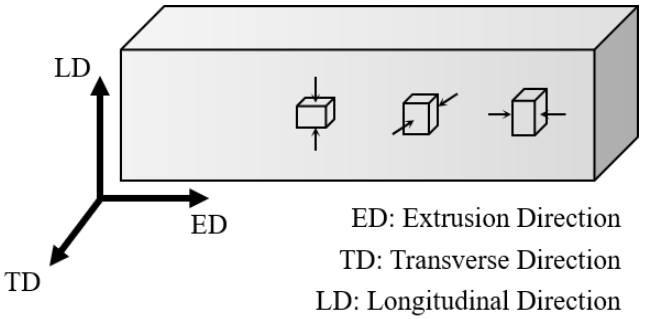

(b) Kolsky bar specimen orientations with respect to block

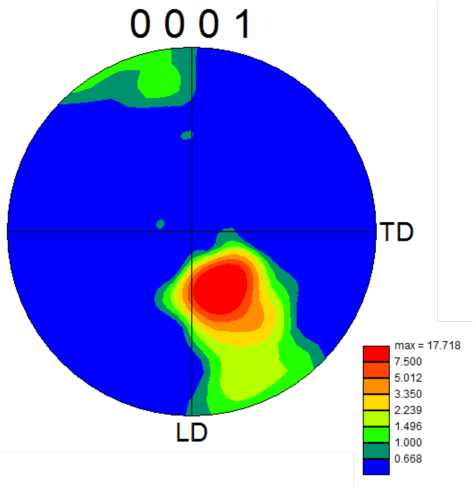

(c) Texture of ECAE block (Krywopusk et al. [36])

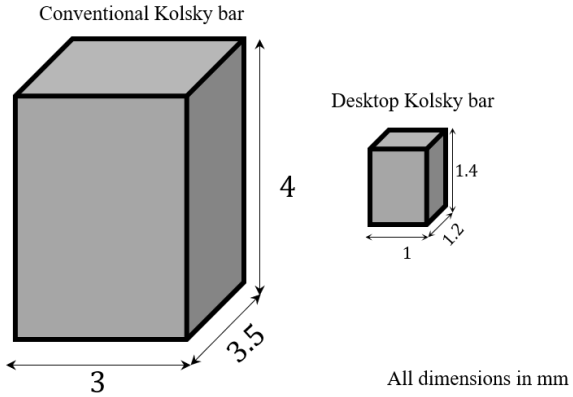

(d) Specimen geometry

Figure 2.1: Descriptions of the ECAE process, texture of the ECAE block and specimen orientations with respect to the principal directions of the ECAE block

refined to $\sim 2.5\,\mu m$ from $\sim 20\mu m$.

2.3 Experimental methods

Quasi-static and high strain rate compression experiments were performed on specimens sectioned from the ECAE block.

2.3.1 Quasi-static compression

Quasi-static data were obtained from experiments performed by Krywopusk et al. [36]. The experiments were performed at rates between 10^{-4} and $10^{0}\ s^{-1}$ using an Instron 5582 Universal Testing Machine. The details of the experimental procedure can be found in the paper by Krywopusk et al. [36].

2.3.2 High strain rate compression

Kolsky bars are the most common experimental tools used to study high rate material behavior (Ramesh [37]). The use of Kolsky bars has continuously evolved over the last six decades to understand high rate material behavior under various stress states and strain rates (Chen and Song [38]). A generic schematic of a compression kolsky bar is shown in Figure 2.2. The apparatus consists of a gas gun firing a cylindrical projectile. The projectile strikes the end of an incident bar of the same material and diameter as the projectile, sending a one-dimensional elastic stress/strain pulse down

the bar. The specimen is held between the incident bar and a transmitted bar (also of the same material and diameter as the incident bar and the projectile). Once the stress pulse reaches the specimen, the specimen deforms plastically, sending another elastic pulse through the transmitted bar, that is characteristic of the specimen stress. At the same time, the impedance mismatch between the specimen and the bars results in a reflected pulse propagating back through the incident bar. This reflected pulse is a measure of the spatially averaged strain rate in the specimen. The experiment is designed such that the specimen has a lower impedance than the bars and the bars remain elastic at all times.

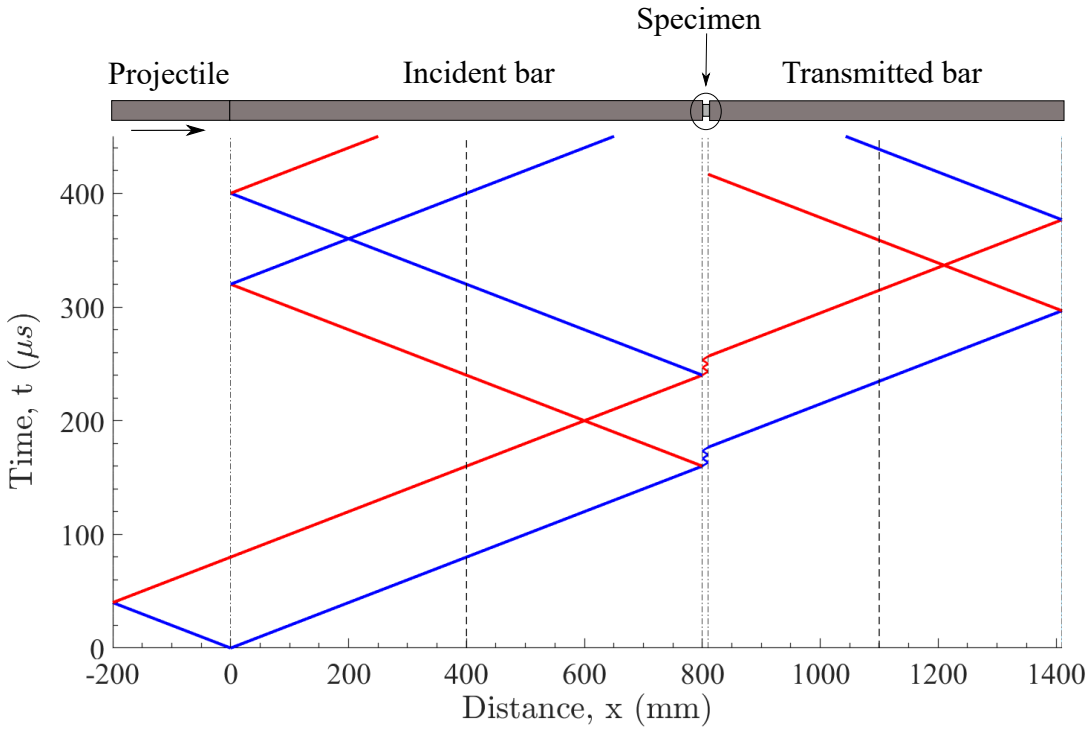

Figure 2.2: Schematic of the compression Kolsky bar. The plot below the schematic is the Lagrangian x-t diagram showing the wave propagation through the bars.

The plot below the schematic (Figure 2.2) shows the Lagrangian $x-t$ diagram (sometimes referred to as the $x-t$ diagram), where the x-axis is distance along the bars and the y-axis is time in micro-seconds. The lines are characteristic lines of the one-dimensional wave equation given by

$$x \pm ct = \text{constant},$$

where c is the longitudinal elastic wave speed in the bar. The blue lines are compressive waves and the red lines are tensile. A pair of compressive and tensile waves (or vice versa) forms a pulse. Measurement of the strains in the bar is usually made using strain gages mounted at specific positions on both the incident and transmitted bars (marked by the dotted lines on the x-t diagram).

The one-dimensional elastic strains measured on the bar can be used to calculate the engineering strain rate $\dot{e}(t)$, strain $e(t)$ and stress $S(t)$ histories in the specimen as,

$$\dot{e}(t) = -2\frac{c_l}{l_s}\varepsilon_{ref}(t) \tag{2.3.1a}$$

$$e(t) = \int_0^{t_f} \dot{e}(t)dt \tag{2.3.1b}$$

$$S(t) = \frac{A_b}{A_{so}}E_b\varepsilon_{trans}(t) \tag{2.3.1c}$$

where c_l is the longitudinal elastic wave speed in the bar defined as $c_l = \sqrt{\frac{E}{\rho}}$ (E is the Young's modulus and ρ is the material density), l_s the length of the sample along the loading direction, A_b and A_{so} are the cross-sectional areas of the bar and the specimen respectively and E_b is the elastic modulus of the bar. ε_{ref} and ε_{trans} are the

measured reflected and transmitted strains in the bars respectively. Measured incident and reflected signals are numerically corrected for wave dispersion effects caused due propagation of strain pulses down the bar (Gorham [39]). Data are plotted as true strain rates ($\dot{\varepsilon}(t)$), strains ($\varepsilon(t)$) and stresses ($\sigma(t)$) in the specimen, calculated as,

$$\dot{\varepsilon}(t) = \frac{\dot{e}}{1-e}, \tag{2.3.2a}$$

$$\varepsilon(t) = -\ln(1-e) \tag{2.3.2b}$$

$$\sigma(t) = S(1-e) \tag{2.3.2c}$$

All measures described above are compressive in nature, which means e is positive, numerically.

We used maraging steel Kolsky bars to uniaxially compress samples along the three principal directions of the ECAE block within the strain rate range of $10^3 - 10^4\ s^{-1}$. A conventional Kolsky bar was used to achieve strain rates of the order of $10^3\ s^{-1}$, and a small scale 'desktop' Kolsky bar (Jia and Ramesh [40]) was used for the higher strain rates (order of $10^4\ s^{-1}$).

2.3.2.1 Conventional kolsky bars

Two types of experiments were performed: (1) experiments designed to capture the full stress-strain history with *in-situ* high-speed imaging, and (2) recovery experiments (also with *in-situ* imaging) for post-mortem microscopy. The bars used for the former type of experiments were 9/32" in diameter and for the latter were 1/2". Recovery experiments were performed using hardened steel collars (Huskins et al. [41])

that slide over the specimen and are ground to the length required to stop further deformation of the specimen after a pre-determined strain. Recovery was performed after compression along two different orientations at 5-6% and 10-12% strains for post-mortem microscopy.

The bars were instrumented with foil strain gages, and all signals were captured simultaneously using a 12-bit digital high speed oscilloscope (LeCroy HDO4034, Bandwidth= 350 MHz, Maximum sampling frequency= 2.5 GHz).

2.3.2.2 Desktop kolsky bars

The desktop Kolsky bar is used to achieve higher strain rates, of the order of $10^4\ s^{-1}$ (Jia and Ramesh [40]). We use 3 mm diameter bars made of maraging steel and instrumented with semiconductor strain gages that are recalibrated in real-time (procedure described in section A.2). Specimen strain rate, strain and stress histories are calculated using the same equations in subsubsection 2.3.2.1. A normal displacement interferometer (NDI) was used on the transmitted bar (Casem et al. [42]) to verify the transmitted semiconductor strain gage measurements.

The NDI works as a Michelson interferometer and is used to measure the back surface displacement history on the transmitted bar. The detailed working principle of the NDI adapted to a miniature Kolsky bar can be found in Casem et al. [42]. A schematic of the NDI setup built in-house is shown in Figure 2.3a. An example raw signal obtained from the photodiodes is shown in Figure 2.3b. The inset allows us

to clearly visualize the interference fringes, each fringe corresponding to ~ 256 nm of back surface displacement of the transmitted bar.

The back surface displacement history of the transmitted bar is calculated as,

$$s(t) = \frac{N(t)\lambda}{2} \tag{2.3.3}$$

where $N(t)$ is the number of fringes measured as a function of time and λ is the wavelength of our laser source (532 nm). Using elastic wave propagation, the engineering stress in the bar can be calculated as,

$$S(t) = \frac{1}{2}\rho_b c_l v(t) \tag{2.3.4}$$

where ρ_b is the density of the transmitted bar, c_l is the longitudinal elastic wave speed in the bar (also used in Equation 2.3.1a) and $v(t)$ is the back surface velocity history in the transmitted bar obtained, by taking the numerical derivative of Equation 2.3.3.

Figure 2.4a shows the displacement of the back end of the transmitted bar, calculated from the raw data in Figure 2.3b. The two simultaneous signals agree very well with each other. The back surface velocity $v(t)$ of the transmitted bar was calculated using a moving average differential of the displacement data, and the engineering stress in the specimen is shown in Figure 2.4b. No recovery was performed during the desktop Kolsky bar experiments.

2.3.2.3 Specimen preparation

For the Kolsky bar experiments, cuboidal specimens of dimensions $3 \times 3.5 \times 4$ mm (conventional Kolsky bar) and $1 \times 1.2 \times 1.4$ mm (desktop Kolsky bar) were made

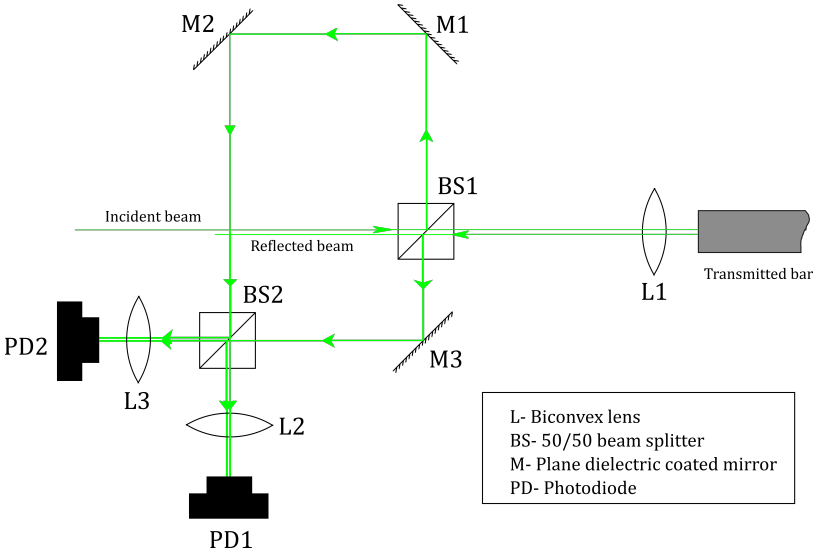

(a)

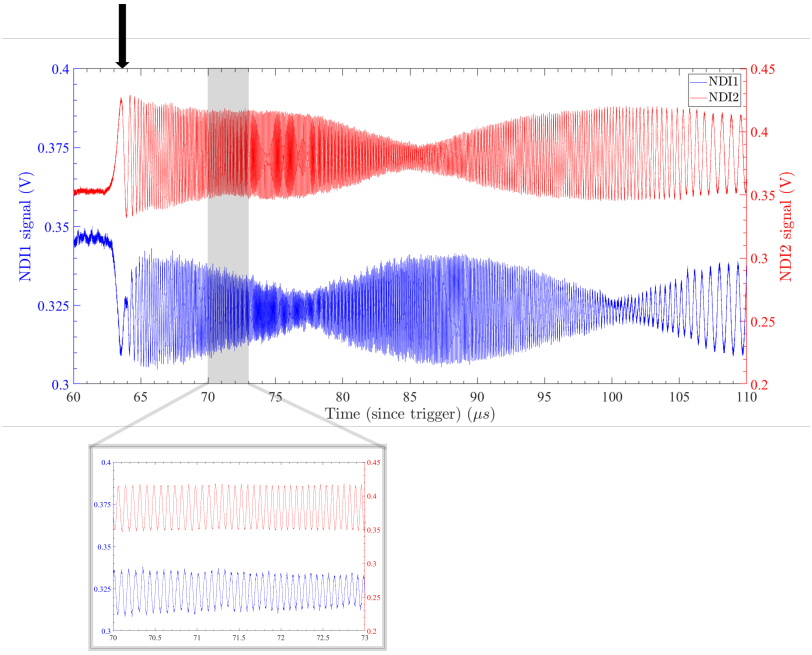

(b)

Figure 2.3: *Normal Displacement Interferometer* (a) Schematic of the NDI setup at the back of the transmitted bar; (b) Raw NDI signal from two photodiodes (PD1 and PD2). Data from each photodiode is labeled NDI1 and NDI2 in the legend. The black arrow shows the arrival time of the wave at the back surface of the bar. The inset shows a zoomed in a version of the fringes.

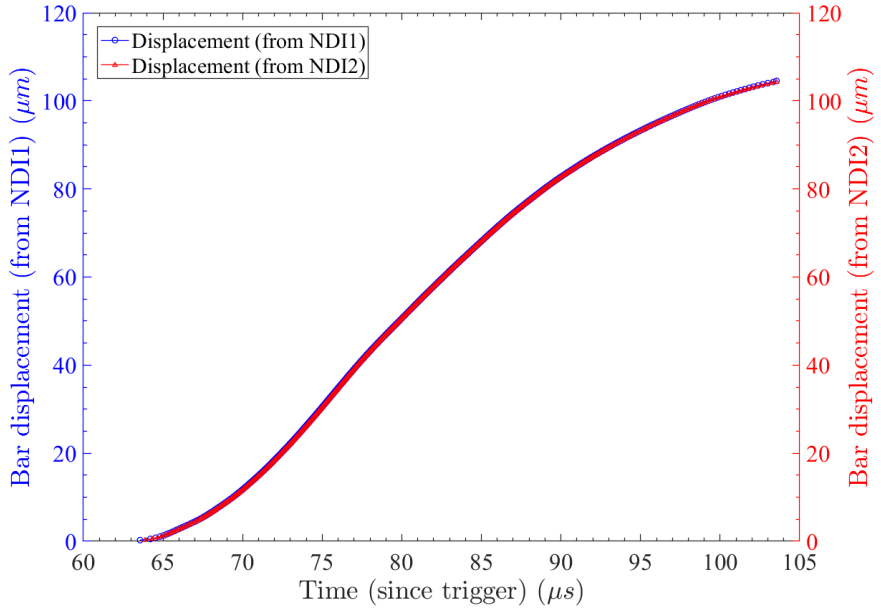

(a) Bar displacement calculated from NDI signal

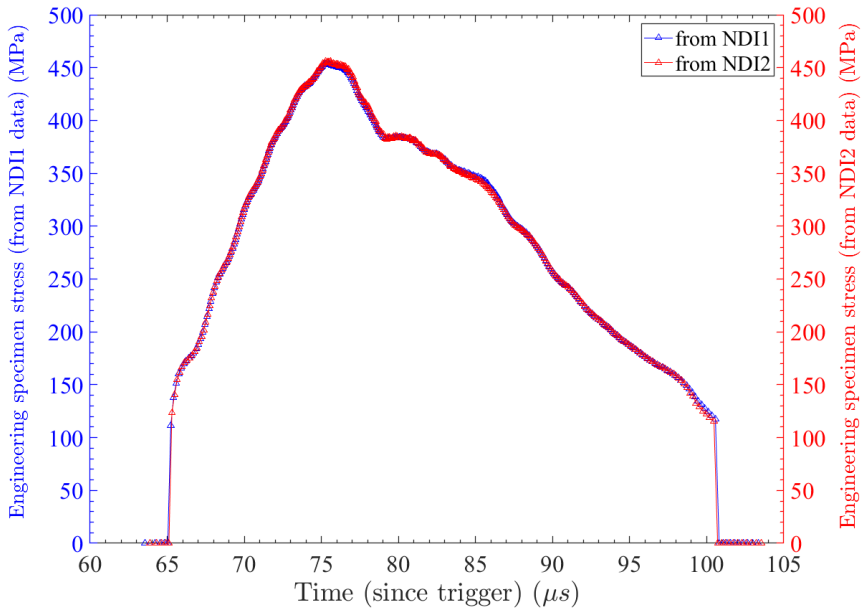

(b) Specimen stress calculated from NDI signal

Figure 2.4: Normal Displacement Interferometer (NDI) data and processing. All x-axes are on the same scale. The two simultaneous signals agree very well with each other.

from the as-processed ECAE block along the three principal orientations i.e. ED, TD and LD. Specimens of slightly larger dimensions were first cut from the interior of the block (to avoid scatter from edge effects during extrusion) using wire-Electrical Discharge Machining. The specimens were then polished down to the desired sizes with a final surface finish of 5 μm. Specimen surfaces on which the *in-situ* imaging was performed were polished down to 50 nm surface finish. Care was taken to ensure that all surfaces were parallel after polishing. Details about the imaging setup are provided in section 3.2.

2.4 Results

2.4.1 Constitutive response at high strain rates

Figure 2.5 shows representative true stress-true plastic strain curves from compression experiments, performed at quasi-static rates ($10^{-4} - 10^{0} s^{-1}$, green curves), high strain rates ($\sim 10^{3}\ s^{-1}$, blue curves) and very high strain rates ($\sim 10^{4}\ s^{-1}$, red curves). In order to make meaningful comparisons between the low and high rates, all true stress-true total strain data were converted to true stress-true plastic strain. The procedure for the conversion of the high and very high strain rate data is outlined in the supplementary section (section A.3). Representative high strain rate true stress-true total strain curves are also provided in the supplementary section (Figure A.9).

The hcp crystal schematic shown in Figure 2.1b indicates the average orientation

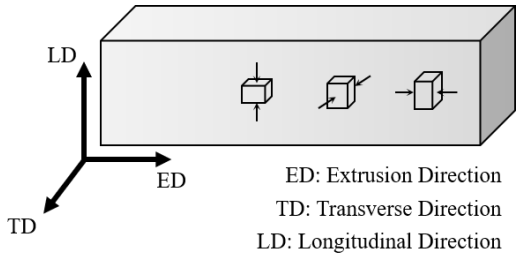

(a) Kolsky bar specimen orientations with respect to block

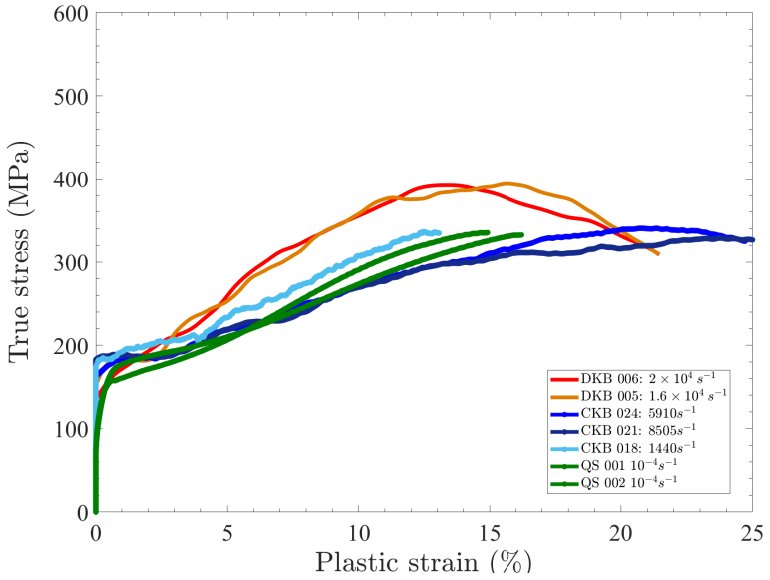

(b) ED compression: True stress Vs True plastic strain

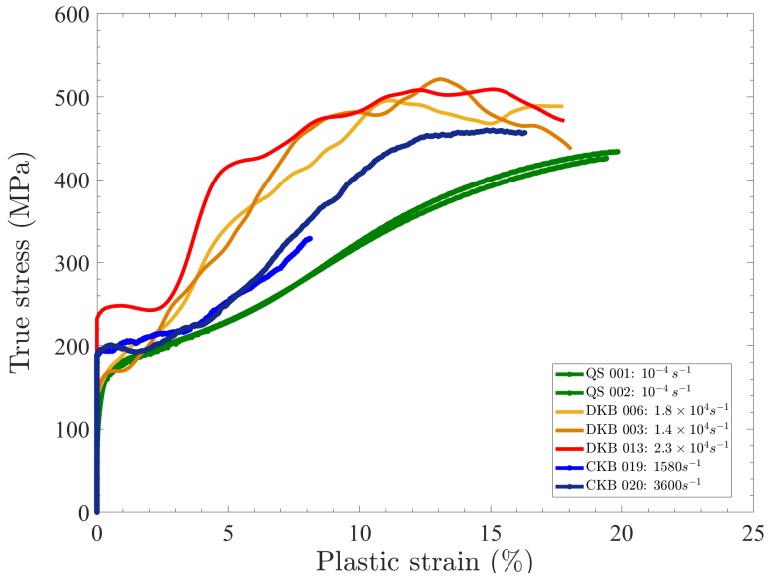

(c) TD compression: True stress Vs True plastic strain

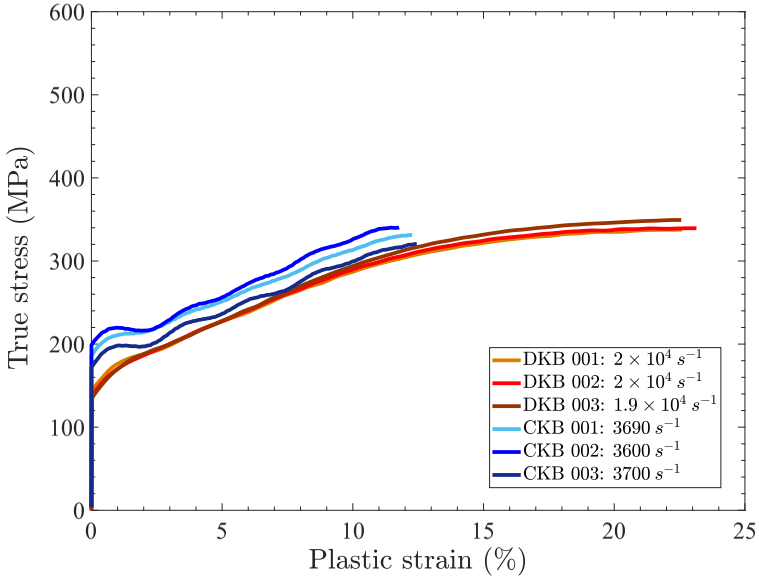

(d) LD compression: Stress Vs Plastic strain

Figure 2.5: True flow stress as a function of true plastic strain at different strain rates.

of the grains in the ECAE block based on the texture shown in Figure 2.1c. Specimens compressed along the ED, TD and LD directions are henceforth called ED, TD and LD specimens respectively. Representative true stress versus true plastic strain curves for the three orientations are shown in Figure 2.5. These will be referred to as 'true stress-plastic strain curves' through the rest of the chapter.

The mechanical response of the LD oriented specimens were originally expected to be similar to that along the ED orientation (due to similar texture with respect to the loading orientations), and so only three experiments at each strain rate were performed along the LD orientation to verify this hypothesis. However, we see that the true stress-plastic strain response during compression along the ED and LD (Figure 2.5b and Figure 2.5d) were similar only at strain rates of the order of $10^3\,s^{-1}$ after 3% plastic strain, with discrepancies at the very high strain rates. Lacking sufficient data in the LD orientation to understand this discrepancy, we restrict most of our focus to the ED and TD orientations in this chapter. At the high strain rates, around 10 experiments were performed along each of the ED and TD orientations for each strain rate range (a total of 40 datasets). All the high strain rate experiments are listed in Table A.1.

Compressive true stress-true plastic strain curves (Figure 2.5) along the extrusion direction (ED) at quasi-static ($10^{-4}s^{-1}$) and high ($10^{+3}s^{-1}$) strain rates show an initial region of small slope till $\sim$ 3% plastic strain and then relatively constant hardening which eventually gives way to mild softening at the largest strains ($\sim$ 25%). This

softening will be shown to correlate to plastic strain localization in chapter 3. At the very high strain rates of the order of $10^4\ s^{-1}$ (red curves in the same figure), it is difficult to distinguish the initial small slope, stronger hardening is observed than that at the lower strain rates, and the steady hardening regime occurs over a smaller range of plastic strain ($5-15\,\%$). The earlier onset of softening at $10^4\,s^{-1}$ strain rates indicates that failure (in the form of shear localization or crack formation) initiates at smaller strains for the higher strain rates.

Compression along the transverse direction (TD) at quasi-static and high strain rates results in a similar initial region of small slope (up to $\sim$ 5% plastic strain), followed by stronger hardening than in the ED compression experiments. This type of response has been shown to be related to twinning (Ulacia et al. [43]) to some degree. At the very high strain rates (red curves), this feature is less prominent. The strains at the onset of softening decrease with increasing strain rate similar to the ED orientation.

During compression along the LD (Figure 2.5d), the curves follow a more conventional hardening profile that is typically associated with dislocation slip mechanisms.

Comparing the curves from the three orientations at high strain rates ($\sim 10^3\ s^{-1}$), both the ED and TD orientations show an initial region of limited hardening followed by an increase in the work hardening rate. The overall hardening for the ED and LD specimens are similar. The hardening along the TD is much stronger than that observed along the ED and LD, while both of the ED and TD orientations show an

onset of softening during these dynamic compressive deformations. Nearly adiabatic temperature rise is a potential phenomenon that could give rise to thermal softening during high strain rate loading (Meyers [14]). The spatially averaged temperature rise ($\Delta\Theta$) at any given plastic strain ε_p was calculated using,

$$\beta \int_0^{\varepsilon_p} \sigma d\varepsilon_p' = \rho C_p \Delta\Theta \tag{2.4.1}$$

where β is the ratio of plastic work converted to heat also known as the Taylor-Quinney factor, ρ is the density of the material and C_p the specific heat capacity. The value for C_p was chosen from Lee et al. [44] and that for β from measurements by Ghosh et al. [45]. The temperature rise calculated were very small, the maximum reaching barely 20°C (Table 2.1). Adiabatic temperature rise causing softening and failure could reach orders of 100°C sometimes even approaching melt (Meyers [14]). However, these are local temperatures over very small regions (of thickness $\sim 100\mu m$) resulting in localized deformation and failure. Our temperature calculations are spatially averaged and hence not a good reflection of local temperature changes in the sample. It will be be shown later that significant heterogeneity in the deformation occurred (chapter 3), strengthening the hypothesis that local temperature rise was much higher than calculated.

The strain at which softening begins will be referred to as 'failure strain' through the remainder of this chapter, using the concept that this is the strain at which the material begins to lose its load-carrying capacity or becomes plastically 'unstable'. This 'failure strain' is observed to decrease with an increase in strain rate along both

Plastic Strain (%)	Orientation	Strain rate range (s^{-1})	Temperature Rise (°C)	
			Mean	Standard deviation
17	ED	10^3	16.0	0.7
		10^4	19.1	1.5
	TD	10^3	19.2	1.8
		10^4	22.0	1.4
	LD	10^3	N/A	N/A
		10^4	12.3	0.1

Table 2.1: Temperature rise during high strain rate loading at 17% plastic strain.

the ED and TD orientations.

2.4.2 Rate-dependence of the flow stress

Figure 2.6a shows the flow stress measured at fixed plastic strains (3%, 7% and 10%) across the range of strain rates investigated for the ED compression experiments. The grey region highlights an intermediate strain rate range where we do not have data. Figure 2.6b presents the same data normalized by the corresponding mean flow stress at $10^{-4}\ s^{-1}$ strain rate. This figure presents the flow stress at all strain rates relative to the quasi-static rate data at $10^{-4}\ s^{-1}$. The same quantities are plotted for the TD specimens in Figure 2.6c and Figure 2.6d respectively. The dotted arrows are used to track the apparent changes in flow stresses between the low and high strain rate regime. The vertical error bars represent scatter in the data. Vertical

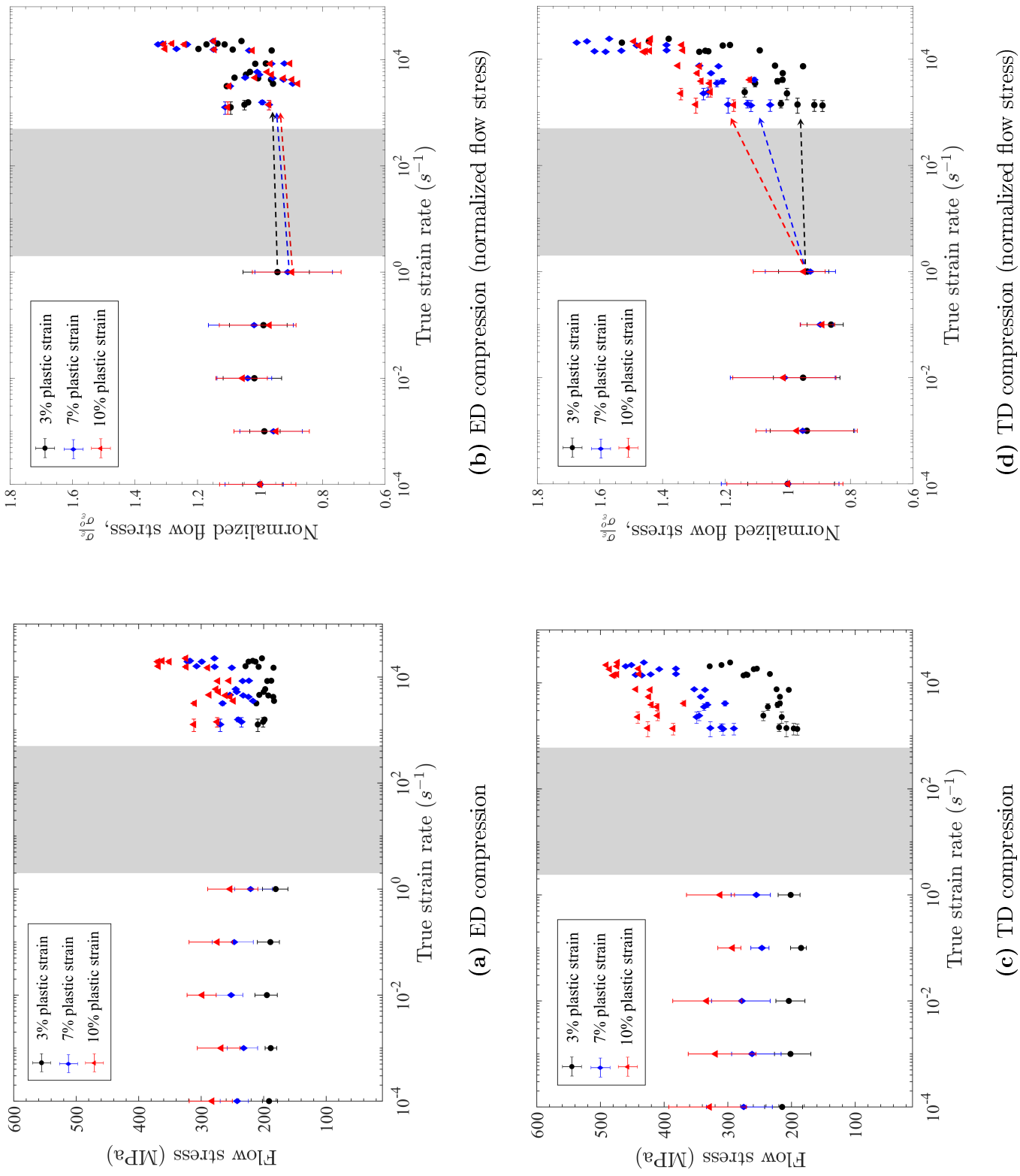

Figure 2.6: Effect of strain rate on flow stress at three different plastic strain levels for compression along the ED and TD.

error bars are plotted only for the quasi-static experiments due to the large number of datasets collected ($\sim$ 40 at each strain rate). All data points from the high strain rate dataset are plotted. The horizontal error bars that are shown for the high rate experiments represent the variability in strain rate within each experiment, whereas at quasi-static rates, the variability in strain rate within each experiment is negligible. These comments apply to later figures as well.

The normalized flow stress plot (Figure 2.6b) allows a comparison of the trends in flow stress with strain rate for ED compression. At 3% plastic strain (black filled circles), the flow stresses are similar across the entire range of strain rates with a slight increase at $10^4\,s^{-1}$ strain rates. At strain rates of $10^0\,s^{-1}$ however, a small drop in the mean value of flow stress is observed. At 7% plastic strain (blue filled rhombi), a similar drop in mean flow stress is observed at $10^0\ s^{-1}$ strain rates. In addition, an increase in flow stress is observed beyond $10^4\ s^{-1}$. These trends are maintained at 10% plastic strain (red filled triangles). Note that the drop in mean flow stress at $10^0\ s^{-1}$ is observed consistently at all three plastic strains. At the high strain rates (beyond $10^3\ s^{-1}$), the rate dependence of flow stress is very similar at 7 and 10% plastic strain. The data at 3% plastic strain shows lower normalized flow stresses at the maximum strain rates than the data at plastic strains of 7% and 10%. The rate dependence of flow stress is hence weaker at 3% plastic strain in comparison to 7% and 10%.

Similarly, a normalized comparison between the three plastic strains is shown in

Figure 2.6d for the TD loading orientation. A clear increase in flow stress with strain rate is seen after $\sim 10^3\ s^{-1}$. This increase is observed at all three plastic strains (3,7 and 10%). The decrease in flow stress at quasi-static rates is also observed for these specimens at $10^{-1}\ s^{-1}$ strain rates (an order magnitude lower than the ED oriented samples). The drop in the mean flow stress is much more evident (than for ED) at $10^{-1}\ s^{-1}$ for all three plastic strains. At 3% plastic strain (black filled circles), little increase in flow stress (indicated by the black dotted arrow) is observed between the quasi-static and high strain rate regimes, but the flow stresses rise significantly (by ~40%) at $\sim\ 10^4\ s^{-1}$ strain rates. At 7% plastic strain, the blue arrow indicates a relative increase in flow stress (~25%) between 10^0 and $10^3\ s^{-1}$ strain rates. The flow stress continues to rise in the very high strain rate regime beyond $10^3\ s^{-1}$. At 10% plastic strain (red filled triangles), the relative increase in flow stress between 10^0 and $10^3\ s^{-1}$ strain rates (marked by the red arrow in Figure 2.6d) is greater than that observed at 7% plastic strain (~40%), and again the flow stresses continue to increase in the very high strain rate regime. This increase in flow stress is greater than that observed for the ED specimens on a normalized basis.

In summary, both ED and TD oriented specimens show a clear increase in flow stress with strain rate at very high strain rates. At the low strain rates, a drop in the mean flow stress is observed at $10^0\ s^{-1}$ for ED oriented specimens and at $10^{-1}\ s^{-1}$ for TD oriented specimens. An increase in flow stress between the low ($10^0\ s^{-1}$) and high strain rate ($10^3\ s^{-1}$) regimes is observed for TD oriented specimens but not for their

ED counterparts. For compression along the TD, the rate sensitivity of flow stress is also dependent on the instantaneous plastic strain indicating that work hardening is also a function of strain rate. A detailed analysis of work hardening rates follows.

2.4.3 Rate-dependence of work hardening

The work hardening rate/ strain hardening index [46] is defined as,

$$n = \frac{\varepsilon^p}{\sigma}\left(\frac{\partial \sigma}{\partial \varepsilon^p}\right)_{\dot{\varepsilon}^p, \xi_i} \tag{2.4.2}$$

where ε^p is the instantaneous plastic strain, σ is the instantaneous true stress, $\dot{\varepsilon}^p$ is the instantaneous plastic strain rate and ξ_i are as yet unknown internal variables that define the instantaneous micro-structure (Rice [47]). Although this is a generalized

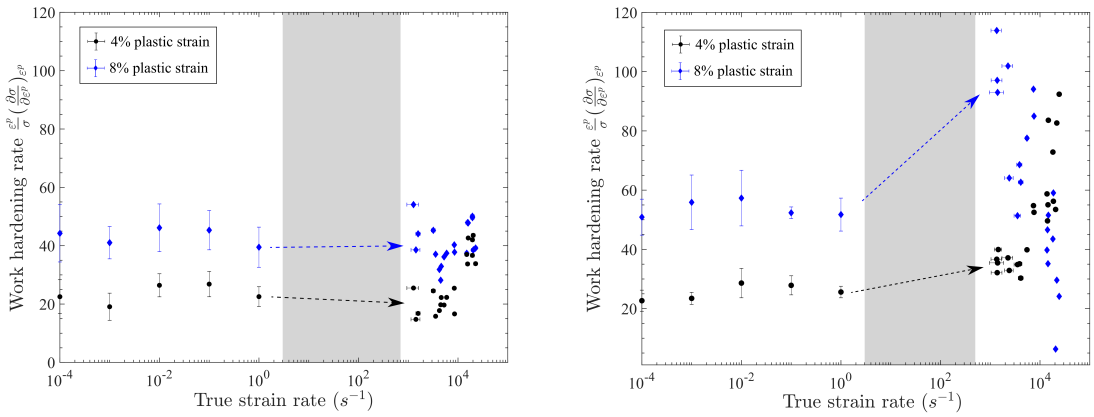

(a) ED compression **(b)** TD compression

Figure 2.7: Work hardening exponent as a function of strain rate for two different plastic strains.

definition of the ability of the material to strain harden, it has sometimes been used as the work hardening exponent for a power law type hardening behavior. We do NOT suggest by any means that work hardening follows a power law in magnesium. The purpose of this work hardening exponent is only to quantify the hardening behavior of the material as a function of strain rate and orientation.

The derivative in Equation 2.4.2 assumes constant plastic strain rate and a fixed micro-structure at the instant n is calculated. In reality, our experiments impose a macroscopic total strain rate which can be expressed as,

$$\dot{\varepsilon} = \dot{\varepsilon}^e + \dot{\varepsilon}^p = \frac{\dot{\sigma}}{E} + \dot{\varepsilon}^p \tag{2.4.3}$$

The maximum values of $\frac{\dot{\sigma}}{E}$ are at least an order of magnitude smaller than the total strain rate. Hence, the plastic strain rates in our experiments, $\dot{\varepsilon}^p$ are approximately equal to the macroscopic applied strain rates $\dot{\varepsilon}$. Our experimental conditions ensure a nominally constant plastic strain rate after the initial rise. Since the numerical derivative of the true stress-plastic strain curve is computed over sufficiently small windows ($\leq$3% plastic strain), we make the assumption that the micro-structure does not change significantly over this window. A caveat to note here is that the starting micro-structure is different at different strain rates (for fixed plastic strains) and hence may affect our interpretation of the work hardening parameter n. Usage of this parameter in computational models must hence be handled with care. A more robust method to identify these parameters for direct use in models is using strain rate jump experiments (Meyers [14]) described in subsection 7.2.1. However, our

parameter can be used to compare the qualitative nature of work hardening and the corresponding mechanisms. Note that the parameter n is a function of plastic strain i.e. the hardening is non-linear.

Figure 2.7 shows the work hardening rate for the two orientations (ED and TD) at two different plastic strains (4 and 8%) across the range of strain rates investigated. During compression along the ED (black circles in Figure 2.7a), at 4% plastic strain, no significant change in the work hardening rate (n) is observed until high strain rates of the order of $10^4\ s^{-1}$, when a 50% increase is observed. At higher plastic strains (8%), no significant difference in work hardening rates is observed (given the scatter) across the full range of strain rates. For compression along the TD at 4% plastic strain (Figure 2.7b), an increase in the work hardening rate with strain rate is observed after $10^3\ s^{-1}$. At 8% plastic strain, however, the trends are different, with a greater increase in the work hardening rates between the low and high strain rate regime, and a decrease in work hardening rates beyond $10^3\ s^{-1}$. Note that the true stress-plastic strain curves for this orientation (Figure 2.5c) showed a decrease in apparent 'failure strain' at very high strain rates in comparison to the high strain rates. Softening mechanisms begin to play a role in this apparent negative rate sensitivity of hardening for this orientation (discussed in detail in chapter 3). In summary, work hardening is a stronger function of strain rate during TD compression than the ED.

2.5 Discussion

The results presented in this chapter bring to light four major characteristics of macroscopic plastic deformation in the ECAE AZ31B magnesium alloy. We will discuss the implications of each of these characteristics.

A1. *The flow stress of the ECAE AZ31B alloy is a function of strain rate.* The macroscopic strain rate during elastic-plastic deformation of a material can be additively decomposed into its elastic and visco-plastic components.

$$\dot{\varepsilon} = \dot{\varepsilon}^{e} + \dot{\varepsilon}^{vp} \tag{2.5.1}$$

In FCC and BCC metals, the most common plastic deformation mechanism is dislocation slip. We can hence attribute the term $\dot{\varepsilon}^{vp}$ entirely to dislocation slip. If the flow stress of the material were rate sensitive, this rate of plastic flow (or dislocation slip) would be a function of the stress (Meyers [14]). In magnesium however, deformation twinning is another dominant mechanism. Hence the term $\dot{\varepsilon}^{vp}$ maybe approximated to an additive decomposition into slip and twinning components i.e.,

$$\dot{\varepsilon}^{vp} = \dot{\varepsilon}^{vp}_{s} + \dot{\varepsilon}^{vp}_{t} \tag{2.5.2}$$

This complicates our problem. While most models consider basal slip to be relatively rate insensitive in magnesium (Zhang and Joshi [2], Chang and Kochmann [48]), prismatic slip and pyramidal slip would be rate sensitive (Zhang and Joshi [2], Ulacia et al. [28]) as per the formal definition for rate sensitivity described above. The

classic rate sensitivity relation (or shear rate vs shear stress relation) for dislocation slip used in most computational codes ([2, 16, 48]) is a power law relation originally developed for fcc metals by Peirce et al. [49]. However the strain rate dependence of twinning is unknown. The question of rate sensitivity of twinning is a complex one and will be discussed multiple times throughout this thesis. Given the initial texture of our material (Figure 2.1c), we would expect significant basal and prismatic slip for ED and LD compression (Yi et al. [26]) while extension twinning is expected to be dominant during TD compression (Barnett [20]). The rate sensitivity of flow stress (Figure 2.6) is likely due to the enhanced activity of twin and dislocation activity at the high strain rates.

A2. *Work hardening is a function of strain rate.* This is also directly related to the evolution of mechanisms. Hardening usually comes from the interaction between mechanisms of the same type (self-hardening) or different types (cross-hardening). Empirically, the rate of evolution of the strength of a slip system (or resistance to slip) in purely slip dominated deformation can be described as (Kocks [50], Asaro [51]),

$$\dot{g}^{\alpha} = \sum_{\beta=1}^{N_s} h^{\alpha\beta}(\gamma^{\alpha})\dot{\gamma}^{\beta} \tag{2.5.3}$$

where g^{α} is the strength of the α slip system, N_s is the total number of active slip systems, $h^{\alpha\beta}$ is an empirical hardening coefficient matrix which describes the interaction between the α and β slip systems. γ is the shear strain on a specific slip system and $\dot{\gamma}$ is the shear rate. Hence, according to Equation 2.5.3, the evolution of the strength

of a slip system is directly related to the activity of the specific slip system relative to all active slip systems in the material. Different slip mechanisms in magnesium have different mobilities (i.e. dislocation velocities as a function of driving forces) and hence evolve differently in the material. With the introduction of twinning, this problem becomes more complex unless the twin is also treated as pseudo-slip. This thesis will show why the treatment of twins as pseudo-slip systems may not be physically realistic for all types of problems.

In summary, the evolution of different slip and twin mechanisms at different loading rates is crucial to accurately model the work hardening response of the material. Figure 2.7 shows that the work hardening increases with strain rate during compression along the ED as well as along the TD at 4% plastic strain. This leads to the hypothesis that the interacting mechanisms contributing to hardening are rate sensitive (evolve differently at different rates). The decrease in work hardening at higher strain rates and 8% plastic strain (Figure 2.7b) for the TD orientation is likely related to the earlier onset of softening with increase in rate (Figure 2.5c).

A3. *The rate dependence of flow stress and work hardening are anisotropic.* With the mechanistic explanation for flow stress and work hardening described above, the anisotropy clearly implies that different mechanisms are activated along different loading orientations or similar mechanisms are activated to a different degree.

A4. *Strains at the onset of softening decrease with increasing strain rate.* Softening mechanisms may be driven by local temperature rise leading to nearly adiabatic shear

localization (Meyers [14]) i.e. thermal softening or by local geometric reorientations of the material i.e. geometric softening. In our material, both these mechanisms are possible. While nearly adiabatic shear localization has been widely observed across material systems only at high strain rates (for eg. Ramesh [46], Marchand and Duffy [52], Meyers et al. [53]), twinning being a re-orientation of the crystal lattice is a potential geometric softening mechanism specific to our material. The re-orientation of some grains in the polycrystalline aggregate relaxes the stresses in these local regions. Literature evidence exists (Bell and Cahn [54]) to show that the nucleation of deformation twins may result in a reduction in flow stresses. Our data (Figure 2.5) also indicates that the rate dependence in these strains at the onset of softening changes with loading orientation (anisotropic).

A detailed discussion based on specific mechanisms active under these different orientations and rates follows in chapter 3.

2.6 Conclusions

The strain rate dependence of macroscopic plastic flow was studied for an AZ31B magnesium alloy processed by ECAE. The conclusions from this study are summarized below.

1. The plastic flow stress of the ECAE AZ31B magnesium alloy increases with strain rate, and the work hardening is also rate sensitive.

2. The rate dependence of both plastic flow and work hardening changes with loading orientation (anisotropic).

3. The strain at the onset of softening is both anisotropic and rate dependent. These 'failure strains' decrease with increase in strain rate.

From the discussion (section 2.5), it is clear that the key to understanding the rate dependence of macroscopic plasticity and failure lies in identifying the active microscopic deformation mechanisms and the strength of their interactions. One way of achieving this goal is by measuring the relative activities of these mechanisms under the different loading conditions and micro-structures. This is the objective of the following chapter. We use a combination of in-situ and post-mortem microscopy techniques on specimens from the same dataset (Table A.1) to meet this objective. We will then embark on deeper discussion to relate the mechanisms observed to the rate dependent macroscopic response discussed in this chapter.

Chapter 3

A mechanistic understanding of rate dependent plastic flow and failure in polycrystalline magnesium alloys

Preface: The following chapter is largely based on a manuscript submitted for publication. The co-authors are Xiaolong Ma, Nicholas M. Krywopusk, Laszlo J. Kecskes, Timothy P. Weihs and K. T. Ramesh. VK was the lead author in this study and performed the high strain rate experiments and related microscopy, data analysis, interpretation and manuscript preparation. XM performed the post-mortem transmission electron microscopy and analysis of the microscopy data. NMK was involved in the material processing and obtained the quasi-static dataset. LJK was involved in material processing and mentorship. TPW and KTR were PI's and involved in

mentorship, problem formulation and data interpretation. All authors contributed towards manuscript preparation and review.

3.1 Introduction and background

A quick recap of the deformation mechanisms in hcp crystals described in section 1.4 follows. In contrast to conventional fcc and bcc materials, deformation mechanisms in hcp materials are significantly more complex due to the asymmetry of the crystal structure. In a single crystal, different dislocation slip systems have significantly different critical resolved shear stresses (CRSS) and slip resistances (hence mobilities) due to this asymmetry (Zhang and Joshi [2], E.W.Kelley [19], Chang and Kochmann [48]). In addition, deformation twinning is another dominant mechanism even under room temperature, quasi-static loading conditions, unlike in fcc and bcc metals. With the introduction of loading rate into the problem, the relative activities of these mechanisms are expected to change.

In polycrystalline magnesium alloys, chapter 2 clearly shows that the texture becomes another important factor in governing the mechanisms activated and subsequent material response. We established that the flow stress, work hardening and failure strains are a function of loading orientation as well as the strain rate. While we discussed the implications of these measurements on the type and evolution rates of possible deformation mechanisms in the material, this discussion remains woefully incomplete without the knowledge of the specific mechanisms that were active under

the different loading conditions investigated.

In this chapter, we present results from in-situ and post-mortem microscopy measurements on samples tested within the same dataset described in chapter 2 (Table A.1). These results, along with the macroscopic measurements, will be used to develop deeper insight into the origins of rate dependent anisotropic plastic deformation and failure of the ECAE AZ31B magnesium alloys.

3.2 Experimental Methods

3.2.1 In-situ high speed imaging

In-situ imaging was performed using a *Specialised Imaging Kirana-05M* high speed camera capable of capturing 768×924 pixels (10-bit) at up to 5 million frames per second (200 ns temporal resolution). The pixel size on the charge coupled device (ccd) sensor is 30 μm, and a 105 mm Nikon lens was coupled to two teleconverter lenses to achieve a good magnification while capturing the entire specimen in the field of view. Two spatial resolutions, one at 10 μm/pixel and another at 5 μm/pixel were achieved. At least three datasets were collected at each of the two magnifications for both loading orientations investigated.

Imaging using the very high shutter speeds of the camera requires very intense light sources. The electronic shutter in this specific camera allows for the shutter speeds to be almost the same as the inter-frame time ($\sim$ 200 ns) with the time for

turning on the electronic shutter lasting <10 ns. Lighting was provided by a 400 W *Specialised Imaging* pulsed laser diode (*SI-LUX640*) of wavelength 640 ± 6 nm. At 5 million fps, the illumination was maintained such that it was ON for 100ns and OFF for the other 100ns over the 200ns interframe time (thus the effective exposure time was 100 ns).

3.2.2 Post-mortem electron backscatter diffraction microscopy

Deformed and recovered specimens were sectioned into slices with a diamond wire saw using water as a coolant to ensure a minimal heat affected zone. The slices were then polished to ensure flatness and a good surface finish ($\sim$ 50 nm) for the next step. The polished slices were then electropolished using a *Struers* twin-jet electropolisher using a solution of lithium chloride, magnesium perchlorate and 2-butoxy-ethanol in methanol as electrolyte at 100 V and -50°C bath temperature. The final surface roughness after this step has not been measured, but is likely lesser than 10 nm. A final cleaning step was performed using a *Fischione* instruments (Model 1060) ion mill at 1-2 kV driving voltage with the Ar ion guns inclined at 3° to the sample surface before mounting it into the scanning electron microscope. The microscope is a *TESCAN MIRA3* scanning electron microscope equipped with an *EDAX* electron backscatter diffraction microscopy (EBSD) detector. EBSD data was collected by

scanning at 20 kV with a working distance of 20 mm and at spatial resolutions of $100 - 150$ nm.

3.2.3 Post-mortem transmission electron microscopy

Transmission electron microscopy (TEM) was performed on the samples recovered at $\sim$5% strain to characterize the underlying dislocation and twin substructure. The EBSD specimens were subsequently mechanically polished down to thicknesses between 100 and 150 μm. These foils were then electrochemically polished until perforation using the same twin jet polisher, electrolyte and operating conditions that were used for surface preparation of the EBSD specimens. Each TEM foil was then cleaned using an ion mill at low voltage on a cold stage maintained at a temperature of -100°C. TEM was performed using a *Thermo Fischer Scientific Tecnai 12 TWIN* microscope operating at 100 kV.

3.3 Results

3.3.1 Post-mortem EBSD: evolution of mesoscale structure during dynamic deformations

Figure 3.1a shows the evolution of the (0001) pole (c-axis) with strain at the high strain rates for ED compression. The data is processed such that the color palette

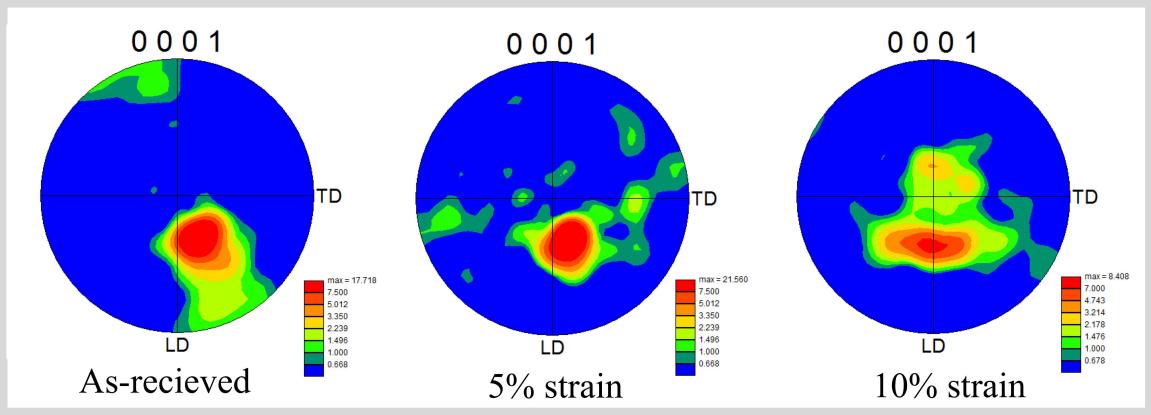

(a)

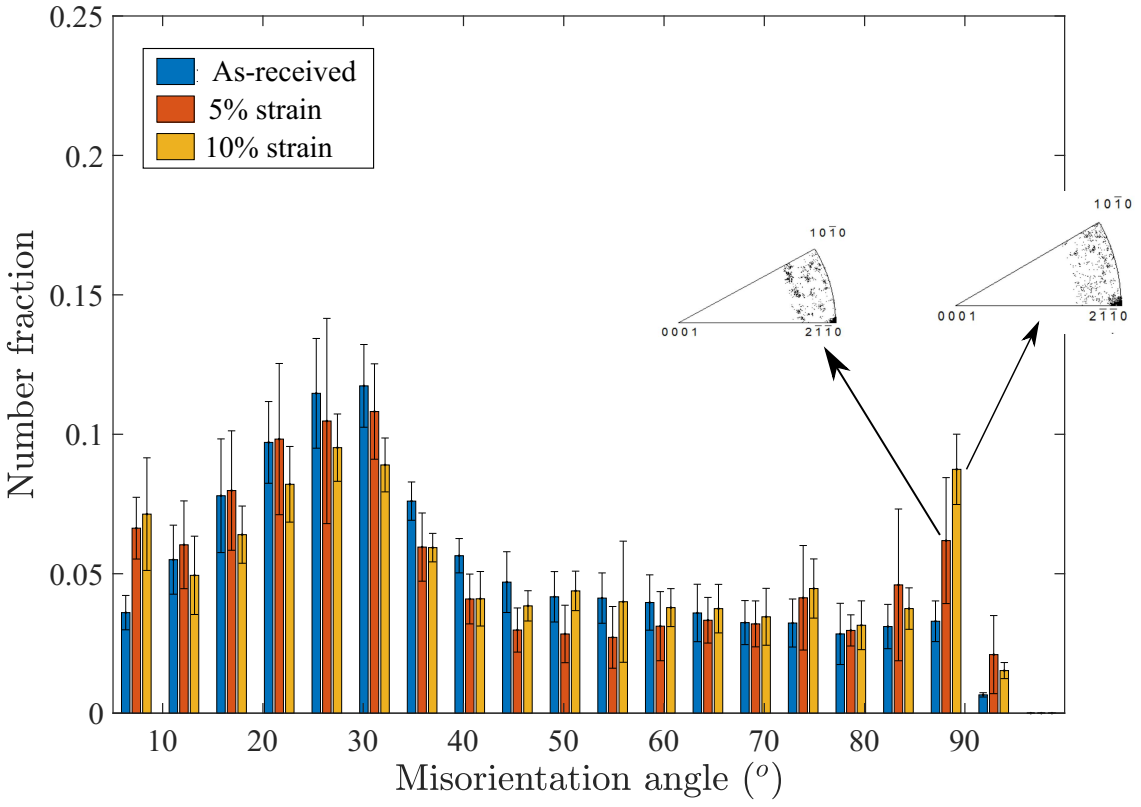

(b)

Figure 3.1: EBSD data from ED samples compressed to ~5% strain at high strain rates: (a) Evolution of the (0001) basal pole; (b) Evolution of mis-orientation angle distribution with strain.

represents similar values of pole intensity. The difference between positive and negative directions of all three orientations was not tracked during specimen preparation. The major intensity is concentrated in the same region after 5% strain, but the poles oriented along the positive and negative LD directions in the as-received material are no longer present, indicating some reorientation has indeed occurred. At 10% strain the major pole has spread over a small angle about the ED direction.

Analysis of mis-orientation angles yields more insight (Figure 3.1b). This bar plot presents the number fraction of boundaries in the EBSD map with specific mis-orientation angles binned into 20 equally spaced values between 0 and 100 degrees. The error bars correspond to the standard deviation obtained from multiple datasets (a measure of scatter due to heterogeneity in deformation rather than error in measurement). The insets in this figure show the mis-orientation axes for the specific peaks marked by the arrows (note that an initial peak at $\sim$30° exists in the as-received material, possibly due to dynamic recrystallization during the ECAE process (Krywopusk et al. [36])). At 5% strain, a slight increase in low angle (0-15°) grain boundary content and a slight decrease in high angle content (25-60°) is observed, but the scatter in the data is large. Beyond 80°, however, a significant increase occurs, especially at 88$\pm$5°. The same trend is observed at 10% strain. The insets at the 88 degree peaks show that the mis-orientation axis corresponding to these angles is the $(2\,\bar{1}\,\bar{1}\,0)$ axis, indicative of extension twin activity. Note that this is for ED compression, where dominant basal slip is expected to occur based on the initial texture

(Figure 2.1c).

The evolution of the c-axis pole after compression along the TD is shown in Figure 3.2a. A significant reorientation of the texture is observed at 5% strain. At 10% strain, this major reorientation of the poles by an angle of ∼90° seems to be complete, followed by some spreading of the poles by smaller angles. The evolution of the mis-orientation angle distribution was also examined in this case (Figure 3.2b), and shows that twinning is dominant at 5% strain (shown by the peak at 88°) during compression along the TD. Also, a significant reduction is evident (compared to the initial distribution) between 10 and 40° mis-orientation angles. The very high angle boundaries (50-70°), in general, remain relatively unchanged. At 10% strain a decrease in the 88° peak from the case at 5% strain is associated with the completion of twinning within grains. These trends provide insight into the type and evolution of mechanisms during deformation, and will be discussed in subsection 3.4.2.

3.3.2 Localized deformation and failure

The in-situ high speed imaging of the dynamically compressed samples showed localized deformation occuring across the polycrystalline samples. Imaging was performed under two configurations. Specimens taken to failure were imaged at spatial resolutions of $\sim 10\mu$m/pixel. To resolve finer details of localized regions in the small strain recovery experiments, the optics were modified to get spatial resolutions of $\sim 5\mu$m/pixel, which enabled quantitative measurements of these bands.

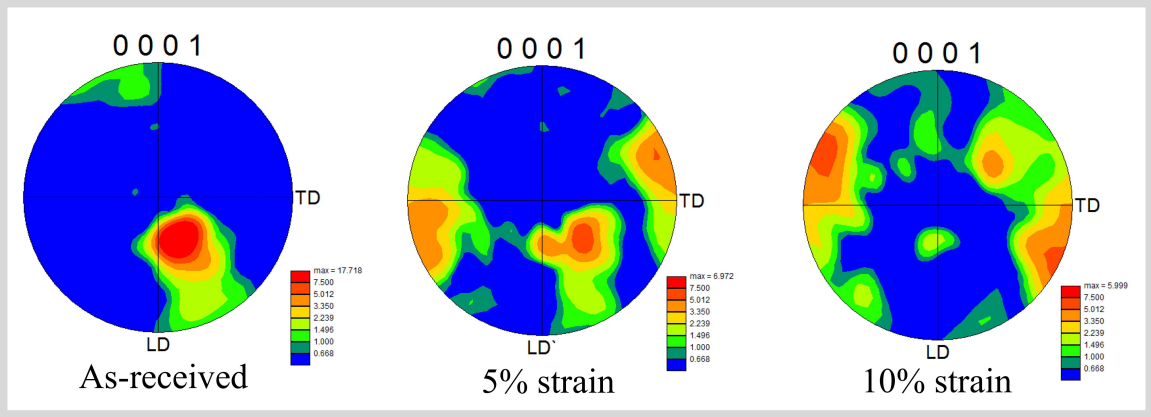

(a)

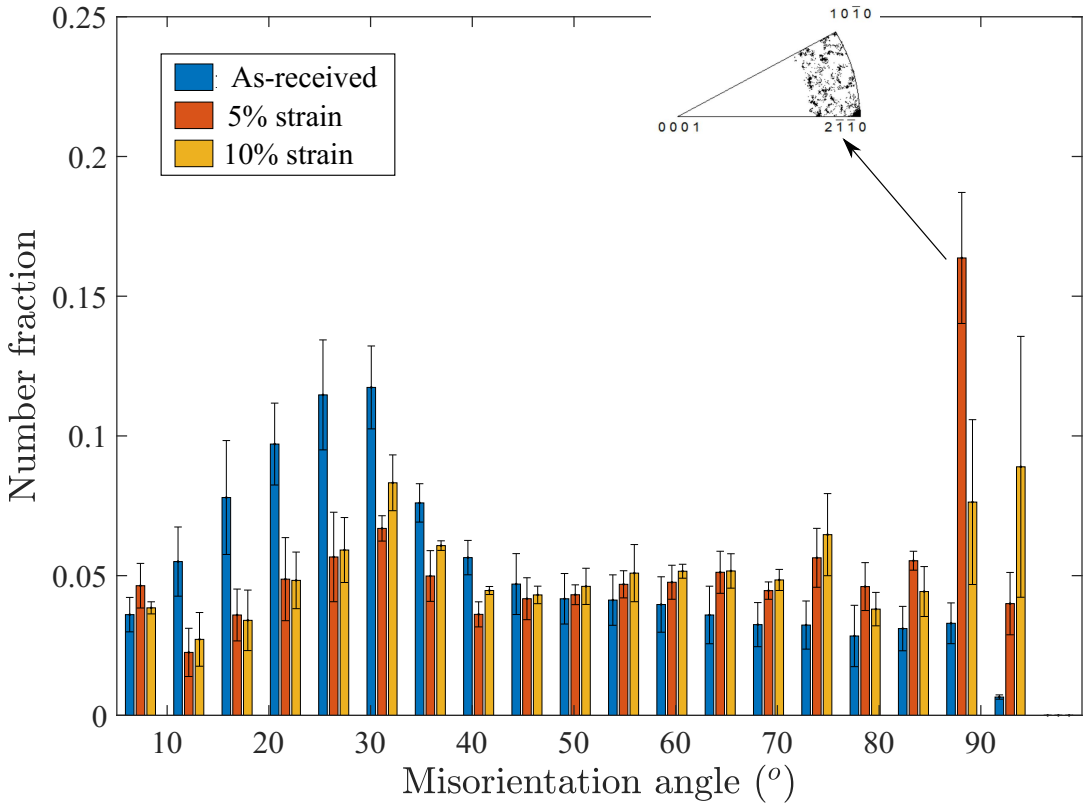

(b)

Figure 3.2: EBSD data from TD samples compressed to ∼5% strain at high strain rates: (a) Evolution of the (0001) basal pole; (b) Evolution of mis-orientation angle distribution with strain.

3.3.2.1 Localization during compression along the ED

The evolution of surface features due to deformation heterogeneities during dynamic compression along the ED is shown in Figure 3.3 as a sequence of high-speed images corresponding to the points marked on the true stress-true total strain curve for that test (at a strain rate $\sim$5000 s^{-1}). Surface features representing strongly heterogeneous deformations are observed beginning with frame 2, at approximately the apparent yield point. The heterogeneities become progressively stronger in subsequent frames. Coalesced bands of deformation are seen in frames 5, 6 and 7 (band thickness $\sim 80\mu m$). Most of the subsequent deformation above 23% strain appears to occur along these bands, followed by failure along a single band (marked by the black arrow in frames 8, 9 and 10) at $\sim$23-25% total true strain. Note from the stress-strain curve that this is where the slope becomes negative. The angle between the band normal and the loading axis is 42°. Notice that this band appears curved (in image 10), indicating that it interacts with the specimen edges, hence resulting in structural failure of the specimen. The evolution of the incipient failure process is easier to visualize in the full image sequence which is provided in the supplementary data. This localized failure phenomenon was observed in all experiments compressed along this orientation.

A specific example of a recovery experiment imaged using the high magnification configuration is shown in Figure 3.4. Since this was a recovery experiment, the strain history is available only for the first $5-6\%$ strains. Measurement resolution makes the strain measurement at each image within this region inaccurate. However, we

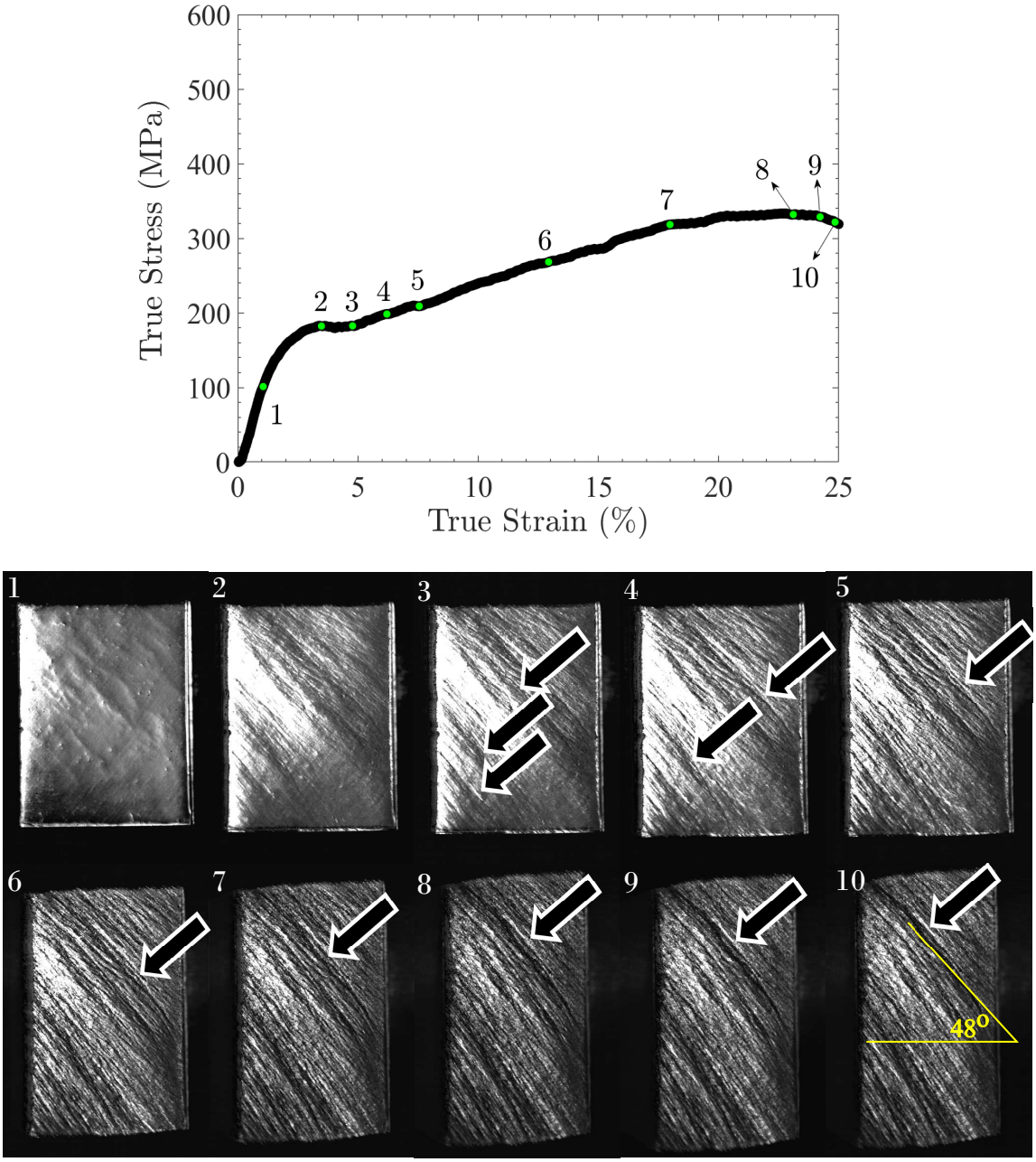

Figure 3.3: *Strain localization during high strain rate compression along the ED ($\dot{\varepsilon} \simeq 5000\, s^{-1}$):* Strain localization observed during in-situ high speed imaging during ED compression

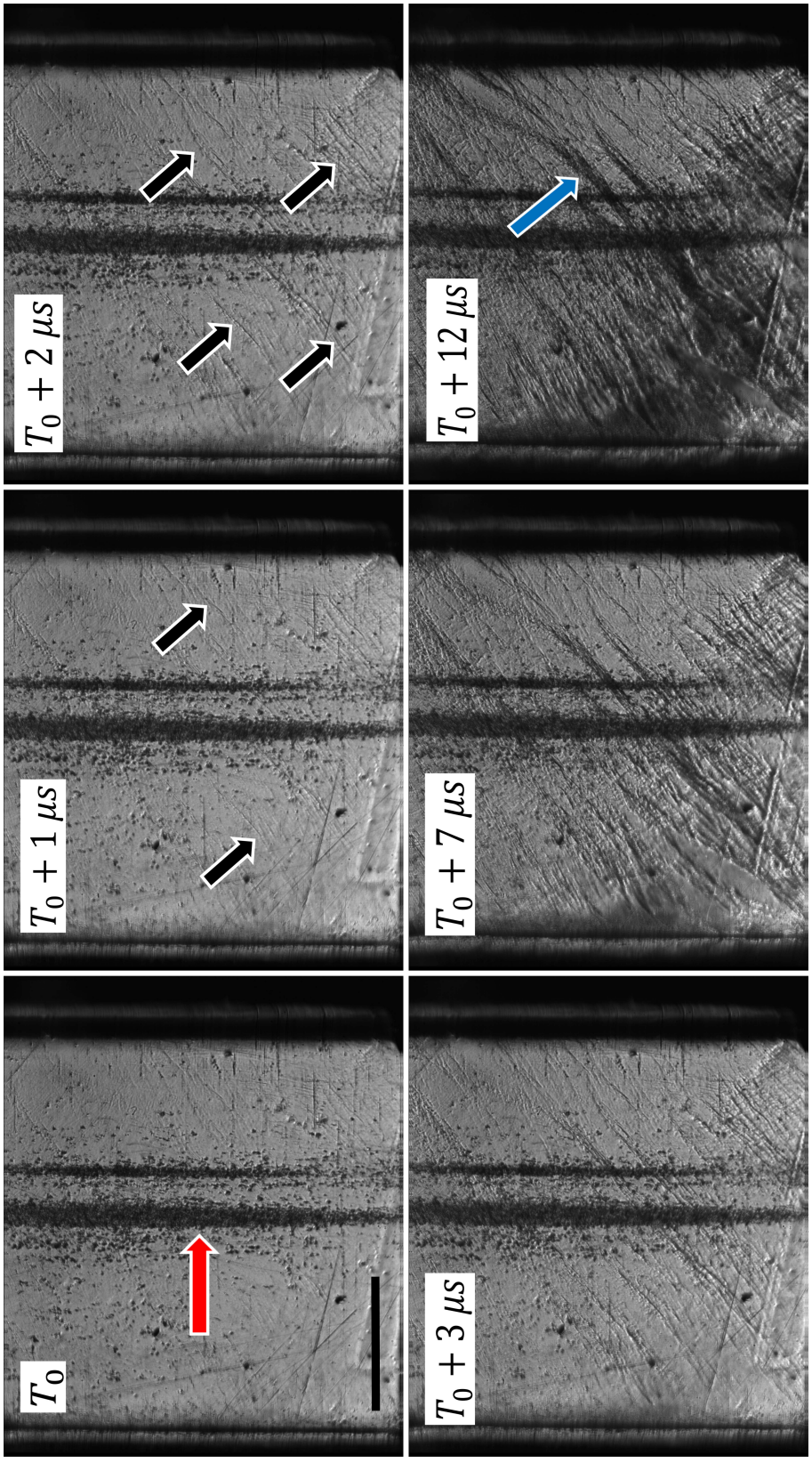

Figure 3.4: *Strain localization during high strain rate compression along the ED:* A magnified series of micro-graphs during recovery experiments performed under ED compression. The scale bar is 1mm.

can make estimates. The red arrow in the frame at a time $T_\circ$ around the start of deformation is a scratch induced during specimen preparation. Just 1μs later ($\varepsilon \sim$ 0.1%), small deformation bands begin to form (indicated by the black arrows). The widths of these bands are $\sim 20\,\mu m$ which amounts to about 8 grains. As deformation progresses, these bands eventually coalesce into a small number of thicker bands (e.g. those marked by blue arrows at time $T_\circ + 12\,\mu s$ corresponding to $\varepsilon \sim 6\%$ in Figure 3.4). The maximum thickness of these bands at this stage of deformation is $\sim$90μm (5 times the thickness of the incipient bands). In this sample, failure was not allowed to occur because the specimen was recovered at small strains for post-mortem analysis. However, an analysis of imaging data from samples taken to failure reveals that the maximum thickness of the band along which failure eventually occurred (e.g. in Figure 3.3) is similar.

3.3.2.2 Localization during compression along the TD

Similar imaging data were obtained for compression along the TD. Figure 3.5 shows a sequence of frames obtained from in-situ imaging with the corresponding points marked on the true stress-true total strain curve (obtained at a strain rate $\sim$7500 s^{-1}). Figure 3.5 shows the nucleation of thin localized regions of deformation (frame 2) even before apparent macroscopic yield. The propagation of these deformation bands is rapid (the time between frames 2 and 3 is 500 ns) and they begin to branch (black arrow in frame 3). As deformation progresses, increased nucleation of these

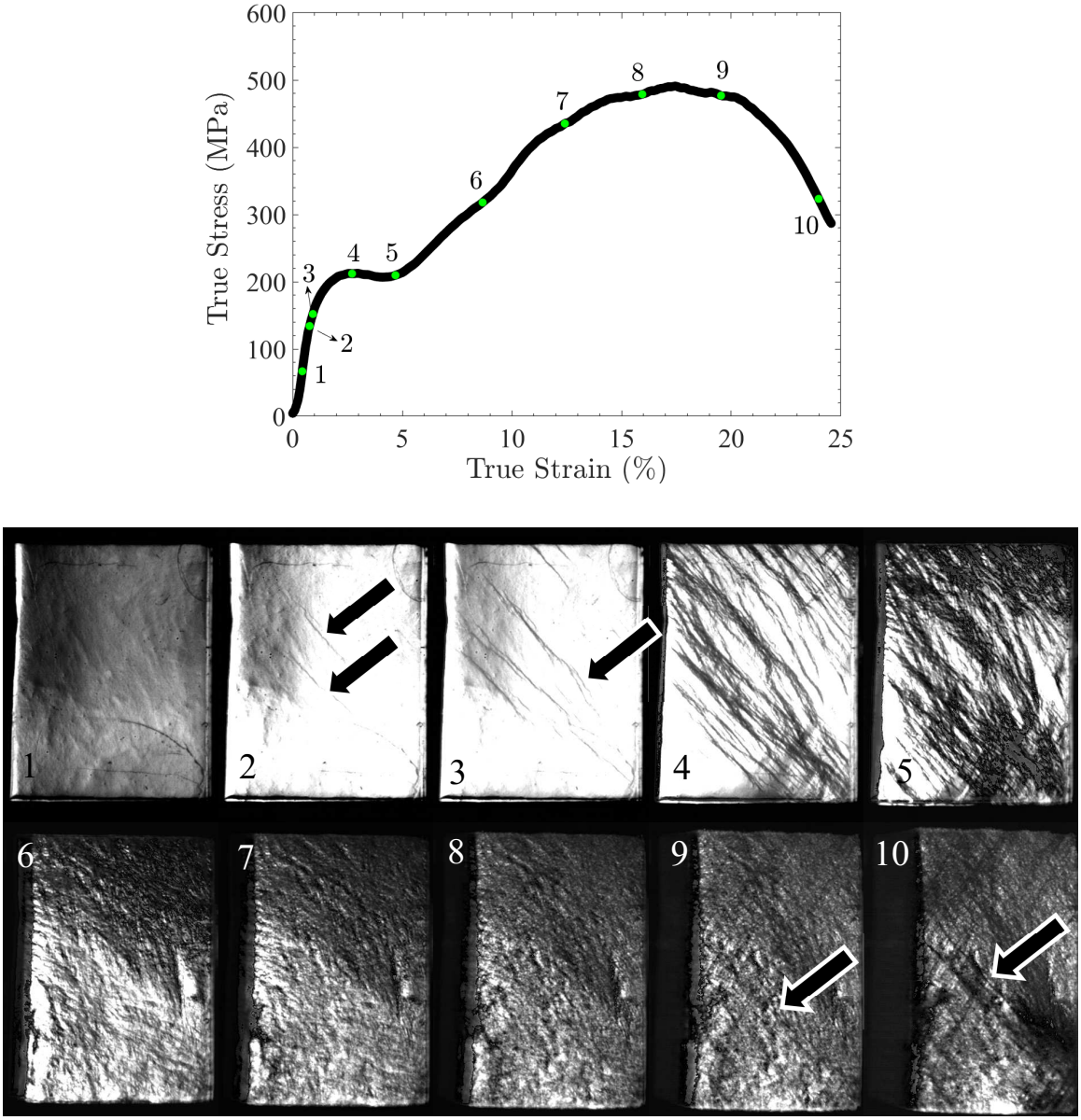

Figure 3.5: *Strain localization during high strain rate compression along the TD ($\dot{\varepsilon} \simeq 7500\ s^{-1}$):* Strain localization observed during in-situ high speed imaging during TD compression

bands is observed, and eventually they coalesce and become thicker (frames 4 and 5). This coalescence and thickening is associated with nearly perfect plastic behavior as observed from the true stress-true total strain curve (similar phenomena have been associated with twinning in literature for eg. E.W.Kelley [19], Kannan et al. [23]). Notice that many of these bands in frame 4 nucleate from the specimen edges. Later still, in frames 6 and 7, the interacting bands have generated a more diffuse, less heterogeneous deformation, and this is associated with the strong strain hardening in the true stress-true total strain curve. Finally, macroscopic 'shear' bands begin to form (arrow in frames 9 and 10) resulting in catastrophic failure.

The high magnification images (Figure 3.6) reveal that the local deformation bands formed early at strains $< 5\%$ during TD compression (marked by the black arrows in Figure 3.6) are of similar widths ($\sim 20\,\mu m$) as those observed previously during ED compression. The evolution of these localized regions is rapid, with a nucleated band growing across the 4 mm field of view within $2\mu s$. As deformation evolves, these bands multiply rapidly and grow slightly thicker to widths of $\sim 30\,\mu m$. At $\sim 7\mu s$ ($\varepsilon \sim 1.5\%$) from the first frame, the red arrows clearly show the presence of new bands along a different direction. These bands were observed to nucleate as early as 4μs after the first frame (marked by red arrows at time $T_\circ + 4\mu$s). The angles between the two dominant directions of localized deformation is $\sim 79^\circ$ which corresponds to the angle between conjugate twin planes of the hcp crystal (Kannan et al. [23]). We hypothesize that the interactions of these bands lead to the diffuse deformations and

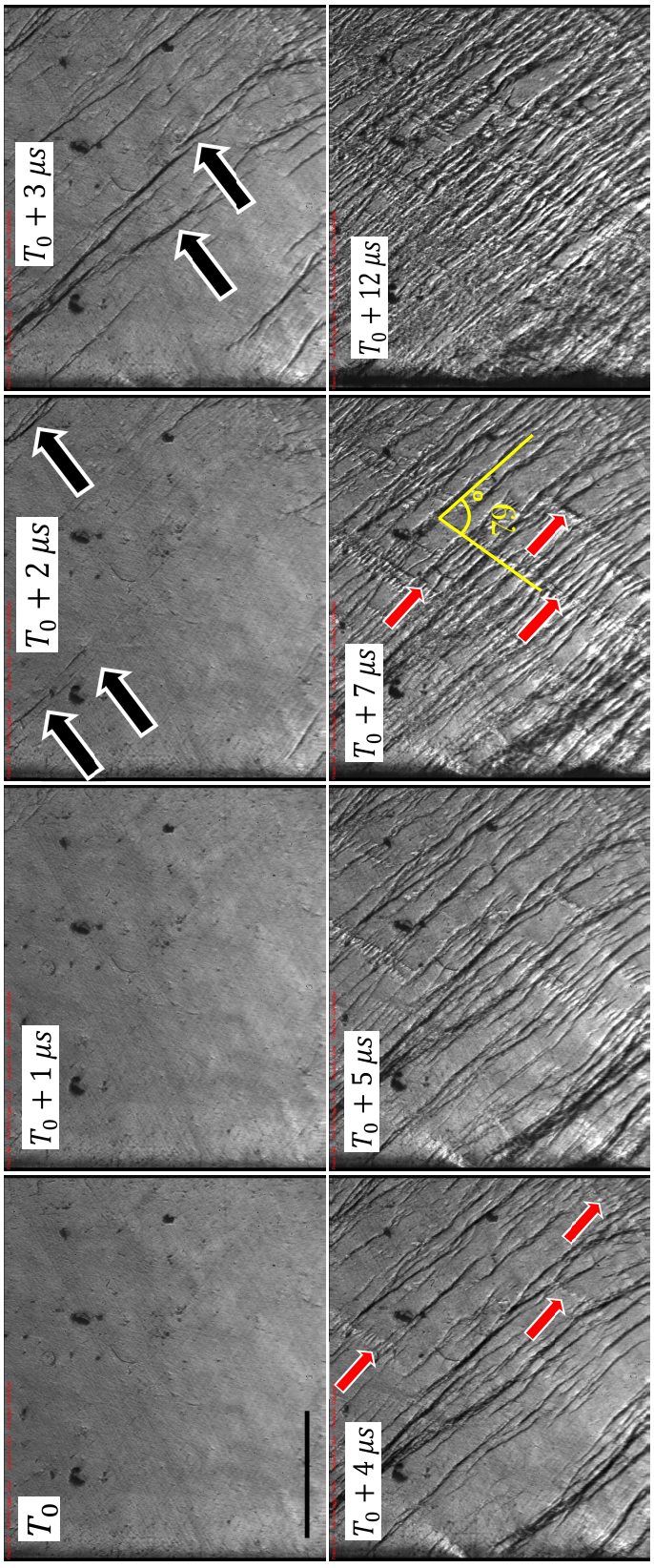

Figure 3.6: *Strain localization during high strain rate compression along the TD:* A magnified series of micro-graphs during recovery experiments performed under TD compression.

hardening due to pyramidal slip systems at later strains.

3.4 Discussion

In this section, we focus on building a mechanistic understanding of plastic flow at high strain rates by relating the macroscopic response to the activated mechanisms, based on our observations as well as the literature.

3.4.1 Compression along the ED

Compression along the ED is expected to activate predominant basal slip based on the texture (Figure 2.1c) since this is the easiest deformation mode. The spread in the initial orientation distribution, however, may result in the activation of non-basal deformation mechanisms as well. The pole figure evolution in Figure 3.1a shows the disappearance of (0001) poles that were originally oriented along the LD directions, likely because compression along the ED has reoriented these grains by twinning (which would account for the initial limited slope of the true stress- plastic strain curves (Kannan et al. [23])). This is further confirmed by the increase in number density of the $88\pm5^{\circ}$ mis-orientation peak in Figure 3.1b. The axis about which the crystal is reoriented (insets in Figure 3.1b) confirms that there has indeed been extension twinning in some grains.

TEM analysis was performed on the recovered samples that were used for EBSD

microscopy. The two beam condition was used to identify $\langle c \rangle$ and $\langle a \rangle$ components of dislocations in the same spatial location. Figure 3.7a and Figure 3.7b reveal the $\langle a \rangle$ and $\langle c \rangle$ dislocation components at the same spatial location in a specimen compressed along the ED to 5% strain. The red arrows indicate the direction of the diffraction/ scattering vector $\mathbf{g}$ used in the $\mathbf{g}.\mathbf{b} = 0$ invisibility criterion to determine dislocation nature. Significant $\langle a \rangle$ slip with very little $\langle c \rangle$ character was observed (note that only two-thirds of the $\langle a \rangle$ components are visible in this imaging mode). Thus one of the dominant active mechanisms was basal $\langle a \rangle$ slip during compression along the ED, as expected, even at 5% strain. Based on crystallography, the specific slip mechanisms are basal and prismatic slip the latter of which has been known to be rate sensitive.

Beyond 5% strain, the dynamic stress-plastic strain curves for ED compression (Figure 2.5b) rise with a nearly constant slope. Basal slip by itself is known to be weakly-interacting and does not cause significant hardening, while prismatic slip may interact with other dislocation variants. In addition, the twinning peak in Figure 3.1b keeps increasing until 10% strain, indicating that twinning continues to reorient crystals as the strains increase from 5% to 10% strain. Although we have not looked extensively in our samples, previous studies like the one by Koike et al. [34] have found the presence of non-basal dislocations in the matrix for similar loading orientations. Previous experimental evidence (Dixit et al. [22]) has also shown that non-basal slip within twinned regions results in significant hardening at later strains (beyond 6%). It appears, therefore, that the work hardening arises due to interactions between

twin boundaries and slip mechanisms and between basal and non-basal slip outside twinned regions.

A spread in the texture is observed (Figure 3.1a) at 10% dynamic strain in the ED direction. Data was collected from different regions in the specimen and this spreading of texture was consistent across the datasets. A possible hypothesis for this spread is the formation of new boundaries due to the the interaction between twin boundaries of different variants (Bian and Shin [55]). A second hypothesis relates to the formation of dislocation cells in regions of very large deformation and high temperature. While localization of deformation was observed at early strains in our dynamic experiments (Figure 3.3 and Figure 3.4), no dislocation cells were observed during TEM analysis. While the presence of small grains in the ECAE material would preclude the formation of dislocation cells, a more detailed TEM study over larger regions is necessary to verify this claim.

The reduction of the slope of the stress-plastic strain curves beyond 25% plastic strain (Figure 2.5b) is related to the coalescence of deformation bands (Figure 3.3 and Figure 3.4) formed during dynamic compression along the ED. Figure 3.3 shows that the formation of these coalesced bands correlates to the onset of softening in the stress-plastic strain curve. Classical studies (Meyers [14]) have shown that strain softening can be related to nearly adiabatic temperature rise reaching homologous temperatures of 0.4 up to 0.8 (for eg. Zhou et al. [56]) in localized regions during dynamic loading. Our measurements of the band thickness may provide clues about

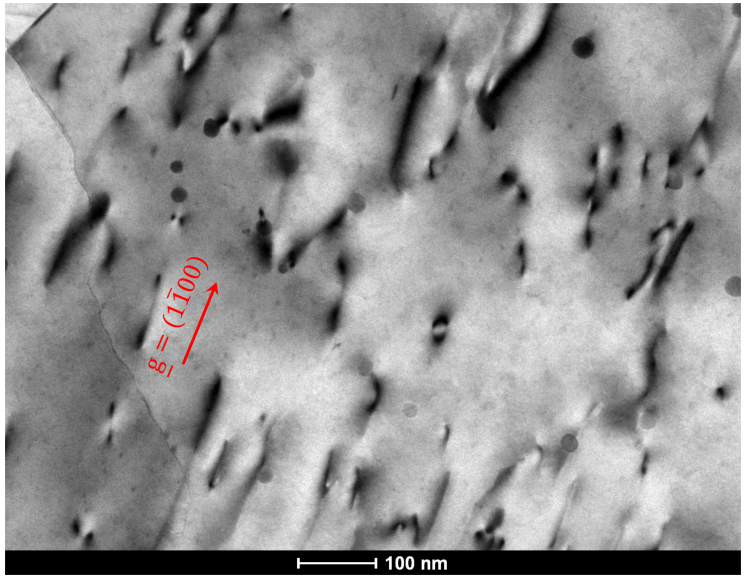

(a) ED compression ($\langle a \rangle$ components)

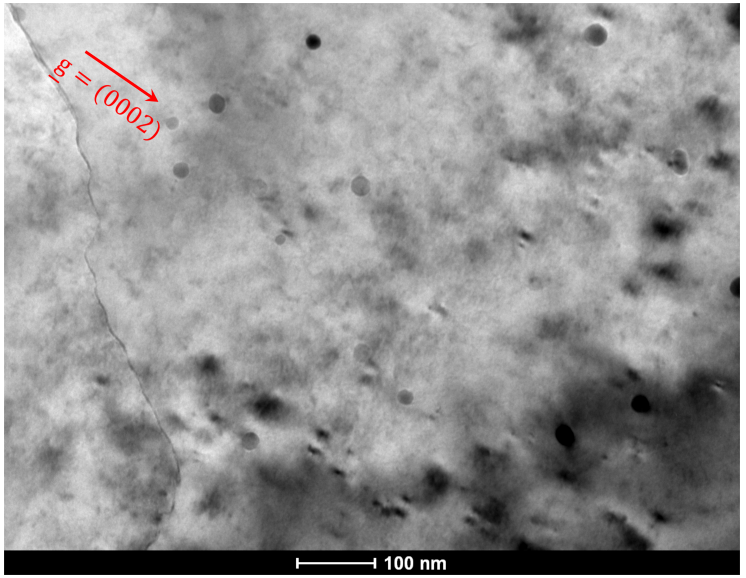

(b) ED compression ($\langle c \rangle$ components)

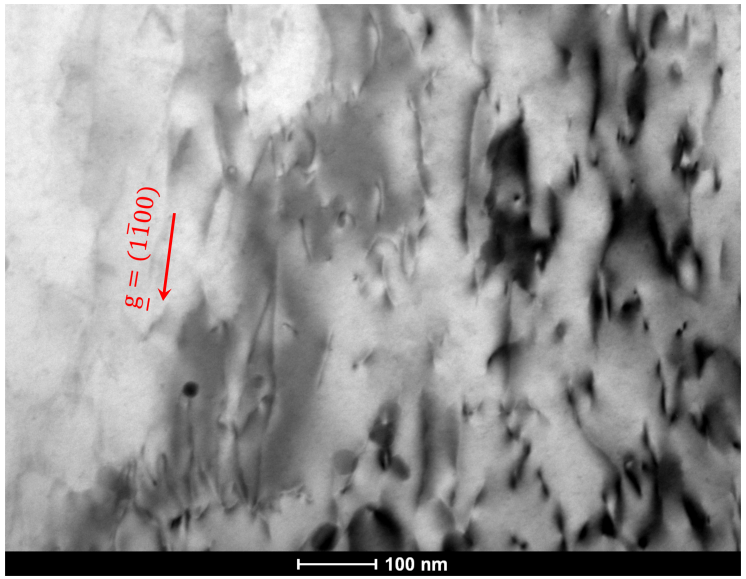

(c) TD compression ($\langle a \rangle$ components)

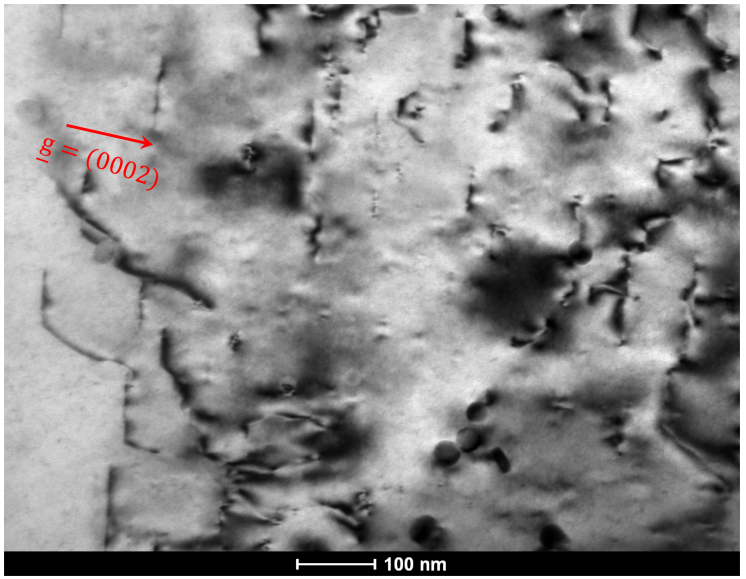

(d) TD compression ($\langle c \rangle$ components)

Figure 3.7: TEM studies to characterize dislocations active under high strain rates at 5% recovered strain. Notice predominant basal $\langle a \rangle$ dislocations are active for compression along the ED, while multiple $\langle c \rangle$ and $\langle c+a \rangle$ components are active for compression along the TD.

the extent of local temperature rise within these bands, but understanding high temperature constitutive response is necessary for this analysis. Figure 2.5b also shows that the apparent 'failure strain' at the onset of softening is lower (∼17%) for the very high rate experiments, which is consistent with a local thermal softening hypothesis. Hardening is also different at different strain rates and the earlier onset of softening may be related to the earlier saturation of hardening at higher strain rates.

3.4.2 Compression along the TD

According to the texture shown in Figure 2.1c, compression along the TD compresses most of the grains at nearly perpendicular angles to the c-axis. The spread in texture ensures that some basal slip is always activated. However we expect significant extension twinning to also be active. This is consistent (for eg. E.W.Kelley [19], Ulacia et al. [57]) with the typical 'sigmoidal' profile of the stress-strain curve, where plasticity is marked by an initial small slope followed by hardening and finally a lower slope again.

The region of initial small slope is observed till strains of about 4-5% plastic strain (Figure 2.5c), and this region is more prominent than the corresponding region observed for ED oriented specimens (comparing Figure 2.5b and Figure 2.5c). The evolution of the (0001) pole (Figure 3.2a) at 5% strain shows clear signs of pole splitting from an angle ∼45° to the extrusion direction closer to the transverse direction. Analysis was performed using the average orientation of each grain and indicates that

a larger fraction of grains have twinned for the TD loading orientation than for the ED loading orientation. This is expected, given the texture of the material (Figure 2.1c) relative to the loading orientation. Further analysis of the mis-orientation angle distribution (Figure 3.2b) confirms this claim. A strong increase in the number fraction of the 88° peak is observed at 5% strain. The reorientation axis (inset) confirms that this mis-orientation corresponds to a $\{10\bar{1}2\}$ extension twin variant. This increase in boundaries with mis-orientation angles ∼88° confirms profuse twin activity by 5% strain. At the highest strain rates of the order $10^4\ s^{-1}$, Figure 2.5c shows that the initial small slope of the stress-plastic strain curve extends across a smaller range of strains. This is perhaps due to an increase in the rate of twin evolution at the higher rates, which has been observed in other hcp materials systems (Chichili et al. [58], Brown et al. [59]).

While twinning is a dominant mechanism at lower strains for this loading orientation, dislocation slip is also active. Figure 3.7c and Figure 3.7d reveal the presence of $\langle c \rangle$ and $\langle a \rangle$ dislocation components in the specimens recovered at 5% strain. The grain in which this observation was made was twinned, and TEM shows the dominance of non-basal slip in these twinned grains.

Beyond 5% plastic strain under dynamic loading, an increase in the hardening rate is observed (Figure 2.5c). This increase in hardening is associated with texture evolution due to twinning (Figure 3.2a) and the corresponding activation of non-basal slip (Figure 3.7c and Figure 3.7d) as observed in our study as well as in literature

E.W.Kelley [19], Dixit et al. [22], Ulacia et al. [43]. Extension twinning reorients the preferred grains by ∼88° (Figure 3.2a). The range of angles reported in literature range from $86° - 90°$. Once the reorientation has occurred, a majority of the grains are oriented such that compression is along the c-axis. This tends to activate the hardest $\langle c + a \rangle$ pyramidal slip system as the softer slip systems have zero Schmid factors (of course, the texture is enough to ensure that some basal slip will occur).

At 10% strain under dynamic loading, the texture data (Figure 3.2a) indicates that the reorientation of the (0001) pole by extension twinning is nearly complete. In addition, a spread in the basal pole texture is observed at 10% strain. The exact reason for this spreading is unknown. However, note that the mis-orientation angle peak corresponding to twinning ($88 \pm 5°$) has dropped at 10% strain (Figure 3.2b). Hence, the reduction in grain/twin boundary content corresponding to twin mis-orientation angles ($\sim 88^o$) is likely due to the near saturation of twinning at these strains.

The increase in hardening between 5 and 10% plastic strain may be attributed to the twin-twin and twin-dislocation interactions. While simultaneous quantification of twin volume fraction and dislocation evolution rates would be invaluable to understand the effect of these interactions, our data cannot resolve this information. In-situ diffraction experiments in synchrotron radiation facilities have developed excellent high speed measurement capabilities that could begin to provide information of this nature.

At the meso-scale ($>10\mu m$), in-situ high speed imaging data (Figure 3.5) shows the formation of localized deformation bands at early strains. These bands nucleate and propagate rapidly and eventually coalesce. The initial nucleation and growth are accompanied by the small slope of the true stress-true total strain curve (Kannan et al. [23]). High magnification in-situ images (Figure 3.6) at these early strains reveal that this localized deformation occurs along two directions. The angle between these two directions was measured to be $\sim 79^{\circ}$ which corresponds to the angle between conjugate twinning planes (Kannan et al. [23]). Beyond 5% total strain (after frame 5 in Figure 3.5), more diffuse less heterogeneous deformation follows coalescence at the meso-scale, and is associated with more rapid strain hardening. The coalescence of these bands by 5% strains is also the reason we could not observe the discrete bands during post-mortem microscopy. EBSD data at 5% strain (Figure 3.2a) shows that most of the material was already re-oriented by twinning. We hence propose that the localized deformation bands are controlled by twin nucleation and growth within specific grains in the micro-structure. Previous studies (eg. Dixit et al. [22], Nave and Barnett [60]) have also related the re-orientation of grains by twinning to subsequent non-basal dislocation slip and an associated increase in hardening. The kinetics of these proposed twin-mediated bands would help understand the strain hardening rate and subsequent failure of the material.

The onset of softening in the dynamic stress-plastic strain curves beyond 10% plastic strain (Figure 2.5c) seems to be associated with the formation of a new meso-

scale shear band (image 9 and 10 in Figure 3.5) followed by cracking and catastrophic failure. At these strains, most grains are reoriented and hence compression now occurs along the c-axis of a majority of the grains. This orientation is known to be strong and 'brittle' due to the activation of contraction twins and non-basal slip (Barnett [20], Prasad and Ramesh [21], Zhao et al. [61]). However, our results do not show signs of contraction twinning. Real-time imaging techniques at the small length scales and fast time scales are required to confirm our hypotheses of orientation-dependent failure mechanisms.

3.4.3 Compression along the longitudinal direction

Figure 2.5d shows that the stress-plastic strain response follows a power law type behavior with no strain rate dependence in the dynamic regime. Quasi-static data was not collected for this orientation.

The shape of the true stress-plastic strain response for LD compression indicates that the predominant deformation occurred by dislocation slip (Prasad et al. [9]). Based on the texture relative to the loading orientation, basal slip is expected to be the primary mode of deformation. The slopes of the true stress-plastic strain curve at different strain rates also indicates weak interactions between active slip systems, consistent with our hypothesis that basal and prismatic slip may be the most active slip mechanism along this loading orientation. These slopes are very similar to that observed for the ED oriented samples at $10^3\ s^{-1}$ strain rates. Previous studies by

Koike et al. [34] indicate that at these small grain sizes, some non-basal slip is also expected.

3.4.4 Strain rate sensitivity of flow stress and hardening

The texture evolution at quasi-static rates for ED compression looks very similar to what we observe at the high strain rates (Figure 3.1a). Figure 3.8 compares the quantitative mis-orientation angle distributions from EBSD data collected in this study at high rates and by Krywopusk et al. [36] at quasi-static rates. Figure 3.8a and Figure 3.8b present this comparison for ED oriented samples at 5% and 10% recovered strains respectively. Similar datasets are presented for TD oriented samples in Figure 3.8c and Figure 3.8d.

Figure 3.9 compares the grain size distribution between the as-received material (green line plot) and after a compressive strain of ∼5% both at quasi-static (blue) (data from Krywopusk et al. [36]) and high strain rates (red) along the ED (Figure 3.9a) and the TD (Figure 3.9b). While Krywopusk et al. [36] report significant grain growth at quasi-static rates, we do not see any signs of grain growth at the high strain rates.

For ED compression, from Figure 3.8a, at 5% strain it is evident that the 88° peak corresponding to twinning is stronger at the higher strain rates ($O(10^3\,s^{-1})$). Instead,

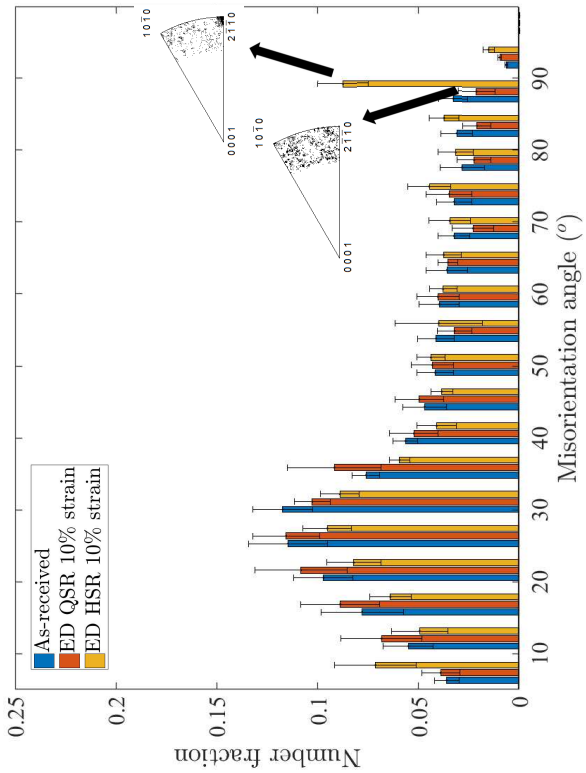

(b) Extrusion Direction: 10% strain

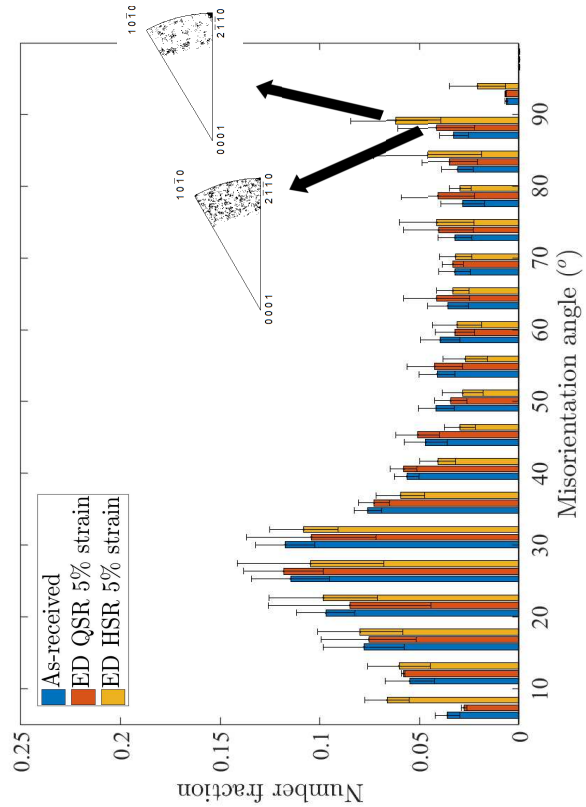

(a) Extrusion Direction: 5% strain

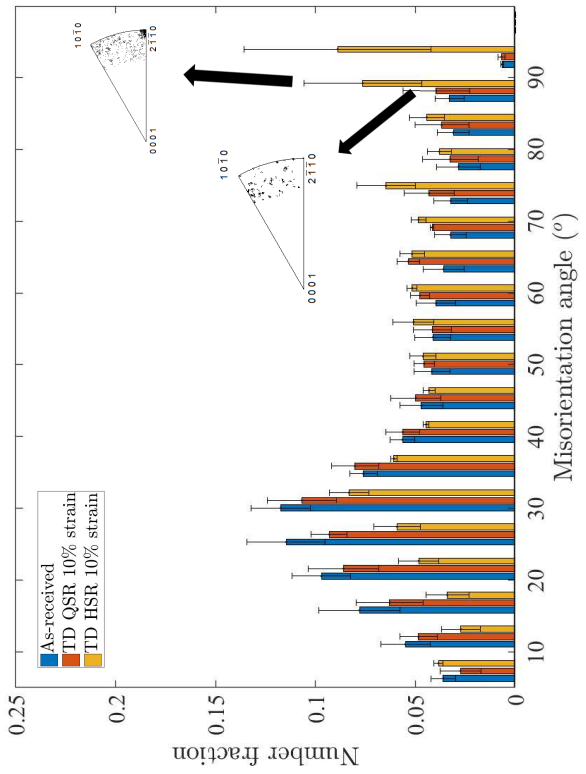

(d) Transverse Direction: 10% strain

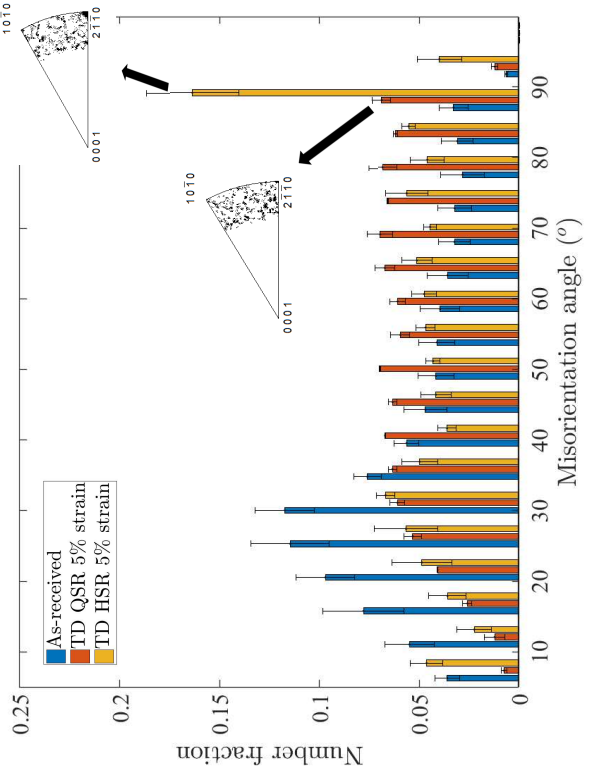

(c) Transverse Direction: 5% strain

Figure 3.8: The effect of strain rate on misorientation angle distribution at 5 and 10% strains.

at quasi-static rates, grain growth is observed as a dominant feature of evolving microstructure (Figure 3.9a), while no signs of grain growth occur at the high strain rates. The difference in the 88° misorientation angle peak increases at 10% strain. Assuming that the same mechanisms active at the high strain rates ($O(10^3\, s^{-1})$) are also active at the 'very high' rates ($O(10^4\, s^{-1})$), we expect the twin peak to further increase at these rates as well. The corresponding increase in flow stress with rate (Figure 2.6a) is perhaps due to this increase in the evolution rate of twins at higher strain rates. In hcp materials, dislocation velocities are likely dependent on the nature of dislocations. For example, basal slip is known to be relatively rate insensitive while prismatic slip and non-basal $\langle c+a \rangle$ are rate sensitive (Prasad et al. [9]). The rate sensitivity of twinning will be discussed in subsection 3.4.5. The effect of strain rate on latent

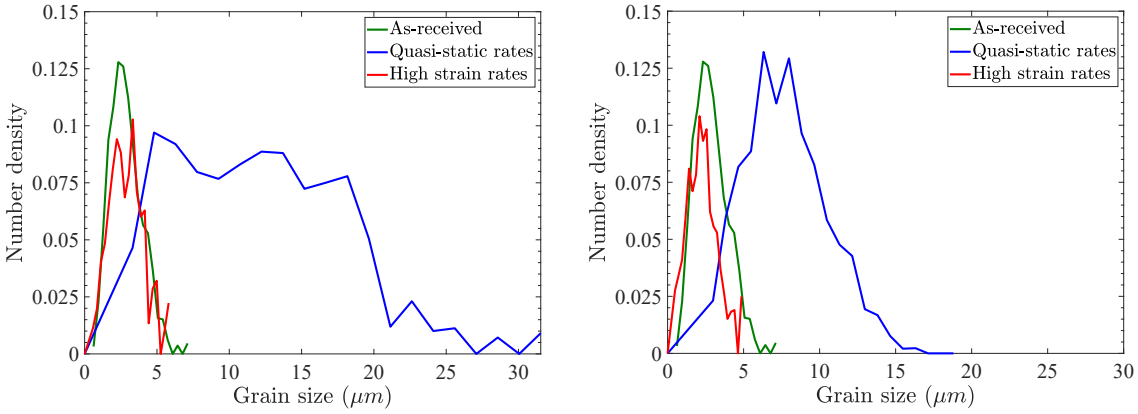

(a) ED compression (5% strain) **(b)** TD compression (5% strain)

Figure 3.9: Grain size distributions at 5% strain for the quasi-static and the high strain rates. Notice significant increase in grain sizes at quasi-static rates but not at the high strain rates.

hardening is also unknown and maybe important to capture in models.

The TD oriented samples on the other hand show a stronger effect of strain rate on flow stress and hardening in comparison to the ED. Figure 2.7b shows that, at 4% plastic strain, the work hardening rate in TD compression increases with strain rate from $10^3\ s^{-1}$. This strain is around where twinning is nearly saturated in the material (Figure 3.2a). Hence, subsequent (and rate-dependent) non-basal slip will contribute to this rate dependence in hardening (Prasad et al. [9], Zhao et al. [61]). Note that the onset of non-basal dislocations inside twins depends on the dynamics of twin evolution, and measurements show that twin dynamics are different at the high strain rates in comparison to that at quasi-static rates (Kannan et al. [23], Ulacia et al. [28], Chichili et al. [58]).

At higher plastic strains (8%) for TD compression, the work hardening as a function of strain rate is non-monotonic. First, an increase in work hardening is observed between the quasi-static and high strain rate regimes and this increase is stronger than that observed at lower plastic strains (4%). Post-mortem EBSD data from Krywopusk et al. [36] at quasi-static strain rates indicate that very little twinning at the meso-scale (μm length scale) was observed in comparison to our data at the dynamic strain rates (Figure 3.8c and Figure 3.8d). Krywopusk et al. [36] observed significant grain growth at the quasi-static strain rates as opposed to our observations of predominant twinning at the high strain rates (Figure 3.9b). However, grain growth is not known to accommodate plastic strain. The grain growth mechanism is a kinet-

ically slower process and consequently allows for activation of slip and twin systems at lower stresses once the grain size increases (the Hall-Petch effect). These ensuing plastic deformation mechanisms after grain growth, accommodate plastic strain. Krywopusk et al. [36] also observed significant reorientation of the basal pole at 5% strain (over a wider range of angles), indicating that the grain growth mechanism was accompanied by a spread in the texture. Hence, the subsequent plastic deformation mechanisms activated would be different than what we observe at the high strain rates. Clearly, extension twinning was not dominant even at 10% strain, at the lower strain rates (Figure 3.8d). This transition in the dominant mechanism from grain growth to twinning appears to be the reason behind the increase in work hardening rates with strain rate at larger plastic strains (8%) in Figure 2.7b.

Within the high strain rate regimes at 8% plastic strain, the work hardening rates for TD oriented samples decrease with increasing strain rate (Figure 2.7b). The true stress-plastic strain data (Figure 2.5c), indicates that this falls around the strains where a reduction in slope occurs. This is typically associated with a softening mechanism. The source of softening was discussed in subsection 3.4.2. Much after twinning has saturated, shear bands form in the reoriented specimen causing cracking and catastrophic failure. At very high strain rates, the reorientation of twinned grains appears to occur more rapidly (i.e. the twinning rate increases) resulting in the early onset of hardening due to non-basal slip at the higher rates of loading. Our hypothesis for the softening mechanism along this orientation explains the correlation between

the increase in work hardening rates and the reduction in the 'failure strains' at the onset of softening with increasing strain rate (Figure 2.5).

3.4.5 The effect of strain rate on deformation twinning

Several studies suggest that twinning is insensitive to strain rate (e.g. Prasad and Ramesh [21], Yu et al. [33], Meyers et al. [62]) in the sense that twin nucleation appears to depend on a critical stress rather than a critical strain rate. The common argument made in support of this hypothesis is that the initial yield stress during twin dominated deformation is insensitive to rate. However, this view is somewhat limited, because twin dynamics is involved in the effects of twin evolution (i.e., twin evolution involves both twin nucleation and twin growth, and the latter may have associated dynamics). Consider again the additive decomposition of a scalar shear strain rate γ,

$$\dot{\gamma} = \dot{\gamma}^e + \dot{\gamma}^{vp} \tag{3.4.1}$$

where $\dot{\gamma}^e$ is the elastic shear strain rate and $\dot{\gamma}^{vp}$ is the visco-plastic shear strain rate. If both twins and dislocations are active,

$$\dot{\gamma}^{vp} = \dot{\gamma}^d + \dot{\gamma}^t \tag{3.4.2}$$

where $\dot{\gamma}^d$ and $\dot{\gamma}^t$ are the visco-plastic shear strain rates due to dislocations and twins respectively.

For a constant rate of visco-plastic shear strain, the sum of the rate contributions from dislocations and twins is then constant. However, both dislocations and twins have limiting rates of evolution. Our measurements (Kannan et al. [23]) presented later in this thesis (chapter 4) have shown peak twin tip velocities in single crystal magnesium under dynamic loading (order of $10^3\ s^{-1}$) to be limited to $\sim$1.5 km/s, while twin thickening velocities were limited to $\sim$20 m/s. Thus, at sufficiently high strain rates, a competition develops between dislocation and twin contributions to the total visco-plastic rates, and manifests as a rate effect on macroscopic flow stresses. A key to understanding this effect lies in the relative kinetics of twinning and dislocation slip. Our results presented in chapter 2 and the current chapter indicate that at high strain rates, the evolution of twinning in the micro-structure may have important implications on the effects of strain rate on flow stress, strain hardening and failure (discussed in subsection 3.4.2 and subsection 3.4.4) in this magnesium alloy and perhaps in other hcp metals.

Current methods of incorporating strain rate effects into computational models use energy-based formulations (e.g., Chang and Kochmann [48]), where the stored energy includes effects of self-hardening and cross-hardening (or latent hardening) for every slip and twin system. Strain rate hardening was incorporated using 'dissipation potentials' (Ortiz and Stainier [63]). The dissipation potentials used for twins vary, with some studies setting them to zero (Chang and Kochmann [48]) (implying no rate dependence) and some others using an empirical power law (Zhang and Joshi [2]). In

reality however, the rate dependence of twinning required to accurately identify these parameters is unknown.

Experimental evidence in the past has reported an increase in twin activity at higher strain rates in magnesium (e.g., Ulacia et al. [43], Dudamell et al. [64]) and also in other hcp metals like beryllium (Brown et al. [59]) and titanium (Chichili et al. [58]). Note that none of these studies, except the one by Chichili et al. [58], reached strain rates of the order $10^4\ s^{-1}$. However, contrary evidence does exist in literature as well. Dudamell et al. [65] noted a decrease in twin activity at higher strain rates in a magnesium-manganese-neodymium alloy containing 1wt% of neodymium (MN11). Hence, the choice of alloying elements may also affect rate sensitivity of twin evolution.

We present the argument that the 'rate dependence of twinning' should imply not just the nucleation stresses but also the plastic flow and hardening characteristics due to twin evolution and the competition between dislocation and twin dominant deformation. In this context, twinning is likely to be rate dependent. The transition in mechanisms reported in this chapter between significant grain growth with little twinning (at the meso-scale) at the low strain rates to significant twin nucleation and growth at the high rates (subsection 3.4.4) presents some evidence in support of this argument. It is hence necessary to discuss nucleation, growth and interaction of twins as distinct phenomena with independent strain rate dependencies.

3.4.6 The effect of grain size on twinning: Strain rate dependence

Literature has also cited cases where twinning has been suppressed at small grain sizes (for e.g., Yang and Ghosh [66], Barnett et al. [67], Barnett [68]). The most common interpretation for this grain size effect comes from the Hall-Petch relation (Meyers et al. [62]). The slope of the Hall-Petch curve for twinning has empirically been found to be higher than that of slip in fcc, bcc and hcp metals. An interesting short paper by [68] offers a rationale for these observations based on scaling. The fundamental assumptions made are (1) twins nucleate at grain boundaries; (2) grain size limits the maximum size of the twin and (3) the twin density is dictated by the local stresses at the grain boundary. The argument presented indicated that for a *constant number density of twins per unit grain boundary area*, the number of twins per unit volume scales as d^{-1} where d is the grain size. However, the number of twins per grain scales as d^2. We present the argument that these physical explanations for the Hall-Petch effect however, need to have rate effects (or timescales related to twin nucleation and growth) incorporated in them.

The following chapter in this thesis (chapter 4) will show that twin nucleation rates in magnesium may be rate dependent with additional twin nucleation preferred over growth at high strain rates. Another assumption in Barnett [68] states that the twin density is dictated by local stresses at the grain boundary. Many results point

to this being true for eg., Aghababaei and Joshi [69]. Notice that the deformation fields during the dynamic experiments are heterogeneous (Figure 3.6) implying that local stresses within these heterogeneities maybe very high. If twin nucleation were stress-driven as has been suggested by studies in the past, this would imply a local increase in the number density of twins around heterogeneities. The stress fields at quasi-static rates may also be heterogeneous, but results in literature suggest that this would contribute to grain growth.

While twinning may be suppressed at smaller grain sizes at quasi-static strain rates, increasing the strain rate of loading may increase the propensity of the material to twin. Modifying existing kinetic models for twin nucleation and growth have implications on the flow stress, strain hardening and failure mechanisms in polycrystalline magnesium as has been shown in chapter 2 and the current chapter. Our results open up the need for a more systematic study of twin dynamics not only as a function of grain size but also strain rate. One can imagine building a phase map that represents twin activation stresses (nucleation stresses of the first twin(s)), twin nucleation rates and growth rates as functions of grain size, strain rate along with other variables such as temperature and alloy composition. The recent advancement in in-situ experimental science with high temporal and spatial resolutions available at synchrotron sources (for eg. [3]) makes these studies more possible now than ever before. A 'phase map' so conceived would be very useful in building robust theoretical models for twin evolution to incorporate into larger scale plasticity models and

eventually contribute towards a mechanism-based materials design methodology for magnesium.

3.5 Conclusions

In chapter 2, the strain rate dependence of plastic flow was studied for a textured AZ31B magnesium alloy processed by Equal Channel Angular Extrusion under uniaxial compression over a wide range of strain rates, including results from Krywopusk et al. [36]. In this chapter, the mechanistic basis for these macroscopic measurements were discussed using a combination of in-situ and post-mortem microscopy techniques. Some of the key conclusions from this work are reiterated below.

1. Two principal orientations of the ECAE block were investigated. For the dynamic compression experiments, significant basal dislocation slip along with some extension twinning was observed for compression along one orientation ($\sim$45° to the dominant c-axis texture).

2. For compression along a transverse orientation (nearly perpendicular to the dominant c-axis texture), significant extension twinning was observed with $\langle c+a \rangle$ and $\langle c \rangle$ dislocations active within the twinned grains. At the lower rates however, Krywopusk et al. [36] observed little signs of meso-scale twinning. Instead, significant grain growth was observed with grain sizes increasing by an order of magnitude along both loading orientations.

3. This transition in mechanism between the low and high rates is associated with an increase in macroscopic flow stress and work hardening rates between the low and high strain rate regimes reported in chapter 2.

4. Heterogeneous deformations leading to localization of deformation was observed at the high strain rates for both loading orientations. The localization eventually leads to strain softening and failure. The strain at the onset of softening was observed to decrease as strain rate increased.

At this point, we delve deeper into deformation twinning as a specific plastic deformation mechanism in hcp metals with applications towards magnesium. The rest of this thesis covers the mechanics and crystallography of twin evolution in single crystal magnesium with greater focus on the former. We use pure magnesium single crystals for this study to avoid complexities arising from other defects in the material such as grain boundaries and precipitates.

Chapter 4

The mechanics of dynamic twinning in single crystal magnesium[†]

Preface: The following chapter is largely based on an article published in the Journal of the Mechanics and Physics of Solids (Kannan et al. [23]). The co-authors were Kavan Hazeli and K. T. Ramesh. VK was the lead author in this study. KH performed two dimensional post-mortem EBSD microscopy on recovered samples and helped review the manuscript. KTR was the principal investigator and was involved in the problem formulation, data interpretation and manuscript preparation.

The previous two chapters were focused on understanding the rate dependent plastic deformation and failure in polycrystalline magnesium alloys from a mechanistic basis. Both dislocation slip and deformation twinning were identified as dominant

[†]This chapter is largely based on an article published by Kannan et al. [23] in the Journal of the Mechanics and Physics of Solids.

deformation mechanisms depending on loading orientation relative to material texture. In particular, deformation twinning was much more common at high strain rates than at lower strain rates where grain growth (accompanied by a spread in texture) was identified as being common, leading to subsequent plastic deformation within these grains (Krywopusk et al. [36]). We concluded that twin activity is strain rate sensitive and the kinetics of deformation twinning is expected to explicitly relate to work hardening and implicitly to failure. In the latter half of this thesis, we will explore deformation twinning in greater detail. The presence of multiple grains in polycrystalline aggregates, makes direct observations and modeling of these twins difficult. We hence restrict our focus to specific types of deformation twins in pure single crystal magnesium.

4.1 Introduction and background

Twins are commonly found in metals and some ceramics, and often appear as lenticular bands containing a local reorientation of the crystal lattice. The atomic arrangement inside the twin is a mirror-image of that outside, and hence the name. Observations of twins in metals have shown twin sizes spanning the nanoscale to meso-scale (up to 10's of microns). Understanding twinning, therefore involves understanding physical phenomena active over a range of length scales (from atomistic to grain size) as well as a wide range of time scales. While commonly observed in hcp metals, twins also are seen in fcc metals and in bcc metals at low temperatures

and/or high rates of loading (e.g. Takeuchi [70], Johnson and Rohde [71]). An excellent review of the crystallography of deformation twinning is provided by Christian and Mahajan [11].

Twin evolution is controlled by two processes: nucleation and growth. A quantitative description of nucleation requires a criterion for twin nucleation and an understanding of the nucleation rate. Defining a critical condition for nucleation requires knowledge of the microscopic structure of the twin nucleus. In general, twin nuclei are bounded by an ensemble of partial dislocations. The specific details of this ensemble vary between fcc, bcc and hcp structures with hcp being the most complex. No consensus has been achieved on the structure of a twin nucleus in hcp systems, but molecular dynamics has been used extensively in the recent past to provide insight into the structure of twin nuclei (for example, Serra et al. [72], Aghababaei and Joshi [69]). At larger length scales, the formation of stable nuclei has been modeled by energy minimization methods for an inclusion with a sharp interface in a continuum (Yoo and Lee [15], Lebensohn and Tome [73]). Accurate descriptions of the interfacial energy however still depend on knowledge of the interfacial structure at smaller length scales. The rate of formation of these stable twin nuclei in a larger crystal has not been studied carefully (an exception being Beyerlein and Tomé [74]).

With respect to growth, observations of needle-shaped lenticular twins (for example, Barnett [20]) indicate that twin growth occurs by extension of a fast twin tip followed by a coordinated slower migration of the boundaries. Measurements of

twin boundary growth rates have been made for some limited loading conditions (e.g. Wang and Huang [75], Prasad and Ramesh [21]). However, twin tip velocity measurements are challenging. Takeuchi [70] used strain gages placed at two locations on an iron single crystal specimen measuring tip velocities of $\sim$ 2500 m/s. Soon after, Brunton and Wilson [76] used a high speed camera to look at propagating twin tips in zinc and tin single crystals reporting velocities of 600 m/s. Using another novel, albeit indirect technique, Williams and Reid [77] measured tip speeds similar to that of Takeuchi [70] in single and polycrystalline silicon-iron at liquid nitrogen temperatures. While these were very impressive measurements for the time, the twins were developed under knife-edge loading conditions and hence it was difficult to determine the stress state. Surprisingly, Takeuchi's estimates are better known than Brunton and Wilsons' measurements. Dixit et al. [78] used post-mortem microscopy on single crystal magnesium plates subjected to plate impact loading to estimate twin tip velocities of greater than 1 km/s. However, such post-mortem analyses provide limited information on the spatio-temporal evolution of the twin growth process. Here we report the first direct in-situ measurements of twin tip velocities in single crystal magnesium under controlled dynamic loading. Measurements of macroscopic stress, strain rate and twin dynamics (using in-situ images) are made simultaneously. It is important to recognize that substantial dislocation slip also occurs in these experiments (Dixit et al. [22]). While we focus on the twinning mechanism in this chapter, the contribution of dislocation slip to plastic strain is also approximated. Measurements

of the crystallographic nature of twins in some of these experiments are discussed in chapter 6.

4.2 Experimental methods

4.2.1 Conventional compression Kolsky bar

We use Kolsky bars to compress magnesium single crystals along one specific crystallographic axis in order to activate twins. The general compression kolsky bar setup is similar to the one used for conventional kolsky bar experiments in chapter 2 and chapter 3.

A schematic of the specific setup for in-situ imaging during dynamic loading is shown in Figure 4.1. To achieve stress equilibrium of the deforming specimen it typically takes the time equivalent to about 3 reverberations (Davies and Hunter [79]) of the elastic longitudinal wave inside the specimen. Given the size of our specimen and the wave speed, this time corresponds to $\sim 2\,\mu s$. This is consistent with our experimental verification of force balance, however an exact numerical comparison is difficult because the transmitted signals are much weaker than the incident and reflected signals. Hence the difference between the incident and reflected signals have greater signal to noise ratio than the transmitted. We can verify that the transmitted force signal overlaps with the mean of incident bar force signal (when matched in time). A description of the analysis of kolsky bar data is provided in Appendix A. A

more detailed and general description of the kolsky bar may be found in the book by Chen and Song [38].

The bars used in our setup were made of 1/2" diameter maraging steel. The incident bar was instrumented with conventional foil strain gages, but because the transmitted strain is very small in our experiments, semiconductor strain gages were used on the transmitted bar. All signals were captured simultaneously using a high speed digital oscilloscope (LeCroy HDO4034).The incident and reflected signals from the recorded data were corrected for wave dispersion effects (Gorham [39]) due to propagation of waves down the bar. Transmitted signals were not corrected because they had little high frequency content, so that dispersion of the propagating wave is minimal for the transmitted signal.

We used this apparatus to explore the nucleation and growth of twins in single crystal magnesium under dynamic loading. Since our focus is on the dynamics of twin evolution, the temporal histories of stress and strain are interpreted in conjunction with the imaging data. Note that the strains we measured were the total strains, which also include substantial plastic strains due to dislocation slip.

4.2.2 High speed imaging

Imaging was performed using a Specialised Imaging Kirana high speed camera capable of capturing 768×924 pixels (10-bit resolution) of data at 5 million frames per second (200 ns temporal resolution). The pixel size on the charge coupled device

(ccd) sensor is 30 μm/pixel, and an optical arrangement was used to achieve a good magnification while capturing the entire specimen in the field of view. A schematic of the optical setup is shown in Figure 4.1. A 105 mm Nikon lens was coupled to two teleconverter lenses to increase magnification. Further improvement was achieved by attaching bellows between the lens system and the sensor, thus effectively increasing the magnification. The spatial resolution of measurements achieved in these experiments was $\sim 5\,\mu m$/pixel.

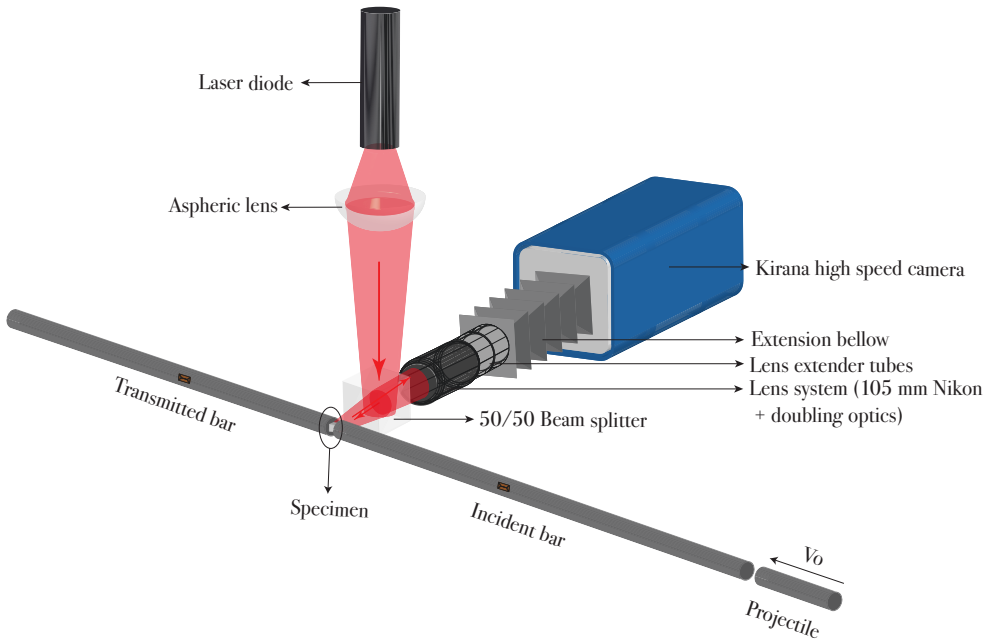

Figure 4.1: Schematic of the experimental setup. The bars are $\frac{1}{2}$" diameter made of maraging steel. The imaging setup is shown too with a 105 mm and 2 telecentric lenses (doublers) separated from the camera by hollow bellows. Lighting is provided by a 400 W pulsed laser diode.

Imaging using the very high shutter speeds of the camera requires very strong light sources. The same light source and settings used in chapter 3 were used here. The electronic shutter in this specific camera allows for the shutter speeds to be almost the same as the inter-frame time ($\sim$ 200 ns) with the time for turning on the electronic shutter lasting <10 ns. Based on the spatial resolution of measurement, no effect of motion blur was observed due to the finite but very short exposure time of the pulsed laser ($\sim$100 ns). The laser diode offers a diffuse light source and hence an aspheric lens was introduced to focus the beam onto the specimen. An effective beam diameter of $\sim$ 5 mm was achieved. The beam was focused normally onto the specimen surface using a 50/50 beam splitter, thus providing nearly uniform lighting across the entire specimen.

4.2.3 Image processing

Quantitative image processing was used to extract twin characteristics from the images with all the processing routines written in Matlab. First, every image was adjusted to increase the dynamic range of intensities available. To smooth out random white noise, a Matlab in-built median filter was then applied. Every pixel was replaced with the median of the intensity of a 3×3 matrix of pixels in its neighbourhood. This would coarsen the resolution of the twin area fractions measured from these images (described later in the chapter). In order to resolve features along specific directions in the image, directional gradients were calculated along two iden-

tified directions of interest. Hence, for each raw image, two images were generated to identify twins along two specific directions. To identify whether a pixel was within a twin or not, adaptive thresholding techniques were used on each gradient image. Based on thresholds chosen, each gradient image was converted to a binary image. A final post processing step was performed on the processed binary image to remove noise based on size, eccentricity and orientations of features in the image. Since no detwinning was observed in the images and, to ensure that no information from the previous image was lost, every image was cross-verified with the image in the previous time step. The processing parameters for every dataset were chosen independently to ensure mimimal loss of information due to specific variations in imaging conditions between specimens.

Another issue specific to the camera used is called 'ghosting'. One effect of ghosting is the superimposition of a previous image on a current image (this occurs at every 10th frame). In our specific experiments, the twins from the previous image remain hidden (the same twins have grown in the current image) while the absolute intensity of the ghosted image goes up. First, we were able to minimize ghosting issues optically by reducing the aperture of the lens system. We came to the empirical conclusion that part of the ghosting was from saturating the sensor and part from hardware issues associated with transferring data from the sensor.

To reduce the effect of ghosting on the processed data, the parameters used for thresholding images used statistics from the current image being processed instead of

using a single parameter for all images in a dataset. The threshold value for a dataset was chosen as

$$T = \bar{\mathcal{I}} + c\sigma_{\mathcal{I}}$$

where $\mathcal{I}(x, y)$ is the gray scale intensity distribution of pixels in an image, $\bar{\mathcal{I}}$ and $\sigma_{\mathcal{I}}$ are the mean and standard deviation of this intensity distribtuion and c is an empirical factor that depends on the specimen surface quality and lighting for each dataset. c was optimized and fixed for all images in a single dataset. Hence, the parameters for the ghosted image account for the shift in mean intensity of that particular image resulting in a more continuous area fraction evolution. Not accounting for ghosting would result in spikes in the area fraction history at every 10th frame.

4.2.4 Uncertainties arising from the imaging

Twin tip and boundary velocities were calculated by manually picking the twin tip or boundary position at each time step and then analyzing this data. A twin tip is blurred over several pixels due to the limitations in magnification achieved by the imaging setup. The number of pixels containing a twin tip was measured to be about 10 pixels, which is effectively the uncertainty in measurement of twin tip position. The resulting uncertainty in twin tip velocity was found to be ± 50 m/s. Twin boundary velocities were even harder to quantify because of the slow speeds. Note that the twin grows as a lenticular structure and hence the boundary velocities are different along a single twin (especially for the larger ones). In this study we pick a point on

the twin boundary to make this estimate. The uncertainty was quantified in a similar fashion as for the twin tips. A data point was collected every three images. Thus the uncertainty in the twin boundary velocity is ± 8 m/s which is a significant fraction of the velocity measured.

The image processing scheme explained in subsection 4.2.3 was used to extract twin area fractions from images. Uncertainty in this case was calculated from the noise measured by the image processing code before the first twins appeared on the images for each dataset. As the twins evolve on the specimen surface, this background noise (in the form of features formed on the image due to surface preparation) becomes smaller with respect to the useful signal. Hence the maximum uncertainty is that which is measured before occurrence of the first twins and is a conservative estimate. This was used as the uncertainty in measurement of twin area fractions.

4.3 Material Investigated

The material investigated was 99.999% pure magnesium single crystals from Metals Crystals and Oxides Ltd., UK. Single crystal magnesium is a very soft metal and extremely delicate to handle. Special care was taken to avoid inducing twins during specimen preparation procedures. To ensure twinning was activated as the main mechanism of deformation (at least during early times), compression was performed along one of the $\langle 11\bar{2}0 \rangle$ crystallographic directions and imaging was performed on the $\{10\bar{1}0\}$ plane (Figure 4.2). Specimen dimensions were $3.4 \times 3.7 \times 4.3$ mm with

compression along the 3.4 mm direction and imaging on the surface with cross-section 3.7×4.3 mm. The variability in specimen dimensions was $\sim 500\,\mu m$ as the focus was on ensuring minimum damage to the specimen and not on maintaining exactly the same specimen dimensions. A schematic of the specimen and corresponding crystallographic orientations is presented in Figure 4.2.

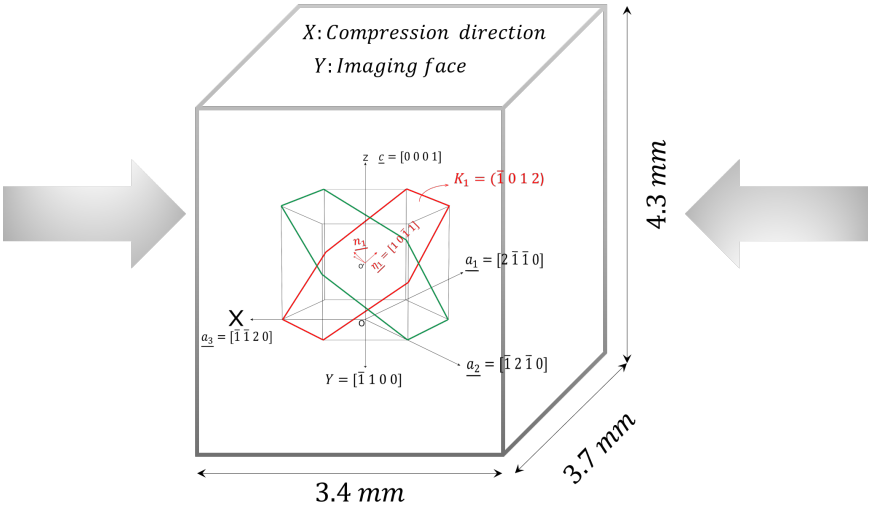

Figure 4.2: Specimen schematic with crystallographic orientations. The blue arrows represent the direction of compression. Imaging was performed on the $[10\bar{1}0]$ crystallographic plane. The normal to this plane is denoted as the Y-direction.

Cuboidal specimens were cut using wire EDM (Electro Discharge Machining). Machining was done inside dielectric water to insulate the wire from the workpiece and also for cooling. This ensures a very small heat affected zone and minimum damage during cutting. The specimens were later etched using a 10% solution of nitric acid (HNO_3) in water to remove the damage region caused by the machining. Optical microscopy was used to ensure minimum damage on the surface of as-etched

samples. Next mild mechanical polishing of the specimen ends was performed to ensure parallelism. Imaging faces were polished down to a 50nm surface finish using a colloidal silica suspension to get an optimum surface for imaging.

4.4 Macroscopic response

A total of twelve experiments were performed at strain rates of the order of $10^3\ s^{-1}$. The sample naming convention was chosen based on samples prepared and not successful experiments performed, resulting in experiment labels indicating numbers up to 016. The list of experiments performed as a part of this dataset are listed in Table A.2. Some samples were recovered for post-mortem analysis, the results of which will be discussed in chapter 6. Our sample naming schemes are determined within our experimental database system, and are intended to assist with large-scale data sharing.

Considerable variability was observed in the stress-time response with stresses at $\sim 1\%$ total strain varying between 20 and 40 MPa (for strain rates varying from 1000 to 3500 s^{-1}). These variabilities are inherent to the deformation of these single crystals because of the stochasticity in nucleation and growth rate of twins at early times. The stochasticity in nucleation mentioned in this context refers to the uncertainty in the spatial distribution of nucleation sites and hence in number density of nucleated twins. The stochasticity in growth refers to the uncertainty in twin growth rates due to local microstructure around the propagating twin. The effect of rate on the macroscopic

response could also be a potential cause but this has not been studied in detail yet.

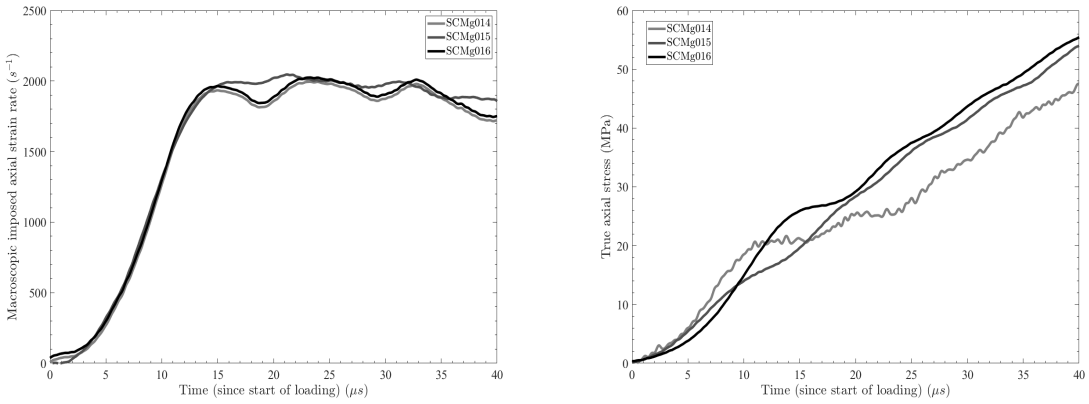

(a) Imposed macroscopic strain rate **(b)** Stress-time response

Figure 4.3: Macroscopic imposed initial conditions and material response for single crystal magnesium loaded dynamically along the a-axis

We will discuss three representative tests that were performed at nearly the same strain rate (Figure 4.3a). The average true strain rates in the specimen reached a steady value of ~ 2000 s^{-1} after a rise time of $\sim 15\,\mu s$. Note that for each test, 180 images are collected over $36\,\mu s$ from around the start of loading.

Figure 4.3b shows the measured stress-time response from the three experiments. The low frequency oscillations are due to the dispersion of propagating waves in the bars. Generally, a signature in all these curves is a change in slope at $\sim 10 - 12\,\mu s$. Test SCMg014 shows a slightly different stress history at early times for reasons discussed later. The specimens were unloaded after about $56\,\mu s$, but we will focus on the phenomena observed during the loading phase.

Figure 4.4 shows representative true stress-true strain curves (including those

corresponding to the experiments presented in detail in this chapter). Notice the sigmoidal profile that has classically been associated with the occurrence of extension twinning (Barnett [12]). For the experiments discussed in this paper, tests were stopped before the last hardening region beyond 10% was reached. Another detail to note here is the elastic portion. The elastic portion is typically more compliant than the elastic response of the material due to wave propagation effects during the initial stages of deformation.

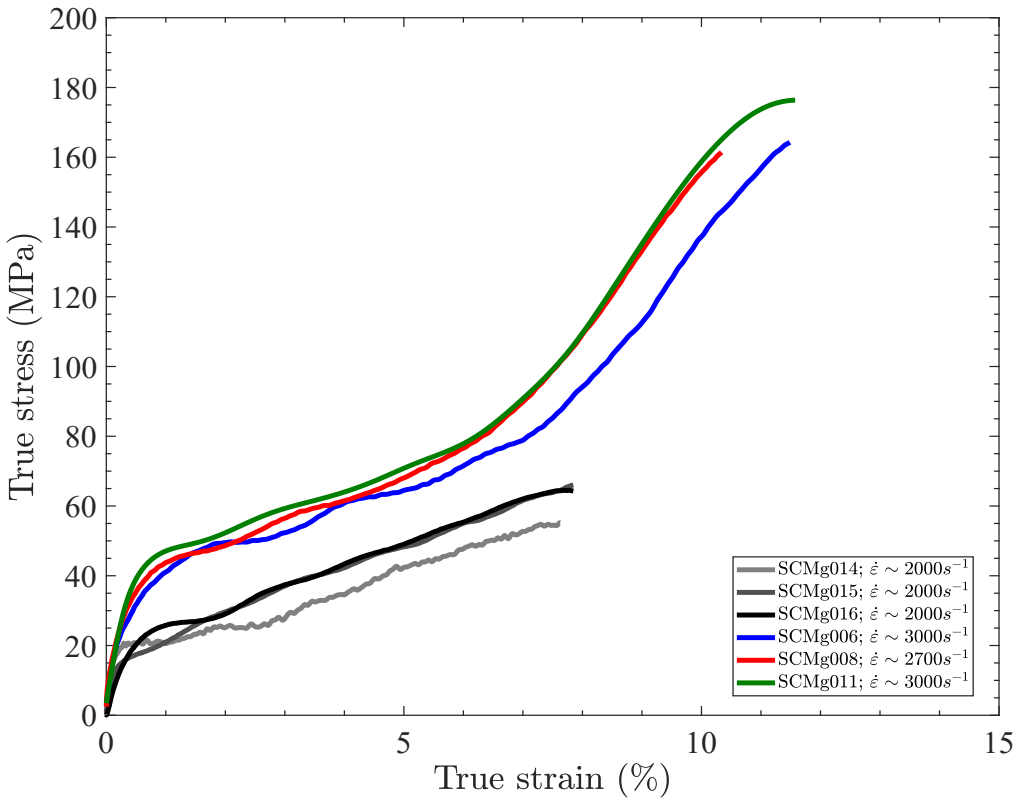

Figure 4.4: Representative dynamic true stress-true strain curves from experiments conducted during this study.

To the authors' knowledge, till date, no experimental study has been performed on the strain rate sensitivity of single crystal magnesium extending into the strain rate regime of $10^3\ s^{-1}$. The variability in the data presented in Figure 4.4, could be attributed to two effects. One effect is the variability in the dynamics of twin nucleation and growth. Since the initial number of twins activated and the spatial evolution of twins have some variability, the macro scale response could be affected by this stochasticity. Another source of the stochasticity could be attributed to the distribution of atomic level faults induced during crystal growth. A second hypothesis that needs more probing is rate effects. Notice that the stress-strain curves that have a higher flow stress correspond to experiments performed at a slightly higher strain rate. While strain rates are within an order of magnitude, the rate sensitivity of twin evolution at this length scale is unknown and cannot be ignored. While beyond the scope of work covered in this thesis, this problem merits deeper studies.

4.5 In situ observations of twinning

Figure 4.5 shows a sequence of selected images from one experiment (Test ID: SCMg015; macroscopic applied true strain rate $\sim 2000\ s^{-1}$). The compressive loading was performed along the horizontal direction in the images which is along the shortest dimension of the specimen. The scale bar in the first image corresponds to 1 mm. Black arrows in the first frame indicate thin scratches on the surface of the specimen induced during specimen preparation. These are not twins. Nucleation of the first

twins occurs at $\sim 11.4\,\mu s$ in this experiment as shown by the red arrow in the second frame. Many of the first twins nucleate near the edges of the specimen. This is due to stress concentrations at the edges of the specimen. After nucleation of these first twins, additional twins (marked by green arrows) nucleate from within the matrix in the vicinity of existing twins. The twins are long and narrow, with rapidly extending tips and little broadening. After nucleation of first twins, the twin tips grow rapidly across the surface. As deformation progresses and the first twins stop growing, nucleation of additional twins (we refer to these as Gen2 twins) is observed (light orange and blue arrows in the frame at time $\sim 17.4\,\mu s$) from existing twin boundaries. Negligible twin broadening in comparison to twin extension is observed in most twins contrary to quasi-static observations (Barnett [20], Prasad and Ramesh [21]). By $\sim 27\,\mu s$, twins have nucleated throughout the matrix.

A brief overview of the crystallography is useful at this juncture. Figure 4.6a is a schematic of the hcp crystal structure with relevant directions and planes marked. With respect to the figure, the specimen was compressed along the $\boldsymbol{a_3}$ direction and imaging performed along the Y-direction. Note that crystallographic directions are specified with respect to the four index notation and planes denoted according to the Miller index notation. A twin variant is described by its plane (K_n) and the direction of shear (η_n) where n refers to a specific variant. The two active twin variants observed during the experiment (Figure 4.6b) in this case are (K_1, η_1) variant shown in the (the red plane) and a similar $(K_2 = (01\bar{1}2), \eta_2 = [01\bar{1}1])$ variant (the green plane)

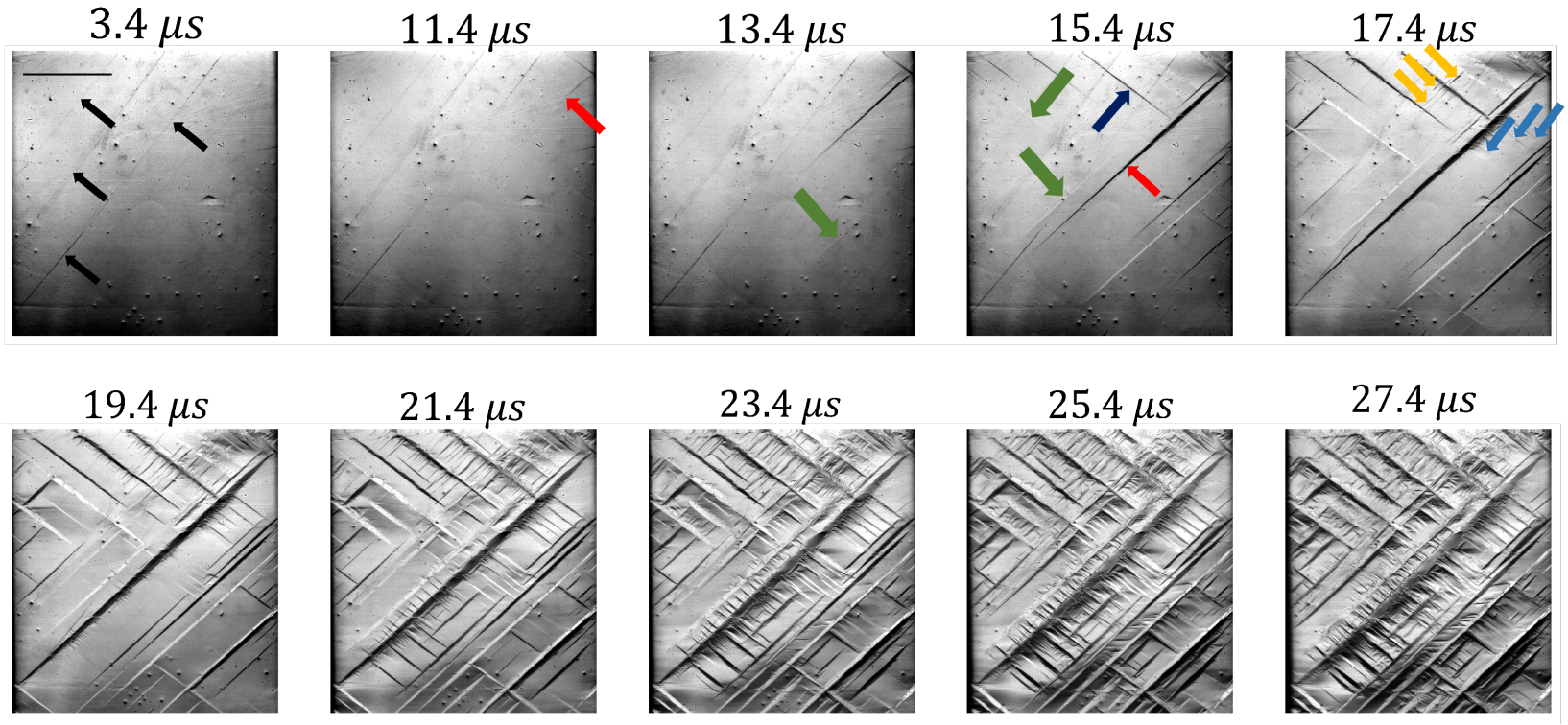

Figure 4.5: Selected sequence of in-situ images from one experiment. Scale bar in the first image corresponds to 1mm. The black arrows in frame 1 (at time 3.4 μs from the start of loading) point to thin scratches on the surface. In frame 2 (11.4 μs), the red arrow shows the nucleation of one of the first twins. First twins of each variant are shown in the fourth frame at 15.4 μs by the deep blue and red arrows. The nucleation of Gen2 twins is shown (light orange and blue arrows) in the fifth frame at 17.4 μs. The green arrows point to twins that nucleated from within the specimen and not at the edges. (Specimen ID: SCMg015)

(chapter 6). We refer to these as the 'Var1' and 'Var2' variants. What we observe are projections of the twin variants on the imaging plane (crystallographic prismatic plane). Other variants were also found in the complementary study presented in chapter 6 which were not captured during the high speed imaging.

Geometrically, the unique common line that forms the intersection of two planes is perpendicular to the normals to both planes. The line along which twins form on the imaging surface is the intersection between the twin plane and the imaging prismatic plane. Employing the crystallography of each twin variant, the dot product of the projected line with the crystallographic a-axis yields an angle of 39^o. Hence, the angle between the two twin variants as observed on an image is expected to be 78^o. The experimentally measured angles shown in Figure 4.6b are very close (within $\pm 1^o$).

In what follows, twins on each of the conjugate twin plane are named 'Var1' (variant1) and 'Var2' (variant2) respectively. For each conjugate, twins that appear to nucleate from the matrix are called 'Gen1' and twins that nucleate from existing twin boundaries are called 'Gen2'.

Note that twins observed in this study are extension twin variants which means that the c-axis is under extension. Post-mortem microscopy studies have revealed multiple twin variants present under similar loading conditions. There have been observations and predictions of other variants that both extend and contract the c-axis. Christian and Mahajan [11] report some studies of these variants. More recently

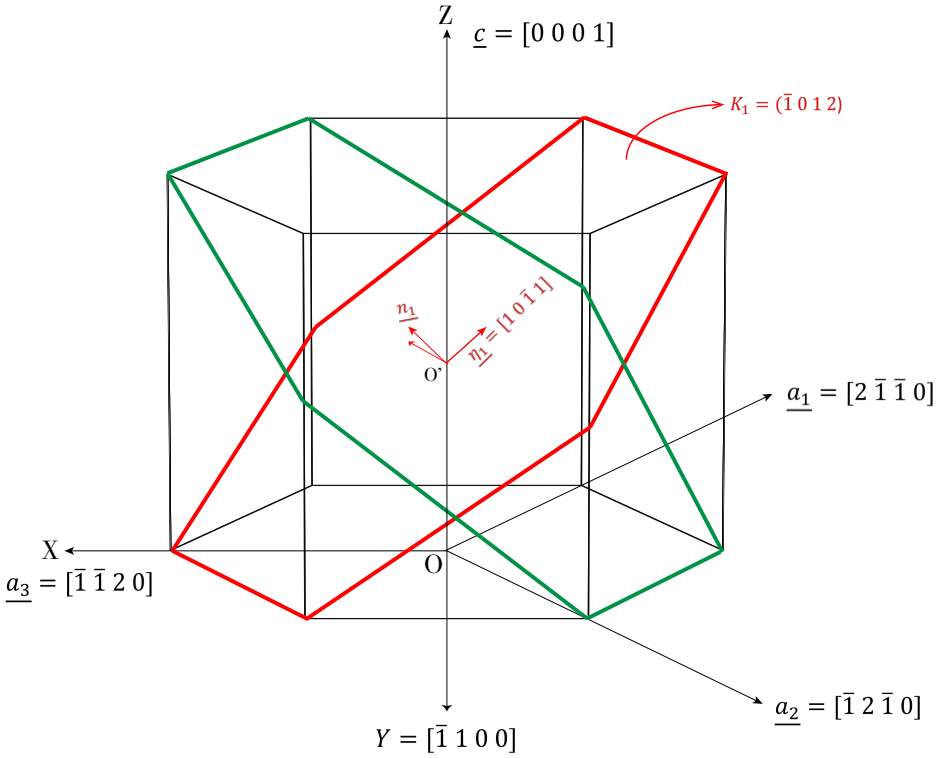

(a) Schematic of the hcp crystal

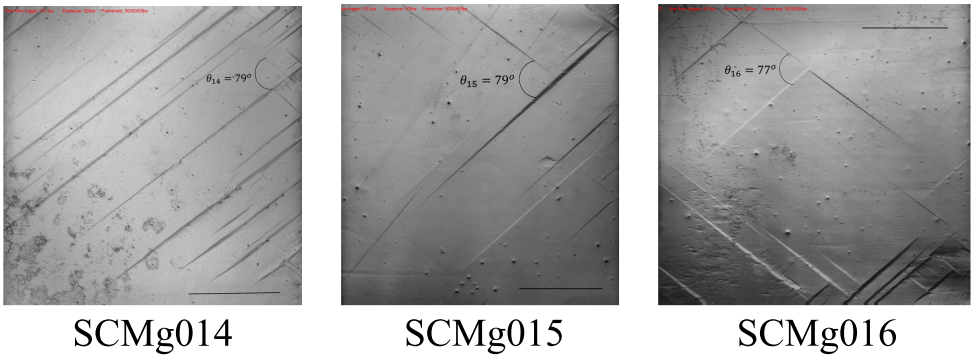

(b) Var1-Var2 twin angles from images

Figure 4.6: Crystallography of conjugate twins and angle between them as observed on the imaging plane. Note that the measured angles agree very well with expected values of 78^o. Scale bar corresponds to 1 mm.

atomistic calculations by Sun et al. [80] revealed the existence of numerous other variants that limited experimental studies have observed and passed off as anomalous. The dynamics of these other twin variants are indeed interesting problems to pursue but the conditions for nucleation of these variants are unknown.

4.6 Relating macro-scale response and twin dynamics

Figure 4.7 shows the macroscopic stress-time curve (Figure 4.7a) as measured from one experiment (SCMg014), together with select images taken at specific times (Figure 4.7b). Each of the images in Figure 4.7b corresponds to the times indicated by the red data points on the stress-time plot in Figure 4.7a. It is apparent that the change in slope of the stress-time curve corresponds to nucleation of the first twins in the material (images 4 and 5). The change in stress rate with the nucleation of first twins is consistent with the observations of Bell and Cahn [54]. We observe that the stress in the specimen remains essentially unchanged over the next 5 μs or so, and the images (frames 5-8) show that during this time more twins nucleate and fly across the specimen. Noting that this is an experiment with an imposed macroscopic strain rate, it appears that the continued nucleation of twins occurs at near constant stress at this strain rate. At later times, after frame 8, the stress begins to climb again. Frame 8 and later images suggest that this maybe related to the obstruction

of the growth of the large number of Gen2 twins that are nucleated from Gen1 twin boundaries beginning around frame 6. We return to this topic in section 4.8.

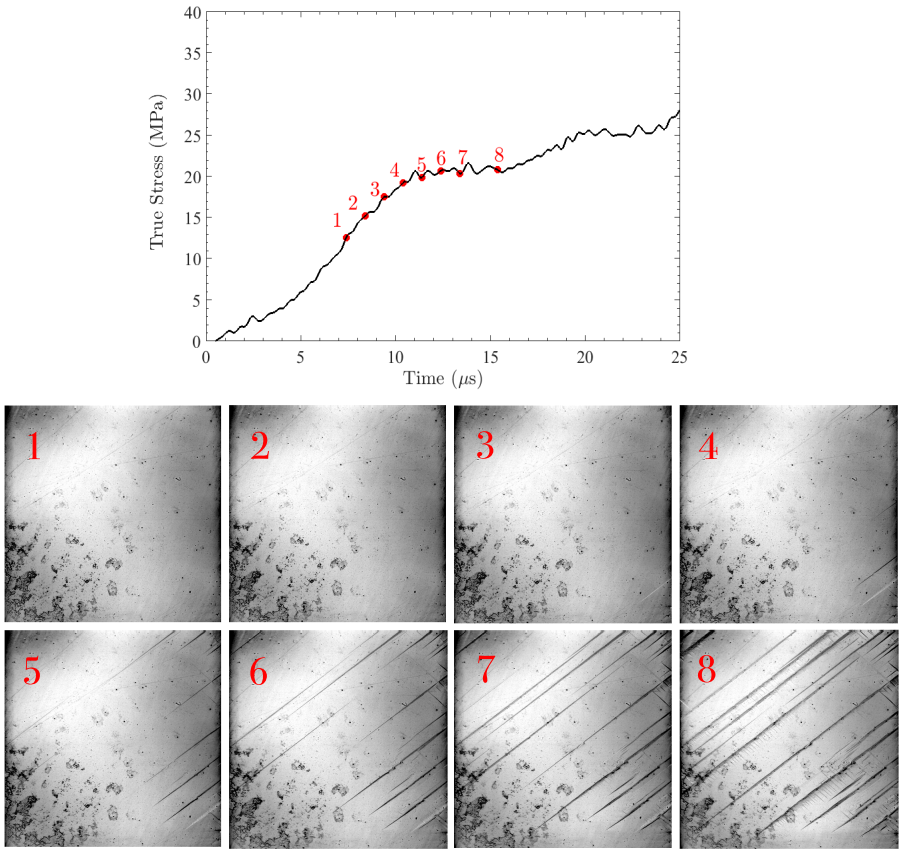

Figure 4.7: Macroscopic stress-time curve with corresponding images indicating a correlation between nucleation of the first twin and change in the stress-strain curve. Specimen width along loading direction (horizontal axis of the image) is 3.4 mm

4.7 Dynamics of twin evolution

Measurements of twin nucleation rate and growth rate can provide important insights into the physics of the twinning mechanism. We begin with nucleation.

4.7.1 Twin nucleation

At any given time, we define the number density $\rho(t)$ of a given variant of twins as

$$\rho(t) = \frac{N(t)}{A} \tag{4.7.1}$$

where A is the imaged area (here corresponding to one entire imaging surface) and $N(t)$ is the number of twins in every image. Figure 4.8 shows the total number density of the first twins as a function of the resolved shear stress on the twin plane (the total number density is the sum of number densities of all variants of twins observed). The resolved shear stresses were calculated by transforming the average uniaxial stress tensors to the twin coordinate system (section B.2). For these three experiments, the first twins appear to nucleate within a resolved shear stress range of $5 - 7$ MPa. A similar plot results with respect to the resolved normal stress. These results thus provide some support to the idea that nucleation is governed by a critical stress. We discuss related literature in subsection 4.8.2. Note that once a critical stress is reached, the twin number density grows very rapidly with very little increase in stress. Increased twin nucleation alone does not appear to cause hardening.

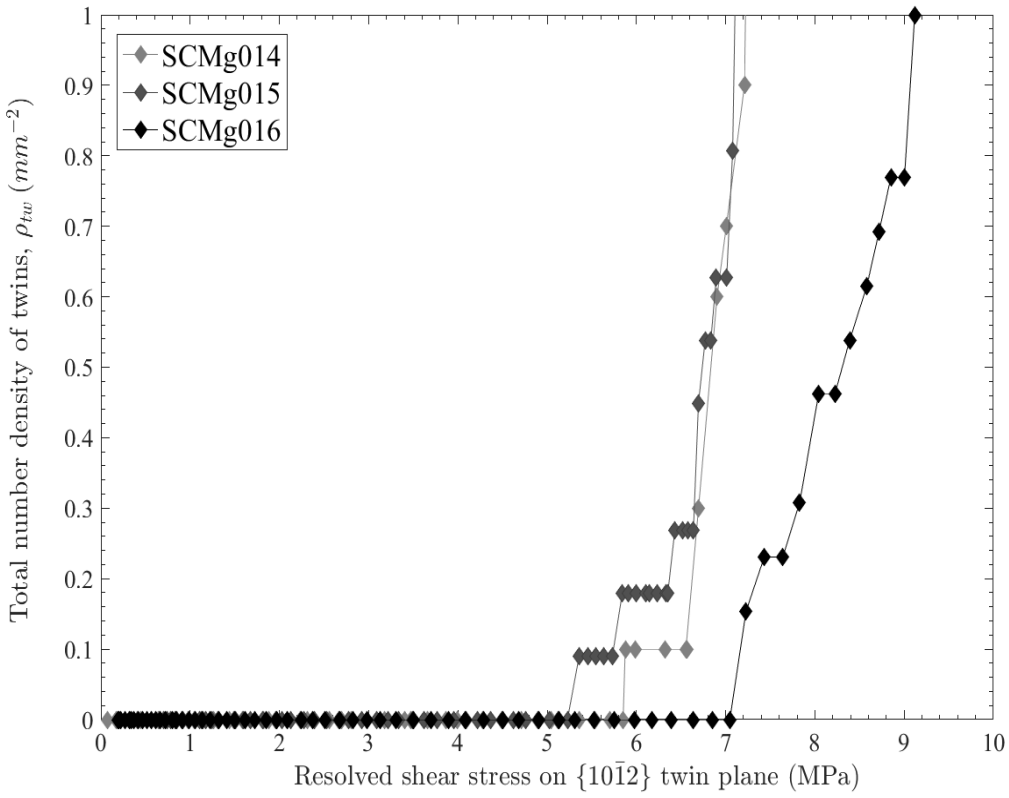

Figure 4.8: Nucleation of first twins as a function of resolved stress along the twin plane. Note the similarity in the nucleation of first twins.

Nucleation rates are best estimated by examining the evolution of ρ with time. Figure 4.9 shows the evolution of the total twin number density observed on the imaging surface with time. The inset shows that the first twins nucleate at times between $8 - 12\,\mu s$ (corresponding to the shear stress range of 5-7 MPa), with a low initial nucleation rate followed by a regime of very rapid nucleation. We discuss the nucleation rate history in section 4.8.

4.7.2 Twin tip velocities

Once the twins have nucleated, the most apparent aspect from the in-situ visualization is the high velocity of propagation of the twin tips. At early times, the first twins are propagating with no other twins obstructing their paths. We measure the velocities of the tips of these twins from the time-resolved images. These velocities are lower bounds, as the orientation of twin propagation in three dimensions is currently unknown. The velocity histories are transient (as shown in Figure 4.12) and typically show oscillations with an 800 ns timescale, perhaps because of release wave interactions with specimen boundaries.

Figure 4.10 shows the peak tip velocities of initially nucleated twins from all three experiments. A total of 8 such twins were examined. Peak velocities of the Var1 twins are shown in blue and those of Var2 twins are shown in red. The peak tip velocities of Var1 twins are centered around 1300 m/s with a standard deviation of ~ 300 m/s while the corresponding values for Var2 twins are 1000 m/s and 100 m/s. The error

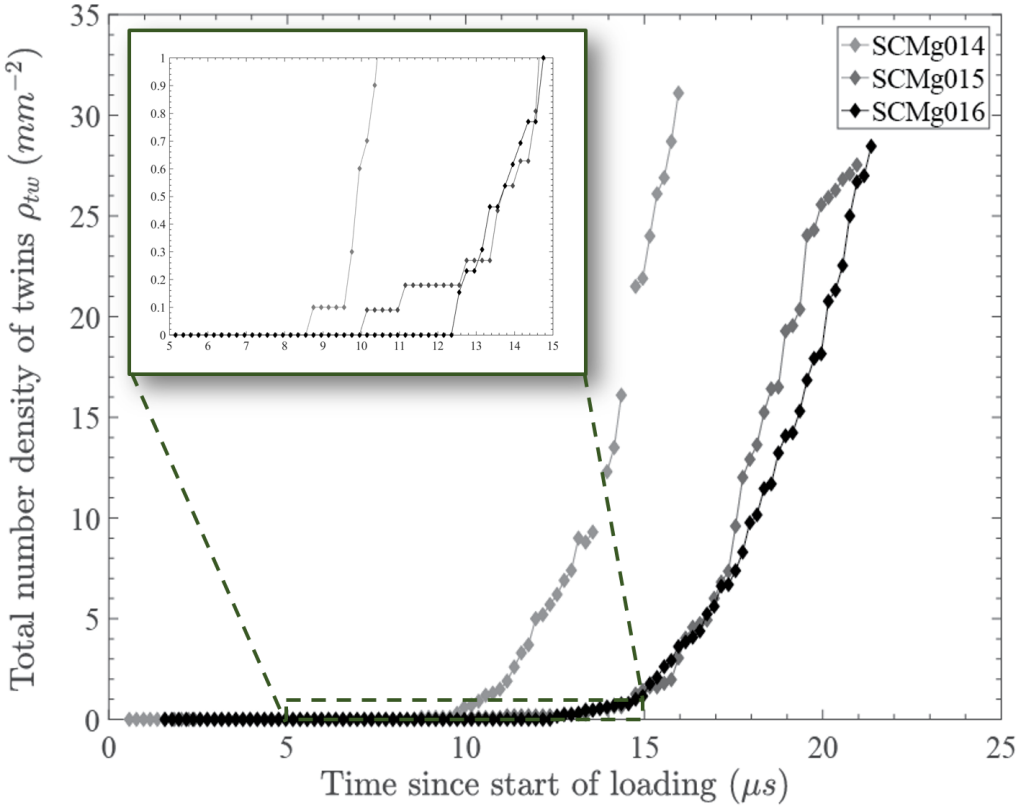

Figure 4.9: Nucleation of twins as a function of time. The inset is a zoomed in version showing the times of nucleation of first twins in each experiment. Twin nucleation is slow initially and then increases rapidly (due to the nucleation of Gen2 twins). At some point nucleation will saturate. This region is not captured by the data because twins become imperceptible beyond a specific density and the images cannot be analyzed any more.

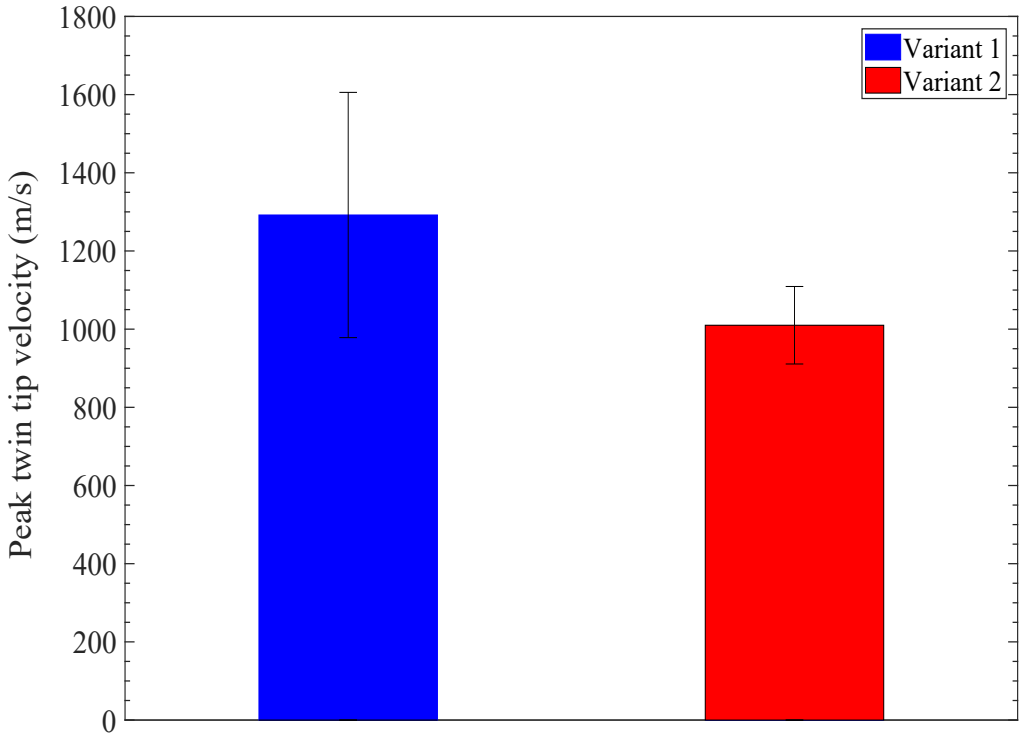

Figure 4.10: Peak velocities of first non-interacting twins across the three datasets

bars in Figure 4.10 indicate standard deviation. Note that all of these measured are for the first free-flying twins.

It is now possible to examine the peak twin tip velocities of the first twins as a function of the resolved shear stresses on the corresponding twin planes at the time corresponding to the peak twin tip velocity (Figure 4.11). The different colored symbols refer to results from specific experiments as shown in the legend. The error bars in stress space correspond to variation due to small oscillations and limitations in temporal resolution of the stress-time signal. The resolved shear stresses at the

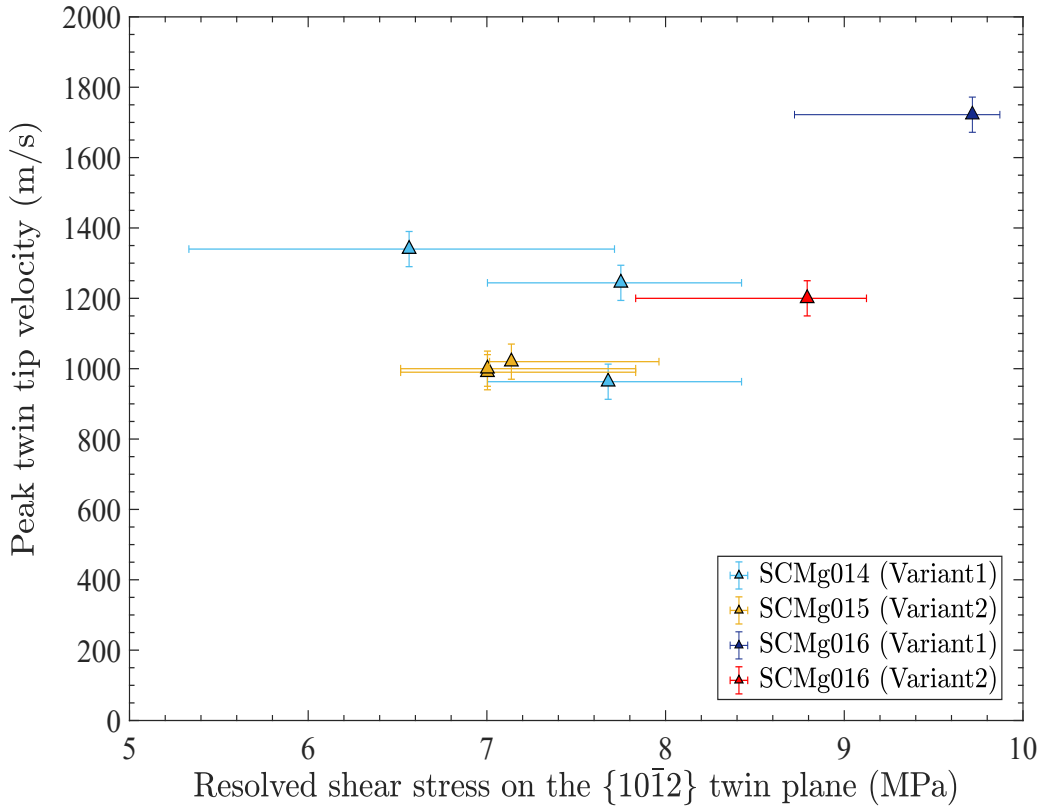

Figure 4.11: Peak velocities of first non-interacting twins as a function of the resolved shear stress on the twin plane.

time of peak velocity all fall in the range of $6 - 10$ MPa, values slightly higher than the twin nucleation stresses shown in Figure 4.8. Examining velocity data separately for each variant, it is possible that the twin tip velocity increases with shear stress. The data point with the highest tip velocity of ~ 1700 m/s corresponds to the highest tip stress.

At later times, the measured tip velocity histories give us an idea of the effects of interactions on tip growth. Data for some twins from all three experiments growing

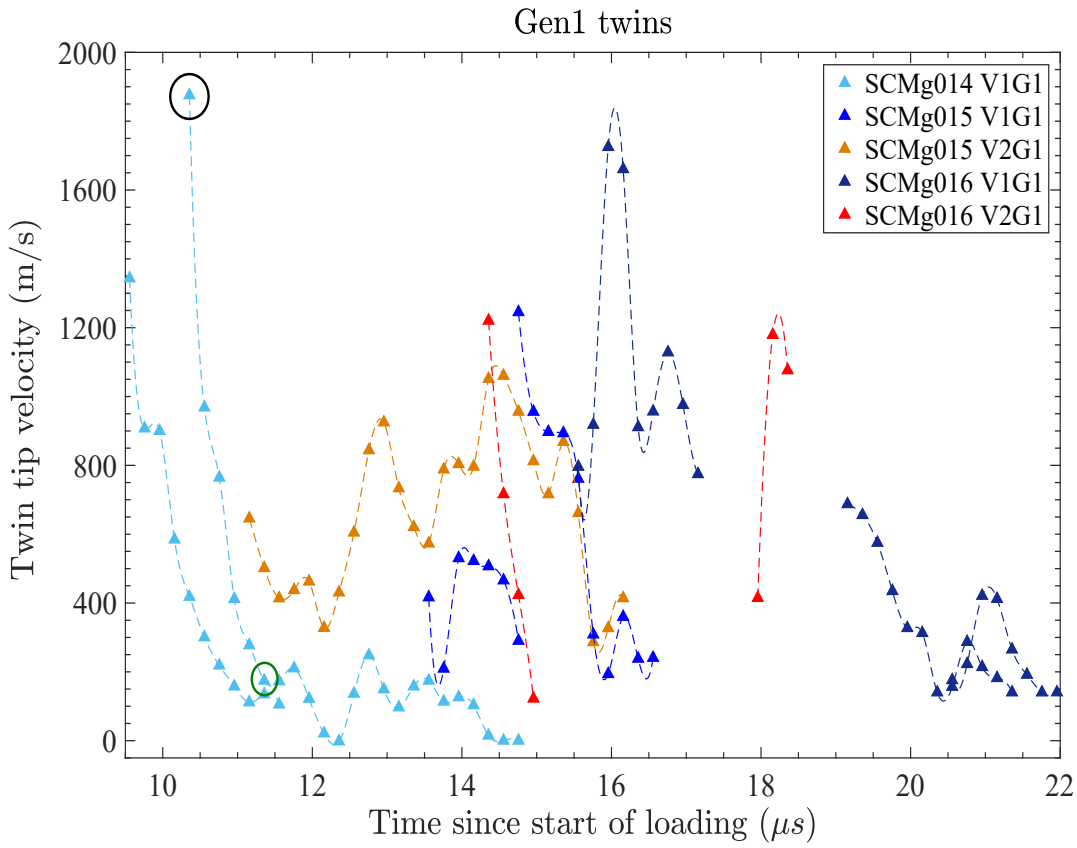

(a) Velocity histories of multiple Gen1 twins from all three experiments

Figure 4.12: Twin tip velocity history

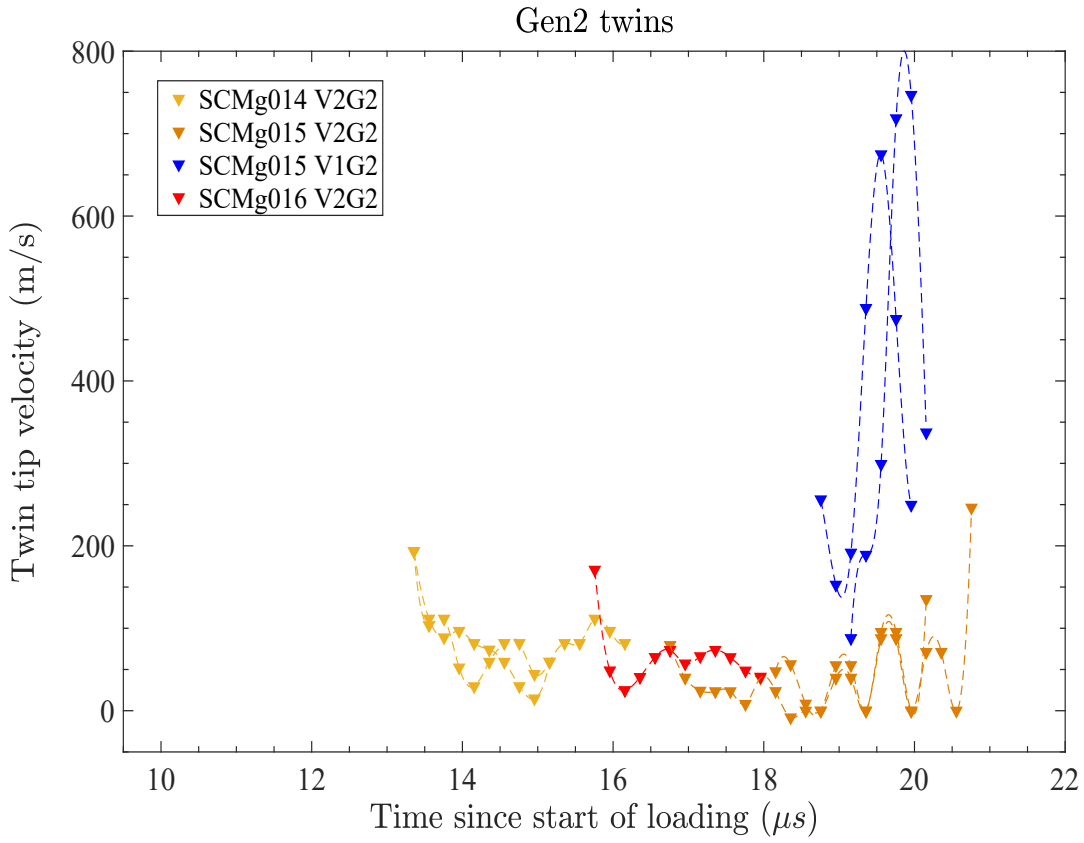

(b) Velocity histories of multiple Gen2 twins from all three experiments

Figure 4.12: Twin tip velocity history

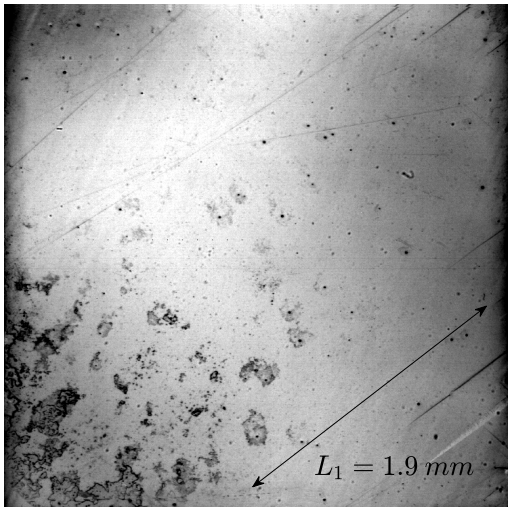

(c) Frame corresponding to time $10.4\,\mu s$ marked by the black circle in Figure 4.12a (Test ID: SCMg014)

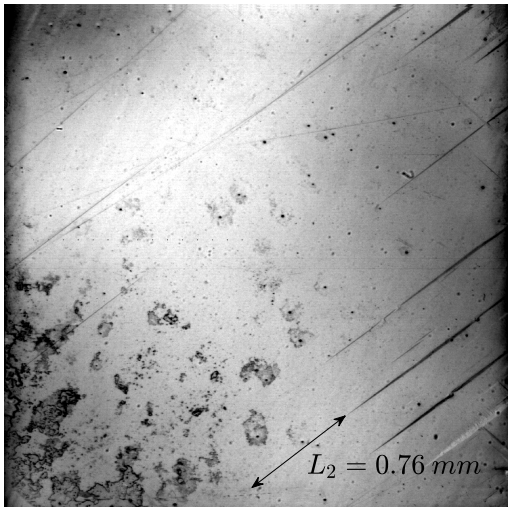

(d) Frame corresponding to time $11.4\,\mu s$ marked by the green circle in Figure 4.12a (Test ID: SCMg014)

Figure 4.12: Twin tip velocity history

in the specimen are shown in Figure 4.12, with the entire velocity history of discrete twins presented as a function of time since the start of loading. Some twins have a high initial velocity which rapidly falls to lower velocities, while others start slow and speed up. Figure 4.12a shows the velocity histories of Gen1 twins and Figure 4.12b shows that of Gen2 twins. Figure 4.12c and Figure 4.12d are two frames corresponding to the two data points marked in Figure 4.12a. The velocities (both peak and mean velocities) of Gen1 twins appear to be higher than those for Gen2 twins (which generally have small mean free paths).

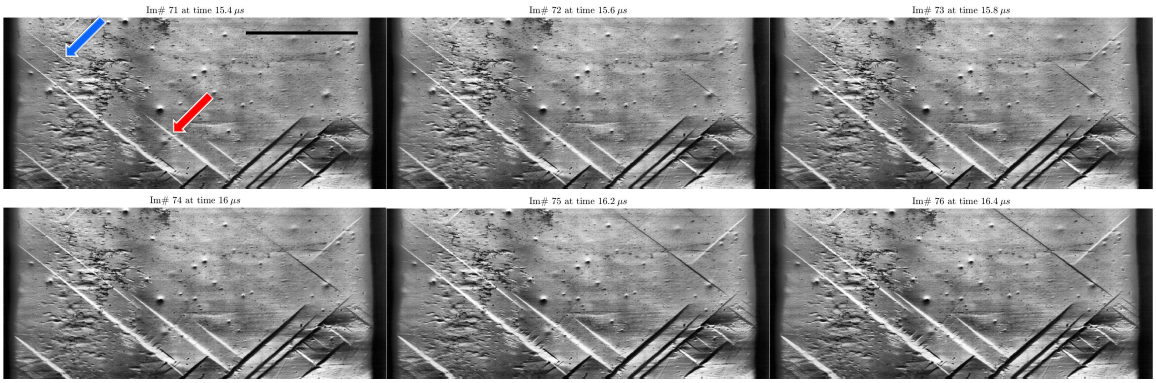

(a)

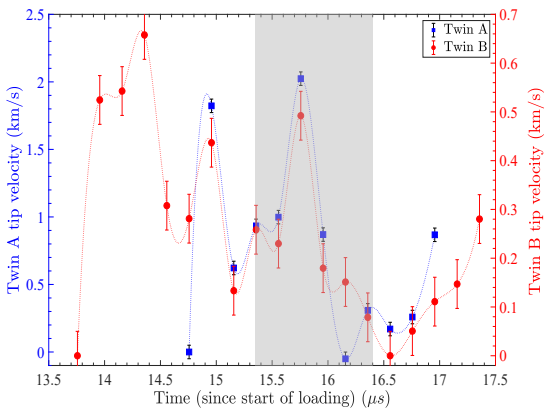

(b)

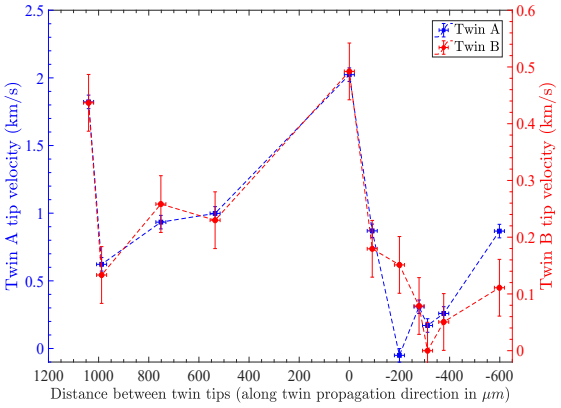

(c)

Figure 4.13: Twin tip interactions Velocity histories of two twins are shown along with corresponding in-situ images from one experiment. (a) In-situ images showing the growth of two twins marked by the two arrows (blue arrow is designated Twin A and the red Twin B) across each other. The scale bar corresponds to 1mm (Test ID: SCMg016); (b) Tip velocity histories of both Twin A and B. The shadowed region marks the times during which images are shown in (a); (c) Tip velocities of twins A and B as a function of the distance between tips. Negative distances mean that the twins have crossed each other.

Figure 4.13 presents a particular example of twin-twin interactions (from test SCMg016). Figure 4.13a shows a sequence of images during an experiment showing two specific twins (marked by the blue arrow (Twin A) and the red arrow (Twin B)). Figure 4.13b shows the velocity histories of these two twins, with the shadowed region corresponding to the time interval over which the images in Figure 4.13a were recorded. Figure 4.13c is a plot of the tip velocities as a function of the distance (along the line of travel) between the two corresponding twin tips showing that the twins speed up as they approach each other. Negative distances mean that the twins have passed each other. Once the two twins have passed each other, they become very slow. This has also been observed in a few other instances including in other experiments. It appears, therefore, that the twin tips are interacting dynamically at these timescales, with interaction distances of about 500 μm. The velocity histories (Figure 4.13b), contain information about the length scales associated with the stresses at twin tips, as well as the interaction dynamics, and would be good targets for computational simulations.

4.7.3 Twin boundary velocity

Limitations in the spatial resolution of our imaging system make it difficult to provide an in-depth description of twin boundary velocities (as was possible for twin tips in figures Figure 4.12a and Figure 4.12b). The measured velocities are a lower bound because twin boundary growth, like twin tip growth, is also a three-dimensional phe-

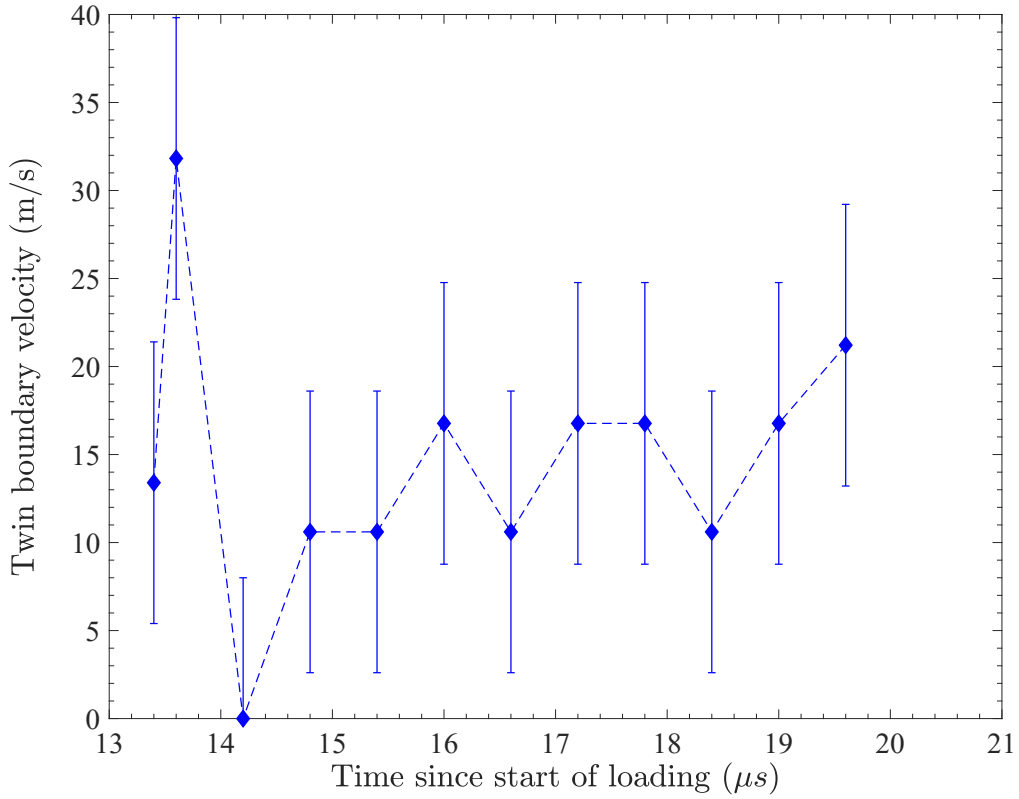

Figure 4.14: Twin boundary velocity measured at a specific location along a twin. Notice that the velocities start of at a higher value of $\sim 30\, m/s$ and then drop to $\sim 12\, m/s$

nomenon. With these caveats, some regions along a twin were analyzed. An example of the results for one such region are shown in Figure 4.14. We estimate that the twin boundary velocities are less than 30 m/s, dropping to smaller velocities ($\sim 12\, m/s$) after a few microseconds. Previous studies have estimated twin boundary velocities of ~ 35 nm/s (e.g Prasad and Ramesh [21]) at quasi-static rates and ~ 35 m/s from plate impact experiments by Dixit and Ramesh (Dixit [81]) which are more comparable to these measurements. An implication of these measurements will be discussed

in Figure 4.14.

4.7.4 Growth of twin volume fraction

We now turn to examining the overall twin volume fraction evolution history. Since we observe only surfaces, what we measure is really an area fraction. For each twin variant, we define the area fraction as the ratio of the twinned area to the total imaged area.

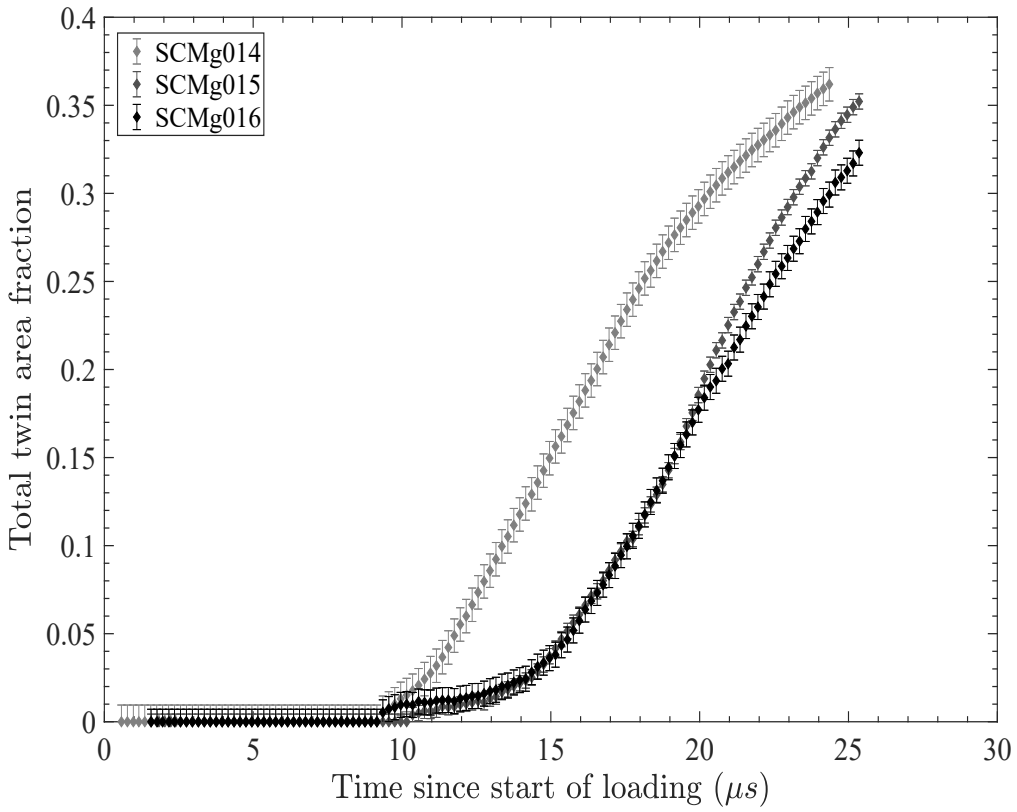

Figure 4.15: Total twin area fraction measured on the imaging surface as a function of time.

Figure 4.15 presents the total area fractions of all twins as a function of time (since start of loading). All of the experiments show a similar evolution despite stochasticity in nucleation and growth rates across experiments. Once a significant number of twins has nucleated (Figure 4.9), the rate of growth of the twin area/volume fractions increases dramatically and is similar for all experiments for a significant time. Eventually the growth rate begins to decrease. Note that once the area fractions become larger than 35%, the twins become too dense such that they are not distinguishable any more. In other words, the spacing between twins become too small (comparable to the imaging resolution) such that accurate identification of twins is no longer possible hence making the twin tracking algorithm unreliable beyond this point.

For each twin variant, we may define the plastic velocity gradient due to twinning as,

$$\boldsymbol{L_t} = \dot{\gamma}_{tw}(\boldsymbol{k_{tw}} \otimes \boldsymbol{n_{tw}}) \tag{4.7.2}$$

where the vectors $\boldsymbol{k_{tw}}$ and $\boldsymbol{n_{tw}}$ are the directions of the twinning shear and the twin plane normal, known from crystallography while $\dot{\gamma}_{tw}$ is the shear rate due to twinning for each twin variant. This latter term may be expressed as,

$$\dot{\gamma}_{tw} = \dot{f}_{tw}\gamma_{tw} \tag{4.7.3}$$

where f_{tw} is the volume fraction of twins of a specific crystallographic variant and γ_{tw} is the twinning shear defined as the shear strain associated with the lattice reorientation.

The measurements we make are from 2-dimensional images of 3-dimensional twins.

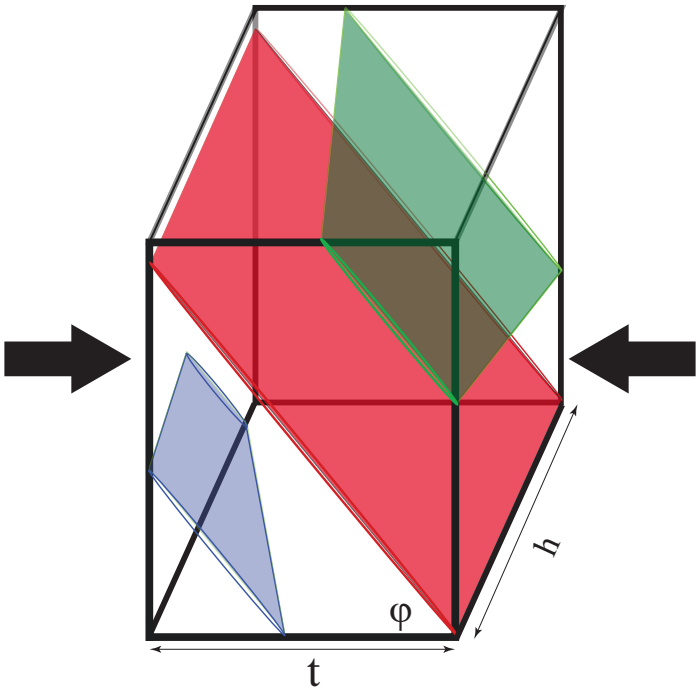

Figure 4.16: An idealized schematic of twin lamellae in the specimen. The bold arrows indicate direction of compression. t is the thickness of the specimen along the compression direction and h thickness along the imaging direction. ϕ is the angle of the twin lamellae to the base of the specimen. Notice that the crystallographic orientation and spatial position of the twin would affect its 3 dimensional geometry.

The twins are assumed to be plate-like structures, extending into the bulk of the crystal (also see Remy [82] and Mitchell and Hirth [83]). However in a finite crystal, the crystallographic orientation of the twin plane and the spatial distribution of twins results in the actual twin volume fraction being lower than that calculated assuming that all twins extend to back of the specimen (see Figure 4.16). The actual twin volume fraction can be expressed as βf_{tw}^{meas}, where f_{tw}^{meas} is the measured area fraction of twins observed in the images and β is an unknown correction factor which should

be derived from stereology. If $\beta = 1$, our idealization of the twins extending through the entire thickness of the sample is true and the twin volume fraction f is equal to the measured twin area fraction f_{tw}^{meas}. If $\beta = 0$, this is equivalent to a surface twin. An estimate of β will be provided in subsection 4.8.9 and for the moment we will set $\beta = 1$. With this idealization, the twin volume fraction of a specific twin variant at an arbitrary time t is,

$$f = \frac{1}{V}\sum_{i=1}^{N_t} h l_i w_i = \frac{h}{V}\Big(l_1 w_1 + l_2 w_2 + l_3 w_3 + ... + l_{N_t} w_{N_t}\Big) = \frac{1}{A}\Big(l_1 w_1 + l_2 w_2 + l_3 w_3 + ... + l_{N_t} w_{N_t}\Big) \tag{4.7.4}$$

where N_t is the number of twins of the specific variant under consideration, l_i and w_i are the length and thickness of the i^{th} twin and $\frac{V}{h} = A$ is the cross-sectional area of the specimen. Because nucleation of new twins and growth of existing ones occur simultaneously, at time $t + \Delta t$ the volume fraction becomes

$$\begin{aligned} f + \Delta f = \frac{1}{A}\Big[&(l_1 + \Delta l_1)(w_1 + \Delta w_1) + (l_2 + \Delta l_2)(w_2 + \Delta w_2) \\ &+ ... + (l_{N_t} + \Delta l_{N_t})(w_{N_t} + \Delta w_{N_t}) + l_{N_t+1} w_{N_t+1} + ... l_{N_{t+\Delta t}} w_{N_{t+\Delta t}}\Big] \end{aligned} \tag{4.7.5}$$

Expanding this and ignoring higher order terms we obtain,

$$\begin{aligned} f + \Delta f = \frac{1}{A}\Big[&\{l_1 w_1 + l_2 w_2 + l_3 w_3 + ... + l_{N_t} w_{N_t} + ... + l_{N_{t+\Delta t}} w_{N_{t+\Delta t}}\} \\ &+ \{l_1 \Delta w_1 + w_1 \Delta l_1 + ... + l_{N_t} \Delta w_{N_t} + w_{N_t} \Delta l_{N_t}\}\Big] \end{aligned} \tag{4.7.6}$$

The increment in volume fraction is hence,

$$\Delta f = \frac{1}{A}\left(\sum_{i=N_t+1}^{N_{t+\Delta t}} l_i w_i + \sum_{j=1}^{N_t}(l_j \Delta w_j + w_j \Delta l_j)\right) \tag{4.7.7}$$

The rate of volume fraction evolution now becomes,

$$\dot{f} = \lim_{\Delta t \to 0} \frac{\Delta f}{\Delta t} = \frac{1}{A} \lim_{\Delta t \to 0} \left(\frac{1}{\Delta t} \sum_{i=N_t+1}^{N_{t+\Delta t}} l_i w_i + \frac{1}{\Delta t} \sum_{j=1}^{N_t} (l_j \Delta w_j + w_j \Delta l_j) \right) \tag{4.7.8}$$

where the first term represents the contribution from newly nucleated twins and the rest represent the contributions from twin broadening and twin tip growth. We assume that all newly nucleated twins have initial sizes that are small and fixed, with some small length l_o and thickness w_o. With reference to our experiments, it is important to note that these two length scales lie below the resolution of our imaging system and hence cannot be observed directly. Then the rate of growth of the twin volume fraction is,

$$\dot{f} = \lim_{\Delta t \to 0} \frac{\Delta f}{\Delta t} = \frac{1}{A} \lim_{\Delta t \to 0} \left(l_o w_o \frac{\Delta N}{\Delta t} + \frac{1}{\Delta t} \sum_{j=1}^{N_t} (l_j \Delta w_j + w_j \Delta l_j) \right), \tag{4.7.9}$$

where $\Delta N = N_{t+\Delta t} - (N_t + 1)$ is the increase in number of twins in time Δt, so that

$$\dot{f}(t) = l_o w_o \dot{\rho}(t) + \frac{1}{A} \sum_{j=1}^{N_t} (l_j \dot{w}_j(t) + w_j \dot{l}_j(t)) \tag{4.7.10}$$

where ρ is the number density of twins.

In our experiments, we observe that $\dot{w}$ is generally small ($\sim 15\, m/s$), while the twin tip velocity $\dot{l}$ is relatively large ($\sim 1\, km/s$). In the next section, we discuss our results in the context of the literature.

4.8 Discussion

4.8.1 The phenomenology of twinning at high rates of loading

Once the first twins have nucleated, the tips move across the entire specimen at high velocities of the order of 1 km/s (Figure 4.10). In quasi-static experiments it has been shown that the end of twin tip propagation is followed by twin boundary growth to accommodate deformation (Prasad and Ramesh [21]). This idea that rapid twin tip propagation is followed by a slower twin boundary growth has been adopted by many researchers in the modeling of crystalline material systems deforming by discrete twin nucleation and growth (Johnson and Rohde [71], Kumar et al. [84], Kumar et al. [85], Cheng and Ghosh [86]). Consequently a lot of experimental, analytical and computational studies have focused on understanding the mechanisms contributing towards twin boundary migration at various length scales, some notable studies being Daphalapurkar et al. [87], Cheng and Ghosh [86], Wang and Huang [75], Yoo and Lee [15]. At high rates of loading, however, we see that a second generation of twins (our Gen2 twins) nucleate from existing twin boundaries (Figure 4.5) as opposed to the traditional twin boundary growth mechanism. We hypothesize that the possible rates of twin boundary migration are too small to sustain the prescribed rate of deformation resulting in this transition to the faster mechanism of nucleation and tip propagation

(Figure 4.5).

Summarizing our observations, the phenomenology of twinning can be described as follows. Twin nucleation can be classified based on nucleation sites as: 1. nucleation from specimen boundaries; 2. nucleation from a twin-free matrix; and 3. nucleation from existing twin boundaries. The first nucleated twins propagate across the twin-free specimen at very high velocities of the order of 1 km/s. Nucleation has been observed on two conjugate twin planes. At high rates of loading, nucleation of Gen2 twins from existing twin boundaries is favorable over traditional twin boundary growth.

4.8.2 Criteria for twin nucleation

Figure 4.8 suggests that twin nucleation is stress-controlled, perhaps with critical shear stresses resolved on the twin plane of within $5 - 7$ MPa for magnesium. We note that Kelley [88] suggested that critical resolved shear stresses for twinning in single crystal magnesium fall in the $2 - 3$ MPa range based on constrained compression tests. Twin nuclei may be formed within a pristine crystal (homogeneous nucleation) or due to local stress concentrations caused by defect structures (heterogeneous nucleation). Large stresses and low surface energies are typically thought to be necessary for homogeneous twin nucleation (Christian and Mahajan [11]). Bell and Cahns' experiments in 1957 showed substantial pyramidal slip before twinning, indicating that twin nucleation is preceded by a defect structure. This indicates that

heterogeneous nucleation seems to be preferred for twin nucleation in single crystals of magnesium. Computational studies (Cottrell and Bilby [89], Thompson and Millard [90], Serra et al. [72]) have focused on trying to determine this defect structure. For example, molecular dynamics simulations by Aghababaei and Joshi [69] suggest that the twin nucleus in single crystal magnesium involves an ensemble of partial dislocations dissociating on more than one crystallographic plane. At larger length scales, the twin nucleus has been modeled as an inclusion with a well defined sharp interface (Yoo and Lee [15], Lebensohn and Tome [73]). The stability requirement for a twin embryo has classically been obtained by a minimization of the Gibbs free energy and a stable embryo size has been suggested to be atleast 8 lattice planes for $\{10\bar{1}2\}$ twins from atomistic calculations (Wang et al. [91]). This indicates a non-trivial stress state at the twin nucleus. Hence the common assumption of twin nucleation driven by a critical shear stress alone may well be over-simplistic. However, our data do support the notion that twin nucleation is stress-driven.

4.8.3 Twin nucleation rates

Immediately after the application of the mechanical load, the nucleation rate is initially slow (Figure 4.9). Once the initially nucleated twins stop growing as they reach the specimen edges or intersect a twin boundary of the conjugate variant, the twin boundaries of existing twins then become active nucleation sites for Gen2 twins, and the nucleation rate rises rapidly as the stress increases. The curves in Figure 4.9

do not show saturation, because the twins become indistinguishable at high number densities (approaches the limit of the spatial resolution of our imaging system). However, the first two regimes (slow then very rapid nucleation) are evident. Similar phenomenology has been reported in the phase transition literature (eg, Avrami [92], Olson and Cohen [93]). Avrami [92] refers to the process of nucleation of a new phase as being driven by a distribution of 'germ nuclei'. This distribution is dependent on temperature (in the context of temperature-driven phase transitions). An analogous case can be made in our problem where the 'germ nuclei' are really nucleation sites which are stress-driven. With the increase in strain rate, the number of these sites evolve with the increasing surface area of existing conjugate twins. Hence, we may be able to adapt these ideas to model the dynamics of twin nucleation at the macroscopic scale. A clearer comparison can be obtained from Olson and Cohen [93] who were studying stress and strain induced nucleation of martensite and describe an 'auto catalytic nucleation' phase where a sudden triggering of additional nucleation sites occurs. This may be analogous to our increase in twin nucleation rates with the nucleation of Gen2 twins (the auto catalytic phenomenon marked by a rapid increase in nucleation rate in Figure 4.9).

4.8.4 Twin tip growth rates

The peak twin tip velocities measured are of the order of 1 km/s, similar in order to those estimated using post-mortem measurements from plate impact experiments by

Dixit et al. [78]. It is useful, at this juncture, to briefly discuss the sources of the error bars in Figure 4.10. We hypothesize that one source is from 3-dimensional effects. The growth of twins in the third dimension (through the thickness of the specimen) would potentially affect the growth dynamics in the other two directions.

While our measured twin tip velocities of $1-2$ km/s are high, they are substantially smaller than the 'sound velocities' sometimes assumed in the literature (Takeuchi [70], Williams and Reid [77]). Rosakis and Tsai [17] suggested, using theory, that for semi-infinite twin lamellae terminating in cusps, subsonic *steady* twin growth could never occur when a kinetic relation (describing a monotonic increase of velocity component normal to local curvature of the twin tip with applied stress) was imposed. Our results (figures Figure 4.12a and Figure 4.12b) do indicate however, that twin growth is a *transient* process. Shape changes of the twin tips are hard to visualize with the current resolution of our imaging setup.

Is there a limiting velocity for twin tips, analogous to the shear wave speed limit for dislocations? Understanding limiting tip velocities ideally requires knowledge of the twin tip structure. The high tip speeds that we observe make recovery experiments (to examine twin tip structure using post-mortem microscopy) hard to perform. As a first approximation, we may assume a phenomenological kinetic relation for twin growth dynamics. A theoretical continuum mechanical framework that allows for prediction of twin growth dynamics is presented in chapter 5. An improvement in the model would be to assume that the twin tip/ boundary is composed of an ensemble

of dislocations which would refine the theory to incorporate micro mechanics of deformation at the twin boundaries themselves. Experiments designed to capture the specific structure along the twin boundaries up to the tips would be very useful as inputs to these types of models.

4.8.5 Twin boundary growth rates

In comparison to twin tip velocities, mean twin boundary growth rates are observed to be very small ($\sim$ 15 m/s). Final twin widths of initially nucleated Gen1 twins were of the order of 50 μm. Moreover, our data shows the preference for the nucleation of Gen2 twins over twin boundary growth at these high strain rates . Prasad and Ramesh [21] measured the twin boundary velocity in-situ in polycrystalline magnesium under quasi-static tensile loading, measuring a peak velocity of $\sim$35 nm/s. More recent work by Dixit [81], estimates a lower bound velocity of 35 m/s (nine orders of magnitude higher) from post-mortem microscopy of specimens subjected to plate impact (note that plate impact experiments are uniaxial strain experiments while the current study is under uniaxial stress). The maximum measured twin boundary velocities in the literature and from our imaging are significantly smaller than the tip velocities measured in the current study. It appears that the inability of the twin boundary to move sufficiently rapidly to accomodate the prescribed macroscopic strain rate leads to the nucleation of the Gen2 twins. The conditions for this transition may be estimated using our Equation 4.7.10 for rate of twin volume fraction

evolution.

$$\dot{f}(t) = l_o w_o \dot{\rho}(t) + \frac{1}{A}\sum_{j=1}^{N_t}(l_j \dot{w}_j(t) + w_j \dot{l}_j(t))$$

Once the twin tip has grown across the crystal, the tip velocities $\dot{l}_j$ become 0, so that

$$\dot{f}(t) = l_o w_o \dot{\rho}(t) + \frac{1}{A}\sum_{j=1}^{N_t} l\dot{w}(t)$$

For a given twin, the shear rate due to twinning upon continued deformation is,

$$\dot{\gamma}_t = \dot{f}_{tw}(t)\gamma_{tw} = \frac{\gamma_{tw}}{A} l\dot{w}(t)$$

where γ_{tw} is the twinning shear. Hence when a single twin exists in the system,

$$\dot{\gamma}_t = \frac{\gamma_{tw}}{A} l\dot{w}(t) + \gamma_{tw} l_o w_o \dot{\rho}(t)$$

Suppose for the moment we assume that all of the imposed shear rate $\dot{\gamma}$ were to be accommodated only by twinning (we relax this assumption in subsection 4.8.11) then, if the system wants to deform only by growing the existing twins ($\dot{\rho} = 0$), the boundary velocity required would be,

$$\dot{w} = \frac{A\dot{\gamma}}{\gamma_{tw} l}$$

For a single representative Gen1 twin in our specimen of size $\sim 3.5 \times 4 \times 4.5$ mm, the maximum length that has been observed is ~ 4 mm. The area of cross-section of the specimen is ~ 15.75 mm^2. The calculation of shear rate along the twinning direction is done using estimates of the size of a representative twin and the rate of volume fraction evolution of the twin. In short, we use the very definition of shear

rate due to twinning from the time this representative twin nucleated to the time it took for the twin to stop growing (note we use the Gen1 twins and hence these will be larger than the average twin size). For a twin of length ~ 4 mm and thickness $\sim 75\,\mu m$ that has grown over a time of $\sim 4\,\mu s$ (these numbers were extracted from experimental data of what was considered a representative Gen1 twin at early times) the rate of twin volume fraction is,

$$\dot{f} = \frac{\Delta f}{\Delta t} \simeq 4800\ s^{-1} \tag{4.8.1}$$

The shear rate is hence, $\dot{\gamma} = \dot{f}\gamma_{tw}$. The value of twinning shear for the specific twin variant in this study has been studied theoretically (for e.g. Christian and Mahajan [11]). Molodov et al. [94] measured the twinning shear of the same variant to be 0.126 (very close to the theoretical value of 0.129). Using Molodov's measured value, the required value of $\dot{w}$ is calculated to be about 19 m/s. Note that this is an ideal case and in the real experiment there were multiple twins of Gen1 type at the time of nucleation of the first Gen2 twins. Hence we would expect a slightly higher twin volume fraction rate than what is calculated here.

The boundary velocities measured from our experiments are initially high but then fall to smaller velocities ($\sim 15\,m/s$) while the macroscopic strain rate is maintained at the constant high rate (Figure 4.3a). It is possible, therefore, that the slow twin boundary velocities are not able to accommodate the deformation fast enough at these rates by twin boundary growth, resulting in a transition to nucleation of Gen2 twins. The high tip speeds (Figure 4.10) suggest that tip growth rates ($\dot{l}$) contribute the

most to the twin growth terms in Equation 4.7.10 at least at early times. In contrast, in low rate experiments the twin boundary velocities are sufficient to accommodate the rate of macroscopic deformation, resulting in broadening of existing twins (Prasad and Ramesh [21]). Inherent to these finite growth times is the mechanisms active at the twin boundary. It has been observed that twin boundaries migrate by the motion of twinning dislocations on the twin boundary (Wang and Huang [75]). This is true of hcp metals too (for eg. Tu and Zhang [95]). The structure of the twin boundary in hcp metals has been reported in Tu and Zhang [95] and are found to be composed of a sequence of atomic steps (called facets) along which the twinning dislocations propagate. The time scales for twin boundary migration hence depend on the specific dynamics of these twinning dislocations. This has been studied computationally for fcc metals (Daphalapurkar et al. [87]), but not for hcp. A deeper understanding of how these twinning dislocations propagate could provide insight into controlling twin boundary motion for materials design. A specific example study by Nie et al. [96], shows some evidence of solutes pinning twin boundaries as a strengthening mechanism in a Mg-Gd alloy.

4.8.6 The effect of crystallography on twin growth rates

It is useful to compare our measures of twin tip and boundary velocities with other hcp metals in literature. The major use lies in understanding the effect of the c/a ratios of the hcp lattice on twin growth. One one hand, the specific twin variants nucleated depend on this ratio (Yoo and Lee [15]) and this allows us to understand how fast different twin variants grow. On the other hand, the driving forces on the twin boundary (and hence the propagation velocities) may be affected by the mobilities of dislocations nucleated in the matrix and the twinned regions. The specific type of dislocations active in the matrix (and their mobilities) are also affected by the c/a ratio. This allows us to understand the effect of dislocations on twin growth (both tip and boundary).

Unfortunately, there are very few datasets on direct measurements of twin growth rates in single crystal hcp metals in literature. For hcp metals, twin velocity measurements on zinc single crystals by Brunton and Wilson [76] and on cadmium crystals by Thompson and Millard [90] seem to be the only ones available. The c/a ratio for magnesium is 1.62, while those for zinc and cadmium are 1.86 and 1.89 respectively. The most common deformation twin type in each of these crystals is also $\{10\bar{1}2\}$, but for a caveat. While these twins cause *extension* of the c-axis of the magnesium crystal, they tend to cause *contraction* of the c-axis in the zinc and cadmium crystals,

due to the difference in c/a ratios (Yoo and Lee [15]).

The maximum twin tip velocities measured by Brunton and Wilson [76] were 780 m/s with an average of 600 m/s, considerably slower than our measured velocities of 1 km/s for magnesium. The most common slip mechanism in zinc single crystals is $\{0001\}\langle 11\bar{2}0\rangle$ basal slip (Florando et al. [97]), similar to magnesium. As a consequence, we would expect similar dislocation mechanisms around the twin boundary for both zinc and magnesium. The difference in twin tip velocities, hence, may come from the different strain states imposed on the crystal i.e. contraction of the c-axis in zinc versus extension in magnesium. No twin tip velocity data were found for cadmium in Thompson and Millard [90]'s work.

With respect to twin boundary velocities, Brunton and Wilson [76] report maximum velocities of 35 m/s. Mean twin boundary velocities in magnesium have been found to vary between 35 nm/s (Prasad and Ramesh [21]) and 20 m/s (this work), with maximum values reported at 35 m/s (this work and Dixit et al. [78]). These data indicate that the macroscopic strain rate may play a role in the twin boundary growth rates. However, unlike twin tip velocities, it appears that the maximum twin boundary velocities are similar for both zinc and magnesium. The data from Thompson and Millard [90] does not give us accurate twin boundary velocities for cadmium (due to their measurement resolution), but they estimate the value to be $\sim$ 1 cm/s, considerably slower than known values for zinc and magnesium. The c/a ratios for zinc and cadmium are similar and hence, similar mechanisms are expected

to be active. Note that Thompson and Millard [90]'s experiments were on thin wires and hence the experimental geometry may affect the measured velocities.

While these are initial clues, a lot more data on a wider range of hcp metals are needed to lay statistical claims to the dependence of twin growth rates on crystallography. For example, titanium has a c/a ratio of 1.59 with prismatic slip being the most favored slip mechanism, unlike magnesium, which prefers basal slip instead. The $\{10\bar{1}2\}$ twins in titanium, however, cause extension along the c-axis (similar to magnesium). A similar study on titanium would allow us to better understand the effects of dislocation cores and mobilities on $\{10\bar{1}2\}$ extension twin growth rates.

4.8.7 Twin tip driving stresses

What do our results say about the driving forces on twin tips? Figure 4.11 suggests a correlation between twin tip velocities and the driving stresses. However, it is important to state a few assumptions before carrying the discussion forward. At this point we are only able to measure macroscopic (specimen-averaged) stresses. One may expect a strong gradient in stresses across the twin tip. Our resolved stresses can be thought of as being averaged over a local region around the twin much greater than the length scale at which the gradient is active, and may only be useful for the very first widely-spaced twins.

The data in Figure 4.10 also indicates that the velocity of Var1 twins are consistently higher than Var2 twins. Reasons for this are currently unknown and it is

possible that we do not have a statistically significant number of twins of each variant to make this claim. It may however be observed from Figure 4.11 that for each variant, twins with higher tip velocities are driven by a higher stress, adding value to the argument that a relation exists between tip velocities and driving stresses. In addition, there may also be a case made for the kinetics of twin growth being a function of the crystallographic twin variant, although this is still based on preliminary data.

4.8.7.1 Effect of stress state on twin growth

The effect of stress state on twin growth is not understood as yet. Very few indirect examples exist in literature. For example, Dixit et al. [22] observed very thin and long twins in single crystal magnesium under plate impact loading. However, factors like loading rates and durations make direct comparisons between different experimental techniques very difficult.

Figure 4.17a plots the exact same data as in Figure 4.11 for twin tip velocities of first twins as a function of resolved shear stress on the twin plane. Figure 4.17b plots the resolved normal stress on the twin plane for the same set of first twins. As expected, the magnitudes of resolved shear stresses and normal stresses are comparable. However, this does not answer the original question: Is twin growth stress state sensitive? The pressure shear plate impact experiment (Klopp et al. [98]) has great potential to offer answers to this question.

4.8.8 Twin tip velocities and twin interactions

Direct observations of the effect of interactions require in-situ diagnostics to evaluate local stress and strain fields. However, the plots of the tip velocity history shown in Figure 4.12 offer some insight.

Two hypotheses are proposed to explain the observed velocity history. The first involves reflection of unloading waves from nearby specimen free surfaces, thus relaxing the driving stresses at the propagating twin tip. Figure 4.12c and Figure 4.12d show two snapshots from one experiment at times 10.4 μs (data point marked by a black circle in Figure 4.12a) and 11.4 μs (marked by a green circle in Figure 4.12a). The time for an elastic shear wave to travel from the tip in Figure 4.12c to the free surface and back to the tip in Figure 4.12d is roughly the same as the time difference

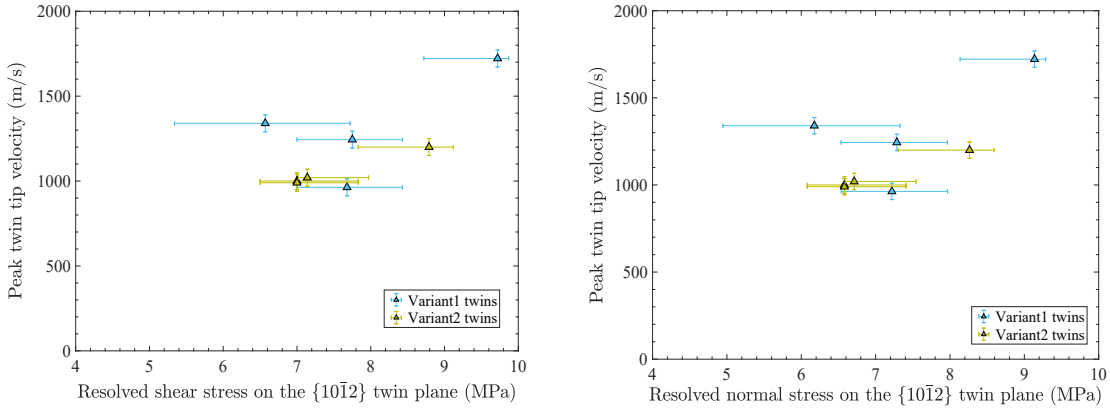

(a) Resolved shear stress **(b)** Normal stress

Figure 4.17: Peak twin tip velocities of first twins as a function of resolved shear stresses (same data as Figure 4.11) and normal stresses on the twin plane.

between the two images i.e. $\sim 1\,\mu s$, indicating that the reduction in twin tip velocity could be due to interaction of the elastic wave with the twin tip. Note that the twins stop at a very small distance above the sample edge. This is due to damage layers (induced by twins and/or dislocations) caused during specimen handling. While special care was taken to ensure minimum damage to the specimen, damage at the edges is impossible to completely avoid.

The second hypothesis is related to long term (near-equilibrium) interactions of the stress field around the twin tip with the neighboring boundaries (these may be specimen edges or a nearby twin interface). An example is shown in Figure 4.13 where two twins seem to interact with each other. The velocities of both twins increase as they approach each other and drop as they cross each other. The data indicates that interactions occur from as far as $500\,\mu m$.

The in-situ images in Figure 4.5 clearly show that Var1 and Var2 twins inhibit each others' growth. As a result, the coexistence of both variants of type Gen1 result in smaller free path lengths and hence smaller times for interactions to kick in.

4.8.9 Evolution of twin volume fraction

Results (Figure 4.5) seem to indicate that twin nucleation and growth are strongly coupled in these dynamic experiments. The relative contributions of nucleation and growth to twin volume fraction interact to satisfy the imposed macroscopic strain rates within the constraints provided by the available initial distribution of nucleation

sites. It is thus likely that twin volume fractions evolve differently at higher rates of deformation than at quasi static rates. An argument for why this transition may occur is presented in subsection 4.8.5.

Figure 4.15 shows an initial slow evolution of twin area fractions, followed by a rapid increase. This is followed again by a reduction in rates of twin area fraction evolution and eventually would saturate. Similar behavior is observed in phase transitions (for e.g. Avrami [92], Olson and Cohen [93]). We attempt to explain this behavior using simple arguments. The total axial plastic strain rate along the compression direction can be additively decomposed into a plastic strain rate due to dislocations ($\dot{\varepsilon}^d$ both inside and outside twins) and twins ($\dot{\varepsilon}^{tw}$).

$$\dot{\varepsilon}^p = \dot{\varepsilon}^d + \dot{\varepsilon}^{tw} = \dot{\varepsilon^d} + \alpha\gamma_{tw}\dot{f},$$

where α is a geometric factor that transforms the shear strain rate on the twin plane to the axial strain rate along the specimen compression direction, γ_{tw} is the twinning shear and $\dot{f}$ is the rate of evolution of twin volume fraction. It follows that,

$$\dot{f} \leq \frac{\dot{\varepsilon}^p}{\alpha\gamma_{tw}} \tag{4.8.2}$$

The geometric factor α was calculated by assuming shear strain rate concentrated on the twin plane and transforming this shear rate tensor to the specimen/ laboratory coordinate system. The transformation has been described in section B.3.

Molodov et al. [94] show that the twinning shear, γ_{tw} is ~ 0.126. Using these values in Equation 4.8.2 for a strain rate of $2 \times 10^3\ s^{-1}$ (used in the experiment)

results in limiting twin volume fractions rates,

$$\dot{f}^{lim} \leq 2.1 \times 10^4 \, s^{-1} \tag{4.8.3}$$

Hence the rate of change of twin volume fraction cannot exceed this value at these macroscopic rates of loading.

However, in our experiments we measure only the area fractions on the imaging surface (denoted as $\dot{f}^{meas}$). The volume fraction rate can be approximated to be $\beta \dot{f}^{meas}$, where β is a correction factor between 0 and 1, 0 meaning that the twins stop at the surface (infinitely thin in the third direction or surface twin) and 1 meaning they travel through the entire thickness of the specimen in the direction normal to the imaging plane. If one assumes, entirely ad hoc, that most of the plastic strain during the first 4 μs is only due to twinning, this factor can be calibrated using early time data from one experiment (SCMg014) and is found to be 0.6. This factor is then assumed to be the same across our experiments. Using this factor, our estimated volume fraction rate from the data is

$$\dot{f}^{calc} = 0.6 \times 3 \times 10^4 s^{-1} = 1.8 \times 10^4 s^{-1}$$

which is very close to the limiting rates calculated using Equation 4.8.2 in Equation 4.8.3. Hence, the maximum twin volume fraction rates are limited by the imposed rate of loading. The reduction in the slope of the area fraction-time curves (Figure 4.15) at later times could be because of dislocation slip becoming increasingly active at these times.

4.8.10 Preliminary direct measurements of the geometric correction factor β

The geometric correction factor β can be estimated in other ways. Shivaraman et al. [99] have recently performed femto-second laser serial sectioning experiments along with EBSD on post-mortem samples to determine the 3-dimensional microstructures of the twinned crystals. The β estimated from our first preliminary dataset is 0.9-1 (note that this is a measure obtained after a substantial strain of 3%). It is possible that β evolves during the deformation. However, the 3D microscopy was performed over a small domain of 200 $\times$ 140 $\times$ 100 μm, perhaps not large enough for statistical sampling of twins observed from the in-situ imaging.

Three-dimensional datasets of this nature may also be used to identify twin nucleation sites and the orientation of twin propagation through the bulk of the crystal. The latter would help us make more accurate estimates of twin tip and boundary velocities measured on the imaging surface.

4.8.11 Plasticity due to dislocation slip

With all of the caveats above, Figure 4.18 presents the net plastic strain along with the contributions of twinning and dislocation slip to plastic strain along the specimen loading direction. Net plastic strains are shown by the solid lines and were calculated from stresses (to obtain the elastic strains) and total strains measured directly

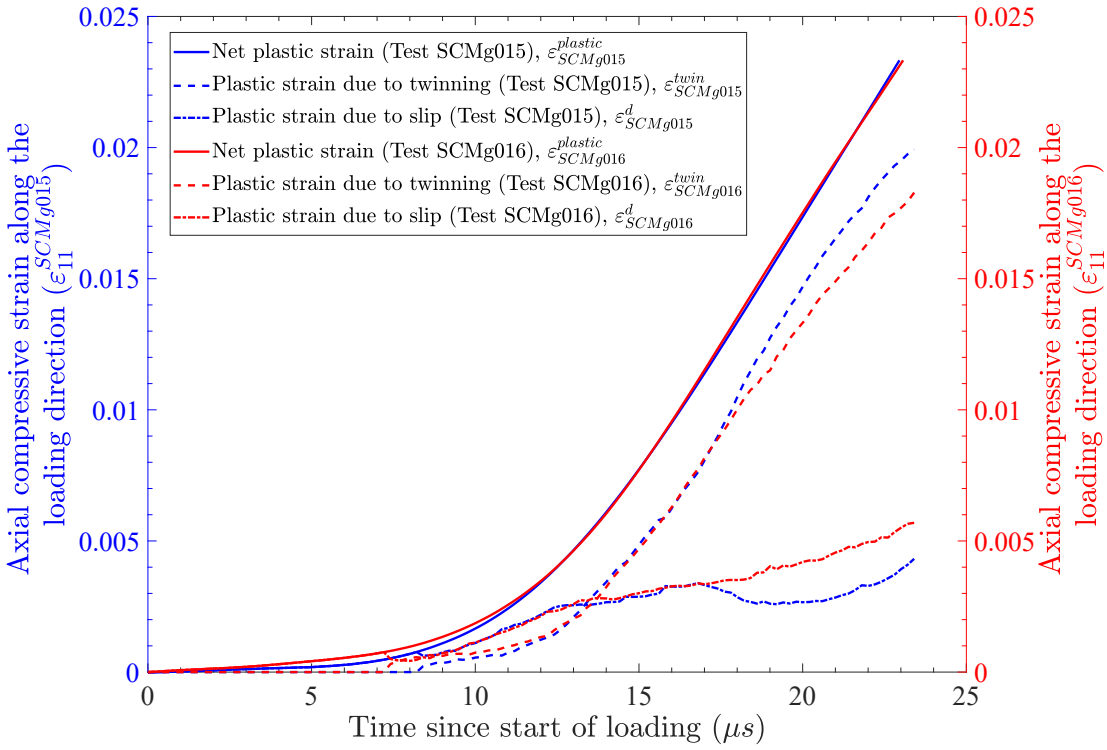

Figure 4.18: Net plastic strains plotted with contributions from twinning and dislocations to plastic strain along the specimen loading direction for two experiments. Each color refers to a specific experiment. Solid lines are net plastic strains, dashed lines contribution of twinning to plastic strain and dash-dot lines are contributions of dislocations.

from the experiment. The contribution of twinning to plastic strain is defined as $\gamma^t = \beta\alpha\gamma_{tw}f^{meas}$, where $\beta \simeq 0.6$ is the correction factor calibrated using the experiment SCMg014 (it hence does not make sense to present data from SCMg014 in Figure 4.18). α is a geometric factor derived from crystallography to transform the shear strain on the twin plane to axial strain along the loading direction (section B.3). γ_{tw} is the twinning shear and f^{meas} is the measured twin area fraction (Figure 4.15).

The contribution of dislocation slip is calculated simply by subtracting net plastic strains from twinning plastic strains.

Figure 4.18 suggests that twinning dominates plastic deformation in these experiments at early strains. The contribution of dislocation slip to plastic strain is about 20% while the rest appears to come from twinning. Nevertheless, it should be noted that the contribution of dislocation slip to plastic strain is still significant and cannot be neglected.

The sustained increase in plastic strain due to twinning is due to the increased nucleation of Gen2 twins (Figure 4.5, Figure 4.19c and Figure 4.19d). Once the entire volume was twinned, dislocations increase their contributions to plastic strain resulting in a decrease in the rate of twin volume fraction evolution (Equation 4.8.2).

4.8.12 The competition between twin nucleation and growth

The objective of this section is to understand the relative contributions of nucleation and growth to the evolution of twin volume fraction. A phenomenological interpretation is first presented based on the data shown. A mathematical simplification of the theory presented in subsection 4.7.4 helps represent this competition quantitatively and resolve further details.

We start with an example. SCMg014 shows greater nucleation rates at early times

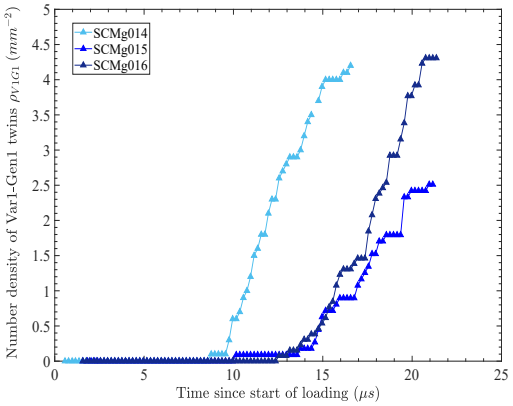

(a) Nucleation of Var1-Gen1 twins

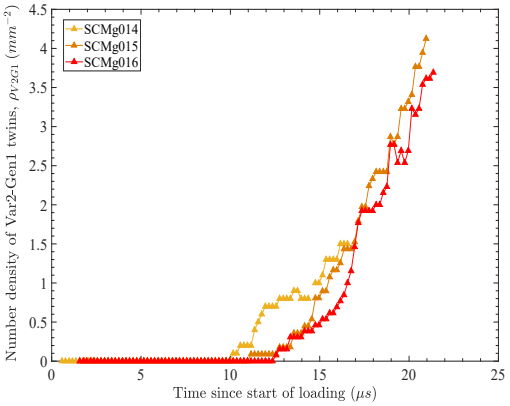

(b) Nucleation of Var2-Gen1 twins

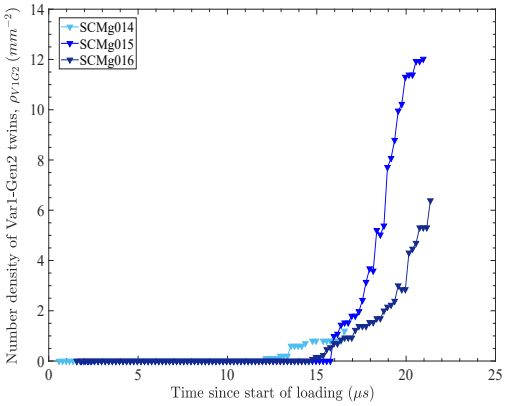

(c) Nucleation of Var1-Gen2 twins

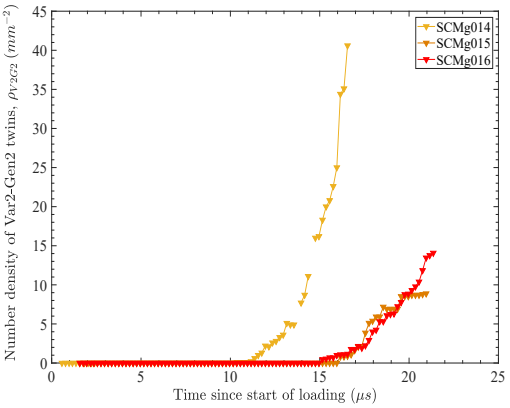

(d) Nucleation of Var2-Gen2 twins

Figure 4.19: Nucleation of each identified twin type. Note the bias towards nucleation of V1G1 twins and V2G2 twins for experiment SCMg014.

while nucleation is rather slow for the other two experiments (Figure 4.9). Figure 4.19 presents the number density of each type of twin in all three experiments. Notice that in experiment SCMg014, most Var1 twins are of Gen1 nature (Figure 4.19a) while Gen2 twins of Var1 type are negligible (Figure 4.19c). Subsequently most Var2 twins are of Gen2 nature (Figure 4.19d).

Equation 4.7.10 for the rate of growth of twin volume fraction may be rewritten simply as,

$$\dot{f} = \dot{f}^n + \dot{f}^g \tag{4.8.4}$$

where

$$\dot{f}^n(t) = l_o w_o \dot{\rho}(t) \tag{4.8.5}$$

is the rate of volume fraction from nucleation and

$$\dot{f}^g(t) = \frac{1}{A}\sum_{j=1}^{N_t}(l_j(t)\dot{w}_j(t) + w_j(t)\dot{l}_j(t)) \tag{4.8.6}$$

from growth of existing twins. These equations hold for specific twin variants, but sub-scripts have been ignored for brevity. Here we simplify the discrete formulation to an average one. At any given time, we can define a representative twin area Q^R(in a snapshot) such that,

$$Q^R = \frac{Q}{N_t} \tag{4.8.7}$$

where Q is the total area of twins in the matrix and N_t the total number of twins in the matrix at that time. Then the rate of evolution of twin volume fraction is simply,

$$\dot{f} = \frac{\dot{Q}}{A} = \frac{1}{A}\left(\dot{Q}^R N_t + Q^R \dot{N}_t\right) = \dot{Q}^R \rho_t + Q^R \dot{\rho}_t \tag{4.8.8}$$

so that,

$$\dot{f} = \dot{\rho}_t Q^R + \rho_t Q^R \Big(\frac{\dot{Q}}{Q} - \frac{\dot{N}_t}{N_t} \Big) \tag{4.8.9}$$

While it is easier to represent these terms from experimental data, the nucleation and growth terms are clearly coupled.

In Equation 4.8.7, both the numerator and denominator are evolving terms. Generally, the area of the 'representative' twin increases if the total rate of increase in twin area is faster than the nucleation rate, and decreases if the opposite is true. The term $\dot{\rho}_t Q^R$ can be thought of as representing pure nucleation only when the representative twin area is a constant. This term deviates from pure nucleation when a large number of small twins are nucleated or predominant growth occurs (in either case Q^R changes).

Figure 4.20 are plots of the left hand side of Equation 4.8.9 (rate of twin volume fraction, $\dot{f}$) as a function of the first term $\dot{\rho}_t Q^R$ on the right hand side for each variant. To calculate the rates of measured variables, a smoothing spline fit was applied to the discrete data and then a moving average differentiation performed (thus this plot should only be used to interpret global trends). A further discussion of this figure requires definitions of the three regions described as I, II and III in Figure 4.20.

Consider Equation 4.8.9 again. When $\dot{f} > \dot{\rho}_t Q^R$, two possibilities exist (regions I and II). If $\frac{\dot{Q}}{Q} >> \frac{\dot{N}_t}{N_t}$ (region I), twin growth is dominant. For region I marked in the figure, $\frac{\dot{Q}}{Q} > 10 \times \frac{\dot{N}_t}{N_t}$ such that $\dot{f} > 10 \times \dot{\rho}_t Q^R$. As the difference $\left(\frac{\dot{Q}}{Q} - \frac{\dot{N}_t}{N_t} \right) > 0$ decreases, a transition occurs (into region II) from high growth rates and small nucleation rates

to smaller growth rates and larger nucleation rates. $\dot{Q}^R$ is negative if $\frac{\dot{Q}}{Q} < \frac{\dot{N}_t}{N_t}$. In other words, our representative twin becomes smaller because nucleation occurs faster than increase in twin area or simply a large number of very small twins are formed. In this case, $\dot{f} < \dot{\rho}_t Q^R$. This is region III. The transition from growth-dominant to nucleation-dominant deformation may hence be described using the representative twin area Q^R. Large values of Q^R imply twin growth-dominant deformation. As Q^R becomes smaller, we transition to twin nucleation-dominant deformation (note that Q^R can become negative in this formulation). Two critical points are identified here. The first is on the y-axis which lies in region I. On the y-axis only twin growth occurs with no nucleation (obviously unphysical). On the x-axis purely twin nucleation occurs with no growth of existing twins.

A map such as this helps reveal the relative contributions of nucleation and growth in greater detail. Figure 4.20a describes the relative contributions of nucleation and growth to the volume fraction of Var1 twins. After nucleation of the first twins, growth dominates twin evolution with the first twins traveling at velocities of the order of $1\,km/s$ (Figure 4.10). Subsequently these twins are impeded by a specimen boundary or twin boundary very quickly (within $1 - 2\,\mu s$), resulting in additional nucleation. This is where a transition from growth-dominant deformation (region I) to deformation balanced by both nucleation and growth (region II) occurs. Note that twin tip growth dominates twin volume fraction rates due to comparatively small twin boundary velocities. The effect of twin boundary velocities, if any, should

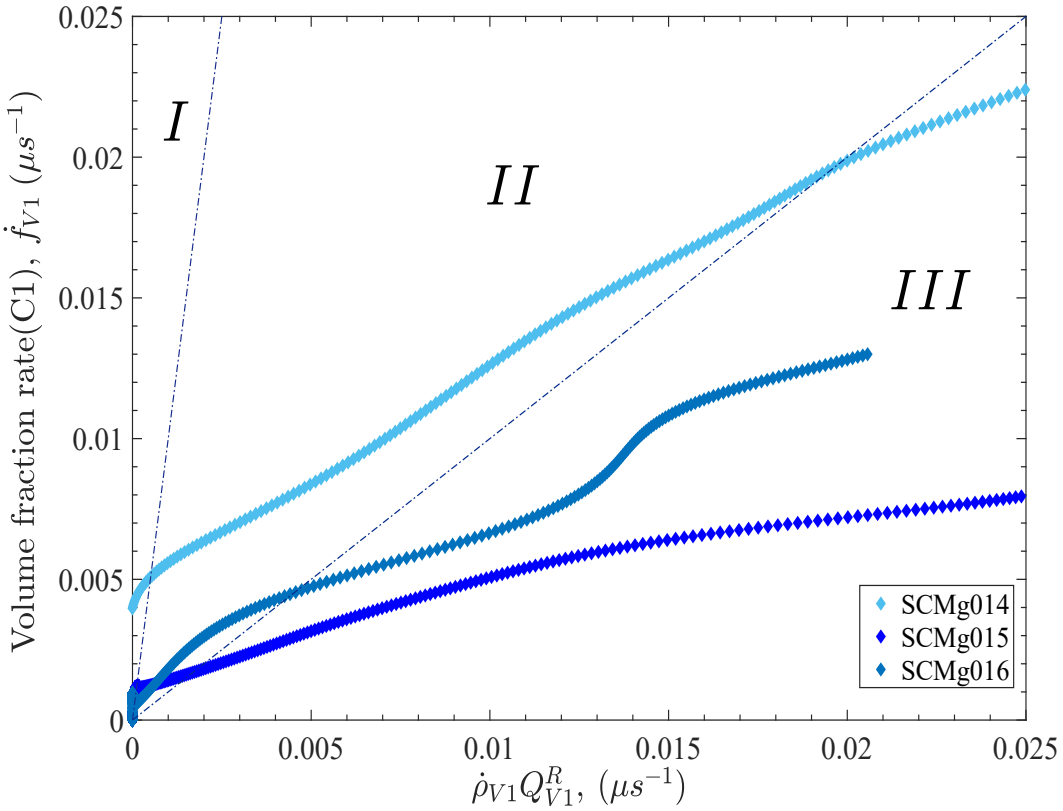

(a) Variant1 twins

Figure 4.20: Competition between nucleation and growth. Region I represents growth-dominant behavior, Region II represents an increase in nucleation rates and slight decrease in growth rates and Region III represents nucleation-dominant (of small twins) behavior. Notice that Var1 twins for experiment SCMg014 stay in a growth dominant regime longer than the other two experiments and Var2 twins quickly transition to the nucleation-dominant regime for the same experiment. Nucleation of negligible Var2-Gen1 twins allow greater free path length for Var1-Gen1 twins to grow. Similarly most Var2 twins are of type Gen2 which are primarily nucleation-driven. This has been experimentally verified in Figure 4.19.

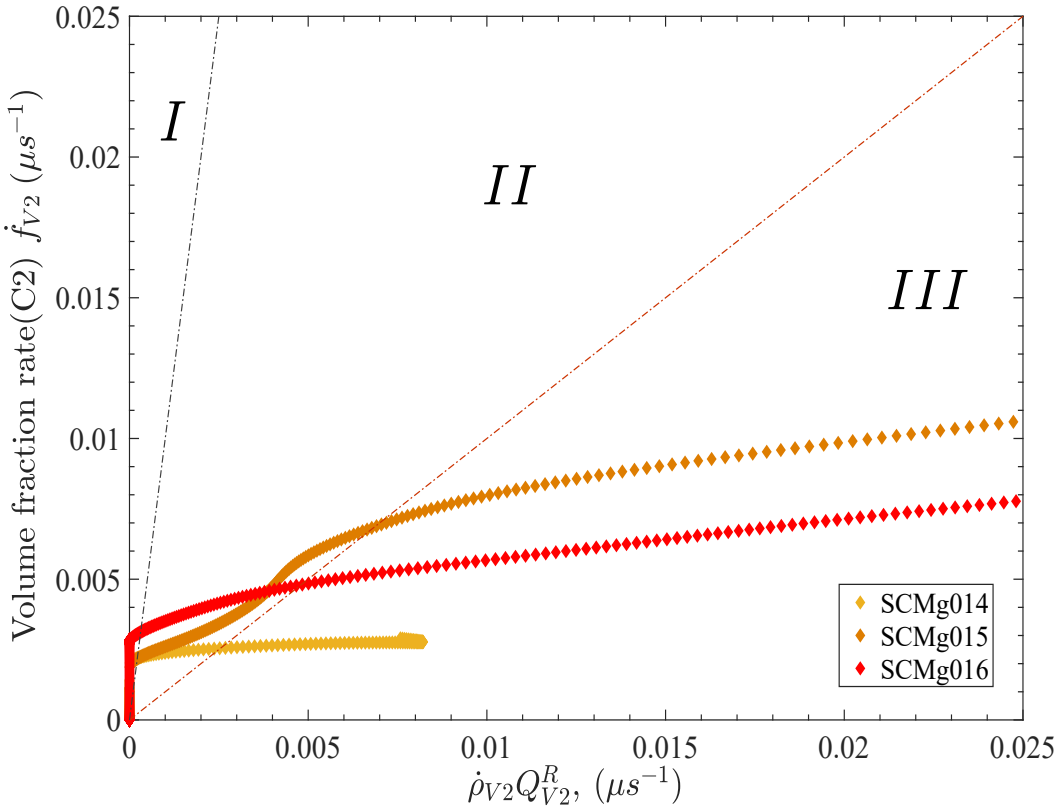

(b) Variant2 twins

Figure 4.20: Competition between nucleation and growth (cont). Region I represents growth-dominant behavior, Region II represents an increase in nucleation rates and slight decrease in growth rates and Region III represents nucleation-dominant (of small twins) behavior. Notice that Var1 twins for experiment SCMg014 stay in a growth dominant regime longer than the other two experiments and Var2 twins quickly transition to the nucleation-dominant regime for the same experiment. Nucleation of negligible Var2-Gen1 twins allow greater free path length for Var1-Gen1 twins to grow. Similarly most Var2 twins are of type Gen2 which are primarily nucleation-driven. This has been experimentally verified in Figure 4.19.

show up in region II. The presence of a few twins results in additional nucleation of twins under continued imposition of the macroscopic strain rate. As the matrix is not completely populated by twins yet, growth of these newly nucleated twins also occurs. As the matrix becomes more densely populated by twins, growth becomes harder and faster nucleation of smaller twins begins to dominate deformation pushing the system into region III. The transition to region III occurs quite early during deformation (at $\sim 10\,\mu s$ from the start of loading for SCMg014 and $\sim 13\,\mu s$ for SCMg015 and SCMg016) and the system remains in a nucleation-dominant region for the remaining duration within which we can extract quantitative data from the images. A similar trend is observed for Var2 twins as well (Figure 4.20b). A useful detail to note is curves that are closer to the x-axis in region III have on average nucleation of smaller twins. From our images (Figure 4.5), the smallest twins are Gen2 in nature.

As an example of the use of such a map, let us focus on the light blue curve in Figure 4.20a and the light orange curve in Figure 4.20b both representing data from experiment SCMg014. The light blue curve remains in regions I and II longer than the other two indicating that nucleation and growth of larger twins dominate deformation for a longer time in comparison to the other two curves. Conversely, the light orange curve in Figure 4.20b is the lowest indicating that large nucleation of small twins dominates the evolution of the Var2 twin volume fraction. Going back to the images corresponding to this experiment (Figure 4.21), most Var1 twins are of Gen1 nature implying that these twins can grow unimpeded through the entire

matrix (and hence are large). Most Var2 twins are of Gen2 type and are observed to be very small.

4.9 Closing remarks

Current models for twinning are largely phenomenological, and generally do not account for the influence of strain rate or local multi-axial stresses. This work specifically identifies limiting rates of twin-dominant plastic flow in magnesium, and demonstrates that these effects cannot be ignored in applications that develop extreme conditions (such as very high strain rates). We suggest that it is important to develop robust nucleation and growth criteria for twins, and we provide some of the core experimental evidence needed to do so.

The twin nucleation stresses identified here are slightly higher than those reported in the literature from quasi-static deformation. This may indicate a rate effect on nucleation. While our data indicates that nucleation may be stress-driven, we are unable to identify the general tensorial stress state associated with nucleation. It would be useful to perform controlled multiaxial loading experiments together with careful atomic resolution microscopy to understand the nature of twin embryos, and then to couple these experiments with modeling at the atomic scale as well as at the microscale (to account for stress gradients). Note that much of the literature on twin nucleation in fcc metals may not apply to these hcp metals. The evolution of twin nucleation rates also seems to be rate dependent with the additional nucleation of

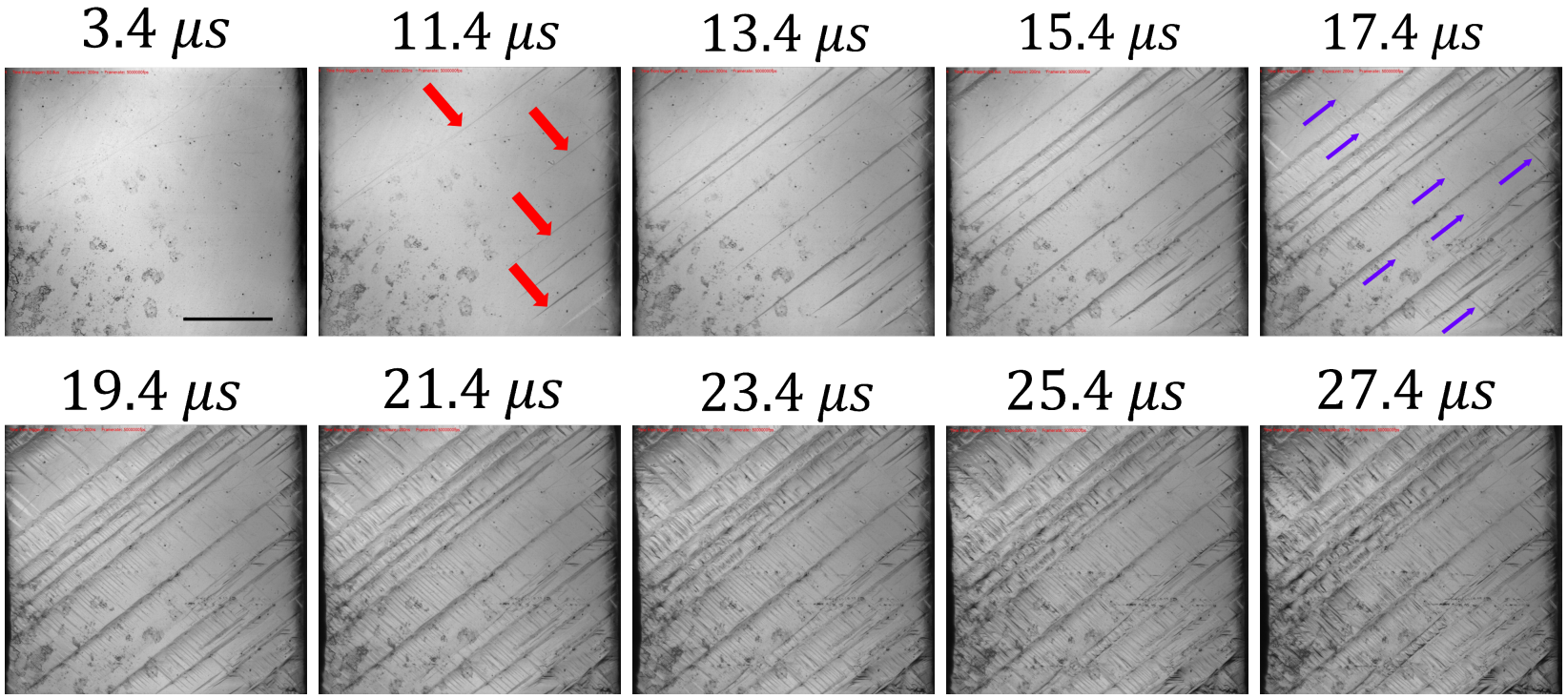

Figure 4.21: Selected sequence of in-situ images from one experiment. Scale bar in the first image corresponds to 1mm. In frame 2 (11.4 μs), the red arrow shows the first Gen1 twins. Gen2 twins are shown (blue arrows) in the fifth frame at 17.4 μs. Note that in contrast to Figure 4.5 all Var1 twins are of Gen1 type and Var2 are Gen2 type. (Specimen ID: SCMg014)

Gen2 twins observed exclusively at high loading rates.

On the aspect of twin growth, models that provide an understanding of the coupling between the driving forces on twin tips, the energies associated with twin boundaries, and the twin tip velocity would be of great interest. In this regard, we note that the twin tip propagation is typically not steady-state. With multiple twins evolving together, interactions would begin to play an important role in the dynamics of twin evolution and consequently the macroscopic response.

Predicting the complex spatial distribution of twins, observed in this chapter, requires an understanding of twin spacings. Figure 4.5 and Figure 4.21 clearly indicate the presence of a length scale that governs twin spacing, below which additional twins are not allowed to nucleate (at the length scales we are probing). Literature evidence has pointed to the presence of facets or discontinuities on the twin interface (eg. Tu and Zhang [95]). However, the spacing between these facets are much too small to govern the twin spacings that we observe in our experiments. Two potential mechanisms for these twin spacings are discussed: kinematics and twin boundary stresses. When the rate of twin boundary migration is too small to accommodate the rate of macroscopic plastic deformation, other nucleation sites are activated. Hence, the spacing between these nucleation sites are governed by the limiting rates of twin boundary migration and the rate of twin nucleation. A spacing calculated based on this kinematic argument would decrease with increasing loading rate (at a specific plastic strain). The latter hypothesis refers to twin boundary stresses. When a twin

is nucleated, a local stress gradient exists around this twin. As the twin begins to grow, the change in this gradient may result in a local relaxation of some components of stresses around the twin and a relative increase in other components. This may activate a local nucleation site nearby, resulting in the nucleation of another twin. The spacing between these two twins would be governed by the size of the evolving stress field around the pre-existing twin. If we knew the stress field around a twin, this length scale may be derived from equilibrium relations. Analysis of our data can directly provide validations for the theory. Knowledge of this length scale will offer more insight into the competition between twin nucleation and growth, and may provide avenues to control these dynamics and material strength.

4.10 Conclusions

In-situ high speed optical imaging has been used as a powerful tool to understand twin nucleation and growth in single crystal magnesium under dynamic loading. The following are our primary conclusions from in this chapter.

1. Two variants of twins are observed to nucleate, with each variant having twins nucleating either from the matrix or from pre-existing twin boundaries.

2. Twin nucleation appears to be stress-driven with resolved shear stresses in the range of 5-7 MPa. Other components of stress may also affect nucleation but this is not determined from our experiments.

3. After nucleation of the first twin(s), these twin tips propagate at very high speeds with peak velocities reaching $\sim 2\,km/s$.

4. At these strain rates, once the twin tip stops growing, nucleation of additional twins from pre-existing twin boundaries is preferred over traditionally observed twin boundary growth.

5. Twin volume fraction evolution is initially dominated by growth. At later times, nucleation of additional twins begins to contribute significantly to twin volume fraction evolution.

Understanding, predicting and controlling the phenomena of twin evolution described in this chapter, hence involve building models that can adequately capture the dynamics of evolution of nucleation and growth. One important quantity that we need to understand in greater detail is the limiting rates of twin growth. The next chapter, hence focuses on building a micro structurally informed continuum mechanical framework to predict the dynamics of twin growth.

Chapter 5

A thermodynamically consistent framework for twin dynamics

This chapter seeks to understand the driving force on a twin boundary and the associated propagation velocity. We present a micro-mechanics based continuum mechanical framework to capture the driving forces on twin boundaries in an anisotropic elastic-plastic continuum.

5.1 Introduction and background

We first setup the basis for building such a framework. Recall that the rate of plastic deformation due to twinning was defined as,

$$\dot{\gamma}_t = \dot{f}\gamma_{tw} \tag{5.1.1}$$

where $\dot{f}$ is the rate of twin volume fraction evolution in a representative volume element (RVE) and γ_{tw} is the crystallographic twinning shear. Our experimental evidence indicates that twin evolution is primarily stress-driven, although other factors like temperature may also play a role. The term $\dot{f}$ directly represents the stress-driven dynamic evolution of a specific twin variant. The analytical relation for $\dot{f}$ was given by Equation 4.7.10 as,

$$\dot{f}(\boldsymbol{\sigma}) = \underbrace{l_o w_o \dot{\rho}_t(\boldsymbol{\sigma})}_{\text{Nucleation rate}} + \underbrace{\frac{1}{A}\sum_{j=1}^{N_t}(l_j \dot{w}_j(\boldsymbol{\sigma}) + w_j \dot{l}_j(\boldsymbol{\sigma}))}_{\text{Growth rate}} \tag{5.1.2}$$

where l_o and w_o are the initial lengths and widths of twin nuclei when they become stable (this can be thought of as a critical length scale for twin nucleation), ρ_t is the twin number density, A is the cross-sectional area of the specimen, N_t is the total number of existing twins in the material, l_j is the length of the j^{th} twin and w_j is it's width. $\dot{(\,)}$ represents the time derivative.

In this approach, the independent variable for the nucleation and growth rate terms is the Cauchy stress tensor $\boldsymbol{\sigma}$. The two terms labeled in Equation 5.1.2 hence represent the nucleation and growth kinetics as a function of the driving field (in this case the stress). An example micrograph showing the length and width of a twin is presented in Figure 5.1. This in-situ high speed image shows a snapshot of twins in a dynamically compressed single crystal magnesium sample (from the experimental dataset in chapter 4). Note that the width of the twin varies to some degree along its length. The driving stress is, in general, a function of position and hence the growth

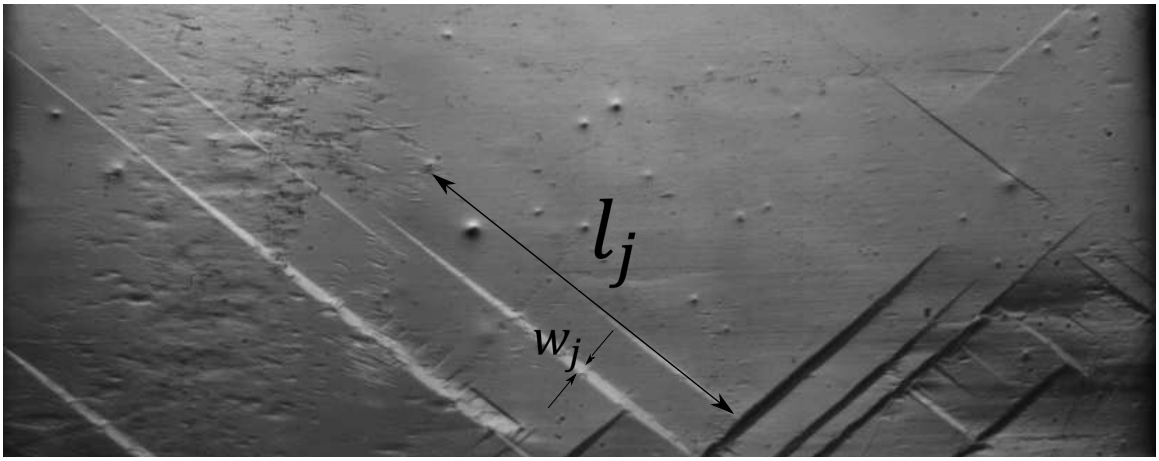

Figure 5.1: A representation of lengths and widths of a twin in a real image. Notice that twin width is also a function of space.

rates (Equation 5.1.2) are implicit functions of position as well. Thus the presence of a stress gradient along the length of a twin could result in different $\dot{w}$ values at different points along the twin boundary (effectively causing curvature). While this feature remains in the general theoretical framework developed here, it will be ignored in the specific examples discussed.

In this framework, we assume the twin boundary to be a discontinuous interface in a macroscopic elastic-plastic continuum. We define the 'twin boundary' to mean the interface between the twinned and untwinned regions of the crystal. This includes both the lateral twin boundary and the twin tip used in chapter 4. We focus on capturing the driving forces on this twin boundary. The kinetic relations serve to close the set of governing field equations (Abeyaratne and Knowles [100]). We do not derive kinetic relations here, although this is a necessary next step in the development

of the model (a scheme is proposed in subsection 7.2.2).

Much of the theory presented in this chapter is inspired by work on phase transitions in the early 90's, where propagating phase boundaries were modeled as discontinuities in a non-linear elastic continuum (Abeyaratne and Knowles [100]). In these models, the free energy density for each phase in the material may be defined as a function of deformation gradient $\boldsymbol{F}$ and temperature Θ. For the specific example of a two-phase material, the strain at which both phases exist in equilibrium would be governed by the driving forces on the phase boundary (slopes of the free energy densities as a function of $\boldsymbol{F}$). The resulting free energy density for the two-phase material, in equilibrium, will be a double-well function with two local minima, one for each phase (Abeyaratne and Knowles [100]).

This idea was later adapted to deformation twinning in bcc metals by Rosakis and Tsai [17], who assumed the strain energy of the material to have multiple potential wells, each representing a stable twin type. Using a combination of this stored energy function and fundamental balance laws, the velocity fields around the propagating twin were estimated analytically (Rosakis and Tsai [17]). The stored energy function allowed for the selection of twin morphologies and their relative arrangement. We simplify some of these arguments by assuming a specific twin variant already present in the continuum. Unlike any of the previous studies mentioned, the current framework considers the matrix and twinned regions as being elastic-plastic, allowing for plastic strain to accumulate in the material. Plastic deformation in the matrix and

twinned regions is incorporated using micro-mechanics based free energy functions for each of these regions.

Section 5.2 presents the basic kinematic definitions and rules in each of the matrix and twinned regions. Section 5.3 states the balance of mass, linear momentum and angular momentum. The balance of micro-mechanical forces conjugate to microscopic rates of deformation (due to dislocations) is described in section 5.4. In section 5.5, energy balance laws due to conventional macroscopic field variables and microscopic (or internal) variables are treated. With the basic balance laws established, section 5.6 states the constitutive relations and uses thermodynamic restrictions from section 5.5 to ensure physical consistency. Section 5.7 focuses on defining the specific free energy density functions in the matrix and the twinned regions. Ways of incorporating strain rate dependence are also discussed using simple examples. The next step is to identify compatibility conditions at the twin boundary which is treated using jump conditions in section 5.8. Using these conditions, a relation for driving traction on the twin boundary, originally developed by Abeyaratne and Knowles [1], is reiterated and its use in understanding driving forces at the twin boundary in our problem is summarized. We end with a summary of the framework and its implications for future use.

5.2 Kinematics

Consider the general three dimensional problem shown in Figure 5.2. The matrix

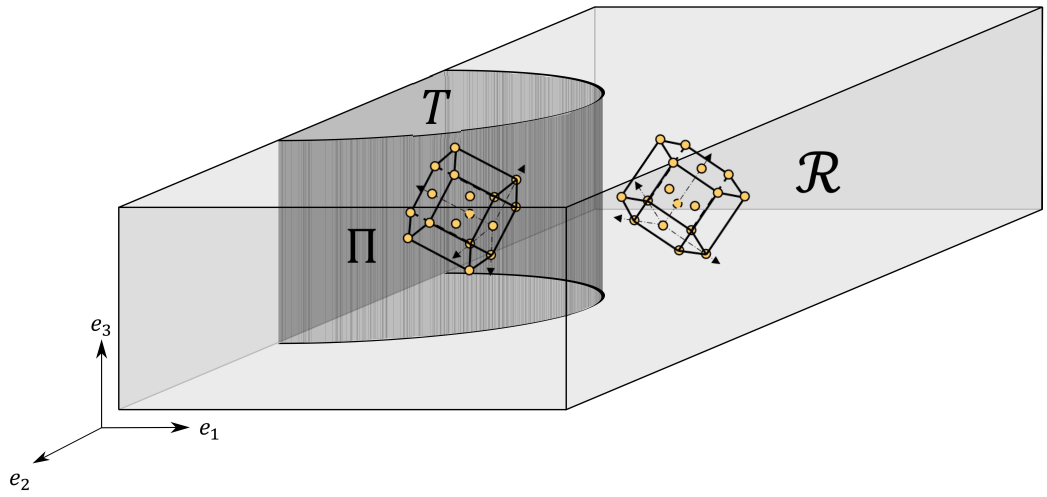

Figure 5.2: A schematic of the two dimensional plane strain problem with a discontinuity of arbitrary shape representing the twin boundary.

region is represented as $\mathcal{R}$ with a given crystallographic orientation (marked by the hcp schematic in the picture). The twinned region is represented by T, and Π is the twin boundary of arbitrary shape. In three dimensions, this is a surface defect. For our current purposes, this is the discontinuity. We prescribe piecewise continuous displacement fields across the twin boundary. The gradient fields are discontinuous. The theory is three dimensional, but examples and implications will be discussed after simplification to two dimensions.

If $\boldsymbol{X}$ represents a position vector in the continuum in the initial configuration (material coordinates) and $\boldsymbol{x}$ the corresponding position in the deformed configuration (spatial coordinates) that follows the mapping $\boldsymbol{x} = \boldsymbol{\chi}(\boldsymbol{X}, t)$ at time t, the displacement of a material point is,

$$\boldsymbol{u}(\boldsymbol{X}, t) = \boldsymbol{x} - \boldsymbol{X} \tag{5.2.1}$$

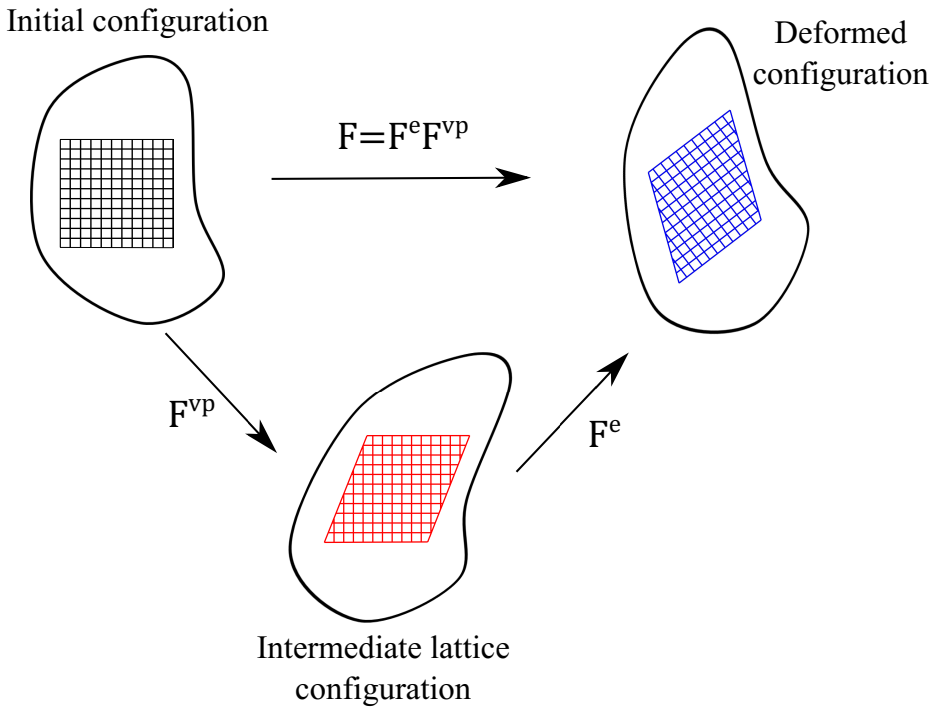

Figure 5.3: Kroner decomposition for crystal plasticity

The deformation gradient $\boldsymbol{F}$ can be calculated as,

$$\boldsymbol{F} = \boldsymbol{\nabla}_{\boldsymbol{X}} \boldsymbol{x} = \frac{\partial \boldsymbol{x}}{\partial \boldsymbol{X}} \tag{5.2.2}$$

The deformation gradient can be decomposed into elastic and visco-plastic components (Lee [101]) as,

$$\boldsymbol{F} = \boldsymbol{\nabla}_{\boldsymbol{X}} \boldsymbol{x} = \boldsymbol{F}^{\boldsymbol{e}} \boldsymbol{F}^{\boldsymbol{vp}} \tag{5.2.3}$$

Figure 5.3 represents this decomposition schematically. The grid in each configuration is a representation of a crystal lattice. The pre-deformed configuration is called the 'initial configuration'. The final configuration after imposing the deformation gradient $\boldsymbol{F}$ is called the 'deformed configuration', where the crystal lattice has

deformed both elastically and plastically. The decomposition between these two components is made possible by the assumption of a fictitious intermediate configuration called the 'lattice configuration'. Notice that the lattice remains undistorted but the continuum is deformed. This is a representation of plastic flow mechanisms (e.g. dislocations) that move through the lattice without changing the lattice structure itself. The initial configuration is related to this intermediate lattice configuration by the visco-plastic deformation gradient $\boldsymbol{F^{vp}}$. The lattice configuration is then related to the final deformed configuration by the elastic deformation gradient $\boldsymbol{F^{e}}$, where the lattice is distorted by elastic deformation and rotated by rigid body rotations if any.

We define the Green-Lagrange strain tensor which will be useful in our future discussions of deformation rate:

$$\boldsymbol{E} = \frac{1}{2}(\boldsymbol{F^{T}F} - \boldsymbol{\mathcal{I}}) \tag{5.2.4}$$

where $\boldsymbol{\mathcal{I}}$ is the identity tensor.

We define two frames of reference which will be of use through the remaining part of this chapter. A frame of reference where the reference points are tied to the material points is called the 'material configuration' (Lagrangian description) and that which has its reference points fixed to space is called the 'spatial configuration' (Eulerian description).

If $\boldsymbol{v} = \dot{\boldsymbol{u}}$ is the particle velocity in the deformed description, the deformation rate is defined by the spatial velocity gradient, $\boldsymbol{L} \triangleq \boldsymbol{\nabla_x v}(\boldsymbol{x}, t)$ and is related to the

deformation gradient by,

$$\boldsymbol{L} = \dot{\boldsymbol{F}}\boldsymbol{F}^{-1} \tag{5.2.5}$$

Using Equation 5.2.3 in Equation 5.2.5,

$$\boldsymbol{L} = \underbrace{\dot{\boldsymbol{F}}^{\boldsymbol{e}}\boldsymbol{F}^{\boldsymbol{e-1}}}_{\boldsymbol{L^e}} + \boldsymbol{F}^{\boldsymbol{e}}\underbrace{\dot{\boldsymbol{F}}^{\boldsymbol{vp}}\boldsymbol{F}^{\boldsymbol{vp-1}}}_{\hat{\boldsymbol{L}}^{\boldsymbol{vp}}}\boldsymbol{F}^{\boldsymbol{e-1}} = \boldsymbol{L}^{\boldsymbol{e}} + \boldsymbol{F}^{\boldsymbol{e}}\hat{\boldsymbol{L}}^{\boldsymbol{vp}}\boldsymbol{F}^{\boldsymbol{e-1}} \tag{5.2.6}$$

Thus, multiplicative decomposition of the deformation gradient corresponds to an additive decomposition of the velocity gradient as defined above.

Our framework is designed to capture the dynamic evolution of a twin boundary using the micro-mechanics of dislocation slip in the matrix and twinned regions. We therefore introduce internal variables that characterize the shear rate due to specific crystallographic slip systems at the micro-scale as,

$$\{\nu\} \triangleq \{\nu^1, \nu^2, \nu^3, \ldots, \nu^{N_s}\} \tag{5.2.7}$$

where N_s is the total number of slip systems in either the matrix or the twin (note N_s need not be the same in the matrix ($\mathcal{R}$) and the twin (T)). The microscopic shear rates relate to the macroscopic rate of plastic deformation through,

$$\hat{\boldsymbol{L}}^{\boldsymbol{vp}} = \sum_{\alpha=1}^{N_s} \nu^{\alpha}(\boldsymbol{s}^{\boldsymbol{\alpha}} \otimes \boldsymbol{m}^{\boldsymbol{\alpha}}) \tag{5.2.8}$$

where $\boldsymbol{s}^{\boldsymbol{\alpha}}$ and $\boldsymbol{m}^{\boldsymbol{\alpha}}$ are the slip directions and slip plane normals for a given slip system respectively, both defined in the *lattice configuration*. Using the definition of $\hat{\boldsymbol{L}}^{\boldsymbol{vp}}$ in Equation 5.2.6,

$$\dot{\boldsymbol{F}}^{\boldsymbol{vp}} = \sum_{\alpha=1}^{N_s} \nu^{\alpha}(\boldsymbol{s}^{\boldsymbol{\alpha}} \otimes \boldsymbol{m}^{\boldsymbol{\alpha}}\boldsymbol{F}^{\boldsymbol{vp}}) \tag{5.2.9}$$

This is the 'plastic flow rule' and defines the evolution of the plastic strain. This flow rule is defined with respect to micro-mechanical variables (ν^α) that describe shear rates at the micro-scale (Gurtin [18]). We further define $\boldsymbol{M^\alpha} \triangleq \boldsymbol{s^\alpha} \otimes \boldsymbol{\tilde{m}^\alpha}$, where $\boldsymbol{\tilde{m}^\alpha} \triangleq \boldsymbol{F^{vpT} m^\alpha}$, to make the flow rule more tractable. The flow rule is then represented in a simpler form as,

$$\boldsymbol{\dot{F}^{vp}} = \sum_{\alpha=1}^{N_s} \nu^\alpha \boldsymbol{M^\alpha} \tag{5.2.10}$$

Thus $\boldsymbol{M^\alpha}$ defines the crystallography of the slip systems and ν^α defines its dynamics. Notice $\boldsymbol{M^\alpha}$ is a two-point tensor, where $\boldsymbol{\tilde{m}^\alpha}$ is the slip plane normal defined in the material configuration and $\boldsymbol{s^\alpha}$ is defined in the lattice configuration. Since $\boldsymbol{F^{vp}}$ does not cause lattice distortion, $\boldsymbol{m^\alpha}$ and $\boldsymbol{\tilde{m}^\alpha}$ are equivalent.

Equation 5.2.10 is an initial value problem with the initial condition at time $t = 0$ usually chosen as $\boldsymbol{F_o^{vp}} = \boldsymbol{\mathcal{I}}$, implying no initial plastic deformation. Twin propagation as a function of initial plastic deformation is, however, a physically relevant problem. The evolution of twins in an initially worked metal has important implications in material design for specific applications. The initial condition for Equation 5.2.10 may hence be chosen as,

$$\boldsymbol{F_o^{vp}} = \boldsymbol{\mathcal{I}} + \sum_{i=1}^{N_s^o} \bar{\gamma}_o^i \boldsymbol{M^i} \tag{5.2.11}$$

where $\bar{\gamma}_o^i$ is the initial accumulated shear strain on slip system i. A physical interpretation of this follows from the definition of dislocation density. The classical materials

science definition for dislocation density is,

$$\varrho = \frac{\text{Total dislocation line length}}{\text{Volume of spatial domain}} = \frac{N_\perp l}{V} \tag{5.2.12}$$

with dimensions of LENGTH^{-2}, where $N_\perp$ is the number of dislocations and l is the average length of a dislocation line. The initial plastic shear strain for a given dislocation variant i according to this definition is,

$$\bar{\gamma}_o^i = \int_0^{t_c} \varrho_o^i b^i v^i dt = \int \varrho_o^i b^i dx \tag{5.2.13}$$

where ϱ_o^i is the initial dislocation density, b^i is the magnitude of the Burger's vector, v^i is the mean dislocation velocity for slip system i and t_c is an arbitrary time up to which the time integral is calculated. The second integral in Equation 5.2.13 is calculated over the total distance swept by the dislocations. For constitutive models in continuum mechanics, however, the dislocation density is incorporated as a gradient in shear strain. We modify the commonly used definition so that the dislocation density is defined as,

$$\varrho = \frac{N_\perp}{|\boldsymbol{m}|} \tag{5.2.14}$$

where ϱ now represents the number of dislocations per unit length along the slip plane normal ($\boldsymbol{m}$) (Gurtin et al. [102]) and has units of LENGTH^{-1}. Physically, this represents the total slip due to dislocations per unit volume. Then $\bar{\gamma}_o$ in Equation 5.2.11 can be represented as,

$$\bar{\gamma}_o^i = \int \varrho_o^i dx \tag{5.2.15}$$

To complete the statement of the kinematics, note that the symmetric component of the velocity gradient $\boldsymbol{L}$ is the deformation rate tensor $\boldsymbol{D}$ and the anti-symmetric component is called the spin rate tensor $\boldsymbol{W}$.

$$\boldsymbol{D} \triangleq \frac{1}{2}(\boldsymbol{L}+\boldsymbol{L}^{\boldsymbol{T}}) = \underbrace{\frac{1}{2}(\boldsymbol{L}^{\boldsymbol{e}}+\boldsymbol{L}^{\boldsymbol{eT}})}_{\boldsymbol{D^e}} + \underbrace{\frac{1}{2}(\boldsymbol{F}^{\boldsymbol{e}}\hat{\boldsymbol{L}}^{\boldsymbol{vp}}\boldsymbol{F}^{\boldsymbol{e-1}}+\boldsymbol{F}^{\boldsymbol{e-T}}(\hat{\boldsymbol{L}}^{\boldsymbol{vp}})^{\boldsymbol{T}}\boldsymbol{F}^{\boldsymbol{eT}})}_{\boldsymbol{D^{vp}}} \quad (5.2.16a)$$

$$\boldsymbol{W} \triangleq \frac{1}{2}(\boldsymbol{L}-\boldsymbol{L}^{\boldsymbol{T}}) = \underbrace{\frac{1}{2}(\boldsymbol{L}^{\boldsymbol{e}}-\boldsymbol{L}^{\boldsymbol{eT}})}_{\boldsymbol{W^e}} + \underbrace{\frac{1}{2}(\boldsymbol{F}^{\boldsymbol{e}}\hat{\boldsymbol{L}}^{\boldsymbol{vp}}\boldsymbol{F}^{\boldsymbol{e-1}}-\boldsymbol{F}^{\boldsymbol{e-T}}(\hat{\boldsymbol{L}}^{\boldsymbol{vp}})^{\boldsymbol{T}}\boldsymbol{F}^{\boldsymbol{eT}})}_{\boldsymbol{W^{vp}}} \quad (5.2.16b)$$

We also use Equation 5.2.4 to define the strain rate tensor as,

$$\dot{\boldsymbol{E}} = \frac{1}{2}(\dot{\boldsymbol{F}}^{\boldsymbol{T}}\boldsymbol{F}+\boldsymbol{F}^{\boldsymbol{T}}\dot{\boldsymbol{F}}) = \boldsymbol{F}^{\boldsymbol{vpT}}\underbrace{\frac{1}{2}(\dot{\boldsymbol{F}}^{\boldsymbol{eT}}\boldsymbol{F}^{\boldsymbol{e}}+\boldsymbol{F}^{\boldsymbol{eT}}\dot{\boldsymbol{F}}^{\boldsymbol{e}})}_{\dot{\boldsymbol{E}}^{\boldsymbol{e}}}\boldsymbol{F}^{\boldsymbol{vp}}+ \underbrace{\frac{1}{2}(\dot{\boldsymbol{F}}^{\boldsymbol{vpT}}\boldsymbol{F}^{\boldsymbol{eT}}\boldsymbol{F}^{\boldsymbol{e}}\boldsymbol{F}^{\boldsymbol{vp}}+\boldsymbol{F}^{\boldsymbol{vpT}}\boldsymbol{F}^{\boldsymbol{eT}}\boldsymbol{F}^{\boldsymbol{e}}\dot{\boldsymbol{F}}^{\boldsymbol{vp}})}_{\dot{\boldsymbol{E}}^{vp}} \quad (5.2.17)$$

$\dot{\boldsymbol{E}}^{\boldsymbol{vp}}$ and $\boldsymbol{D}^{\boldsymbol{vp}}$ are the same quantities defined in the material and spatial coordinates respectively.

5.3 Macroscopic balance laws

At both the macroscopic and microscopic levels, the field variables are restricted by balance laws. A summary of the macroscopic balance laws in the spatial frame of reference follows. If ρ is the density of the material, then *the balance of mass* is described by Equation 5.3.1.

$$\dot{\rho} + \rho\boldsymbol{\nabla}\cdot\boldsymbol{v} = 0 \quad (5.3.1)$$

where $\boldsymbol{\nabla} \cdot ()$ is the divergence operator. Macroscopic *linear momentum balance* is given by,

$$\boldsymbol{\nabla} \cdot \boldsymbol{\sigma} + \boldsymbol{b}_o = \rho \dot{\boldsymbol{v}} \tag{5.3.2}$$

where $\boldsymbol{\sigma}$ is the Cauchy stress and $\boldsymbol{b_o}$ is the body force. The body force is usually denoted by $\boldsymbol{b}$. However, some texts use $\boldsymbol{b_o}$ for the non-inertial body forces and $\boldsymbol{b}$ for the body forces along with the acceleration term $\rho \dot{\boldsymbol{v}}$. We use the former convention in this chapter. The balance of angular momentum ensures symmetry of the Cauchy stress tensor since no sources of microscopic moments exist in our problem.

$$\boldsymbol{\sigma} = \boldsymbol{\sigma}^{\boldsymbol{T}} \tag{5.3.3}$$

5.4 Microscopic force balance

The basic premise of the 'microscopic' internal variables $\{\nu\}$ is that, like their macroscopic counterparts, they are driven by microscopic forces internal to the material defined as $\{\pi\} \triangleq \pi^1, \pi^2, \pi^3, \ldots, \pi^{N_s}$. When gradients of these shear rates $\boldsymbol{\nabla}\{\nu\}$ exist in the material, these will be driven by microscopic tractions $\{\boldsymbol{\xi}\} \triangleq \boldsymbol{\xi^1}, \boldsymbol{\xi^2}, \boldsymbol{\xi^3}, \ldots, \boldsymbol{\xi^{N_s}}$ also internal to the material. These internal forces and tractions are constrained to be thermodynamically consistent, as shown in section 5.6 (see Gurtin [18] for details). For now we simply state this constraint which we call the 'microscopic force balance'. The microscopic force balance for a slip system α is,

$$\boldsymbol{\nabla} \cdot \boldsymbol{\xi^\alpha} + \tau^\alpha - \pi^\alpha = 0 \tag{5.4.1}$$

where τ^{α} is the resolved shear stress on the slip plane for the slip system α.

5.5 Balance of energy

Each of the driving forces presented in the previous sections i.e. macroscopic stress $\boldsymbol{\sigma}$, body forces $\boldsymbol{b_o}$, microscopic forces $\{\pi\}$, microscopic tractions $\{\boldsymbol{\xi}\}$ and temperature contribute to the stored energy of the material. This section describes the balance between these stored energies.

For a given domain $\mathcal{P}_t$ in spatial coordinates, the balance of energy in its weak form follows,

$$\int_{\mathcal{P}_t} \overset{\cdot}{\overline{\rho\mathcal{E} + \frac{1}{2}\boldsymbol{v}.\boldsymbol{v}}}\, dv = \int_{\partial\mathcal{P}_t} \boldsymbol{t}\boldsymbol{v}.\boldsymbol{n}\, da + \int_{\mathcal{P}_t} \boldsymbol{b_o}\boldsymbol{v}\, dv - \int_{\partial\mathcal{P}_t} \boldsymbol{q}.\boldsymbol{n}\, da + \int_{\mathcal{P}_t} \rho\mathcal{Q}_s\, dv \tag{5.5.1}$$

where $\mathcal{E}$ is the macroscopic internal energy (per unit mass), $\boldsymbol{t} = \boldsymbol{\sigma}.\boldsymbol{n}$ is the traction on the boundary $\partial\mathcal{P}_t$, $\boldsymbol{b_o}$ is the body force, $\boldsymbol{q}$ is the heat flux and $\mathcal{Q}_s$ is a volumetric heat source. The strong form of Equation 5.5.1 is,

$$\rho\dot{\mathcal{E}} = \boldsymbol{\sigma}.\boldsymbol{D} - \boldsymbol{\nabla}\cdot\boldsymbol{q} + \rho\mathcal{Q}_s \tag{5.5.2}$$

where $(.)$ represents the contraction operation i.e. $\boldsymbol{A}.\boldsymbol{B} = A_{ij}B_{ij}$ (using index notation).

Using Equation 5.2.16a, the internal stress power $\boldsymbol{\sigma}.\boldsymbol{D}$ can be written as,

$$\rho\mathcal{P} = \boldsymbol{\sigma}.\boldsymbol{D} = \underbrace{\boldsymbol{\sigma}.\boldsymbol{D}^{e}}_{\mathcal{W}^{e}} + \underbrace{\boldsymbol{\sigma}.\boldsymbol{D}^{vp}}_{\mathcal{W}^{vp}} \tag{5.5.3}$$

The elastic stress power $\mathcal{W}^e = \boldsymbol{\sigma}.\boldsymbol{D^e}$ is assumed to be purely from the macroscopic stress driving the elastic rate of deformation. Plastic deformation in our model is accommodated by dislocation slip dynamics represented using the shear rates of individual slip systems $\{\nu\}$ and their gradients $\boldsymbol{\nabla}\{\nu\}$ (as described in section 5.4). These internal variables are driven by their conjugate driving forces $\{\pi\}$ and driving tractions $\{\boldsymbol{\xi}\}$ respectively (also defined in section 5.4), forming visco-plastic work conjugate pairs (π^α, ν^α) and $(\boldsymbol{\xi^\alpha}, \boldsymbol{\nabla}\nu^\alpha)$ for each slip system α. The visco-plastic stress power in Equation 5.5.3 is hence $\mathcal{W}^{vp} = \sum_{\alpha=1}^{N_s}(\boldsymbol{\xi^\alpha}.\boldsymbol{\nabla}\nu^\alpha + \pi^\alpha\nu^\alpha)$. We expand out Equation 5.5.3 as,

$$\rho\mathcal{P} = \underbrace{\boldsymbol{\sigma}.\boldsymbol{D^e}}_{\mathcal{W}^e} + \underbrace{\sum_{\alpha=1}^{N_s}(\boldsymbol{\xi^\alpha}.\boldsymbol{\nabla}\nu^\alpha + \pi^\alpha\nu^\alpha)}_{\mathcal{W}^{vp}} \tag{5.5.4}$$

It is useful for forthcoming analyses to establish a relationship between macroscopic elastic stress powers in the lattice and spatial configurations. The conjugate pairs in the lattice and spatial configurations are $(\hat{\boldsymbol{\mathcal{S}}}, \dot{\boldsymbol{E}}^{\boldsymbol{e}})$ and $(\boldsymbol{\sigma}, \boldsymbol{D^e})$ respectively. $\hat{\boldsymbol{\mathcal{S}}}$ is the second Piola-Kirchoff stress defined in the lattice configuration. The second Piola-Kirchoff stress and the Cauchy stress are related as,

$$\boldsymbol{\sigma} = \frac{1}{J^e}\boldsymbol{F^e}\hat{\boldsymbol{\mathcal{S}}}\boldsymbol{F^{eT}} \tag{5.5.5}$$

Using Equation 5.2.16a, Equation 5.2.17 and Equation 5.5.5, the stress powers relate as,

$$\boldsymbol{\sigma}.\boldsymbol{D^e} = \frac{1}{J^e}(\boldsymbol{F^e}\hat{\boldsymbol{\mathcal{S}}}\boldsymbol{F^{eT}}).\boldsymbol{D^e} = \frac{1}{J^e}\hat{\boldsymbol{\mathcal{S}}}.(\boldsymbol{F^{eT}}\boldsymbol{D^e}\boldsymbol{F^e}) = \frac{1}{J^e}\hat{\boldsymbol{\mathcal{S}}}.\dot{\boldsymbol{E}}^{\boldsymbol{e}} \tag{5.5.6}$$

The volume ratio is $J^e = \frac{\rho^s}{\hat{\rho}^l}$ where ρ^s is the density in the deformed configuration

and $\hat{\rho}^l$ is that in the lattice configuration. The internal stress power can be rewritten as,

$$\rho\mathcal{P} = \boldsymbol{\sigma}.\boldsymbol{D} = \boldsymbol{\sigma}.\boldsymbol{D}^{\boldsymbol{e}} + \sum_{\alpha=1}^{N_s}(\boldsymbol{\xi}^{\boldsymbol{\alpha}}.\boldsymbol{\nabla}\nu^\alpha + \pi^\alpha\nu^\alpha) \tag{5.5.7}$$

$$= \frac{1}{J^e}\hat{\boldsymbol{\mathcal{S}}}.\dot{\boldsymbol{E}}^{\boldsymbol{e}} + \sum_{\alpha=1}^{N_s}(\boldsymbol{\xi}^{\boldsymbol{\alpha}}.\boldsymbol{\nabla}\nu^\alpha + \pi^\alpha\nu^\alpha) \tag{5.5.8}$$

We now define the Helmholtz free energy Ψ,

$$\Psi = \mathcal{E} - \mathcal{N}\Theta \tag{5.5.9}$$

where $\mathcal{N}$ is the local entropy density and Θ is the temperature. Using the second law of thermodynamics in the strong form, we have

$$\rho\dot{\mathcal{N}} \geq -\boldsymbol{\nabla}\cdot\left(\frac{\boldsymbol{q}}{\Theta}\right) + \frac{\rho\mathcal{Q}_s}{\Theta} \tag{5.5.10}$$

$\boldsymbol{q}$ and $\mathcal{Q}_s$ are defined in Equation 5.5.1. The volume averaged rate of entropy production is defined as $\mathcal{H}(\mathcal{P}_t) \triangleq \int_{\mathcal{P}_t}\rho\dot{\Gamma}\,dv$, where $\dot{\Gamma}$ is the dissipation rate given by,

$$\rho\dot{\Gamma} \triangleq \rho\dot{\mathcal{N}} + \boldsymbol{\nabla}\cdot\left(\frac{\boldsymbol{q}}{\Theta}\right) - \frac{\rho\mathcal{Q}_s}{\Theta} \geq 0 \tag{5.5.11}$$

After using Equation 5.5.9 in Equation 5.5.11 and applying the I law of thermodynamics (Equation 5.5.10) and the constraint $\Theta \geq 0$ we get

$$\rho\dot{\Psi} - \rho\mathcal{P} + \left(\rho\mathcal{N}\dot{\Theta} + \frac{1}{\Theta}\boldsymbol{q}.\boldsymbol{\nabla}\Theta\right) = -\rho\dot{\Gamma} \leq 0 \tag{5.5.12}$$

Using the definition for stress power in Equation 5.5.8,

$$\rho\dot{\Psi} - \boldsymbol{\sigma}.\boldsymbol{D}^{\boldsymbol{e}} - \sum_{\alpha=1}^{N_s}(\boldsymbol{\xi}^{\boldsymbol{\alpha}}.\boldsymbol{\nabla}\nu^\alpha + \pi^\alpha\nu^\alpha) + \left(\rho\mathcal{N}\dot{\Theta} + \frac{1}{\Theta}\boldsymbol{q}.\boldsymbol{\nabla}\Theta\right) = -\rho\dot{\Gamma} \leq 0 \tag{5.5.13}$$

This relation is central in our analysis of free energy functions for the matrix and twinned regions in section 5.6.

5.6 Constitutive restrictions: The Coleman-Noll procedure

We now aim to establish specific functional forms for the constitutive relations. We discuss thermodynamically imposed restrictions on these constitutive relations through the Coleman-Noll procedure (refer Gurtin et al. [102]).

The current micro-mechanics based framework is based on the internal variable theories of plasticity (refer Gurtin [18], Rice [47], Acharya and Shawki [103]) where microscopic evolution rates are driven by conjugate forces which contribute to the overall stored energy in the matrix or the twinned regions. The rate independent case will be discussed first followed by the rate dependent case (the latter is more applicable to our problem).

Two sets of internal variables are defined; one that represents the rates of plastic deformation at the microscopic length scale and another that is used to describe the resistance to those slip mechanisms. The former is characterized using the shear rates on individual slip systems $\{\nu\}$ from Equation 5.2.7. Note that the slip rate ν^α may be written as $\nu^\alpha = \varrho^\alpha v_m^\alpha$, more commonly called Orowan's equation, where ϱ^α is the dislocation density (Equation 5.2.14) and v_m^α is the average velocity of mobile dislocations on slip system α.

The second set of internal variables defines the resistance to slip on each slip

system:

$$\{g\} \triangleq \{g^1, g^2, \ldots, g^{N_s}\} \tag{5.6.1}$$

The kinetics of slip is described by relating the shear rate on a slip system to the slip resistance on that system.

The choice of including internal variables related to microscopic shearing rates in the theory necessitates the presence of conjugate driving fields i.e. microscopic driving forces (π^α) conjugate to the shear rates (ν^α) and driving tractions ($\boldsymbol{\xi^\alpha}$) conjugate to gradients ($\boldsymbol{\nabla}\nu^\alpha$) in the microscopic shear rates. A distinction between these two driving fields is given here. The driving force π^α is a scalar field, constrained to act along the slip direction of a specific slip system α. The driving traction $\boldsymbol{\xi^\alpha}$ however is a vector field that acts on the slip plane of slip system α. The dot product between $\boldsymbol{\xi^\alpha}$ and $\boldsymbol{\nabla}\nu^\alpha$ (second term on the right hand side of Equation 5.5.4) contributes to the visco-plastic stored energy due to a gradient in the shear rate of slip system α.

5.6.1 Constitutive restrictions: Rate independent

The free energy functions discussed in this section are assumed to be additively decomposed into an elastic free energy $\Psi^e = \tilde{\Psi}^e(\boldsymbol{E^e}, \Theta)$, where Θ is temperature and a defect free energy $\Psi^{vp} = \tilde{\Psi}^{vp}(\boldsymbol{F^{vp}}, \{g\}, \Theta)$. *The inclusion of temperature Θ as an independent variable in the viscoplastic free energy is to account for thermal softening effects if necessary.* This additive decomposition ensures that the macroscopic stresses depend only on the elastic strains and temperature. In other words, the

stress is not *explicitly* dependent on internal variables, which will be shown at the end of this section. These are termed 'separable materials' by Gurtin [18].

Rate independence requires that the constitutive relations are independent of the shear rate on slip systems $\{\nu\}$ (proof given in Gurtin [18]). The constitutive relations are stated in their general form below.

$$\Psi = \tilde{\Psi}^e(\boldsymbol{E^e}, \Theta) + \tilde{\Psi}^{vp}(\boldsymbol{F^{vp}}, \{g\}, \Theta) \tag{5.6.2a}$$

$$\boldsymbol{\sigma} = \tilde{\boldsymbol{\sigma}}(\boldsymbol{E^e}, \boldsymbol{F^{vp}}, \{g\}, \Theta) \tag{5.6.2b}$$

$$\tau^\alpha = \boldsymbol{\sigma} : \boldsymbol{s^\alpha} \otimes \boldsymbol{m^\alpha} = \tilde{\tau}^\alpha(\boldsymbol{E^e}, \boldsymbol{F^{vp}}, \{g\}, \Theta) \tag{5.6.2c}$$

$$\pi^\alpha = \tilde{\pi}^\alpha(\boldsymbol{F^{vp}}, \{g\}, \Theta) \tag{5.6.2d}$$

$$\boldsymbol{\xi}^\alpha = \tilde{\boldsymbol{\xi}}^\alpha(\boldsymbol{F^{vp}}, \{g\}, \Theta) \tag{5.6.2e}$$

$$\dot{\boldsymbol{F}}^{\boldsymbol{vp}} = \sum_{\alpha=1}^{N_s} \nu^\alpha \boldsymbol{M^\alpha} \tag{5.6.2f}$$

Equation 5.6.2a shows the additive decomposition of the free energy density function where Ψ is the specific free energy, $\tilde{\Psi}^e$ is the elastic free energy density function (of the elastic strain $\boldsymbol{E^e}$ and temperature Θ) and $\tilde{\Psi}^{vp}$ is the visco-plastic free energy density functoin or defect energy function (of microscopic internal variables and temperature). Equation 5.6.2b is the constitutive relation for the Cauchy stress $\boldsymbol{\sigma}$. Note that the Cauchy stress is, in general, a function of $\boldsymbol{E^e}$, F^{vp}, $\{g\}$ and Θ. Our additive decomposition of free energy (Equation 5.6.2a) will reduce the number of dependent variables (to be shown later in this section). Equation 5.6.2c describes the resolved shear stress τ^α for a slip system α on the slip plane along the slip direction. The

constitutive relation for the internal micro-force π^α that drives the shear rate ν^α on slip system α is shown in Equation 5.6.2d and that for the microscopic traction $\boldsymbol{\xi^\alpha}$ is given by Equation 5.6.2e. Equation 5.6.2f restates the flow rule.

The defect energy (or visco-plastic free energy) Ψ^{vp} is the stored energy due to microscopic defects in the system. We now impose restrictions on the specific forms of the constitutive equations Equation 5.6.2 using the dissipation inequality and the Coleman-Noll procedure. The dissipation inequality in its strong form in spatial coordinates is presented in Equation 5.5.13 and restated here.

$$\rho\dot{\Psi} - \boldsymbol{\sigma}.\boldsymbol{D^e} - \sum_{\alpha=1}^{N_s}(\boldsymbol{\xi^\alpha}.\boldsymbol{\nabla}\nu^\alpha + \pi^\alpha\nu^\alpha) + \left(\rho\mathcal{N}\dot{\Theta} + \frac{1}{\Theta}\boldsymbol{q}.\boldsymbol{\nabla}\Theta\right) = -\rho\dot{\Gamma} \leq 0 \tag{5.6.3}$$

Γ is the dissipation due to irreversible processes in the continuum.

Gurtin [18] imposed a specific evolution law for Γ with assumptions of isothermal, quasi-static dislocation mediated deformation. Our problem is more complex due to the dynamics of a propagating discontinuity. Moreover, rapid temperature rise is a potential phenomenon given the rates of evolution of twin tips studied experimentally in chapter 4. We will hence refrain from using Gurtin's functional form for the dissipation rate.

The variational derivative of Ψ given Equation 5.6.2a is,

$$\dot{\Psi} = \frac{\partial\Psi^e}{\partial\boldsymbol{E^e}}.\dot{\boldsymbol{E}}^{\boldsymbol{e}} + \left(\frac{\partial\Psi^e}{\partial\Theta} + \frac{\partial\Psi^{vp}}{\partial\Theta}\right).\dot{\Theta} + \frac{\partial\Psi^{vp}}{\partial\boldsymbol{F^{vp}}}.\dot{\boldsymbol{F}}^{\boldsymbol{vp}} + \sum_{\alpha=1}^{N_s}\frac{\partial\Psi^{vp}}{\partial g^\alpha}.\dot{g}^\alpha \tag{5.6.4}$$

To represent the derivative terms in Equation 5.6.4 as conjugates of kinematic variables, we make an assumption on the evolution of the slip resistances $\{g\}$ through an

ordinary differential equation called the 'hardening law'. A specific form of the hardening law was proposed by Kocks [50] primarily for cubic metals which is currently being used by crystal plasticity codes (e.g. Zhang and Joshi [2]) for hcp metals as well:

$$\dot{g}^{\alpha} = \sum_{\beta} h^{\alpha\beta}(\bar{\gamma}, \Theta)\nu^{\beta} sgn(\nu^{\beta});\ \bar{\gamma} = \sum_{\alpha=1}^{N_s} \int_0^t \nu^{\alpha}\, dt' \tag{5.6.5}$$

where $h^{\alpha\beta}$ is a hardening coefficient that represents self-hardening when $\alpha = \beta$ and cross-hardening otherwise. Self-hardening and cross-hardening were discussed phenomenologically in chapter 2 (section 2.5). Dislocation evolution is invariant to the positive or negative directions of applied shear. The signum function ensures that this phenomenon of dislocation slip is captured.

We now use the variational derivative (Equation 5.6.4), flow (Equation 5.6.2f) and hardening (Equation 5.6.5) rules in Equation 5.6.3.

$$\begin{aligned}\left[\frac{\partial \Psi^e}{\partial \boldsymbol{E^e}} - \frac{1}{J^e}\hat{\boldsymbol{S}}\right].\dot{\boldsymbol{E}}^{\boldsymbol{e}} + \left[\frac{\partial \Psi^e}{\partial \Theta} + \frac{\partial \Psi^{vp}}{\partial \Theta} + \mathcal{N}\right]\dot{\Theta} \\ + \sum_{\alpha=1}^{N_s}\left[\frac{\partial \Psi^{vp}}{\partial \boldsymbol{F^{vp}}}.\boldsymbol{M^{\alpha}} + \left(\sum_{\beta=1}^{N_s}\frac{\partial \Psi^{vp}}{\partial g^{\beta}}h^{\beta\alpha}\right)sgn(\nu^{\alpha}) - \pi^{\alpha}\right]\nu^{\alpha} \\ - \sum_{\alpha=1}^{N_s}\boldsymbol{\xi}^{\alpha}.\boldsymbol{\nabla}\nu^{\alpha} + \left[\frac{1}{\Theta}\boldsymbol{\nabla}\Theta.\boldsymbol{q}\right] \leq 0\end{aligned} \tag{5.6.6}$$

According to the Coleman-Noll procedure, the dissipation inequality must hold for any arbitrary values of $\dot{\boldsymbol{E}}^{\boldsymbol{e}}$, ν^{α}, $\boldsymbol{\nabla}\nu^{\alpha}$, $\dot{\Theta}$ and $\boldsymbol{\nabla}\Theta$. This imposes restrictions on the coefficients of $\dot{\boldsymbol{E}}^{\boldsymbol{e}}$, ν^{α}, $\boldsymbol{\nabla}\nu^{\alpha}$, $\dot{\Theta}$ in Equation 5.6.6 leaving the heat conduction inequality

to be satisfied. These restrictions are stated below.

$$\hat{\boldsymbol{S}} = J^e \frac{\partial \Psi^e}{\partial \boldsymbol{E^e}} \tag{5.6.7a}$$

$$(\pi^\alpha)^\pm = \frac{\partial \Psi^{vp}}{\partial \boldsymbol{F^{vp}}}.\boldsymbol{M^\alpha} \pm \left(\sum_{\beta=1}^{N_s} \frac{\partial \Psi^{vp}}{\partial g^\beta} h^{\beta\alpha} \right) \tag{5.6.7b}$$

$$\boldsymbol{\xi^\alpha} = 0 \tag{5.6.7c}$$

$$\mathcal{N} = -\frac{\partial \Psi^e}{\partial \Theta} - \frac{\partial \Psi^{vp}}{\partial \Theta} \tag{5.6.7d}$$

$$\boldsymbol{q}.\boldsymbol{\nabla}\Theta \leq 0 \tag{5.6.7e}$$

Setting the coefficient of $\dot{\boldsymbol{E}}^{\boldsymbol{e}}$ (in Equation 5.6.6) to 0 results in Equation 5.6.7a. This relation defines the macroscopic stress-strain relationship. Note that the macroscopic stress is an explicit function of $\boldsymbol{E^e}$ and Θ only, unlike the general form in Equation 5.6.2b. Equation 5.6.7b is obtained by setting the coefficient of ν^α (in Equation 5.6.6) to 0. This relates the microscopic forces $\{\pi\}$ to the viscoplastic stored energy (and hence the internal variables characterizing plastic flow). In our case, we assume that no viscoplastic strain gradients exist. Hence no micro-tractions exist. This is automatically satisfied by setting the coefficients of $\boldsymbol{\nabla}\nu^\alpha$ to 0 (Equation 5.6.7c). Equation 5.6.7d is the thermodynamic definition for entropy and Equation 5.6.7e states that the direction of heat flow is opposite to the direction of the temperature gradient. The dot product in Equation 5.6.7e is simply the negative of the thermal conductivity in the material. An important relation between the resolved shear stress and the microscopic forces on a slip system α is obtained by combining Equation 5.6.7b and Equation 5.6.7c with the microscopic force balance

Equation 5.4.1.

$$\tau^{\alpha} = (\pi^{\alpha})^{\pm} = \frac{\partial \Psi^{vp}}{\partial \boldsymbol{F^{vp}}}.\boldsymbol{M^{\alpha}} \pm \left(\sum_{\beta=1}^{N_s} \frac{\partial \Psi^{vp}}{\partial g^{\beta}} h^{\beta\alpha} \right) \tag{5.6.8}$$

This is the yield criterion for rate independent plasticity. It says that a material will yield when the resolved shear stress on a specific slip system reached a critical value. A description of yield in the context of the current framework is presented briefly. The yield stress is often described in textbooks as the point at which macroscopic plasticity begins on a stress-strain curve. We refer to this point as 'initial yield'. Beyond this initial yield point, the stresses are referred to as 'flow stresses'. Experimental evidence has indicated that during unloading at a specific flow stress (or plastic strain), most metallic materials follow a linear elastic unloading response. Upon reloading the material (at the same strain rate), the material follows the same linear elastic response until it reaches the previously achieved flow stress. In this context, this is a yield stress of the plastically worked material. Equation 5.6.8 captures the yield stress at all plastic strains and not just the initial yield.

5.6.2 Constitutive restrictions: Rate dependent

Gurtin [18] shows that for the constitutive equations to be rate independent, Equation 5.6.2a-Equation 5.6.2e must be homogeneous in ν of zeroth order and the hardening rule Equation 5.6.5 must be of first order. In the case of rate dependence, the

constitutive equations are modified to take the more general form,

$$\Psi = \tilde{\Psi}^{e}(\boldsymbol{E^e}, \Theta) + \tilde{\Psi}^{vp}(\boldsymbol{F^{vp}}, \{g\}, \{\nu\}, \Theta) \tag{5.6.9a}$$

$$\boldsymbol{\sigma} = \tilde{\boldsymbol{\sigma}}(\boldsymbol{E^e}, \boldsymbol{F^{vp}}, \{g\}, \{\nu\}, \Theta) \tag{5.6.9b}$$

$$\tau^{\alpha} = \boldsymbol{\sigma} : \boldsymbol{s^{\alpha}} \otimes \boldsymbol{m^{\alpha}} = \tilde{\tau}^{\alpha}(\boldsymbol{E^e}, \boldsymbol{F^{vp}}, \{g\}, \{\nu\}, \Theta) \tag{5.6.9c}$$

$$\pi^{\alpha} = \tilde{\pi}^{\alpha}(\boldsymbol{F^{vp}}, \{g\}, \{\nu\}, \Theta) \tag{5.6.9d}$$

$$\xi^{\alpha} = \tilde{\xi}^{\alpha}(\boldsymbol{F^{vp}}, \{g\}, \{\nu\}, \Theta) \tag{5.6.9e}$$

$$\dot{\boldsymbol{F}}^{\boldsymbol{vp}} = \sum_{\alpha=1}^{N_s} \nu^{\alpha} \boldsymbol{M^{\alpha}} \tag{5.6.9f}$$

The hardening law in this case is assumed to be,

$$\dot{g}^{\alpha} = \sum_{\beta} \tilde{h}^{\alpha\beta}(\bar{\gamma}, \nu^{\beta}) \nu^{\beta} sgn(\nu^{\beta}) \tag{5.6.10}$$

The hardening coefficient in Equation 5.6.10 has also been modified to include the effects of strain rate. The same procedure is followed as in the previous case (in subsection 5.6.1) resulting in the dissipation inequality,

$$\left[\frac{\partial \Psi^{e}}{\partial \boldsymbol{E^e}} - \boldsymbol{S}\right] . \dot{\boldsymbol{E}}^{\boldsymbol{e}} + \left[\frac{\partial \Psi}{\partial \Theta} + \mathcal{N}\right] \dot{\Theta} + \sum_{\alpha=1}^{N_s} \left[\frac{\partial \Psi^{vp}}{\partial \boldsymbol{F^{vp}}} . \boldsymbol{M^{\alpha}} + \left(\sum_{\beta=1}^{N_s} \frac{\partial \Psi^{vp}}{\partial g^{\beta}} h^{\beta\alpha}\right) sgn(\nu^{\alpha}) - \pi^{\alpha}\right] \nu^{\alpha}$$
$$- \sum_{\alpha=1}^{N_s} \boldsymbol{\xi}^{\alpha} . \boldsymbol{\nabla} \nu^{\alpha} + \sum_{\alpha=1}^{N_s} \frac{\partial \Psi^{vp}}{\partial \nu^{\alpha}} \dot{\nu}^{\alpha} + \frac{1}{\Theta} \boldsymbol{\nabla} \Theta . \boldsymbol{q} \leq 0 \tag{5.6.11}$$

This results in constitutive restrictions similar to Equation 5.6.7 with an additional condition,

$$\frac{\partial \Psi^{vp}}{\partial \nu^{\alpha}} = 0 \tag{5.6.12}$$

Thus, consistency with the thermodynamics restricts the defect energy to remain explicitly independent of the shear rate on each slip system so that $\tilde{\Psi}^{vp}$ is *not* a

function of $\{\nu\}$. Hence the rate dependence in this simple case comes only from the prescribed rate dependent strengths of the slip system (Equation 5.6.10) which are incorporated into the formulation implicitly using a kinetic relation for dislocation slip given by,

$$\nu^{\alpha} = \tilde{\nu}^{\alpha}(\tau^{\alpha}) \tag{5.6.13}$$

The equivalent of the 'yield criterion' (Equation 5.6.8) for rate dependent cases also has a similar form.

$$\tau^{\alpha} = (\pi^{\alpha})^{\pm} = \frac{\partial \Psi^{vp}}{\partial \boldsymbol{F^{vp}}}.\boldsymbol{M^{\alpha}} \pm \left(\sum_{\beta=1}^{N_s} \frac{\partial \Psi^{vp}}{\partial g^{\beta}} h^{\beta\alpha} \right) \tag{5.6.14}$$

In this case however, this is not a 'yield criterion' but a flow surface (Asaro and Needleman [104]). The "yield" in this case depends implicitly on the shear rates on each slip system (as Ψ^{vp} is an implicit function of $\{\nu\}$), which in turn depend on the shear stresses on the specific slip systems in question (according to Equation 5.6.13).

5.7 Free energy functions for the matrix and twinned regions

We now define specific free energy density functions that are relevant to our problem. The thermodynamic restrictions described above are applied to these free energy density functions and results demonstrated for simple single slip conditions.

5.7.1 Linear elastic free energy density

We start first with the elastic free energy Ψ^e. We assume a linear elastic free energy of the form,

$$\Psi^e = \frac{1}{2}(\mathbb{C} : \boldsymbol{E^e}) : \boldsymbol{E^e} + \boldsymbol{\beta}(\Theta - \Theta_o).\boldsymbol{E^e} \tag{5.7.1}$$

where $\mathbb{C}$ is the fourth order elasticity tensor, and $\boldsymbol{\beta}$ is a second-order tensor containing the thermoelastic moduli. Hexagonal close packed single crystals generally have five independent elastic constants (based on crystal symmetry). However, elasticity in magnesium is nearly isotropic (refer chapter 3 in Bower [105]) and hence Equation 5.7.1 can be simplified to the case of isotropic linear elasticity. The thermal expansion coefficient can also be assumed to be isotropic and hence Equation 5.7.1 simplifies to,

$$\Psi^e = \frac{1}{2}(\tilde{\mathbb{C}} : \boldsymbol{E^e}) : \boldsymbol{E^e} + \beta(\Theta - \Theta_o)\boldsymbol{\mathcal{I}} : \boldsymbol{E^e} \tag{5.7.2}$$

where the new elastic tensor $\tilde{\mathbb{C}}$ has only two independent elastic constants.

5.7.2 Visco-plastic free energy density

Similar ad-hoc assumptions for visco-plastic free energy densities (or defect energies) Ψ^{vp} are non-trivial because the physics governing inelastic deformations, especially in anisotropic hcp metals, are much more complex. This is where the Coleman-Noll procedure helps make choices. Traditional dislocation-based crystal plasticity models use a hardening relation (Equation 5.6.10) that governs the strength of slip systems.

The hardening relation is restated here.

$$\dot{g}^{\alpha} = \sum_{\beta} \tilde{h}^{\alpha\beta}(\bar{\gamma}, \nu^{\beta})\nu^{\beta} sgn(\nu^{\beta})$$

Consistency conditions for rate-independent plasticity dictate that the resolved shear stress on a slip system α is equal to its instantaneous strength, g^{α}.

Using a simple example case for single slip i.e. only one slip system α is active, we get,

$$\tau^{\alpha} = g^{\alpha} = g_o^{\alpha} + h^{\alpha\alpha}\bar{\gamma}^{\alpha} \tag{5.7.3}$$

where g_o^{α} is an initial condition for the hardening relation (in this case the CRSS for slip system α), and $\bar{\gamma}^{\alpha}$ is the accumulated shear strain on slip system α. For this simple case we make the assumption of linear hardening such that the hardening coefficient $h^{\alpha\alpha}$ is a constant. We use these phenomenological relations to guess at a general form for the defect energy Ψ^{vp} which incorporates the effects of initial yield, hardening and strain rate sensitivity.

More generally, the defect energy Ψ^{vp} physically describes the instantaneous stored energy in the material due to the existence of defects. In our case, the defects are dislocations and we consider the stored energy to come from two effects 1. hardening due to lattice resistance to the propagation of a dislocation (self-hardening); 2. hardening due to interactions with other dislocation systems (cross-hardening). The defect energy is assumed to take the form,

$$\Psi^{vp} = \underbrace{\sum_{i=1}^{N_s} g_o^i \gamma^i}_{\text{initial lattice resistance}} + \underbrace{\sum_{i=1}^{N_s} \frac{1}{2}\tilde{h}^{ii}\gamma^{i2}}_{\text{self-hardening}} + \underbrace{\sum_{0<i<j<N_s; i\neq j} \frac{1}{2}\tilde{h}^{ij}\gamma^i\gamma^j}_{\text{cross-hardening}} \tag{5.7.4}$$

where $\gamma^i = \int_0^t \nu^i \, dt'$ is the accumulated shear strain on each slip system i and g_o^i is the strength of slip system i.

Note that this is different from the dissipated energy proposed by Gurtin [18]. In our formulation, the net visco-plastic work rate, $\mathcal{W}^{vp}$ is given by Equation 5.5.3. A part of this work contributes towards rearrangement of defects in the material (changing stored defect energy, Ψ^{vp}) and the remaining is dissipated as heat (Γ_Θ). This can be mathematically represented simply as,

$$\mathcal{W}^{vp} = \Gamma_\Theta + \dot{\Psi}^{vp} \tag{5.7.5}$$

The ratio of dissipated heat (Γ_Θ) to the net plastic work ($\mathcal{W}^{vp}$) is called the Taylor-Quinney factor, often used in literature (Rosakis et al. [106]).

In terms of the visco-plastic deformation gradient $\boldsymbol{F^{vp}}$, the defect energy (Equation 5.7.4) can be rewritten as,

$$\Psi^{vp} = \underbrace{\sum_{i=1}^{N_s} g_o^i (\boldsymbol{F^{vp}}.\boldsymbol{M^i})}_{\text{initial lattice resistance}} + \underbrace{\sum_{i=1}^{N_s} \frac{1}{2}\tilde{h}^{ii} (\boldsymbol{F^{vp}}.\boldsymbol{M^i})^2}_{\text{self-hardening}} + \underbrace{\sum_{0<i<j<N_s; i\neq j} \frac{1}{2}\tilde{h}^{ij} (\boldsymbol{F^{vp}}.\boldsymbol{M^i})(\boldsymbol{F^{vp}}.\boldsymbol{M^j})}_{\text{cross-hardening}} \tag{5.7.6}$$

Hence,

$$\frac{\partial \Psi^{vp}}{\partial \boldsymbol{F^{vp}}} = \sum_{i=1}^{N_s} g_o^i \boldsymbol{M^i} + \sum_{i=1}^{N_s} \tilde{h}^{ii} (\boldsymbol{F^{vp}}.\boldsymbol{M^i}) \boldsymbol{M^i} + \sum_{0<i<j<N_s; i\neq j} \frac{1}{2}\tilde{h}^{ij} (\boldsymbol{M^i}(\boldsymbol{F^{vp}}.\boldsymbol{M^j}) + (\boldsymbol{F^{vp}}.\boldsymbol{M^i})\boldsymbol{M^j}) \tag{5.7.7}$$

Using this in Equation 5.6.14 we get the flow criterion,

$$\tau^\alpha = \pi^\alpha = \sum_{i=1}^{N_s} g_o^i \boldsymbol{M^i.M^\alpha} + \sum_{i=1}^{N_s} \tilde{h}^{ii}\gamma^i \boldsymbol{M^i.M^\alpha} + \sum_{0<i<j<N_s; i\neq j} \frac{1}{2}\tilde{h}^{ij}(\gamma^j \boldsymbol{M^i.M^\alpha} + \gamma^i \boldsymbol{M^j.M^\alpha}) \quad (5.7.8)$$

where

$$\boldsymbol{M^i.M^\alpha} \begin{cases} = 1 & \text{if } i = \alpha \\ < 1 & \text{if } i \neq \alpha \end{cases} \quad (5.7.9)$$

A consequence of Equation 5.7.9 is the existence of additional non-zero terms (for $i \neq \alpha$) in Equation 5.7.8. Physically, this means that the resolved shear stress on a specific slip system α drives not just the dislocations on that slip system but also contributes to the shear rates on other slip systems that are not orthogonal to α (albeit to a lesser extent). This may result in non-Schmid effects. However, a detailed experimental study of non-Schmid effects in magnesium will be needed to identify the importance of these terms in the theory.

Considering again the case of a single slip system, from Equation 5.7.8 we recover,

$$\tau = \pi = g_o + \tilde{h}\gamma \quad (5.7.10)$$

which is the same expression as in our previously illustrated single slip example Equation 5.7.3. While our usage of defect energy might seem as ad-hoc as the hardening relation (Equation 5.6.10), the Coleman-Noll procedure does impose restrictions on the usage of Ψ^{vp}.

5.7.3 Implementation of strain rate dependence: Homogeneous single slip test case

We now demonstrate the implementation of rate dependence in the defect energies described in subsection 5.7.2. As previously mentioned, the basic premise of rate dependence is the shear rate on a slip system is a function of stress. The most common functional form for this relation (Peirce et al. [107]) is a power law relation.

We demonstrate the implementation of the power law rate dependence using a two dimensional isothermal single slip example. A schematic is shown in Figure 5.4 where slip is allowed to occur on only one dislocation system with slip direction $\boldsymbol{s}$ and slip plane normal $\boldsymbol{m}$. Assume an applied shear strain κ in the direction of $\boldsymbol{s}$. We assume homogeneous slip with linear hardening in this domain. In the larger context of our problem, this region may be thought of as a subset of the matrix/twinned region in Figure 5.2. The applied deformation is defined by the total deformation gradient,

$$\boldsymbol{F} = \boldsymbol{\mathcal{I}} + \kappa(\boldsymbol{s} \otimes \boldsymbol{m}) \tag{5.7.11}$$

Using the visco-plastic flow rule Equation 5.2.10 and unit boundary conditions (i.e. $\boldsymbol{F_o^{vp}} = \boldsymbol{\mathcal{I}}$), we solve for the visco-plastic deformation gradient.

$$\boldsymbol{F^{vp}}(t) = \boldsymbol{\mathcal{I}} + \bar{\gamma}(t)\boldsymbol{M} \tag{5.7.12}$$

where the $\bar{\gamma} = \int_0^t \nu dt$ is the accumulated shear strain (derived from the internal variable ν) and $\boldsymbol{M} = \boldsymbol{s} \otimes \tilde{\boldsymbol{m}}$. Equation 5.2.3 allows us to calculate the elastic

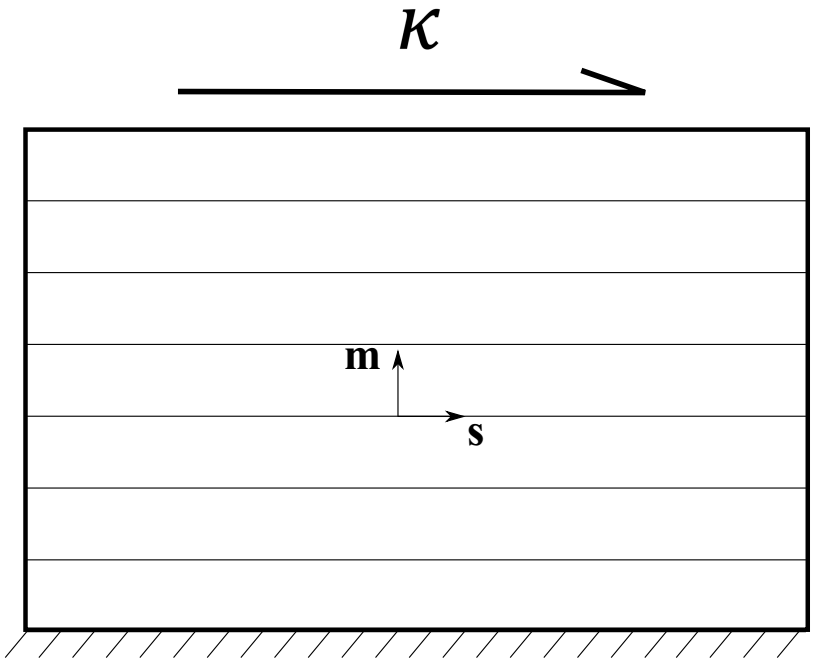

Figure 5.4: A schematic of the single slip example

deformation gradient $\boldsymbol{F^e}$.

$$\boldsymbol{F^e} = \boldsymbol{\mathcal{I}} + (\kappa - \bar{\gamma})\boldsymbol{M} \tag{5.7.13}$$

From Equation 5.6.7a for the stress derived by the Coleman-Noll procedure and the elastic free energy Equation 5.7.2,

$$\boldsymbol{S} = \mathbb{C} : \boldsymbol{E^e} = \mathbb{C} : \boldsymbol{F^{vp-T}}(\boldsymbol{E} - \boldsymbol{E^{vp}})\boldsymbol{F^{vp-1}} \tag{5.7.14}$$

To completely solve for the stress-strain response, we need the evolution of plastic strain $\bar{\gamma}$. This is provided by combining Equation 5.6.7b with the microscopic force balance (Equation 5.4.1) resulting in the flow criterion Equation 5.7.8. Hence,

$$\boldsymbol{\sigma.M} = \tau(\nu) = \pi = g_o + \tilde{h}\bar{\gamma} \tag{5.7.15}$$

For this specific example, our linear hardening assumption implies that $\tilde{h}$ is not a function of $\bar{\gamma}$. Three cases of power law rate dependence are demonstrated here.

1. Initial yield g_o is strain rate dependent

   The relation between initial yield and shear rate follows a power law,

   $$\tilde{g}_o(\nu) = g_o \left| \frac{\nu}{\nu_o} \right|^m \tag{5.7.16}$$

   where g_o is the initial yield at some critical strain rate ν_o and m is a scalar strain rate hardening exponent. Using this expression in the flow criterion (Equation 5.7.15),

   $$\tau = g_o \left| \frac{\nu}{\nu_o} \right|^m + \tilde{h}\bar{\gamma} \tag{5.7.17}$$

   Resolving the 3-D tensorial relation Equation 5.7.14 on the slip plane $\boldsymbol{m}$, along the slip direction $\boldsymbol{s}$ yields the following closed-form simple expression for shear stress as a function of shear strain.

   $$\tau = \mu(\kappa - \bar{\gamma}) = \mu\kappa - \frac{\mu}{h}\left(\tau - g_o\left(\frac{\nu}{\nu_o}\right)^m\right)\mathcal{H}_{\tau - g_o(\nu/\nu_o)^m} \tag{5.7.18}$$

   where $\mathcal{H}$ is the heaviside step function.

   The resulting shear stress-shear strain and shear stress-shear strain rate plots are shown in Figure 5.5. A set of arbitrary parameters were chosen (mentioned in the caption of Figure 5.5). Figure 5.5a shows the shear stress-shear strain plots at specific shear strain rates ν. The initial yield increases with strain rate while the hardening slope remains a constant. This is reflected in Figure 5.5b, where

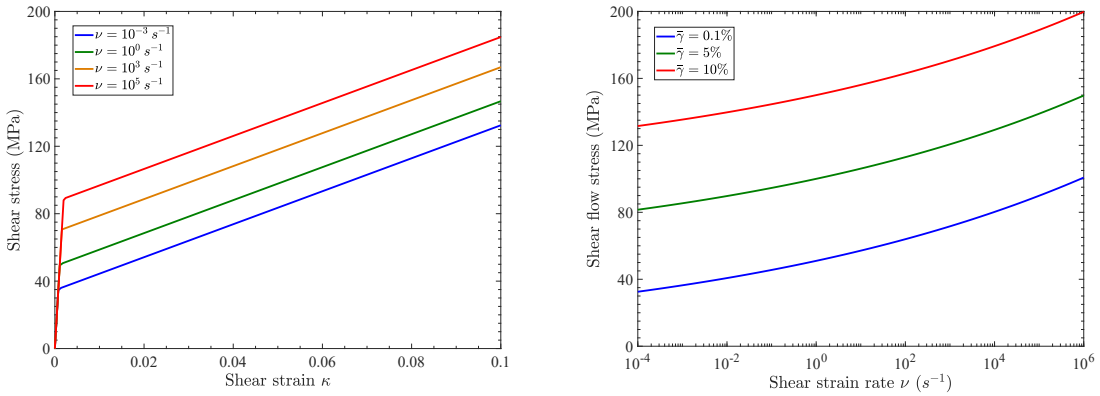

(a) Shear stress Vs shear strain **(b)** Shear stress Vs shear strain rate

Figure 5.5: Rate dependent initial yield stress: Parameters: $m = 0.05$, $g_o = 50$, $h = 1000$, $\mu = 45000$, $\nu_o = 1$

the shear stress is plotted as a function of shear strain rate at three different accumulated plastic strains $\bar{\gamma}$. While the absolute values of flow stresses are different, the increase in flow stress with strain rate is similar at all plastic strains.

2. Hardening is strain rate dependent

   For this case, the hardening coefficient $\tilde{h}$ is a function of microscopic shear rate ν and follows a similar power law relation,

$$\tilde{h} = h\left|\frac{\nu}{\nu_o}\right|^{m_h} \tag{5.7.19}$$

   where the exponent m_h represents the strain rate sensitivity of hardening. Using this relation in Equation 5.7.15,

$$\tau = g_o + h\bar{\gamma}\left|\frac{\nu}{\nu_o}\right|^{m_h} \tag{5.7.20}$$

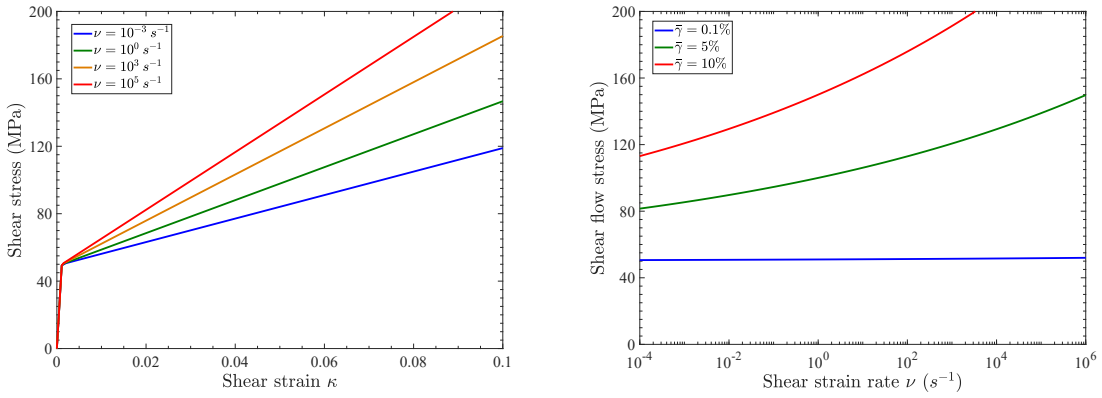

(a) Shear stress Vs shear strain

(b) Shear stress Vs shear strain rate

Figure 5.6: Rate dependent hardening: Parameters: $m_h = 0.05$, $g_o = 50$, $h = 1000$, $\mu = 45000$, $\nu_o = 1$

Equation 5.7.14 results in the closed form expression,

$$\tau = \mu(\kappa - \bar{\gamma}) = \mu\kappa - \mu\left(\frac{\tau - g_o}{h(\nu/\nu_o)^{m_h}}\right)\mathcal{H}_{\tau - g_o} \tag{5.7.21}$$

The results are shown in Figure 5.6. The initial yield stress remains the same across all strain rates (Figure 5.6a), while the slope increases with strain rate. The same is reflected in Figure 5.6b, where the increase in flow stress with strain rate is different (higher) at higher plastic strains.

3. Flow stress is strain rate dependent

   In this case we impose the power law rate hardening relation,

$$\tau = \tilde{g} = g\left|\frac{\nu}{\nu_o}\right|^m \tag{5.7.22}$$

where both the initial yield and hardening are rate sensitive with the same rate

sensitivity exponent m. The resolved shear stress is now,

$$\tau = (g_o + h\bar{\gamma})\left|\frac{\nu}{\nu_o}\right|^m \tag{5.7.23}$$

Finally the closed form expression of stress is,

$$\tau = \mu(\kappa - \bar{\gamma}) = \mu\kappa - \frac{\mu}{h}\left(\frac{\tau}{(\nu/\nu_o)^m} - g_o\right)\mathcal{H}_{\tau - g_o(\nu/\nu_o)^m} \tag{5.7.24}$$

The corresponding material response is shown in Figure 5.7.

Note that both the initial yield and the hardening increase with strain rate as is evident from both the stress-strain plots (Figure 5.7a) and the flow stress-strain rate plots (Figure 5.7b). The phenomena discussed in these figures are a combination of the previous two cases and is hence more general. Our experimental results in chapter 2 indicated that hardening was a stronger function of

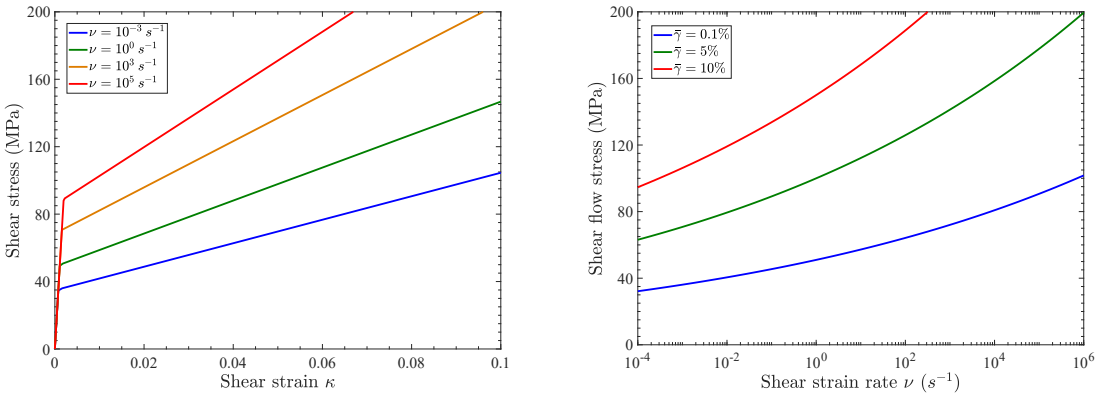

(a) Shear stress Vs shear strain

(b) Shear stress Vs shear strain rate

Figure 5.7: Rate dependent flow stress: Parameters: $m = 0.05$, $g_o = 50$, $h = 1000$, $\mu = 45000$, $\nu_o = 1$

strain rate than initial yield. It should however be noted that the current examples discussed are for single slip cases in single crystals while the experiments involved interactions between slip systems in textured polycrystals. These complex interactions between different dislocation slip systems will affect the rate sensitivity of macroscopic stresses. The current formulation allows us to account for these interactions theoretically as well.

5.7.4 Choice of hardening relations

In the test cases discussed in subsection 5.7.3, we assumed linear hardening i.e. the hardening coefficient $h^{\alpha\beta}$ is independent of accumulated shear. Although experimental evidence in chapter 2 indicated that some parts of the true stress-plastic strain curves were indeed linear, this is not true throughout the stress-strain response. Other studies (for e.g. Dixit et al. [22], Zhao et al. [61], Xie et al. [108]) have also shown that the hardening is not perfectly linear.

A hyperbolic hardening function from Peirce et al. [107] is one common functional form implemented in a crystal plasticity code by Zhang and Joshi [2].

$$h^{\alpha\beta}(\bar{\gamma}) = q^{\alpha\beta} h_o \operatorname{sech}^2 \left| \frac{h_o^{\alpha} \bar{\gamma}}{\tau_s^{\alpha} - \tau_o^{\alpha}} \right| \tag{5.7.25}$$

where $q^{\alpha\beta}$ takes the value of 1 if $\alpha = \beta$, and 2 for all other values. However, this function has not been parameterized for rate sensitivity as yet.

An alternate formulation implemented by Chang and Kochmann [48] uses an exponential self-hardening function and constant latent hardening ($\boldsymbol{H}$) incorporated

into the defect energy.

$$\Psi^{vp} = \sum_{\alpha=1}^{N_s} \sigma_\alpha^\infty \left[\boldsymbol{F^{vp}}.\boldsymbol{M^\alpha} + \frac{\sigma_\alpha^\infty}{h^\alpha} \exp\left\{ \left(- \frac{h_\alpha \boldsymbol{F^{vp}}.\boldsymbol{M^\alpha}}{\sigma_\alpha^\infty} \right) \right\} \right] + \frac{1}{2} \boldsymbol{F^{vp}} \boldsymbol{H} \boldsymbol{F^{vp}} \tag{5.7.26a}$$

$$\Psi^{vp*} = \sum_{\alpha=1}^{N_s} \frac{g_o^\alpha \nu_o^\alpha}{m+1} \left(\frac{\nu^\alpha}{\nu_o^\alpha} \right)^{m+1} \tag{5.7.26b}$$

Chang and Kochmann [48] used Equation 5.7.26b, a 'dissipation potential' (originally from Ortiz and Stainier [63]), to incorporate rate effects. The derivative of this flow potential with ν^α results in its conjugate driving stress (which also the strength of the slip system).

$$g^\alpha = \frac{\partial \Psi^{vp*}}{\partial \nu^\alpha} = g_o^\alpha \left| \frac{\nu^\alpha}{\nu_o^\alpha} \right|^m \tag{5.7.27}$$

The form of rate sensitivity is similar to our previously defined forms in subsection 5.7.3. However, this specific form makes only the intial yield rate sensitive and not the hardening. Incorporating the rate dependence of hardening will help improve predictive capabilities of these models, especially at high strain rates.

All of the aforementioned functional forms for hardening have been parameterized by the corresponding authors for magnesium and may be employed in our problem (but need to be modified for rate effects).

5.8 Jump conditions

The above sections impose restrictions on the kinematics, dynamics and energetics of the continuous regions of the matrix and twinned regions independently. We

next derive the corresponding compatibility conditions across the discontinuous twin boundary. These are more commonly known as 'jump conditions' and have been used in the theories of phase transformations (Abeyaratne and Knowles [109]), shock waves (Gurtin et al. [110]) and even elastic twinning in BCC metals (Rosakis and Tsai [17]). These jump conditions establish boundary conditions at the interface.

Consider again the schematic of a twin in a matrix (Figure 5.2). Figure 5.8 is a two dimensional cut section that shows the matrix ($\mathcal{R}$) and the twinned region (T). The twin boundary which is a surface defect in the material (Figure 5.2) is represented as a line defect in two dimensions (denoted by Π). Note that the shape of the twin boundary is arbitrary. At any position on the boundary, $\boldsymbol{n}$ is the normal to the twin boundary and $\boldsymbol{\vartheta}$ is the tangent. Although these are represented on a 2-D cross-section, the twin boundary is a surface defect in three-dimensional space and

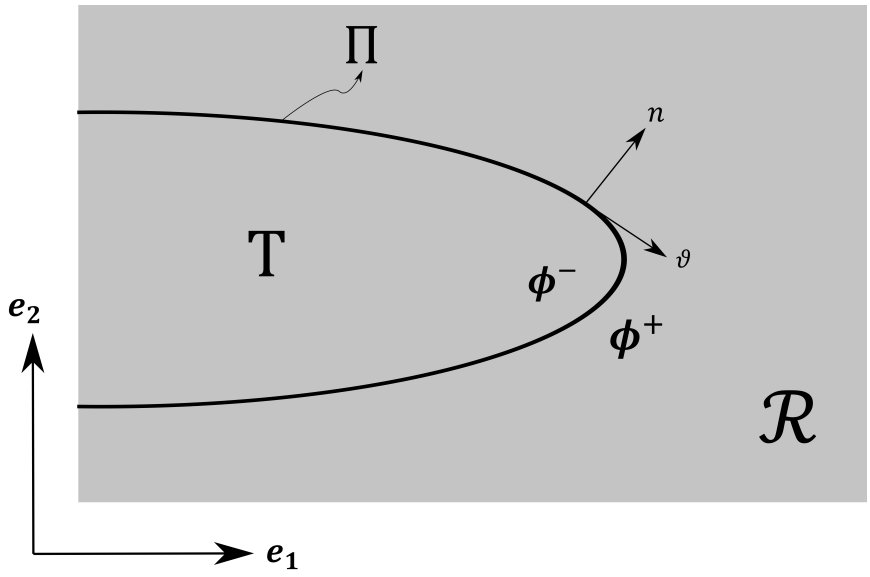

Figure 5.8: Two dimensional cut section of the 3-D schematic in Figure 5.1.

hence the normals and tangents may be pointing out of the plane of the paper.

Any field variable $\boldsymbol{\phi}$ close to the discontinuity is denoted by $\boldsymbol{\phi}^+$ in the matrix region and $\boldsymbol{\phi}^-$ in the twinned region. This is mathematically defined as,

$$\boldsymbol{\phi}^+(\boldsymbol{x},t) = \lim_{\delta\to 0} \boldsymbol{\phi}(\boldsymbol{x} + \delta\boldsymbol{n}(\boldsymbol{x},t),t)$$

$$\boldsymbol{\phi}^-(\boldsymbol{x},t) = \lim_{\delta\to 0} \boldsymbol{\phi}(\boldsymbol{x} - \delta\boldsymbol{n}(\boldsymbol{x},t),t)$$

where $\boldsymbol{n}$ is the normal to the discontinuity in the spatial configuration. The jump in the field variable across the interface is defined as,

$$[\![\boldsymbol{\phi}]\!] \triangleq \boldsymbol{\phi}^+ - \boldsymbol{\phi}^- \tag{5.8.2}$$

5.8.1 Compatibility conditions

Two kinematic constraints are imposed at the interface. These are more commonly known as Hadamard compatibility conditions (refer Gurtin et al. [102]). If $V(\boldsymbol{x},t)$ is the velocity of the interface along its local normal $\boldsymbol{n}(\boldsymbol{x},t)$ and $\boldsymbol{v}(\boldsymbol{x},t)$ is the particle velocity around the twin boudary (all in spatial coodinates) then,

$$[\![\boldsymbol{v}(\boldsymbol{x},t)]\!] + [\![(V(\boldsymbol{x},t) - \boldsymbol{n}(\boldsymbol{x},t).\boldsymbol{v}(\boldsymbol{x},t))\boldsymbol{F}(\boldsymbol{x},t)]\!].\boldsymbol{n}(\boldsymbol{x},t) = 0 \tag{5.8.3}$$

establishes compatibility of the particle velocities normal to the interface i.e. the rate of jump in directional gradients normal to the interface ($\boldsymbol{F.n}$) is equal to the jump in particle velocities ($\boldsymbol{v}$) across the interface.

The second constraint states that the gradient must be smooth along the tangent

to the discontinuity.

$$[\![\boldsymbol{F}(\boldsymbol{x},t)]\!].\boldsymbol{\vartheta}(\boldsymbol{x},t)=0 \tag{5.8.4}$$

where $\boldsymbol{\vartheta}$ is the tangent to the interface.

5.8.2 Some useful rules to derive jump conditions across an interface

If the current deformed configuration of the continuum is denoted by $\mathcal{P}_t$ with a discontinuity Π_t at time t, the Reynold's transport theorem for spatial transport of an arbitrary field variable $\varphi(\boldsymbol{x},t)$ is derived (Casey [111]) using,

$$\overline{\int_{\mathcal{P}_t}\varphi\,dv}^{\cdot}=\overline{\int_{\mathcal{P}_t^+}\varphi^+\,dv}^{\cdot}+\overline{\int_{\mathcal{P}_t^-}\varphi^-\,dv}^{\cdot} \tag{5.8.5}$$

where $\mathcal{P}_t^+$ is the matrix region (denoted by $\mathcal{R}$ in Figure 5.8) and $\mathcal{P}_t^-$ is the twinned region T. For each of the terms on the right hand side of Equation 5.8.5,

$$\overline{\int_{\mathcal{P}_t{}^+}\varphi^+\,dv}^{\cdot}=\overline{\int_{\mathcal{P}_t^{R+}}\varphi^+J^+dv_R}^{\cdot} \tag{5.8.6}$$

where $\mathcal{P}_t^R$ denotes the region of the material in the reference configuration, dv_R is its differential volume and J is the jacobian denoting volume change. Expanding the right hand side of Equation 5.8.6 (using the chain rule) and using the identity $\dot{J}=J\boldsymbol{\nabla}\cdot\boldsymbol{v}$ we get,

$$\overline{\int_{\mathcal{P}_t^+}\varphi^+\,dv}^{\cdot}=\int_{\mathcal{P}_t^{R+}}(\dot{\varphi}^++\varphi\boldsymbol{\nabla}\cdot\boldsymbol{v})J^+dv_R-\int_{\Pi_t^R}\varphi^+J^+V_Rda_R \tag{5.8.7}$$

where Π_t^R is the interface (twin boundary in our case), da_R is a differential area element on the discontinuous interface and V_R is its velocity along the normal, all defined in the material configuration. The last term in Equation 5.8.7 accounts for the rate of propagation of the interface itself. To transform this term to the spatial configuration we use the identity,

$$V = \frac{V_R J}{j} + \boldsymbol{n}.\boldsymbol{v} \tag{5.8.8}$$

where j is the areal ratio i.e. the ratio between surface areas in the spatial and material configurations and V is the velocity of the interface along its normal in the spatial configuration. Equation 5.8.7 is now completely described in the spatial configuration by,

$$\overline{\int_{\mathcal{P}_t^+} \varphi^+ \, dv}^{\cdot} = \int_{\mathcal{P}_t^+} (\dot{\varphi}^+ + \varphi^+ \boldsymbol{\nabla} \cdot \boldsymbol{v}^+) dv - \int_{\Pi_t} \varphi^+ (V - \boldsymbol{n}.\boldsymbol{v}^+) da \tag{5.8.9}$$

Similarly,

$$\overline{\int_{\mathcal{P}_t^-} \varphi^- \, dv}^{\cdot} = \int_{\mathcal{P}_t^-} (\dot{\varphi}^- + \varphi^- \boldsymbol{\nabla} \cdot \boldsymbol{v}^-) dv + \int_{\Pi_t} \varphi^- (V - \boldsymbol{n}.\boldsymbol{v}^-) da \tag{5.8.10}$$

The summation of Equation 5.8.9 and Equation 5.8.10 results in the Reynold's transport theorem in the presence of a propagating interface:

$$\overline{\int_{\mathcal{P}_t} \varphi \, dv}^{\cdot} = \int_{\mathcal{P}_t} (\dot{\varphi} + \varphi \boldsymbol{\nabla} \cdot v) dv - \int_{\Pi_t} [\![\varphi (V - \boldsymbol{n}.\boldsymbol{v})]\!] da \tag{5.8.11}$$

This holds true for vector fields $\boldsymbol{\varphi}$ as well.

The 'divergence theorem' (Equation 5.8.12) is handy while deriving jump conditions for the balance of linear momentum. For a vector field $\boldsymbol{\varphi}$ this theorem states

that (refer to Gurtin et al. [102]),

$$\int_{\partial\mathcal{P}_t} \boldsymbol{\varphi}.\boldsymbol{n}\, da = \int_{\mathcal{P}_t} \boldsymbol{\nabla}\cdot\boldsymbol{\varphi}\, dv + \int_{\Pi_t} [\![\boldsymbol{\varphi}]\!].\boldsymbol{n}\, da \tag{5.8.12}$$

5.8.3 Mass balance

The rate of mass transfer within the continuum with a discontinuity follows from Equation 5.8.11 by setting $\varphi = \rho$, where ρ is the density of the continuum.

$$[\![\rho(V - \boldsymbol{n}.\boldsymbol{v})]\!] = 0 \tag{5.8.13}$$

This implies simply that the rate of mass transfer through the interface is conserved.

5.8.4 Linear momentum balance

The balance of linear momentum is stated in weak form as,

$$\overline{\int_{\mathcal{P}_t} \rho\boldsymbol{v}\, dv}^{\cdot} = \int_{\partial\mathcal{P}_t} \boldsymbol{t}\, da + \int_{\mathcal{P}_t} \rho\boldsymbol{b_o}\, dv \tag{5.8.14}$$

By setting $\boldsymbol{\varphi} = \rho\boldsymbol{v}$ in the transport relation (Equation 5.8.11) along with the divergence theorem (Equation 5.8.12) and the definition for driving traction $\boldsymbol{t} = \boldsymbol{\sigma}.\boldsymbol{n}$ we get the jump conditions for stresses across the interface,

$$[\![\boldsymbol{\sigma}]\!].\boldsymbol{n} + [\![\rho\boldsymbol{v}(V - \boldsymbol{n}.\boldsymbol{v})]\!] = 0 \tag{5.8.15}$$

5.8.5 Energy balance

Setting $\varphi = \rho\Big(\mathcal{E} + \frac{1}{2}\boldsymbol{v}.\boldsymbol{v}\Big)$ in Equation 5.8.11 the specific internal work in the system follows the jump condition,

$$\left[\!\left[\rho\Big(\mathcal{E} + \frac{1}{2}\boldsymbol{v}.\boldsymbol{v}\Big)(V - \boldsymbol{n}.\boldsymbol{v})\right]\!\right] = -[\![\boldsymbol{\sigma}\boldsymbol{v}]\!].\boldsymbol{n} + [\![\boldsymbol{q}]\!].\boldsymbol{n} \tag{5.8.16}$$

In our specific case the jump in heat flux would be 0.

The entropy inequality is obtained by setting $\varphi = \rho\mathcal{N}$.

$$\int_{\mathcal{P}_t}\left(\rho\dot{\mathcal{N}} + \boldsymbol{\nabla}\cdot\frac{\boldsymbol{q}}{\Theta} - \frac{\rho\mathcal{Q}_s}{\Theta}\right)dv - \int_{\Pi_t}[\![\rho\mathcal{N}(V - \boldsymbol{n}.\boldsymbol{v})]\!] + \left[\!\left[\frac{\boldsymbol{q}}{\Theta}\right]\!\right].\boldsymbol{n}\,da \geq 0 \tag{5.8.17}$$

5.9 The notion of a driving traction [1]

In this section we derive an expression for driving traction acting on the twin boundary. This is the formulation originally derived by Abeyaratne and Knowles [1] for the theory of phase transformations. Defining a driving traction allows for subsequent discussion of kinetic relations.

The entropy inequality in the presence of a propagating discontinuity (Equation 5.8.17) is restated here.

$$\mathcal{D} = \int_{\mathcal{P}_t}\rho\dot{\mathcal{N}}dv - \int_{\Pi_t}[\![\rho\mathcal{N}(V - \boldsymbol{n}.\boldsymbol{v})]\!]da + \int_{\mathcal{P}_t}\boldsymbol{\nabla}\cdot\Big(\frac{\boldsymbol{q}}{\Theta}\Big)dv + \int_{\Pi_t}\left[\!\left[\frac{\boldsymbol{q}.\boldsymbol{n}}{\Theta}\right]\!\right]da - \int_{\mathcal{P}_t}\frac{\rho\mathcal{Q}_s}{\Theta}dv \geq 0 \tag{5.9.1}$$

Using the first law of thermodynamics (Equation 5.5.2) and the definition for the

Helmholtz free energy Ψ (Equation 5.5.9),

$$\mathcal{D} = \underbrace{\int_{\mathcal{P}_t} \frac{-\rho(\dot{\Psi} + \mathcal{N}\dot{\Theta}) + \boldsymbol{\sigma}.\boldsymbol{D}}{\Theta}\, dv}_{\mathcal{D}_h} + \underbrace{\int_{\mathcal{P}_t} -\frac{\boldsymbol{q}.\boldsymbol{\nabla}\Theta}{\Theta^2}\, dv}_{\mathcal{D}_c} + \underbrace{\int_{\Pi_t} \Big(-[\![\rho\mathcal{N}(V - \boldsymbol{n}.\boldsymbol{v})]\!] + \Big[\!\Big[\frac{\boldsymbol{q}.\boldsymbol{n}}{\Theta}\Big]\!\Big]\Big) da}_{\mathcal{D}_{tb}} \tag{5.9.2}$$

The first term $\mathcal{D}_h$ is dissipation due to local entropy production in the regions of the material far away from the twin boundary i.e. in the matrix and twinned regions. The second term $\mathcal{D}_c$ is the dissipation due to heat conduction and the final term $\mathcal{D}_{tb}$ is dissipation due to propagation of the twin boundary. The remaining part of this section is devoted to reformulating this term, $\mathcal{D}_{tb}$, to read a physically tractable form,

$$\mathcal{D}_{tb} = \int_{\Pi_t} fV\, da \tag{5.9.3}$$

where $f(\boldsymbol{x}, t)$ is a thermodynamic driving force and V is the velocity of the twin boundary normal to its surface. To eliminate the jump in heat flux from $\mathcal{D}_{tb}$, Abeyaratne and Knowles [1] first identified an algebraic modification,

$$[\![\sigma\boldsymbol{v}.\boldsymbol{n}]\!] = \langle\boldsymbol{v}\rangle[\![\boldsymbol{\sigma}.\boldsymbol{n}]\!] + [\![\boldsymbol{v}]\!]\langle\boldsymbol{\sigma}.\boldsymbol{n}\rangle \tag{5.9.4}$$

where $\langle . \rangle$ is the average across the discontinuity defined as $\langle\phi\rangle = \frac{1}{2}(\phi^+ + \phi^-)$. Using the kinematic jump condition (Equation 5.8.3) and the linear momentum jump condition (Equation 5.8.15) we rewrite the above equation as,

$$[\![\sigma\boldsymbol{v}.\boldsymbol{n}]\!] = -\frac{1}{2}[\![\rho\boldsymbol{v}.\boldsymbol{v}(V - \boldsymbol{n}.\boldsymbol{v})]\!] - \langle\boldsymbol{\sigma}\rangle.[\![(V - \boldsymbol{n}.\boldsymbol{v})\boldsymbol{F}]\!] \tag{5.9.5}$$

We use this expression in Equation 5.8.16 to eliminate $[\![\boldsymbol{q}.\boldsymbol{n}]\!]$, so that

$$[\![\boldsymbol{q}.\boldsymbol{n}]\!] = \Big[\!\Big[\Big(\rho\mathcal{E} - \langle\boldsymbol{\sigma}\rangle.\boldsymbol{F}\Big)(V - \boldsymbol{n}.\boldsymbol{v})\Big]\!\Big] \tag{5.9.6}$$

leading to,

$$\left[\!\left[\frac{\boldsymbol{q}.\boldsymbol{n}}{\Theta}\right]\!\right] = \left[\!\left[\left(\frac{\rho\mathcal{E}}{\Theta} - \frac{\langle\boldsymbol{\sigma}\rangle.\boldsymbol{F}}{\Theta}\right)(V - \boldsymbol{n}.\boldsymbol{v})\right]\!\right] \tag{5.9.7}$$

Using the above expression in the dissipation relation for twin boundary motion (Equation 5.9.2) and the definition for free energy Ψ (Equation 5.5.9),

$$\mathcal{D}_{tb} = \int_{\Pi_t} \left[\!\left[\left(\frac{\rho\Psi}{\Theta} - \frac{\langle\boldsymbol{\sigma}\rangle.\boldsymbol{F}}{\Theta}\right)(V - \boldsymbol{n}.\boldsymbol{v})\right]\!\right] da \tag{5.9.8}$$

$$= \int_{\Pi_t} \left[\!\left[\left(\frac{\rho\Psi}{\Theta} - \frac{\langle\boldsymbol{\sigma}\rangle.\boldsymbol{F}}{\Theta}\right)\right]\!\right] V\, da + \underbrace{\int_{\Pi_t} \left[\!\left[\left(\frac{\rho\Psi}{\Theta} - \frac{\langle\boldsymbol{\sigma}\rangle.\boldsymbol{F}}{\Theta}\right)\boldsymbol{v}\right]\!\right].\boldsymbol{n}\, da}_{\text{Convective term}} \tag{5.9.9}$$

Notice that the first integral term is now similar in form to Equation 5.9.3 and so the driving traction on the discontinuity is defined by (Abeyaratne and Knowles [1]),

$$f(\boldsymbol{x}, t) = \left[\!\left[\rho\Psi - \langle\boldsymbol{\sigma}\rangle.\boldsymbol{F}\right]\!\right] \tag{5.9.10}$$

With our definition of free energy functions for the matrix and twinned regions described in subsection 5.7.2 (Equation 5.7.6), a closed form expression for the driving traction on the twin boundary can be derived. A kinetic relation for twin boundary growth is the missing piece in this formulation to predict twin growth rates. An analytical scheme to predict a kinetic relation for twin growth has been proposed in chapter 7.

5.10 Summary and implications

This chapter describes a thermodynamically consistent micro-mechanics based continuum mechanical framework to capture the driving tractions on a twin boundary

modeled as a discontinuity. The framework is inspired by previous work on shock waves and phase boundaries (for e.g. Abeyaratne and Knowles [1]) and dynamic twin propagation in bcc metals (Rosakis and Tsai [17]). All of these studies looked at the propagation of phase boundaries in non-linear elastic solids. In our case, a driving force exists due to different dislocation slip mechanisms across the twin boundary. This is captured using a visco-plastic free energy or a defect energy in both the matrix and twinned regions. Micro-mechanics is introduced into the problem using a dislocation-based plasticity analysis of visco-plastic deformation in the matrix and the twinned regions. Although the basic functional form of this defect energy remains the same, the specific parameters governing orientation and strength of slip systems will be different in these two regions. The jump in the visco-plastic free energy (or defect energy) due to the different dislocation strengths and mobilities in the matrix and twin, drives the twin boundary.

The framework has important implications in understanding twinning as a mechanism and subsequently as a tool for calibrating larger scale computational codes. In order to discuss this effect, we refer again to the rate of twin volume fraction evolution (Equation 5.1.2) derived in chapter 4, which is central in capturing the material constitutive response due to twin-dominant deformation. The second term in this equation captures the effect of twin growth on the evolution of twin volume fraction. The framework described in this chapter may be useful for parameterizing the effects of twin growth and interactions, whose physics are likely very different from that of

twin nucleation. Many of the current computational codes simply model the total twin volume fraction evolution as a power law similar to dislocation slip (the twins are said to be modeled as pseudo-slip in this case). Much of the physics of twin growth remains obscured in these types of formulations.

Another potential implication of a framework of this type is in material design. The strengths, mobilities and initial dislocation densities clearly affect the growth rate of twins. By varying these parameters in the matrix, the framework may be able to predict a phase map of optimum driving tractions acting on the twin boundary. With a suitable kinetic relation, this will help us make useful decisions regarding material processing (to control material parameters like precipitate morphology and distribution and initial dislocation densities) based on predicted effects on twin growth rates and hence eventual macroscopic deformation rates of the material. The model can be made more sophisticated by introducing strain gradient effects (Appendix C) and much more informed dislocation kinetic laws in the matrix and twinned regions. These include outputs from atomistic and dislocation dynamics simulations. Clearly, a final step is to derive a kinetic relation. A simple analytical scheme to derive a dislocation-based kinetic relation is proposed in section 7.2.

Chapter 6

Crystallographic twin variant selection in single crystal magnesium as a function of strain rate

We have described in detail the effects of strain rate on the mechanical response of magnesium and the role that deformation twinning plays in this rate dependent behavior. Specific focus has been placed on the kinetics of twinning and factors that contribute to the rate of evolution of twins in-situ (chapter 4 and chapter 5). Another important aspect that is intrinsically tied to the dynamics of twin evolution is the crystallographic nature of twins. Recall that our definition of the shear strain rate due to a specific crystallographic twin variant is,

$$\dot{\gamma}_t = \dot{f}\gamma_{tw} \tag{6.0.1}$$

where f is the twin volume fraction and γ_{tw} is the shear strain caused by the twinned lattice reorientation (commonly known as the 'twinning shear'). The twinning shear connects the crystallography of the twin to the strain rate and strain caused by the evolution of twins in the crystal.

We already know that twins nucleate on specific crystallographic planes (these are called 'twinning planes'). Multiple conjugate planes on which twins can nucleate exist in the crystal. The twins that are characterised by the specific conjugate twinning plane on which they nucleate on will be referred to as specific 'twin variants' in this chapter. A more rigorous definition for a twin variant is provided in section 6.1.

Chapter 4 showed that the simultaneous nucleation of different twin variants affects twin-twin interactions. This chapter also indicated that the different twin variants may have different growth rates (Figure 4.11), a non-intuitive result that we have not been able to explain as yet. Deformation twins are favored in materials with low stacking fault energy and/or low crystal symmetry (for example hcp metals). Knowledge of the twin variants selected under specific loading conditions is important in such materials. Finally, a twin nucleation model that complements the twin dynamics model described in chapter 5 would help us understand how a crystal selects the nucleation of specific twin variants. We focus on the effect of strain rate on twin variant selection in this chapter.

6.1 Background

Bilby and Crocker [112] define a deformation twin as "*a region of a crystalline body which has undergone a homogeneous shape deformation in such a way that the resulting product structure is identical with that of the parent, but oriented differently*". A schematic is shown in Figure 6.1. Sun et al. [80] define the twinned region as a region of the crystal (beyond a boundary i.e. the twin boundary) that can be described both by a rotation of the original crystal (the matrix) and by a simple shear transformation. The equivalence of these two operations on the original crystal imposes kinematic restrictions on the available twin variants.

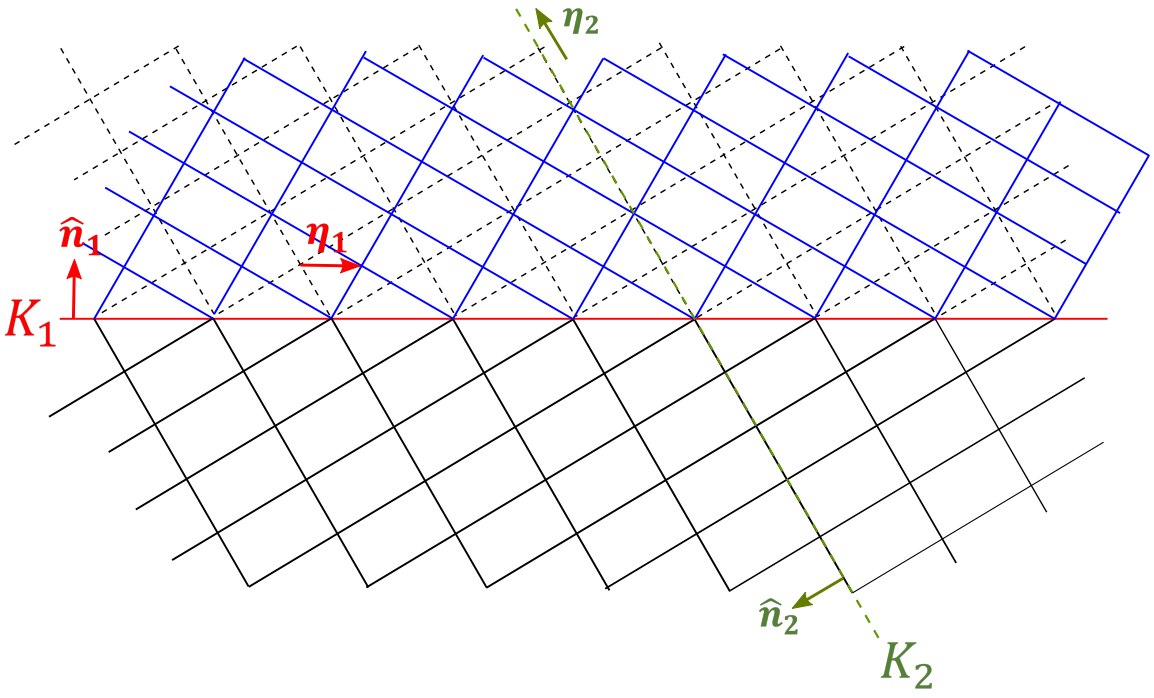

Figure 6.1: A schematic of the crystallography of a twinned region (Sun et al. [80]).

For the matrix and twinned region to remain connected, there must be a common plane (denoted by K_1). Since, the twinned region can be described as a simple shear of the crystallographic lattice, the unit vector in the direction of shear is denoted by $\boldsymbol{\eta_1}$. This is the direction of the twinning shear, the magnitude of which is used in Equation 6.0.1. The fact that the twinned crystal has to remain invariant except for a change in orientation (according to Bilby and Crockers' defintion) implies that there remains a plane K_2 that is undistorted during the transformation. We also define a 'plane of shear' which is the plane formed by the normal to the twin plane $\hat{\boldsymbol{n}}_\mathbf{1}$ and the shear direction $\boldsymbol{\eta_1}$. The intersection of the plane of shear with the undistorted plane K_2 is defined by a unit vector in this direction, $\boldsymbol{\eta_2}$, which also remains undistorted. A twin variant is hence completely defined by the set $\{K_1, \boldsymbol{\eta_1}, K_2, \boldsymbol{\eta_2}\}$.

In bcc and fcc structures, twinning takes place by homogeneous shear along the direction $\boldsymbol{\eta_1}$ (Figure 6.1). However, in hcp structures additional atomic displacements are often required in a direction different from the lattice shear. These atomic scale motions are known as 'shuffles' (Christian and Mahajan [11], Partridge [113]). In this chapter, we will define a twin variant using just the twin plane (K_1) and the direction of shear ($\boldsymbol{\eta_1}$). A 'twin mode' can have multiple twin variants based on the number of equivalent twin planes (within a given family of planes) that exist in the crystal. These equivalent twin planes are also known as conjugate twin planes. Hence, a twin mode is defined by a family of equivalent twin planes and corresponding directions.

Twinning in hcp crystals can accommodate strain along the c-axis of the crys-

tal lattice by either extension $\{10\bar{1}2\}$ or contraction $\{10\bar{1}1\}$ twinning, depending on whether the imposed strain tends to extend or contract the c-axis respectively. In this chapter, we focus on extension twins and discuss contraction twins only when necessary.

The most common extension twin mode observed in magnesium is the $\{10\bar{1}2\}\langle\bar{1}011\rangle$ mode. For this specific twin mode, six conjugate crystallographic twin planes i.e. $(10\bar{1}2)$, $(\bar{1}012)$, $(1\bar{1}02)$, $(\bar{1}102)$, $(01\bar{1}2)$ and $(0\bar{1}12)$ exist. From a simple Schmid factor analysis using a CRSS argument (which we do not know to be valid in the case of twins), the selection of twin variants would depend on the state of loading with respect to the crystal. The existence of shuffles during twin formation, however, is one indication that a simple Schmid factor analysis may not suffice. We note that, in addition to twin variants of a specific twin mode commonly observed in experiments, other additional twin modes have been proposed to exist from atomistic calculations by Sun et al. [80].

This chapter presents an experimental study of the crystallographic twin variants that were active during quasi-static and high strain rate loading. Recovery experiments were performed both at the quasi-static and high strain rates for post-mortem electron back-scattered diffraction (EBSD) microscopy. The list of datasets collected at high strain rates are presented in Table A.2.

6.2 Experimental Methods

6.2.1 Quasi-static compression

Cuboidal compression specimens were cut by electro discharge machining (EDM) from 99.999% pure Mg single crystals (Metals Crystals and Oxides Ltd, UK) following ASTM standard E9 (height to width ratio equal to 2 for a 6 mm width). The quasi-static compression tests were carried out at constant strain rate of $\dot{\varepsilon} \simeq 4.5 \times 10^{-4} s^{-1}$, with compression along the a-axis at room temperature. The axial stresses were calculated from an axial load cell measurement, while the axial strains were calculated by averaging full-field digital image correlation strain data along the axial direction.

6.2.2 High strain rate compression

The general principle and setup for the high strain rate loading experiments has been described in detail in chapter 2. The specimens for dynamic compression were cuboids of dimension $3.4 \times 3.7 \times 4.3$ mm, and the specimen preparation procedure has been described in chapter 4. Recovery experiments were performed within this dataset (Table A.2) using a procedure similar to that described in chapter 2. Specimens were recovered mostly at $\sim 3\%$ strain (refer Table A.2) for post-mortem EBSD analysis. In comparison to the polycrystalline AZ31B specimens (used in chapter 2), very little polishing was performed on these soft single crystals to ensure minimum damage

during surface preparation. Compression was performed along the $\langle 11\bar{2}0 \rangle$ axis of the crystal at room temperature.

6.2.3 Post-mortem microscopy

Samples (of thickness ~ 500 μm) were cut from the deformed samples (both quasi-static and dynamic loading) parallel to a $\{10\bar{1}0\}$ plane (normal orthogonal to the loading axis) using a diamond wire saw for post-mortem EBSD microscopy. Low feed rates and coolant pressures were used to ensure minimum damage during cutting. The sliced samples were then etched using a 10% nitric acid solution in water to remove the damaged layer induced during cutting. The next surface finishing step involved electrochemical polishing using a 90% methanol and 10% nitric acid solution with an applied voltage of 20 V for 1 minute at a temperature of -40 °C. A final finishing step was performed by ion milling (Ar^+) the surface using a *Fischione Model 1050* TEM Mill at a 5° incident angle and driving voltage of 4 kV for 5-10 minutes.

EBSD data was collected using a *TESCAN* scanning electron microscope equipped with an *EDAX* EBSD detector. The accelerating voltage and working distance were set to 20 kV and 19.5 mm respectively. Data was recorded at a spatial resolution of 600 nm on a hexagonal grid.

EBSD was performed on the imaging face normal to the imaging direction marked in Figure 6.2. The same labels will be used in the EBSD and texture maps used throughout the rest of the chapter.

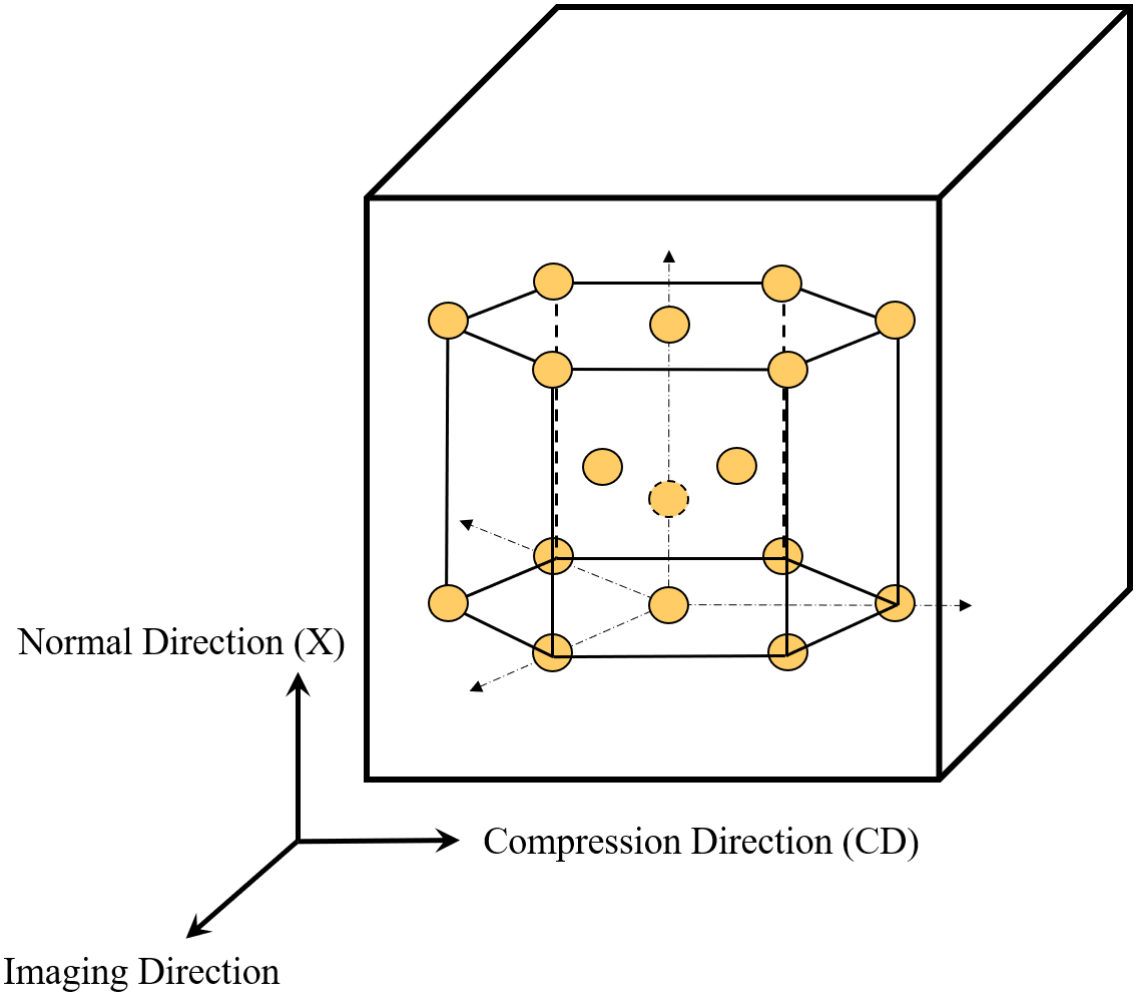

Figure 6.2: A schematic of a compression specimen with the compression and imaging directions marked relative to the crystallographic orientation. These notations will be used in the subsequent EBSD images.

6.3 Macroscopic response as a function of strain rate

The current study was focused on understanding the nature of twin variants nucleated during mechanical loading at different strain rates. In the quasi-static regime, only three experiments were performed two among them being recovery experiments at very small strains. Hence, only one quasi-static experiment was useful to compare the complete stress-strain behavior as a function of strain rate.

As discussed in chapter 4, the stress-strain response of single crystal magnesium at the high strain rates is variable possibly due to the stochasticity in twin nucleation and growth across experiments. Figure 6.3 shows the high strain rate stress-strain data along with the lone quasi-static dataset. A detailed statistical study similar to the dynamic twinning work (Figure 4.4 in chapter 4) and the polycrystalline AZ31B work (in chapter 2 and chapter 3), needs to be performed at the quasi-static strain rates to make valid conclusions on the rate dependent strength of single crystal magnesium. However, it is safe to conclude, based on chapter 4, that the competition between twin nucleation and growth in single crystal magnesium is rate dependent, and this may affect the rate dependence of the macroscopic stress-strain response. The concept of strain rate dependence of twin evolution has been discussed in chapter 3.

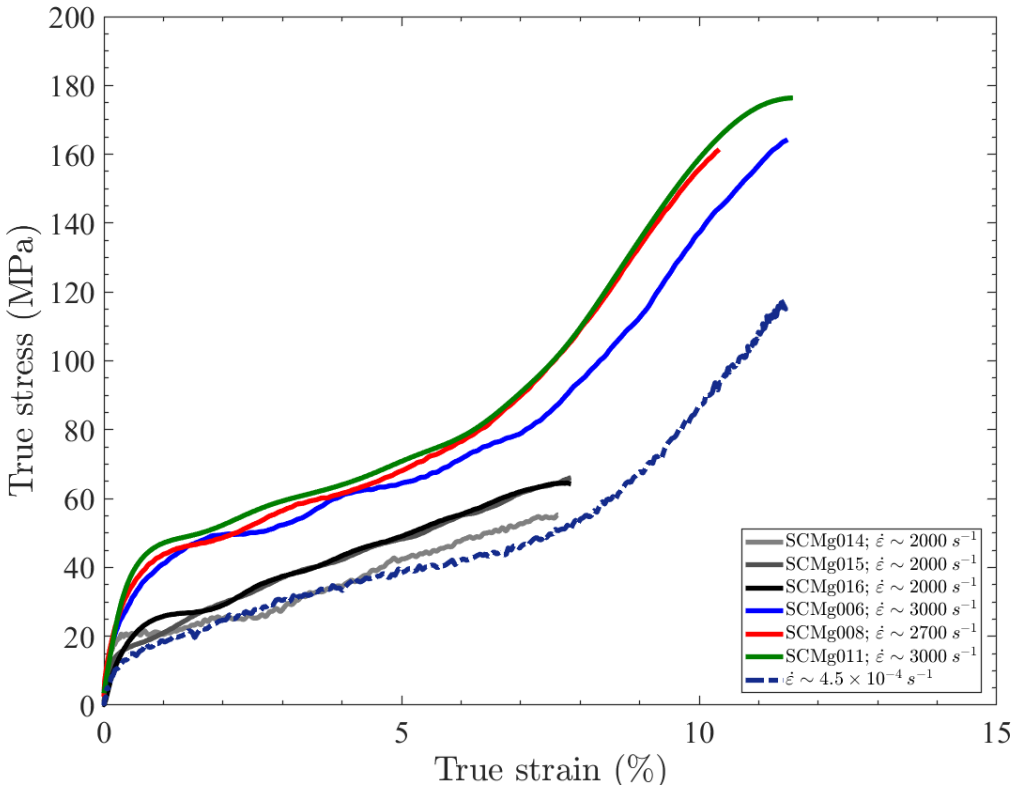

Figure 6.3: Stress-strain curves of single crystal magnesium along with quasi-static data. Note that we do not have a statistical dataset at the quasi-static rates to make any meaningful conclusions about strength as a function of strain rate.

6.4 Twin variant selection at quasi-static strain rates

Figure 6.4a shows an example inverse pole figure (IPF) map generated from EBSD data collected from a specimen compressed to $\sim$ 3% macroscopic strain at quasi-

static strain rates. The colors represent the orientation of the crystal at every spatial position on the map. A (0001) basal pole figure that maps the orientation of basal poles with respect to the specimen coordinate system is shown in Figure 6.4b. All the recorded twins were extension twins reorienting the matrix by $\sim 86°$.

Note that five different twin variants are shown in Figure 6.4. Four sets of primary twins labeled T1, T2, T4 and two sets of double extension twins (extension twins within extension twins) labeled T5 and T6 were found. The matrix is denoted by M. *Hence, in total five different twin variants were found to nucleate under quasi-static loading along the* $\langle 11\bar{2}0 \rangle$ *a-axis of the single crystal.* While T1 and T2 in Figure 6.4b are indistinguishable, point-to-point mis orientation analysis (Table 6.1) indicate that these are indeed two different variants with relative mis-orientation $\sim 6°$. The twin planes and directions are listed in Table 6.2.

6.5 Twin variant selection at high strain rates

Figure 6.5a shows an inverse pole figure map collected from a specimen compressed to $\sim 3\%$ macroscopic strain (similar to the quasi-static experiment) at a high strain rate. Similar to the quasi-static case (Figure 6.4), Figure 6.5b is a (0001) basal pole figure that identifies the dominant orientations of the basal poles with respect to the specimen coordinate axes.

From Figure 6.5, four primary extension twin variants (T1, T2, T3, T4) and only one double twin/ secondary twin variant (T5) were found to be active. The double

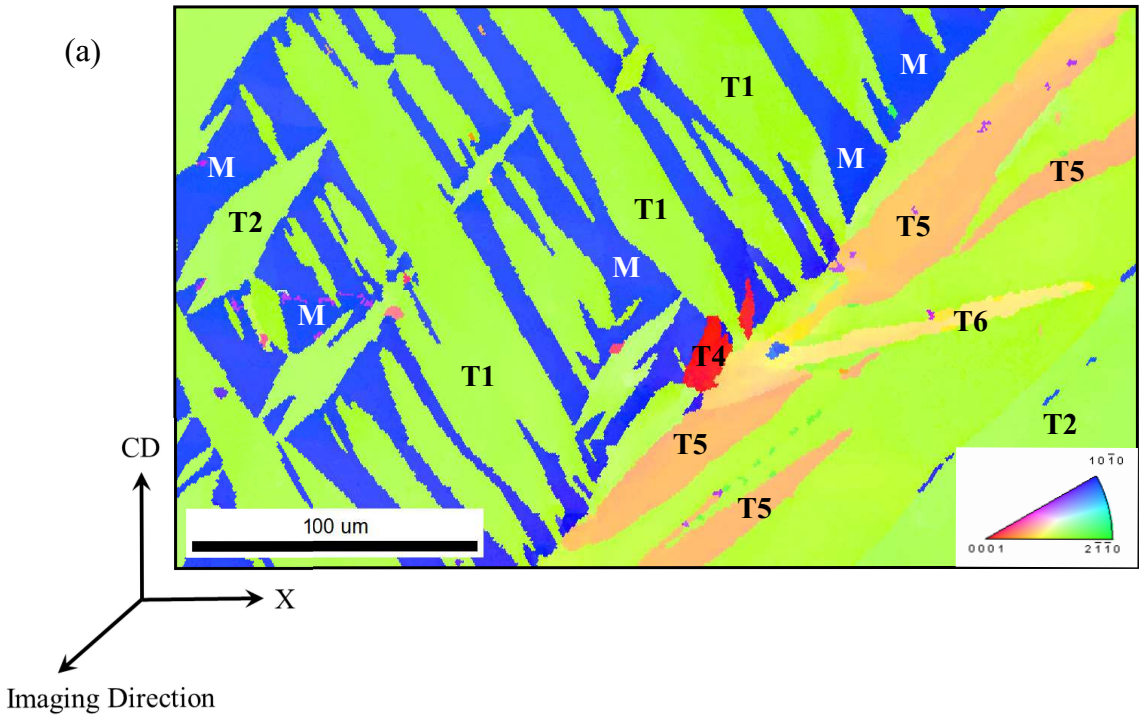

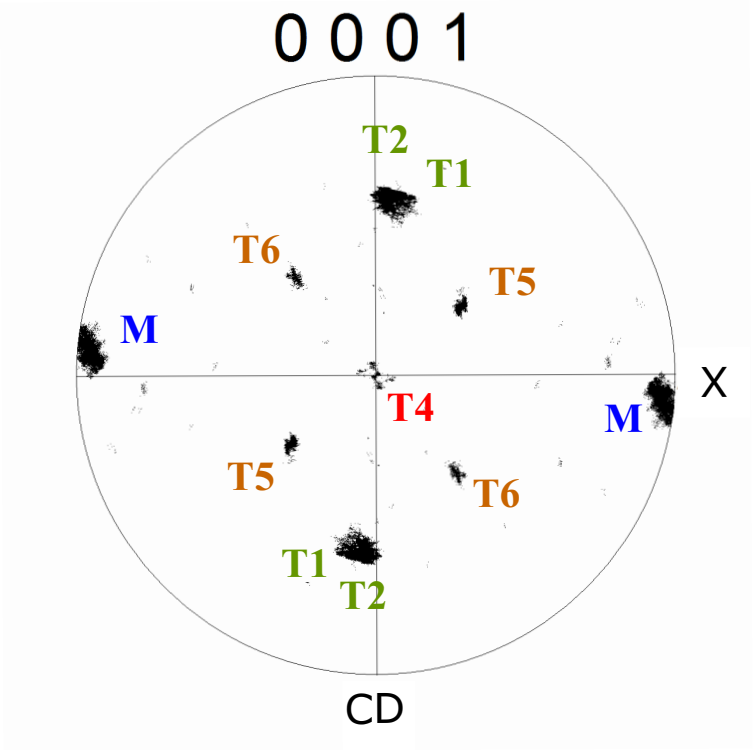

Figure 6.4: EBSD data from a sample compressed to $\sim 3\%$ macroscopic strain at quasi-static strain rates. CD stands for compression direction.

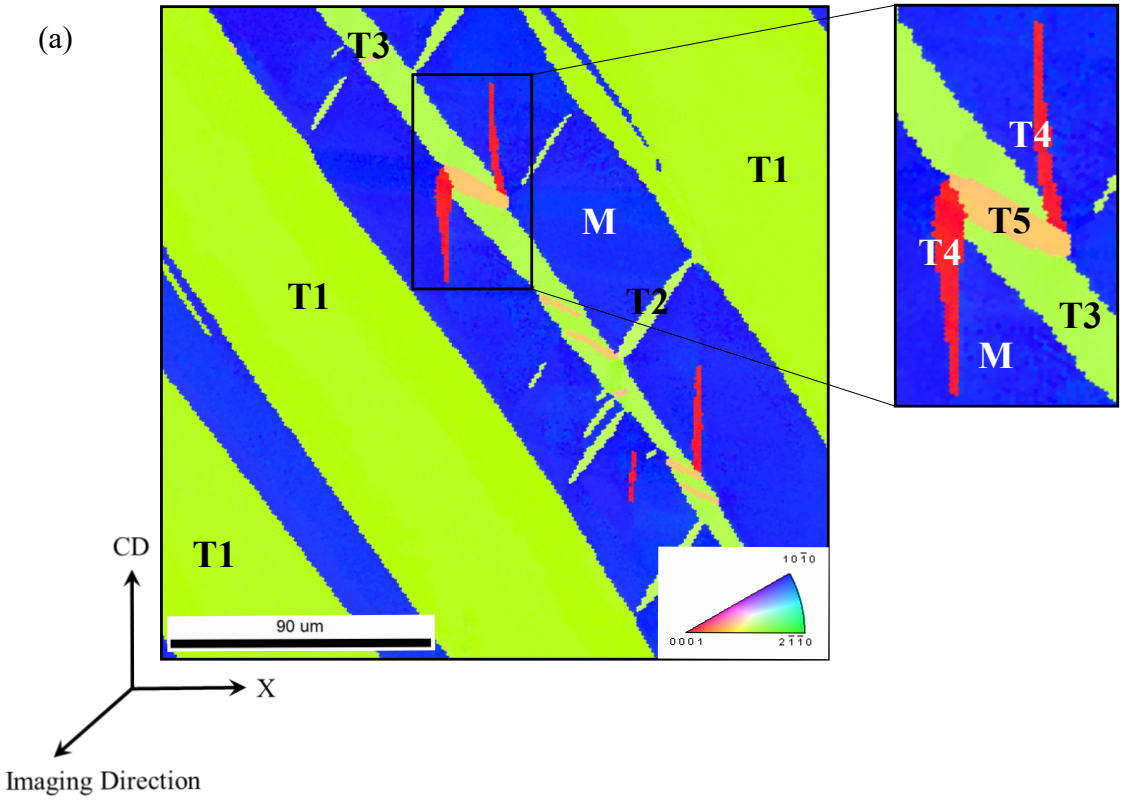

Figure 6.5: EBSD data from a sample compressed to $\sim 3\%$ macroscopic strain at high strain rates (refer to Table A.2 for more details). CD stands for compression direction.

twin variant T5 was found within the primary twin variant T3. No appreciable volume fraction of the second double twin variant T6 (observed in the quasi-statically loaded specimen) was found at the high strain rates. In total, five twin variants were found at the high strain rates. Based on this data, we may make the conclusion that twin variant selection is *not* a strong function of strain rate. The lack of one double twin variant at the high strain rates compared to quasi-static rates might indicate some rate dependence in twin variant selection. However, statistically significant datasets over large regions will be required to make any conclusive statements in this regard.

6.6 Schmid factor analysis

We first analyze the nature of the observed twins both at the quasi-static and high strain rates using the mis-orientation angles between them (Table 6.1). The mis-orientation angles shown in Table 6.1 indicate that T1, T2, T3 and T4 are different variants of primary extension twins with mis-orientation angles $\sim 87°$. The sources of the variability in the angles around 87° are currently unknown. Much more careful high resolution microscopy (possibly using TEM) is needed to understand if the variability of angles is merely experimental uncertainty or reflects the atomistic nature of twin variants nucleated. Given that multiple twin modes may indeed exist from energetic considerations (Sun et al. [80]), the latter may be true.

The twins T5 and T6 have mis-orientation angles $\sim 60°$ with respect to the matrix. However, these twins were found to be double twins inside primary extension twins

Point to point	M→T1	M→T2	M→T3	M→T4	M→T5	M →T6	T1→T3	T1→T5	T3→T6
Misorientation (degree)	86	90	86	87	58	63	6	87	85

Table 6.1: Mis-orientation angles for all twin variants found at quasi-static and dynamic strain rates.

(Figure 6.4 and Figure 6.5). The mis-orientation angles between T1 and T5, T1 and T6 as well as T3 and T5 were found to be nearly 87°, indicating that these are indeed extension twins within extension twins. The occurrence of these twins will be discussed in section 6.8.

The mis-orientation angle analysis has provided evidence that all twins observed were extension twins among which two were double extension twins. For a Schmid factor analysis, knowledge of the twin plane and twinning shear direction is necessary. Using our knowledge of conjugate crystallographic extension twin planes and twinning directions along with the twin traces observed in the data, we make informed guesses at the twin planes and twin directions for each variant observed. Note that an important assumption made here is that the twin grows along the direction of applied twinning shear. Figure 6.6 shows schematically the orientations of the twin plane (marked in red) and twin directions (blue arrow) relative to the loading direction (green arrow). T5 and T6 being double twins have different relative orientations corresponding to their parent twin (T3). Using this analysis we can calculate the Schmid factors defined as,

$$m = \cos\phi \cos\lambda \tag{6.6.1}$$

where ϕ is the angle between the loading orientation and twin plane normal, and λ that between the loading orientation and estimated twinning shear direction.

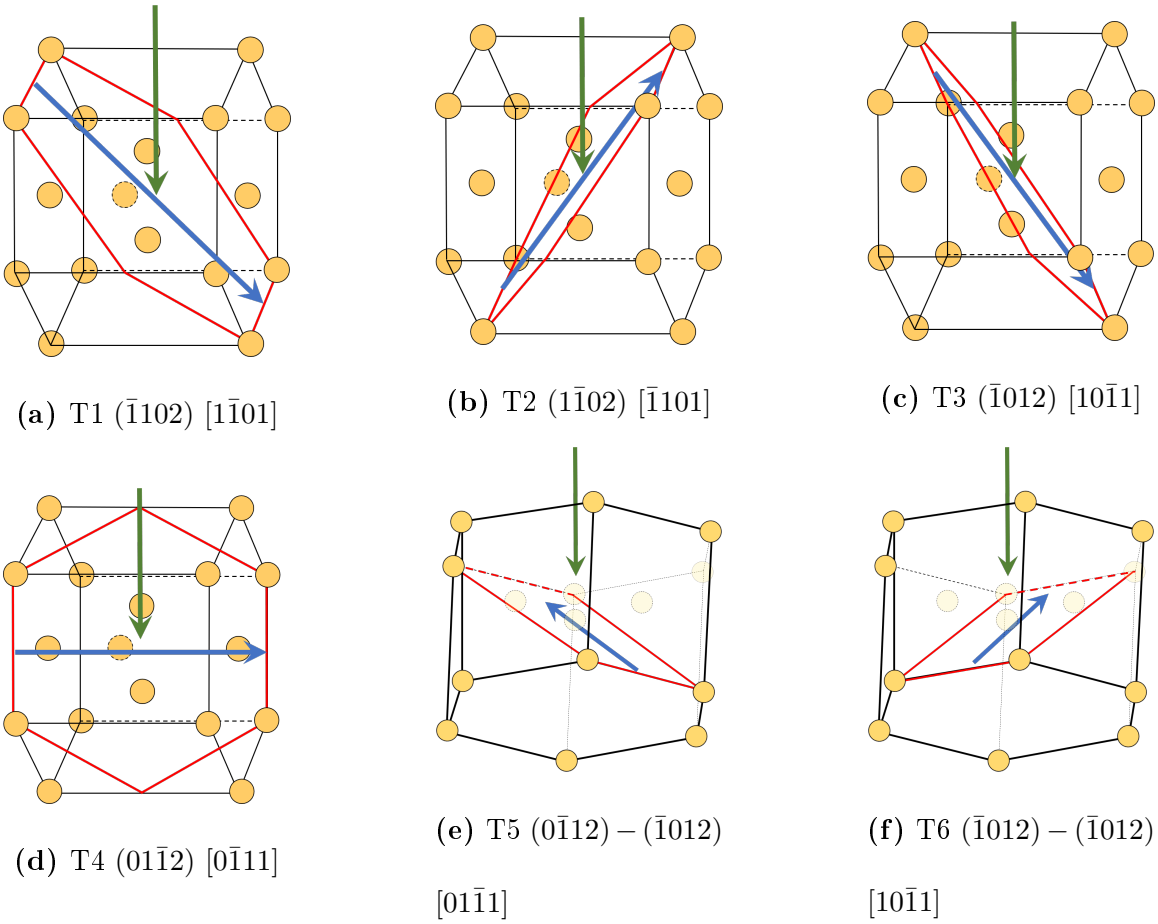

(a) T1 $(\bar{1}102)$ $[1\bar{1}01]$

(b) T2 $(1\bar{1}02)$ $[\bar{1}101]$

(c) T3 $(\bar{1}012)$ $[10\bar{1}1]$

(d) T4 $(01\bar{1}2)$ $[0\bar{1}11]$

(e) T5 $(0\bar{1}12) - (\bar{1}012)$ $[01\bar{1}1]$

(f) T6 $(\bar{1}012) - (\bar{1}012)$ $[10\bar{1}1]$

Figure 6.6: Schmid factor analysis of twin variants. The figures show schematically, the loading orientations (green arrow) and twinning shear directions (blue arrow) for the six different types of twins observed in both quasi-static and high strain rate experiments. T5 and T6 have been identified as double twins within primary twin variant T3.

The Schmid factors are listed in Table 6.2. T1, T2 and T3 have high Schmid factors (~ 0.37). The variant T4 is found to have a Schmid factor of 0 and is considered

to be a non-Schmid twin. These twins did not occupy large volume fractions in the material but were found consistently at both low and high strain rates. The double twins T5 and T6 were estimated to have even higher Schmid factors than T1, T2 and T3. The observations of these twins, however, raises questions, since the macroscopic loading orientation would be expected to result in pyramidal and prismatic slip over extension twinning (Dixit et al. [22]). These questions will be addressed in section 6.8.

Twin variant	Twin plane/direction	Schmid factor
T1	$(\bar{1}102)$ $[1\bar{1}01]$	0.37
T2	$(1\bar{1}02)$ $[\bar{1}101]$	0.37
T3	$(\bar{1}012)$ $[10\bar{1}1]$	0.37
T4	$(01\bar{1}2)$ $[0\bar{1}11]$	0
T5	$(0\bar{1}12) - (\bar{1}012)$ $[01\bar{1}1]$	~0.48
T6	$(\bar{1}012) - (\bar{1}012)$ $[10\bar{1}1]$	~0.48

Table 6.2: Schmid factors for twin variants observed from both the quasi-static and high strain rate experiments post-mortem. The Schmid factors for the double twins T5 and T6 are calculated relative to their parent twins, T3.

6.7 Double twin variant groupings

We dwell a little more on the different possible variants for double extension twinning and the specific variants found in Figure 6.4 and Figure 6.5. In hcp crystals,

six different extension twin variants may exist. Figure 6.7 shows a three-dimensional schematic representation of the possible double extension twin variants within a primary twin variant T3 (both quasi-static and dynamic rates show double twins inside T3). The dotted lines are markers to identify the [0001] c-axis of the crystal. The different variants are divided into four categories based on mis-orientation angles with respect to the matrix. From Table 6.1, it is clear that our double twins must fall within type 3 or 4 (with mis-orientation angles $\simeq 60°$). A further analysis of the crystal orientations within the double twins reveal that T5 was of type 3 and T6 of type 4 (as shown in Figure 6.7).

6.8 Discussion

6.8.1 Primary twin variant selection and local morphology as a function of strain rate

The selection of twin variants is not a strong function of strain rate (Figure 6.4 and Figure 6.5). While the absence of a second double extension twin, T6, at the high strain rates may seem to be the only indication of strain rate effects on twin variant selection, large datasets over multiple experiments will be required to quantify this effect. One possible way of making this comparison quantitative is to measure and compare the number densities and twin volume fractions of the specific variant over

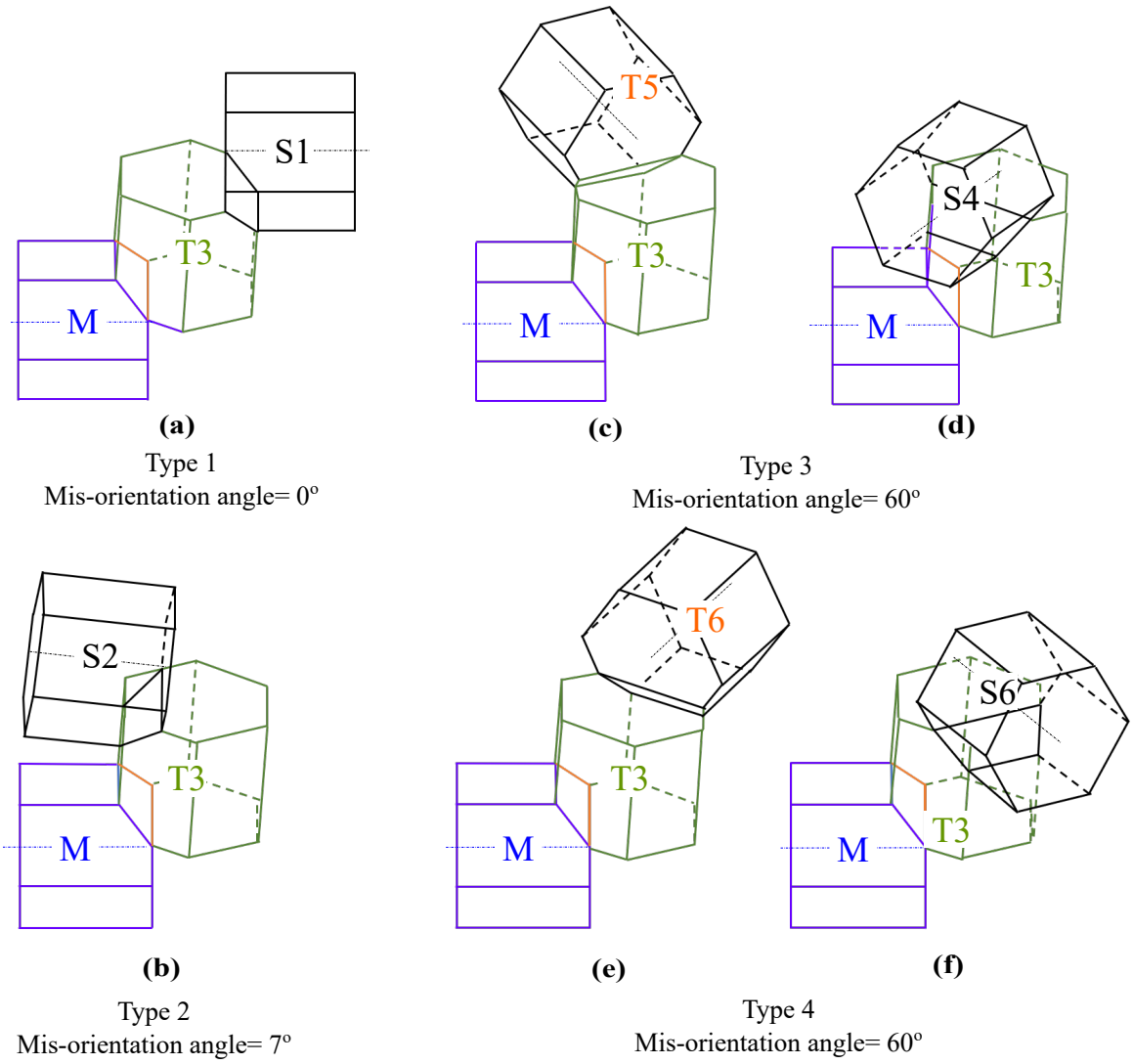

Figure 6.7: Double twin variants in single crystal magnesium. Note that the double twins T5 and T6 were observed inside parent twin T3 (Figure 6.4 and Figure 6.5). The four types of double twin variants were defined based off of the mis-orientations from the matrix M. Both T5 and T6 have high mis-orientation angles with respect to the matrix (Type 3 and Type 4 respectively).

these large datasets at different strain rates. This is beyond the scope of the current thesis but has potential for future studies. In addition, both the inverse pole figure maps, (Figure 6.4 and Figure 6.5), show a qualitative difference in morphology and twin volume fraction at the two different strain rates. These differences play a role in both the strength of the material and may also be important for identifying nucleation sites for localized failure. A detailed discussion follows.

The four primary twins observed were T1, T2, T3 and T4. We will discuss T1, T2 and T3 first. All these three variants have a Schmid factor of 0.37 (Table 6.2). Assuming that these twins follow the Schmid's law for nucleation, this would assign similar probabilities for nucleation of each of these variants. However, in real materials this probability may be biased by the initial nucleation. At the low strain rates (Figure 6.4), the volume fraction of T1 twins are higher than that of T2 twins. However, the volume fractions of T2 and T3 twins are still significant within the field of view. At the higher strain rates (Figure 6.5), the same trend remains although the volume fractions of T1 variants are much higher than T2 twins in comparison to quasi-static rates (Figure 6.4). The twin dynamics study in chapter 4 also indicates that the Gen2 twins are smaller than the Gen1 twins although the number density is higher. The Gen2 twins are mostly of crystallographic type T2 (from Figure 6.5). Comparisons between the EBSD data at low and high strain rates and the twin dynamics study in chapter 4, reveals that increasing the strain rate tends to increase the nucleation rate of T2 twin types (due to enhanced nucleation of Gen2 twins (refer

Figure 4.19)). However, since twin boundary growth is easier at quasi-static rates, the existing T2 twins tend to become larger at quasi-static rates. We hence hypothesize that the nucleation rate of T2 type twins is enhanced with increase in rate, however growth is suppressed. The twin volume fractions of T2 type twins at both quasi-static and high strain rates may hence be comparable in a large sample. However, the enhanced nucleation rates would increase the rate of hardening, resulting in larger flow stresses at larger strains. We do see some preliminary evidence of this phenomena in the macroscopic stress-strain response (Figure 6.3). We do not however understand the nucleation of the T3 twins as yet.

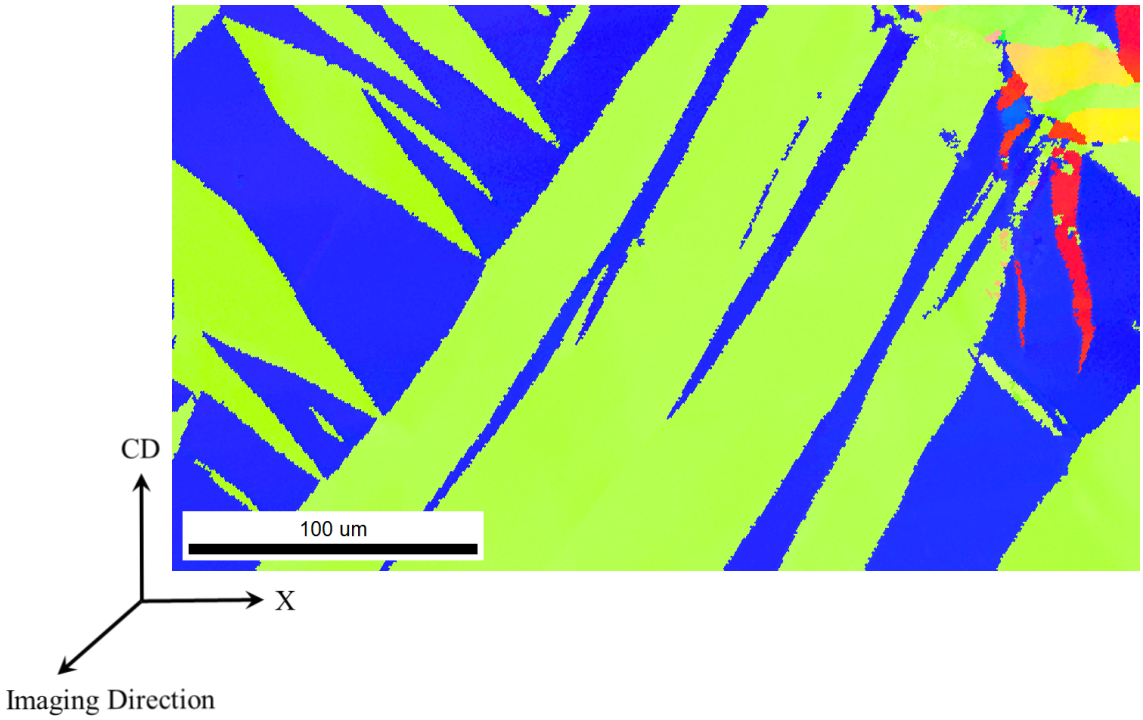

Figure 6.8: Inverse pole figure map from quasi-static specimens of single crystal Mg recovered at $\sim 3\%$ strain showing larger T4 type twins (colored in red).

The T4 primary twin variant has a Schmid factor of 0 (Table 6.2) indicating that these twins are non-Schmid twins i.e. they are not driven by a resolved shear stress. Although these are found only in very small volume fractions in comparison to the other three primary extension twins, they may play a role in controlling nucleation sites for failure. Figure 6.4 shows nearly negligible number and sizes of T4 twins. However, data collected from another region of the quasi-static specimen (twins colored red in Figure 6.8) showed larger twins of type T4. Similar twins of type T4 are observed at high strain rates too (Figure 6.5). Notice that all of the observed T4 twins nucleate from an existing twin boundary. In fact, most of them nucleate from the points of intersection of the double extension twins T5 and T6 with their parent twin boundary of type T3. The nucleation of these non-Schmid twins could hence have their origin in the nucleation and growth of the double extension twins (T5 and T6).

Twin morphologies have a significant impact on twin growth dynamics. Since twin boundary growth is a preferred mechanism at quasi-static strain rates than at dynamic strain rates (refer chapter 4), the presence of gradients in driving forces along the twin boundary allows them to develop curvature. Note that the twin boundaries especially near the tips in Figure 6.4 and Figure 6.8 are much more curved than in Figure 6.5. We expect that the curvature at the twin tip would affect the rate of twin growth. The larger curvature of the twin boundaries at quasi-static rates in comparison to high strain rates indicates that this might be a mechanism that allows

the twin to relax its driving stresses which would reduce its propagation velocity. This however is a hypothesis and needs to be verified by measurements of twin dynamics (similar to chapter 4) at quasi-static rates as well. Also, TEM measurements of the coherence of a twin boundary at quasi-static and dynamic rates would help get an idea of the surface energies associated and hence the driving forces. This allows for a more robust definition of twinning kinetics as a function of strain rate.

In summary, primary twins T1, T2 and T3 are found to nucleate easily in single crystal magnesium at both quasi-static and high strain rates. The number density of T2 twins are larger at higher strain rates but the twins are on average smaller. The reason for this is the enhancement of nucleation and suppression of twin boundary growth at higher loading rates discussed in detail in chapter 4. We hypothesize that this competition between nucleation and growth of specific twin variants may affect the macroscopic hardening and hence plastic flow stresses at larger strains. The larger curvature of twins at quasi-static rates has important implications on the kinetics of twinning and hence twin growth dynamics. In addition, non-Schmid twin variants T4 were found to occur consistently across strain rates albeit with a lesser volume fraction. Inverse pole figure maps show that the intersection between double extension twins and their parent T3 twins are nucleation sites for these primary T4 twins. In the next section, we discuss double twin variants.

6.8.2 Double twin variants in single crystal magnesium under uniaxial loading

Both quasi-static (Figure 6.4) and dynamic compression (Figure 6.5) experiments resulted in the nucleation of double extension twins within the primary twin variant T3. While the Schmid factors for the specific double twin variants are high, the orientation of the parent twin T3 relative to the loading direction is such that the c-axis is more under compression and shear, hence more suited to activate basal and pyramidal slip. No extension twinning would be expected. We hence propose that the extension twin within the parent extension twin of type T3 might be a non-Schmid twin. Notice also that the twin variants T5 in Figure 6.4 are not parallel to each other further indicating that they might not be driven purely by homogeneous shear stresses on the twinning plane alone.

Previous studies on the formation of secondary twins (Beyerlein et al. [114], Barnett et al. [115]) have shown that double twin selection does not follow Schmid predictions and instead is favorable for some orientations, perhaps due to minimization of strain incompatibility between primary extension and secondary contraction twin planes [114, 115]. Cases of secondary extension twins within primary extension twins have also been observed under high strain rate uniaxial *strain* [116], but these have not been studied in sufficient detail to make similar claims.

Another aspect that needs to be discussed is the nucleation of different double twin

variants. Two double extension twin variants T5 and T6 were observed at quasi-static rates in Figure 6.4 while only one was observed in Figure 6.5. A correlation between the parent twin thickness and the number and morphology of double twin variants nucleated within the parent twin may be made from these specific observations. The thickness of the parent twin in the quasi-static specimen is $\sim 75\mu m$ whereas in the high strain rate specimen is $\sim 15\mu m$. Consequently, the double extension twins T5 are much larger than at the high strain rates and T6 is not even observed in the EBSD maps at the high rates. From energetic considerations, we would expect that there must be a specific critical parent twin size for a double twin nucleus to become stable. From our observations, it seems that increase in the parent twin thickness allows for nucleation and growth of more double twin variants. The dynamics of twin boundary growth in this case would govern the nucleation of double extension twins hence controlling the nucleation of T4 primary twins as discussed in subsection 6.8.1. These observations provide crucial insight into how different twin variants interact with each other.

6.8.3 Effect of Schmid factor on deformation twinning

According to Schmid's law, dislocation slip occurs when the resolved shear stress on the slip plane reaches a critical value. The adaptability of this law to twinning however

oversimplifies the problem. The resolved shear stresses in our experiments are simply the applied uniaxial stresses times the Schmid factor (m) defined in Equation 6.6.1. Hence, if twinning were to indeed follow Schmid's law, then twin variant T4 should never have nucleated in the first place. In the case of double twins T5 and T6, although the Schmid factors are high, the direction of loading relative to the parent T3 would not normally be twin-dominant (for eg. Dixit et al. [22]). Moreover, prior studies on other types of double twins by Barnett et al. [115] and Beyerlein et al. [114] indicate that double twins are typically non-Schmid twins. The nucleation of these twins may hence be driven by local stress concentrations.

During twin growth, the three dimensional nature of the twin tip results in complex stress states locally. As explained in chapter 4, it is unclear which components of this stress tensor contributes to twin growth. Hence, while Schmid's law may serve as an empirical guide to predict nucleation and growth of primary twins T1, T2 and T3, it does not in any way explain the occurrence of T4, T5 and T6. Physically however, the three dimensional nature of twin tips makes it unlikely that any of the twins described in this study truly follow Schmid's law. There is a need for both experiments and models at the atomistic scale to define physically robust nucleation and growth laws for different twin variants. These laws could feed very well into efforts to better interpret twin variant selection and evolution dynamics at the length and time scales discussed in this thesis.

6.9 Conclusions

As a complementary study to the twin dynamics work described in chapter 4, this study probes into the crystallography of twins nucleated at both quasi-static and high strain rates using recovery experiments and post-mortem electron backscattered diffraction microscopy. The following are our primary conclusions from this chapter.

1. In total six twin variants were observed at the quasi-static and dynamic strain rates together, all of them extension twin modes.

2. Four primary twins were observed, one of which was a non-Schmid twin. The other two variants were found to be double extension twins i.e. extension twins within extension twins.

3. No significant effect of strain rate was found on the selection of twin variants.

Chapter 7

Concluding remarks and future directions

7.1 Conclusions from this thesis

This thesis has addressed the dynamic behavior of magnesium and its alloys using a mechanisms-based approach. Specific focus has been placed on deformation twinning and its complex dynamics at high loading rates. The direct measurements and analyses of the mechanics of discrete deformation twins have provided insight into these mechanisms at much shorter time scales than previously studied. We now summarize some of the key findings in this thesis.

In chapter 2, we studied the macroscopic strength of a specific textured polycrystalline magnesium alloy made by Equal Channel Angular Extrusion (ECAE) across

eight decades of strain rate. Our measurements revealed that the flow stress, hardening and apparent failure strains were anisotropic and rate dependent. While the flow stresses increased with strain rate for two dominant loading orientations, the strain hardening trend with strain rate was found to increase and then decrease for certain orientations of compression (that were believed to activate significant extension twinning) at larger plastic strains. The decrease in strain hardening at higher strain rates was attributed to the earlier onset of softening during compression along this specific orientation.

To develop deeper insight into these phenomena, we used data from in-situ high speed microscopy and post-mortem electron microscopy studies to interpret the mechanisms activated at the different length and time scales in chapter 3. Two major loading orientations were studied. At the micro length scales within a grain, the two loading orientations revealed dislocation slip-dominant versus twin-dominant deformation at high strain rates explaining the anisotropy in the macroscopic response. This difference in mechanisms activated was due to the texture of the material. The combinations of mechanisms activated, however, were found to be complex given the non-standard texture of the ECAE material in comparison to the conventional rolled alloys more commonly studied in literature.

Deformation twinning was found to occur as expected along a specific orientation under high strain rate loading. However, at the low rates, for the same loading orientation, complementary studies observed significant grain growth but very little

twinning. The data indicated that twin activity is enhanced at the higher strain rates explaining the increasing macroscopic strain hardening trend at smaller plastic strains (Figure 2.7b in chapter 2) during twin dominant deformation.

At the high strain rates, we also explored spatially resolved meso-scale deformation (with resolutions spanning 5-10 μm) at very short time scales of the order of 100's of nanoseconds using high speed imaging. Heterogeneous deformation was observed at these scales with localized deformation bands propagating rapidly across the specimen. These bands eventually led to failure of the specimen being tested. The propagation and coalescence of these bands had different qualitative characteristics along different loading orientations indicating the effect of texture and micro-scale deformation mechanisms on meso-scale deformation and material failure as well. These phenomena at an intermediate length scale and short time scales warrant separate extensive investigation during future studies. One mechanism that showed very interesting characteristics from the first part of this thesis was deformation twinning. We sought a deeper understanding of the mechanics of deformation twinning during the latter part of this thesis.

Three important features of deformation twinning were identified: 1. a nucleation criterion; 2. the kinetics of twin evolution (involving nucleation and growth); 3. the selection of crystallographic twin variants as a function of strain rate. Greater focus was placed on the second phenomena although the other two were also discussed.

To start, we performed extensive experiments and analyses to capture the dynam-

ics of twin nucleation and growth. Using high strain rate compression experiments with in-situ high speed imaging, we were able to measure the rates of nucleation and growth of extension twins in 99.999% pure single crystals of magnesium. Twin nucleation appeared to be stress-driven with first twins nucleating at 5-7 MPa. This may be useful as a first order approximation of a twin nucleation criterion in mathematical models. Once the first twins nucleated, they rapidly evolved into long lenticular-shaped bands with the tips propagating at speeds of the order of 1 km/s. These were first of its kind direct measurements of twin tip velocities. After the twin tip stops growing, quasi-static observations in the past have observed the relatively slow lateral growth of twin boundaries (of the order of 35 nm/s). Apparently, these rates are very slow to accommodate high strain rate deformation. Instead, rapid twin nucleation at the existing twin boundaries was observed. Further analysis of the experimental data revealed that, at high strain rates, the growth of twin volume fraction in the material is initially dominated by growth and soon enough nucleation begins to take over as a dominant mechanism - a phenomenon not known to occur at the low strain rates. With the kinetics of twin nucleation being very different from growth, these measurements indicate the need for more sophisticated models to accurately capture the mechanics of discrete twin evolution.

Chapter 5 is an effort in this direction. Inspired by theoretical models in the past by Gurtin [18], Abeyaratne and Knowles [1] and Rosakis and Tsai [17], we proposed a micro-mechanics based continuum mechanical framework that can capture

the driving forces on a twin boundary in an anisotropic elastic-plastic continuum. The driving forces on the twin boundary exist due to the difference in the strength and mobilities of plastic deformation mechanisms across the boundary. The framework is thermodynamically consistent and has potential applications in understanding and controlling twin growth rates and interactions, driving towards a materials design objective.

An important component in the study of deformation twinning that has received little focus at the high strain rates is its crystallographic nature. Although multiple 'crystallographic twin variants' have been known to activate, the selection of these variants as a function of strain rate remains unknown. This was the subject of chapter 6. Using post-mortem electron microscopy observations of single crystal magnesium samples compressed both at quasi-static and high strain rates, six different twin variants were identified, all of them being of extension twin type. Of the six variants, four of them were primary twins and two were double twin variants. Non-schmid twins were also observed to occur at the intersections of primary and secondary twins indicating that local stress states also play an important role not just in controlling the dynamics but also the crystallography. However, no significant effect of strain rate on the selection of twin variants was observed. While this may simplify our mathematical models a little, capturing the different twin variants activated during plastic deformation have implications in understanding the organization of multiple twins in a matrix and hence the related dynamics of evolution.

7.2 Potential for future studies

A larger objective that the mechanics and materials community is progressing towards is a mechanism-based constitutive model that can accurately capture the strength and failure of a material at different strains, stress states, temperatures and strain rates. While we are quite far off from this understanding, the scientific community is making giant strides in this direction.

The findings presented in this thesis are a small step in this direction. In addition to improving our understanding of fundamental mechanisms at high strain rates in anisotropic metals, it also opens up opportunities for materials design applications. Of course, transferring fundamental knowledge up to the application and design stage is a non-trivial task and needs more work. We suggest some potential future studies that would help us reach this stage while pushing the borders of scientific understanding established here.

7.2.1 Understanding the mechanisms of plastic deformation in polycrystalline anisotropic metals

In chapter 2 and chapter 3, we were able to identify potential plastic deformation mechanisms within grains using post-mortem microscopy studies and their effect on macroscopic material behavior across a large range of strain rates. An assumption

we make while using the rate sensitivities in a mathematical model is that the micro-structure remains a constant. However, at different loading rates, the micro-structure at a given plastic strain is not expected to be exactly the same. Hence, care needs to be taken while using these data to parameterize models or interpreting micro-structural evolution. One way of identifying these parameters and tracking micro-structural evolution with strain rate is by performing strain rate jump experiments (Meyers [14]). In these type of experiments, specimens are compressed to a specific plastic strain at one strain rate (such that the micro-structure at the end of this step is the same) followed by subsequent loading at different strain rates. The increase in flow stress with the jump in strain rate is often used to calculate the rate sensitivity parameter. In our material, this needs to be done at different plastic strains and strain rates, as our flow stresses are functions of both plastic strain and strain rate.

With reference to micro-structural evolution, multiple micro-scale mechanisms were active within the grain and our approach aimed at understanding the relative contribution of these different mechanisms to plastic deformation. Equation 2.5.2 is a mathematical abstraction of this statement and may be expanded out as,

$$\dot{\varepsilon}^{vp} = \underbrace{\dot{\varepsilon}^{vp}_{s1} + \dot{\varepsilon}^{vp}_{s2} + \dot{\varepsilon}^{vp}_{s3} + \dots}_{\text{Dislocation variants}} + \underbrace{\dot{\varepsilon}^{vp}_{t1} + \dot{\varepsilon}^{vp}_{t2} + \dot{\varepsilon}^{vp}_{t3} + \dots}_{\text{Twin variants}}$$

While we have some knowledge of which mechanisms are active, we do not know the relative magnitude of these different terms at the high rates. Detailed studies however have been performed at the quasi-static rates (e.g. Agnew et al. [117]). These studies used a combination of in-situ neutron diffraction measurements to extract

internal strains and an elasto-plastic self consistent polycrystal model to capture the relative activity between different mechanisms during compression. Similar studies have not been performed at the high strain rates primarily due to the lack of temporal resolution in neutron diffraction experiments. However, with the development of modern high intensity X-ray synchrotron capabilities (e.g. Wehrenberg et al. [3], Lambert et al. [118]), we may soon be able to make these measurements at high strain rates. Some measurements of twin volume fraction evolution in polycrystalline magnesium have already been made by Hustedt et al. [119]. In principle, extracting plastic strains due to dislocation slip in-situ is possible using simultaneous optical imaging and synchrotron diffraction techniques. While difficult to perform, these measurements are becoming more feasible.

In the light of these giant strides in experimental mechanics, the potential areas that we can explore are enormous. With significant tension-compression asymmetry in magnesium, stress state becomes an important issue in understanding the relative activation of mechanisms. Plate impact (e.g. Zhao et al. [61], Renganathan et al. [120]) and laser shock experiments (Wehrenberg et al. [3], Sliwa et al. [121]) offer access to different stress states (with varying levels of pressure) at high strain rates in these polycrystalline materials. A schematic of the experimental configuration from Wehrenberg et al. [3] is shown in Figure 7.1. However, these experiments are usually at much higher strain rates (order of $10^7\ s^{-1}$) than those probed in this thesis. To study stress state effects at the more nominal strain rates, torsional kolsky bars (e.g.

Duffy et al. [122, 123]) may be used.

Temperature is another critical field variable to consider especially at the high strain rates. The constitutive response at high temperatures, relies on the change in relative activity and the mobility of the active mechanisms in the material. Dislocation slip has been known to have increased mobility at high temperatures (Meyers [14]) while twinning has been known to have enhanced activity at *lower* temperatures in fcc and bcc metals (Christian and Mahajan [11]). The coupled effects of temperature and strain rate, however, have not been studied in much detail and less so in hcp metals like magnesium.

These studies, through the calibration of known phenomena and the discovery of

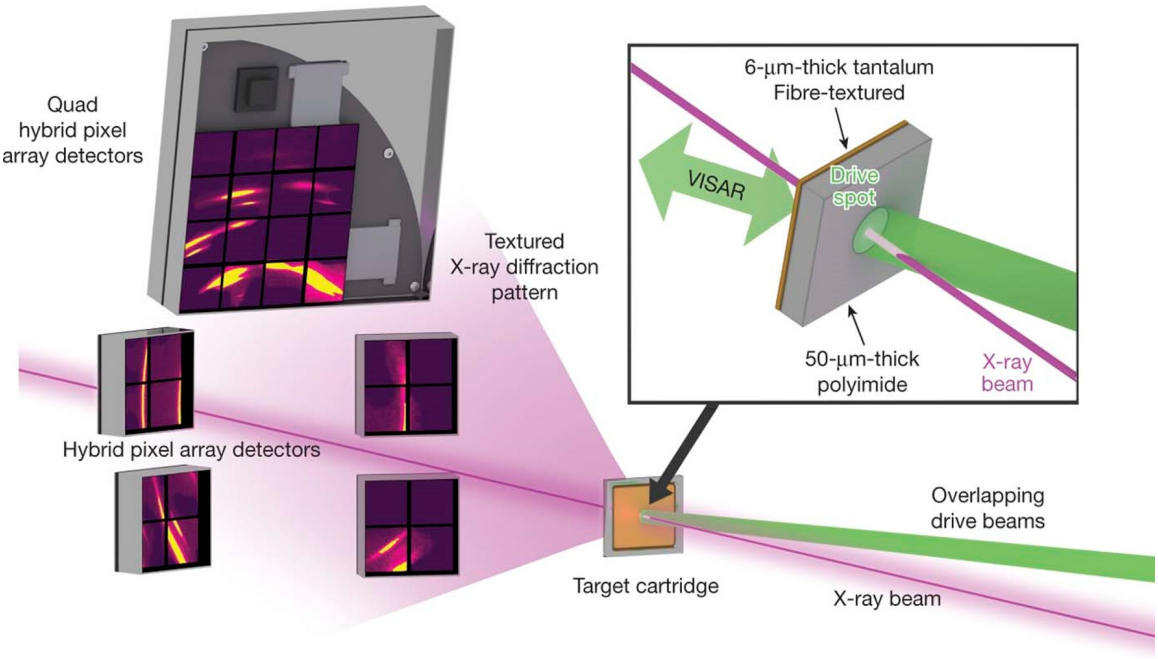

Figure 7.1: A schematic of a laser shock experiment with in-situ x-ray diffraction reproduced from Wehrenberg et al. [3].

unknown phenomena, would help improve the physical accuracy and the robustness of existing computational models and hence the materials-by-design initiative.

7.2.2 The kinetics of deformation twinning

The studies mentioned in subsection 7.2.1 focus on capturing the evolution of mechanisms through a volume of a polycrystalline material and are hence spatially averaged. A more fundamental understanding of this average evolution, specifically the transitions between the nucleation and growth of twins (studied in chapter 4) comes from probing these phenomena at a more spatially resolved scale. These studies also have potential applications in understanding the activation of local failure sites due to twinning (e.g. Barnett [20]). Chapter 4 is an example of how modern laboratory-based instrumentation can offer significant insight in this direction.

Nucleation criteria

While our data indicates that nucleation may be stress-driven, we are unable to identify the general tensorial stress state associated with nucleation. It would be useful to perform controlled multiaxial loading experiments together with careful atomic resolution microscopy to understand the nature of twin embryos. Note that much of the literature on twin nucleation in fcc metals may not apply to these hcp metals.

A kinetic law for twin boundary growth

With respect to twin growth, the first detail we lack is a physics-based kinetic relation for the dynamic propagation of a twin boundary. Such a model should capture the difference between the velocity of the propagating twin tip and the rate of broadening of the twin, and should relate these velocities to the crystallography and the driving stresses. Models that provide an understanding of the coupling between the driving forces on twin tips, the energies associated with twin boundaries, and the twin tip velocity would be of great interest. In this regard, we note that the twin tip propagation is typically not steady-state. A simple setup to estimate the kinetic relation is described here.

Figure 7.2 shows a schematic of the twin boundary as an ensemble of dislocations. This is the fundamental idea of previous dislocation-based studies as well (for e.g. Mitchell and Hirth [83], Lloyd [124]). However, these were quasi-static studies aimed at predicting the morphology of twins that are pinned at their tips. We would like to extend this idea of the twin boundary as a pile-up of dislocations to understand twin tip propagation as well.

Given an equilibrium configuration of these 'twinning dislocations' (or TD's) at zero stress, the application of shear stress τ (Figure 7.2) results in the growth of this ensemble of twinning dislocations and hence the twin boundary. We assume that new dislocation dipoles are nucleated on the TB (at x=0 in Figure 7.2) as the stress at this point reaches a critical nucleation stress. The stress field at the twin tip (or the

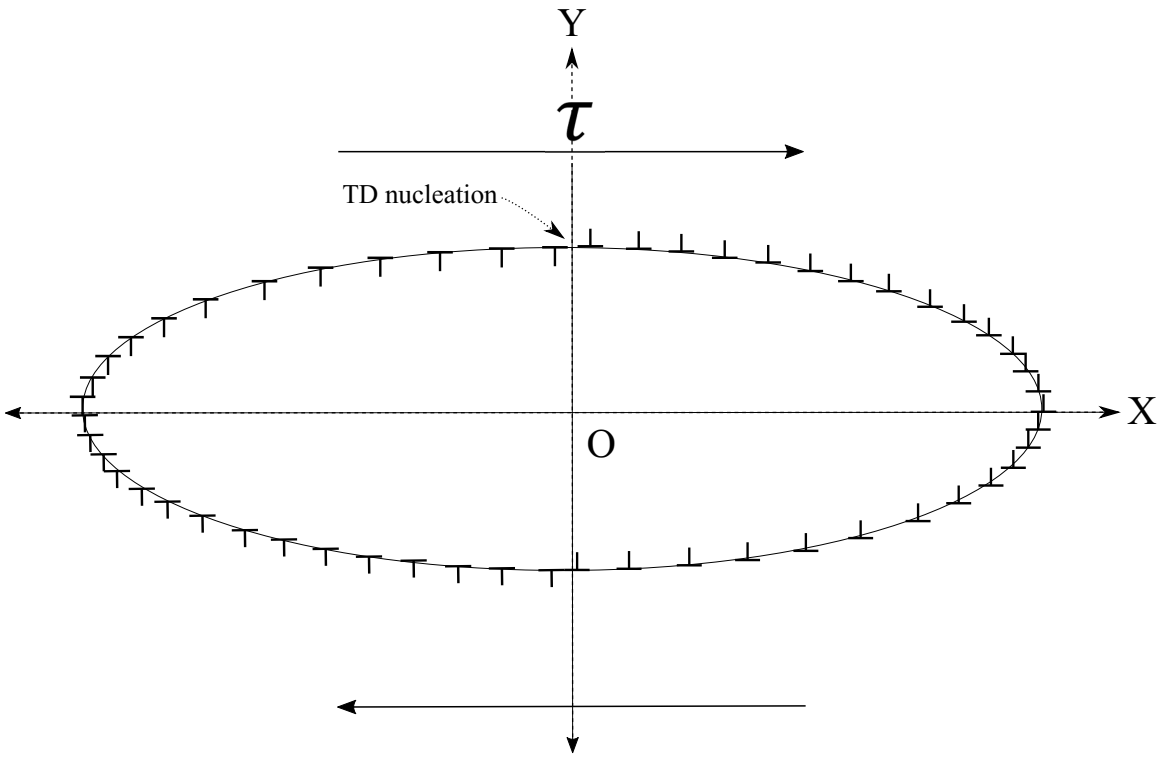

Figure 7.2: A schematic of a dislocation-based setup to estimate twin growth kinetics.

tip of the pile-up) drives the ensemble of twinning dislocations according to a linear drag kinetic law (as a first approximation).

The net force acting on a twinning dislocation in a dynamically propagating dislocation pile-up is written as (Mitchell and Hirth [83]),

$$F_{net} = \tau b - \frac{\mu b^2}{2\pi(1-\nu)} \int_{-l(t)/2}^{+l(t)/2} \frac{n(x',t)(x'-x)}{(x'-x)^2 + (y'-y)^2} dx' = B v_{TD}(\tau) \qquad (7.2.1)$$

where v_{TD} is the velocity of the twinning dislocation and b is the magnitude of it's Burger's vector. B is a linear drag coefficient for the propagation of the twinning dislocation and $n(x,t)$ is the distribution of twinning dislocations on the twin boundary. Note that while Mitchell and Hirth [83] were dealing with equilibrium twin morpholo-

gies in quasi-static problems, we are using this in a dynamic problem where the twins are continuously growing in space and time.

Since the twin is growing in our problem, the twin length l is a function of time. This is given by the simple evolution law,

$$\dot{l} = 2v_{TD}(\tau) \tag{7.2.2}$$

As the twin tip grows, the spacing between neighboring TD's is bound to increase. Similar to Lloyd [124]'s assumption, we assume that the nucleation of dislocation dipoles occurs at x=0 on the twin boundary when the local stress at this point reaches a critical value. This critical stress can be related to a critical spacing between twinning dislocations (l_c). A simple nucleation rate for the twinning dislocations is proposed.

$$\frac{dn}{dt}\Big|_{x=0} = \frac{v_{TD}}{l_{TD}}\mathcal{H}_{|l_{TD}-l_c|} \tag{7.2.3}$$

This can be thought of as an initial condition for Equation 7.2.1, where l_{TD} is the spacing between TD's, l_c is the critical spacing and $\mathcal{H}$ is the heaviside step function. Equation 7.2.1, Equation 7.2.2 and Equation 7.2.3 allow us to solve for the number density of twinning dislocations $n(x,t)$ on the twin boundary. The twin morphology is constrained by the number distribution and the twinning shear ε_T as,

$$\frac{dy}{dx} = \pm\frac{n(x,t)}{\varepsilon_T} \tag{7.2.4}$$

This evolution law in combination with Equation 7.2.2 completely defines the growth rates of the lamellar twin boundary with the applied driving stress. In principle, this

model could be extended to other stress states too.

The model at this stage is rudimentary with simple assumptions on the nature, propagation (Equation 7.2.1) and nucleation (Equation 7.2.3) of twinning dislocations. It remains to be seen if the model in its simplest form captures the kinetics of twin growth accurately. These laws could be improved significantly by inputs from molecular dynamics and discrete dislocation dynamics studies where more sophisticated physics are modeled.

Experimental techniques to better understand twin growth kinetics

On the experimental front, there is a lot that can be done to better understand the collective organization of twins in a grain/ a single crystal. For example, the in-situ high speed images from chapter 4, contain temporal and spatially resolved information about twin nucleation sites and twin spacings. An effective image processing scheme should ideally be able to extract the exact nucleation and growth terms in the twin volume fraction evolution law (Equation 5.1.2) derived in chapter 4. Such an algorithm would be sophisticated and needs more work.

With respect to additional measurements at the larger length scales, it would be very useful to obtain a sense of the strain field ahead of the propagating twin tip. With this information, the mathematical framework in chapter 5 would be able to capture effects of twin-twin interactions quantitatively. These studies will help calibrate larger

length scale models that handle the evolution of twin volume fractions when multiple twins exist in a self-organized fashion. The dynamic interaction of twins will be an added level of sophistication to our understanding of twin evolution.

At the smaller length scales, the structure of the twin boundary at different strain rates would be useful to better understand the energetics of the twin boundary. Some TEM studies do exist for quasi-statically deformed samples (for e.g. Zhu et al. [125]). Quantifying the distribution of twinning dislocations on the twin boundary and the effects of strain rate on this distribution would further help refine the initial configuration and the nucleation law for twinning dislocations on the twin boundary (Equation 7.2.3) used in the previous subsection. In-situ TEM straining experiments like the ones performed by Wang et al. [126] on copper would also be invaluable in validating and refining evolution laws for the twinning dislocations also described in the previous subsection (Equation 7.2.1).

Other problems that have not been given much attention in literature are the effects of stress state and temperature on discrete twin nucleation and growth. These warrant studies similar those suggested in subsection 7.2.1. However, direct in-situ imaging of discrete twin nucleation and growth in torsion kolsky bars, plate impact and laser shock experiments are technological challenges that have not been resolved as yet. Hence, we will have to settle with post-mortem measurements for now.

7.2.3 Heterogeneous deformation and failure at high loading rates in anisotropic metals

Failure was not a major focus in this thesis. However, chapter 3 identified heterogeneous deformation at the meso length scales (spanning 10's of grains) eventually leading to specimen failure. The kinetics of these initial heterogeneities were suspected to correlate to reduction in apparent failure strains with increase in strain rate.

The two common softening mechanisms that may result in failure at high strain rates are thermal softening (Meyers [14]) resulting in 'nearly' adiabatic shear localization and geometric softening. The occurrence of both these mechanisms is plausible in anisotropic hcp metals. The relative activation of these mechanisms especially along different loading orientations will enable greater insight into controlling failure in magnesium alloys.

Thermal softening may be monitored using controlled multi-axial experiments with in-situ high speed infrared measurements (for e.g. Marchand and Duffy [52], Zhou et al. [56]). While techniques to model this phenomenon are well established (Rosakis et al. [106]), the measurements themselves are challenging. A schematic of an experimental setup used to measure the temperature and deformation gradient fields around a dynamically propagating shear band (reproduced from Guduru et al. [4]) is shown in Figure 7.3.

Geometric softening may occur in the form of deformation twinning in the material. An ideal experiment to probe this phenomenon would monitor the spatial evolution of twins and twin-related deformation bands in-situ. The biggest challenge in these experiments lie in the difference in length scales. Discrete twinning occurs within the grains while the localized deformation bands observed in Figure 3.6 span 10's of grains. Small scale imaging techniques at the relevant time scales (like the dynamic TEM) are still in their nascent development stage. On the modeling front, models that could predict the formation of twin-mediated bands under high rate de-

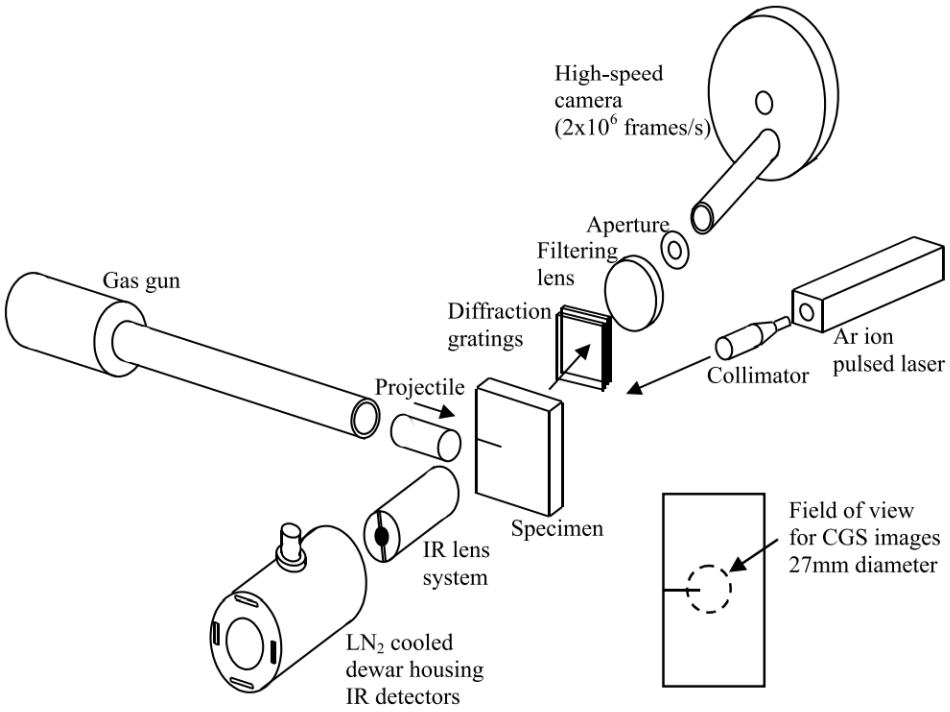

Figure 7.3: A schematic of an experimental setup used to simultaneously measure displacement gradients and local temperature fields in-situ around a dynamically propagating shear band in steel. Reproduced from Guduru et al. [4].

formation do not exist to the author's knowledge. There is hence a lot more potential for exciting and useful mechanics in this area with specific applications for example in high speed manufacturing.

Appendix A

Conventional and desktop kolsky bars: Experimental protocols, data analysis procedures and datasets

A.1 Conventional kolsky bar: Instrumentation, data analysis and experimental protocol

A representative schematic block diagram for the conventional kolsky bar experiments performed in this thesis is shown in Figure A.1.

A single stage gas gun is used to fire a maraging steel cylindrical projectile down

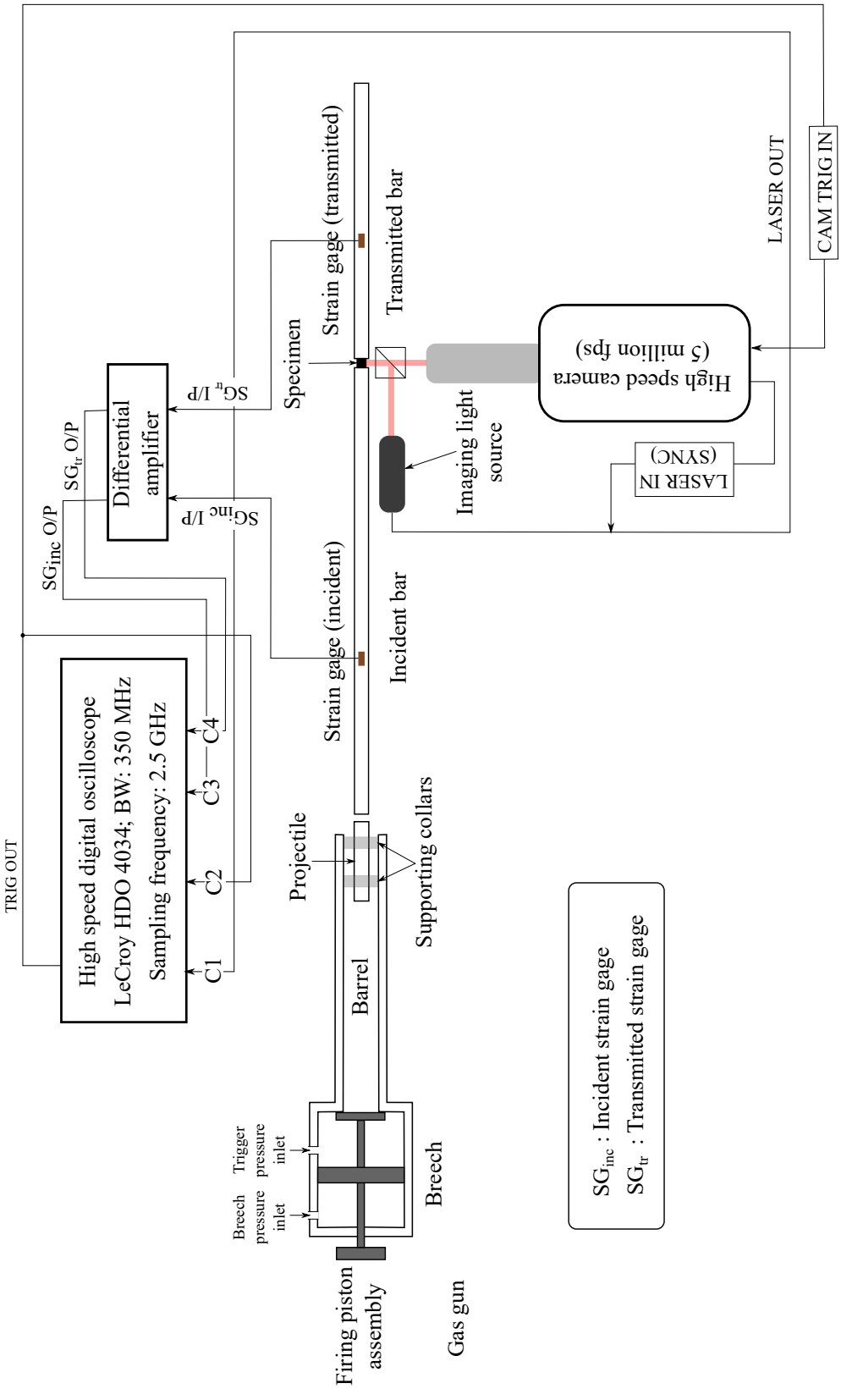

Figure A.1: A schematic block diagram of the conventional kolsky bar with in-situ imaging used in this thesis.

the gun barrel. The projectile is supported by plastic collars in the barrel. Up on impact, linear elastic stress pulses propagate down the bar. The width of a pulse for our experiments were $\sim$100 μs. At a significant distance from the impact end (conventionally chosen to be >10 times the bar diameter), the waves may be assumed as one dimensional.

With respect to data collection, the incident strain gage signal is the earliest event that is captured by the oscilloscope (Figure A.1). This signal triggers the oscilloscope which is then used to trigger the high speed camera (Kirana®) and the imaging light source (a 400 W SI-LUX Pulsed laser diode). Since we know the velocity of the longitudinal wave in the bar, the delay between the incident signal and the camera trigger can be set accordingly. In order to correlate the images to specific stress and strain states in the specimen, the laser pulses were captured on the oscilloscope as well.

A.1.1 Strain gage instrumentation

The strain amplitude in the bars was detected using 1 k-ohm foil strain gages (Micro-Measurements®) with a gage factor of 2.04. For the experiments on polycrystalline AZ31B (chapter 2 and chapter 3), the same type of gages were used on both the bars. However, for the single crystal experiments (chapter 4), higher sensitivity semiconductor strain gages (Kyowa® KSP-2-1K-E4) with gage factors of 162 were used on the transmitted bar due to lower strength of the single crystals.

Two strain gages were mounted at every point of measurement on the bar. The gages were mounted on opposite sides of the diameter to cancel out bending wave effects. Signals from these gages were measured using a Wheatstone's bridge circuit in a half-bridge configuration. The output of the Wheatstone's bridge was sent through a differential amplifier and then to a high speed digital oscilloscope (LeCroy HDO4034) with a bandwidth of 350 MHz and a maximum sampling rate of 2.5 GHz. The strain was calculated from the oscilloscope signal simply as,

$$\varepsilon = \frac{2.1 V_o}{G_F V_i} \tag{A.1.1}$$

where ε is the strain in the bar, V_o is the output voltage, G_F is the strain gage factor and V_i is the bridge excitation voltage (30V for the foil gages and 15V for the semiconductor gages).

A.1.2 Dispersion correction

The incident and reflected strain signals measured were numerically corrected for dispersion effects due to wave propagation down the bar using an empirical relation between the phase velocity and wave number (from C. W. Felice cited by Gong et al. [5]). Felice's analytical relation along with data from Bancroft [127] is plotted in Figure A.2.

This relation was used to modify the phase angle for different frequencies in the experimental signal using a simple fourier-based technique outlined by Gorham [39].

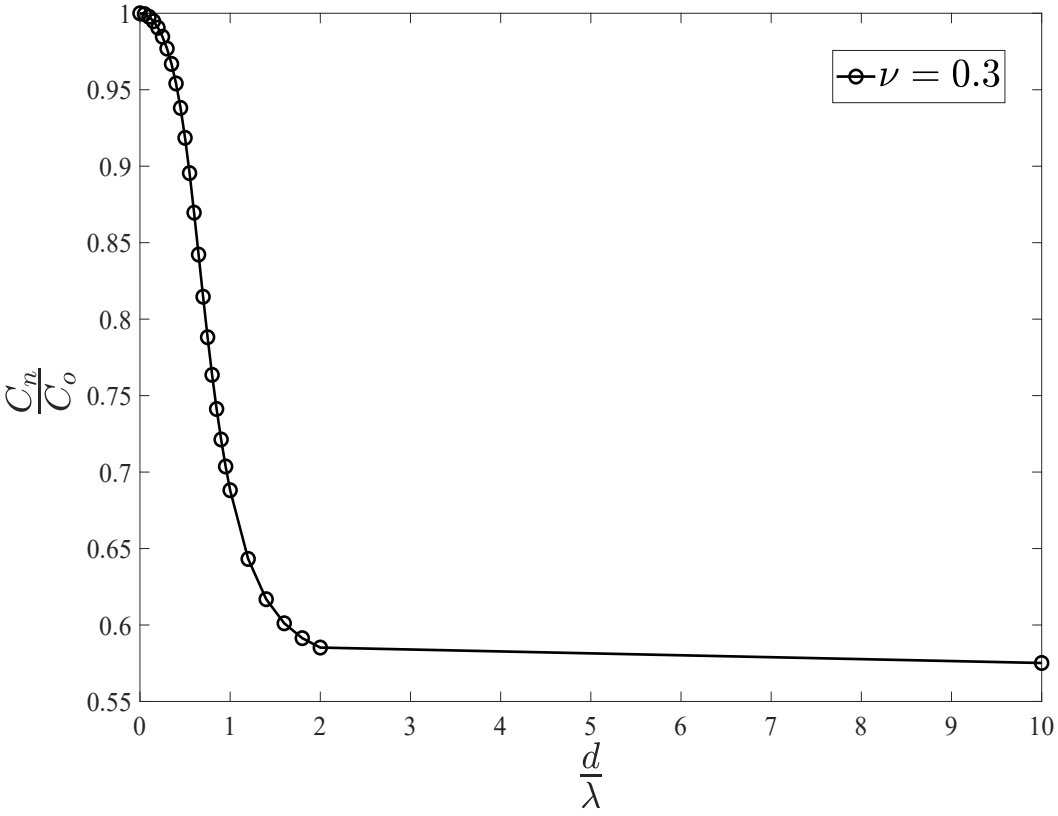

Figure A.2: Dispersion relation generated using an empirical relation from C. W. Felice cited in Gong et al. [5].

The corrected strain signals were then converted to specimen engineering stress-strain curves using Equation 2.3.2.

A.1.3 Experimental protocol

The procedures followed before and after the experiment is outlined here.

- Turn on the power source, oscilloscopes and camera. Ensure that the imaging laser is in LIVE mode before turning the laser safety key to ON.

- Let the gages stabilize for 20-30 minutes.
- Check the alignment between projectile and incident bar.
- Clean the bar ends and apply the pulse shaper (aluminium foil in our case).
- Push the projectile down the gun barrel.
- Check the alignment between incident and transmitted bars.
- Setup the oscilloscope and differential amplifier based on the duration of data being recorded and expected amplitude of signals.
- Make note of the noise in the strain gage signals.
- Balance the Wheatstone bridge boxes.
- Measure specimen dimensions. FILL EXPERIMENTAL SETTINGS AND SPECIMEN DIMENSIONS IN DATA SHEET.
- Position the specimen between the incident and transmitted bars. Apply a very small amount of grease on both ends of the specimen in contact with the bars to minimize frictional effects.
- Close the orifice at the breech-barrel interface by manually pushing the firing piston.
- Focus the imaging laser beam on the specimen. Focus the camera image and set exposure and inter-frame times for both the camera shutter and the imaging

laser source.

- Set the delay time between oscilloscope and camera trigger.
- Re-check strain gage balance.
- FINAL CHECK: Check if the following signals are being captured.
    1. Strain gage signals (balanced)
    2. Camera trigger
    3. Camera output
- Set the oscilloscope to SINGLE trigger mode.
- Set the camera to ARM for trigger.
- DOUBLE CHECK IF ALL SYSTEMS ARE READY FOR TRIGGER.
- Open the nitrogen gas tank.
- Close the needle valve to fill the breech to desired pressure.
- Close the nitrogen tank.
- FIRE!
- Turn the imaging laser source key to OFF.
- Save all data (oscilloscope signals and raw camera images).

A.2 Desktop kolsky bar: Instrumentation, data analysis and experimental protocol

Figure A.3 shows a representative block diagram (similar to Figure A.1) for the desktop kolsky bar experiments.

We attempted in-situ imaging as well, however the small size of samples made it unfeasible to obtain useful images during the experiment. More work needs to be done to improve optics for imaging at these small scales.

Notice that the operating principle for the desktop kolsky bar is similar to that of the conventional kolsky bars. However, the small size (3 mm diameter bars and $\sim 1 \times 1.2 \times 1.4$ mm specimens) demands much more sensitive instrumentation and alignment restrictions.

A.2.1 Strain gage instrumentation

Both bars were instrumented with 120 ohm semiconductor strain gages (Kulite® ACP-120-300) with factory-specified gage factors of 100. The gages were mounted in the same configuration as the conventional kolsky bars with a half Wheatstone's bridge circuit. However, due to variation in the resistance of the gages, Equation A.1.1 needs to be modified as,

$$\varepsilon = \frac{2.8 V_o}{G_F V_i} \tag{A.2.1}$$

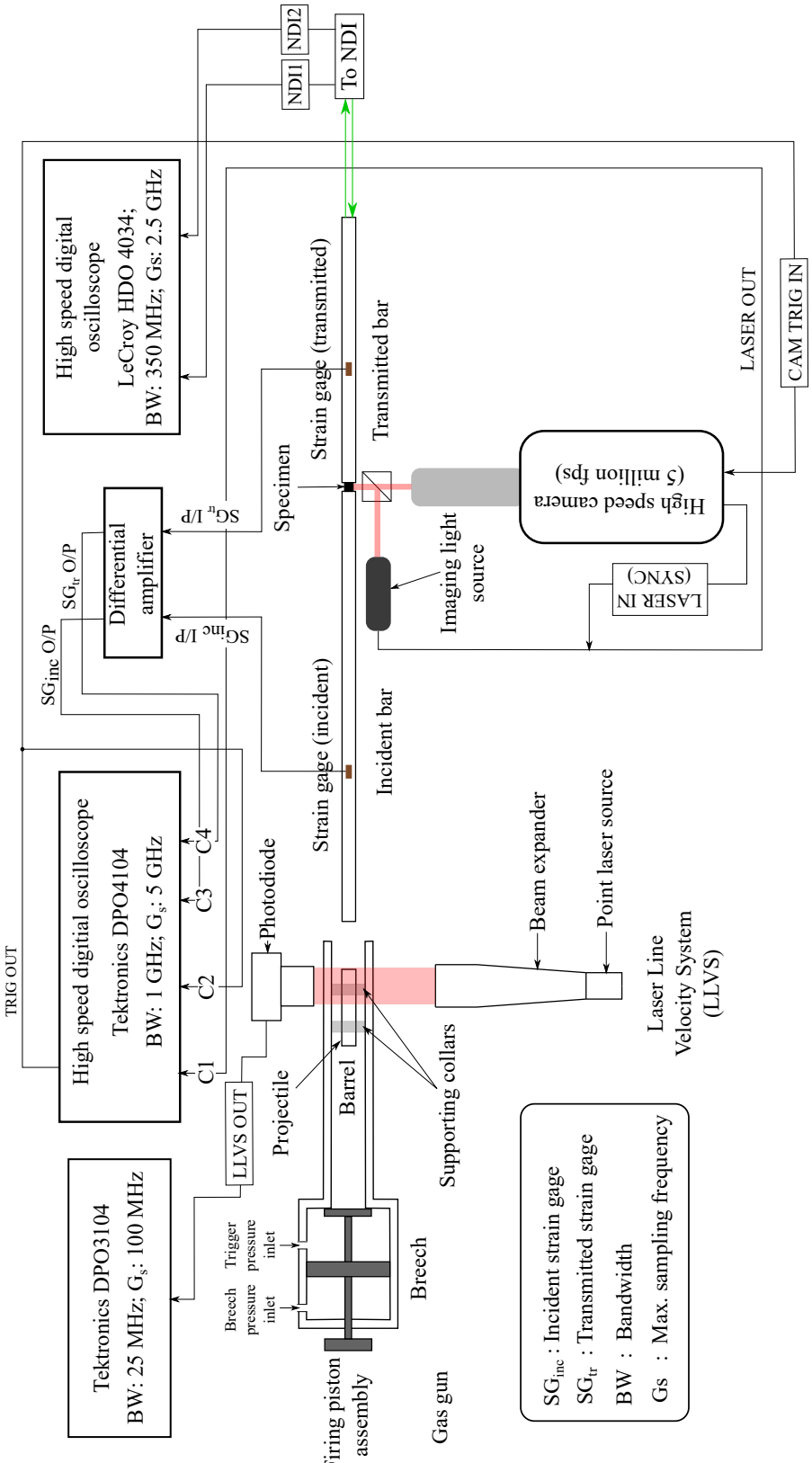

Figure A.3: A schematic block diagram of the miniature desktop kolsky bar with in-situ imaging used in this thesis.

While semiconductor strain gages have very high sensitivity in comparison to conventional foil gages, the gage factors of the former are also very sensitive to environmental conditions like temperature and moisture unlike traditional foil gages. Moreover, mounting these gages on the bar cannot be done using conventional strain gage gluing techniques commonly used for kolsky bars. The gages on the desktop kolsky bar were mounted using a high temperature epoxy instead. This may also affect the strain gage factors. Due to these uncertainties, we introduced additional instrumentation for real-time calibration of the strain gages in both the incident and transmitted bars.

A.2.2 The Laser Line Velocity System

The incident strain gage is calibrated using the Laser Line Velocity System (LLVS) (refer Figure A.3) which was originally developed for lateral strain measurement in tension kolsky bar experiments (Li and Ramesh [128]). We use the LLVS to measure impact velocities of the projectile. The incident bar strain is related to the impact velocity as,

$$\varepsilon = \frac{u}{2c_b} \tag{A.2.2}$$

where u is the impact velocity and c_b is the longitudinal wave speed in the bar. A schematic of the LLVS setup is shown in Figure A.4. The setup involves a point source and optics to generate a collimated light sheet. The beam goes through a slot machined on the gun barrel, downstream, near the impact end and is collected using a

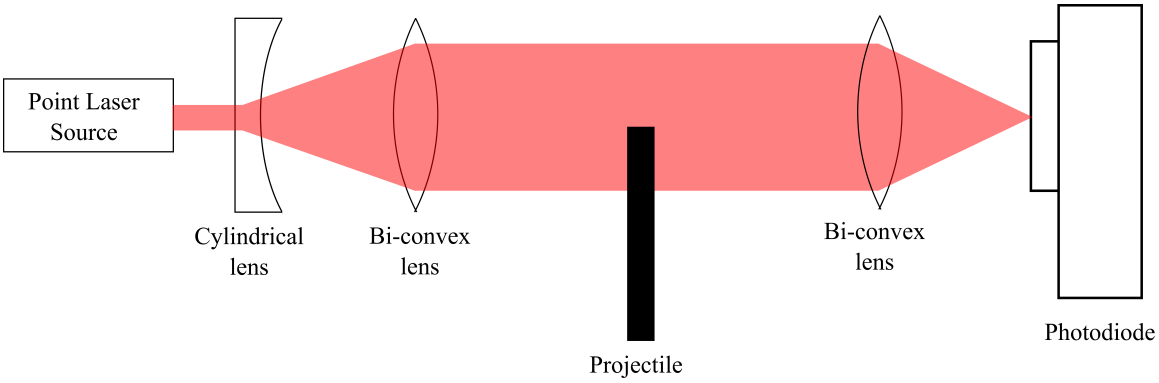

Figure A.4: Schematic of the LLVS setup.

convex lens-photodiode combination. As the projectile passes through the laser sheet, the photodiode records the drop in intensity over time. Using a calibration procedure described next (subsubsection A.2.2.1), the drop in intensity can be correlated to a projectile velocity and acceleration.

A.2.2.1 Calibration of the LLVS

By occluding the laser beam by different displacements (from 1 mm to the maximum width of the laser sheet), the photodiode output voltages are recorded. To ensure minimum error, these measurements are repeated at least twice before every experimental run. A straight line fit is used to relate displacements (s) to the photodiode output (V). Let us denote this function as $s = \mathcal{C}(V)$. During an experiment, this calibration function is related to the projectile velocity and acceleration using simple rigid body kinematics i.e.,

$$s(t) = \mathcal{C}(V(t)) = ut + \frac{1}{2}at^2 \tag{A.2.3}$$

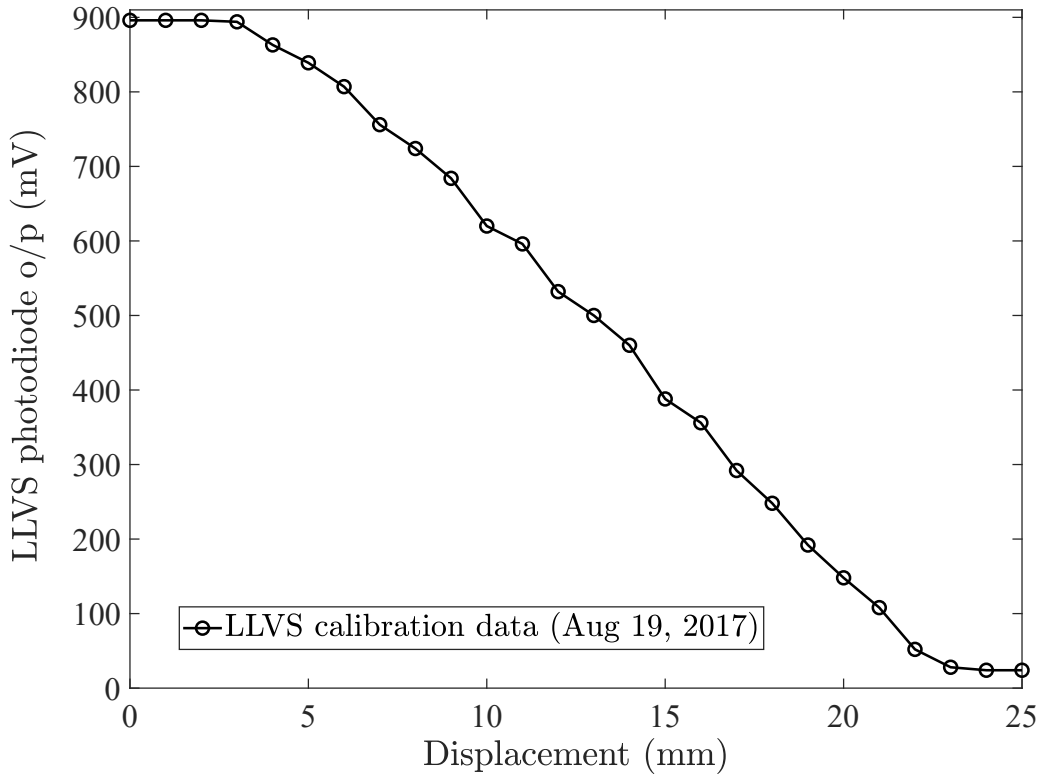

Figure A.5: Calibration of the LLVS.

where u is the impact velocity, t is time and a is the acceleration. The bar design ensures minimum acceleration and hence the second term in Equation A.2.3 may be ignored at lower firing pressures. An example of a raw LLVS signal and the curve fit to extract impact velocities is shown in Figure A.6.

The LLVS is also used for building calibration plots for the gas gun i.e. projectile velocity Vs breech pressure. A calibration plot (data collected in July 2016) is shown in Figure A.7.

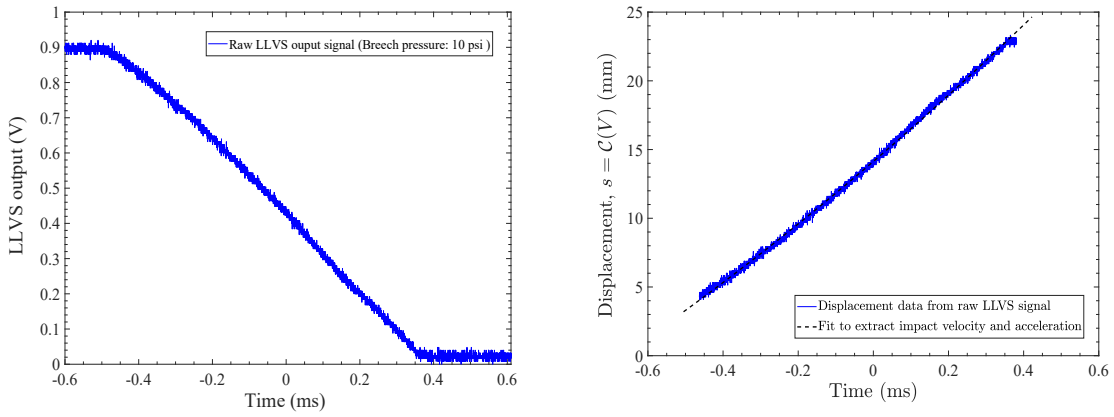

(a) Raw LLVS signal **(b)** Extracting impact velocities

Figure A.6: An example procedure used to extract impact velocities using the LLVS. The experiment was an elastic shot at 10 psi breech pressure.

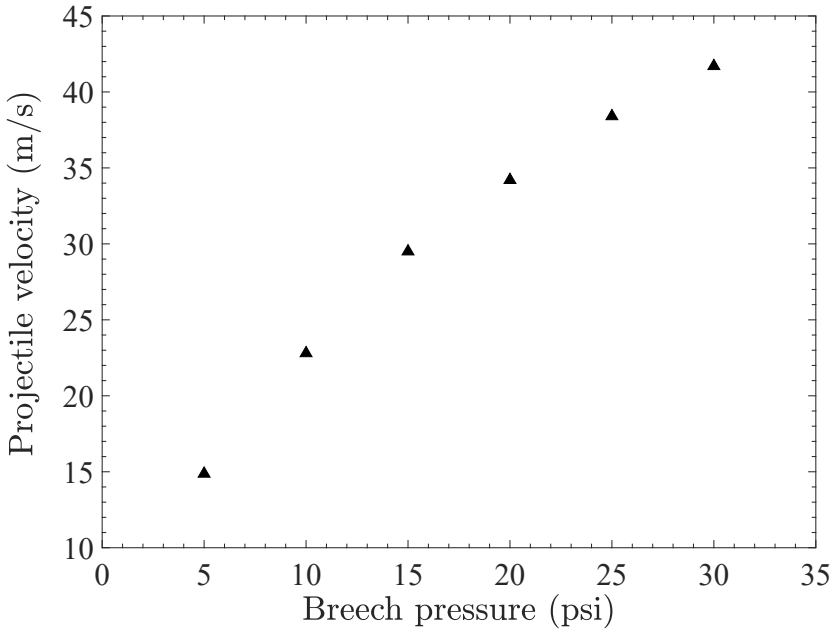

Figure A.7: Desktop kolsky bar gas gun calibration (July 2016).

A.2.3 The normal displacement interferometer

The normal displacement interferometer (NDI) described in section 2.3 (Figure 2.3a) was used for real-time calibration of the transmitted strain gage. The NDI has been used for measuring normal velocities in plate impact experiments (e.g. Klopp et al. [98]) and more recently in miniature kolsky bar experiments (Casem et al. [42]). Our design is similar to that found in Casem et al. [42]. The basic principle of the NDI used in our setup is described in section 2.3 (chapter 2). Here, we describe our data processing procedure.

The objective of this procedure is to detect the peaks in the fringes that directly relate to the back surface displacement history ($s(t)$) of the transmitted bar (refer Equation 2.3.3).

$$s(t) = \frac{N(t)\lambda}{2}$$

where $N(t)$ is the number of fringes as a function of time, λ is the wavelength of the laser source (532 nm).

First, the raw data is filtered using a simple low pass filter written using Matlab®. The data is then smoothed over large enough time steps so as to avoid any erroneous peaks due to noise and small enough so as to not smooth out the fringes themselves. The peaks are detected using an in-built Matlab function (peakfinder). The number of peaks relate to the back surface displacement history of the transmitted bar by Equation 2.3.3. The velocity history ($v(t)$) is calculated by numerically differentiating

the displacement history. Finally, the engineering stress in the specimen is calculated using Equation 2.3.4 restated here.

$$S(t) = \frac{1}{2}\rho_b c_l v(t)$$

The NDI system was initially used to calibrate the transmitted strain gage and is now functional on its own, allowing us to discard the use of semiconductor strain gages on the transmitted bar.

A.2.4 Long term drift in semiconductor strain gages

We show the long term changes in the gage factors of semiconductor strain gages. Figure A.8 shows bar strain signals during an elastic shot (i.e. no specimen was present between the incident and transmitted bars). These signals were collected $\sim$ 3 months after installing the strain gages on the bars. The blue curve (Figure A.8) is data from the NDI, which is the most reliable measurement system in our experiment. The red and the green signals show data obtained from incident and transmitted strain gages. Note that a gage factor of nearly 200 was required to ensure that these signals matched up with the NDI signal (a 100% increase!). The impact velocity obtained from the LLVS signal also agrees with the NDI data indicating that this is indeed the strain generated in the bars.

Hence, while semiconductor strain gages are very useful sensors, care must be taken during application of the gages and during data interpretation. It is important to replace the strain gages at regular intervals and preferably before every new

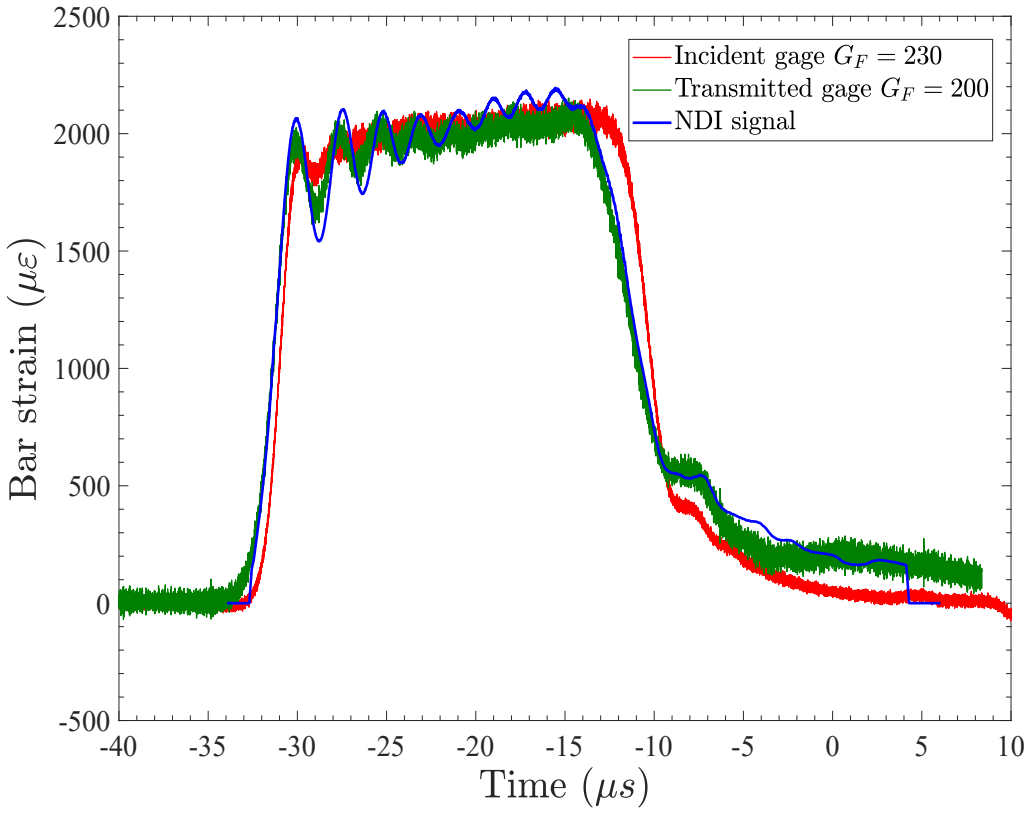

Figure A.8: Drift in semiconductor gage factor. Notice a nearly 100% increase!

sequence of experiments. At the very least, regular calibration checks of the strain gages are necessary.

A.2.5 Experimental protocol

We now list the experimental procedures followed before, during and after a desktop kolsky bar experiment.

- Turn on the power source, oscilloscopes, laser for the NDI and camera. Ensure that the imaging laser is in LIVE mode before turning the laser safety key to

ON. The NDI laser power is usually set between 20-30 mW. For alignment, a lower power (10 mW) is used.

- Let the gages stabilize for 20-30 minutes.
- Adjust the alignment between the projectile and incident bars.
- Clean the bar ends and apply pulse shaper if required. For the end of the transmitted bar (polished to a mirror finish for the NDI) use lens paper and ethanol to avoid scratches.
- Push the projectile down the gun barrel.
- Check the alignment between the incident and transmitted bars.
- Setup all three oscilloscopes (for the strain gage, NDI and LLVS signals) based on length of data being recorded and expected amplitude of signals.
- Record the noise in all signals.
- Balance the Wheatstone bridge boxes.
- Measure the specimen dimensions. FILL EXPERIMENTAL SETTINGS AND SPECIMEN DIMENSIONS IN DATA SHEET.
- Position the specimen between the incident and transmitted bars. Apply a very small amount of grease on both ends in contact with the bars to minimize frictional effects.

- Position the bars such that the laser for the NDI is in focus on the back end of the transmitted bar.
- Align the interferometers. For best accuracy, the number of fringes observed due to the lateral offset between the interfering beams may not exceed three.
- Close the orifice at the breech-barrel interface by manually pushing the firing piston.
- Align the laser line velocity system. *Note:* If calibration is performed before the experiment, do not re-align during this step. If calibration is performed after the experiment, align the LLVS and do not disturb till after calibration.
- Focus the imaging laser beam on the specimen. Focus the camera image and set exposure and inter-frame times for both the camera shutter and the imaging laser source.
- Set delay time between oscilloscope and camera trigger.
- Re-check strain gage balance and interferometer alignment.
- FINAL CHECK: Check if the following signals are being captured.

    1. LLVS signal
    2. Strain gage signals (balanced)
    3. Camera trigger

4. Imaging laser pulse output

5. NDI signal (2 traces)

- Set all oscilloscopes to SINGLE trigger mode.
- Set the camera to ARM for trigger.
- DOUBLE CHECK IF ALL SYSTEMS ARE READY FOR TRIGGER.
- Open nitrogen gas tank.
- Close needle valve to fill breech to desired pressure.
- Close nitrogen tank.
- FIRE!
- Open the vent valve in the gas gun.
- Turn the imaging laser source and NDI laser keys to OFF.
- Save all data (oscilloscope signals and raw camera images).

A.3 Conversion of high strain rate stress-strain curves to stress-plastic strain

The elastic portion of the stress-strain curves obtained from kolsky bar experiments are unreliable. The initial linear portion obtained from the raw data has a slope that

is much lower than the elastic modulus of the material. This is because of continuous wave reverberations in the sample. With each wave reflection from the transmitted bar-sample interface a small portion is transmitted into the bar (Figure 2.2). Hence the effective linear portion that we measure is a summation of multiple little steps that are too small to be resolved by the measurement system.

However, in order to compare this data with quasi-static experimental data, a common measure of strain needs to be used. The true plastic strain is a measure we choose to use as it is most relevant to the problem we address in this study. This section describes a simple method to convert macroscopic total strains measured from kolsky bar experiments to plastic strains.

Figure A.9 shows representative true stress-true strain curves from dynamic compression experiments performed along all three orientations at strain rates of $10^3\ s^{-1}$ (blue hues) and $10^4\ s^{-1}$ (red hues). A total of around 10 valid experiments were performed and analysed along each of the ED and TD orientations for each strain rate range (a total of 40 datasets).

The steps involved in the correction are described below (Figure A.10),

- **Step 1: Identification of the yield point**

  The yield point is identified using an interpolation based method (Figure A.10a and Figure A.10b). The minimum strain at which the data is accurate is chosen (ε_l) manually. An upper limit is chosen as $\varepsilon_u = \varepsilon_l + 0.03$ (Figure A.10a). It is assumed that the slope of the stress-strain curve (m_h) is constant in this small domain. The

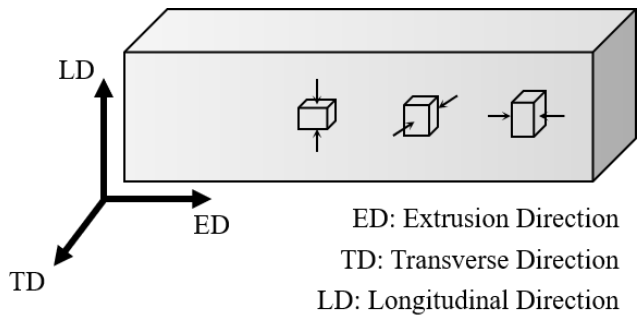

(a) Orientation of specimens with respect to texture

(the hcp crystal is representative of the texture)

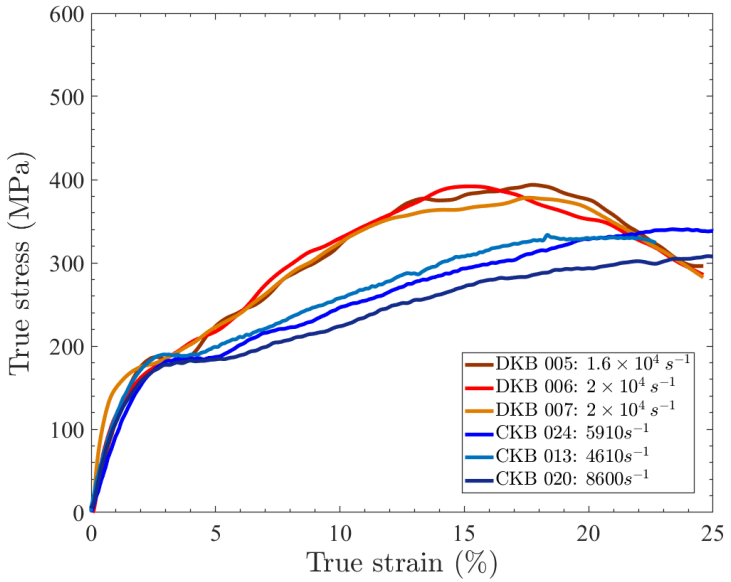

(b) ED compression

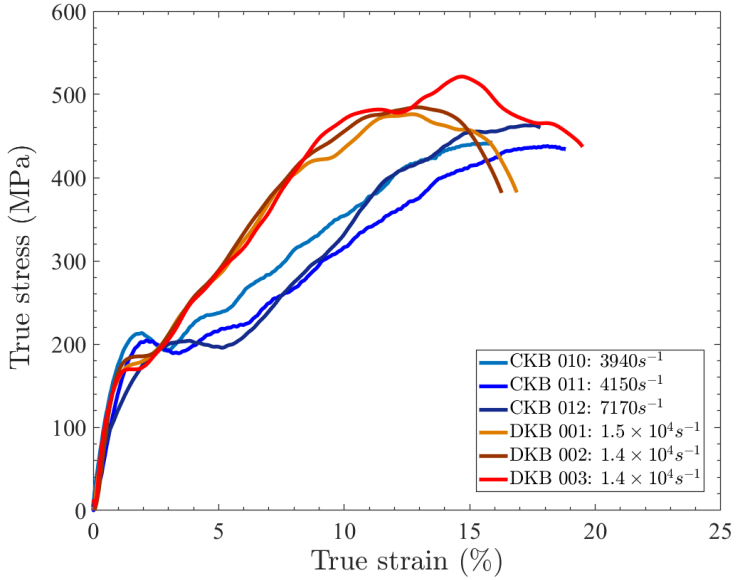

(c) TD compression

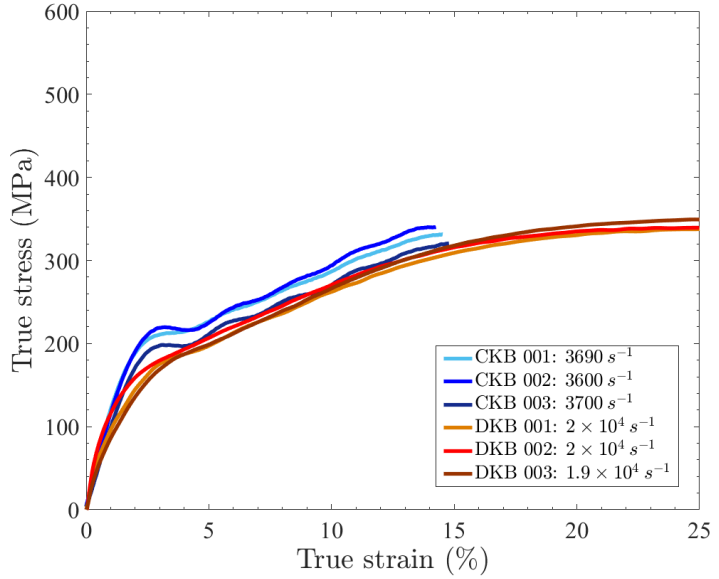

(d) LD compression

Figure A.9: Full true stress-true strain data from high strain rate experiments

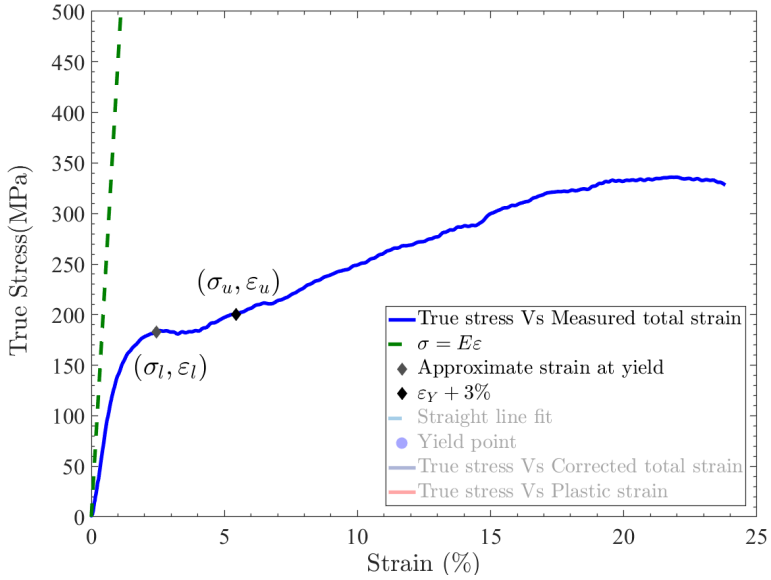

(a) Identification of $(\sigma_l, \varepsilon_l)$ and $(\sigma_u, \varepsilon_u)$ on the stress strain curve.

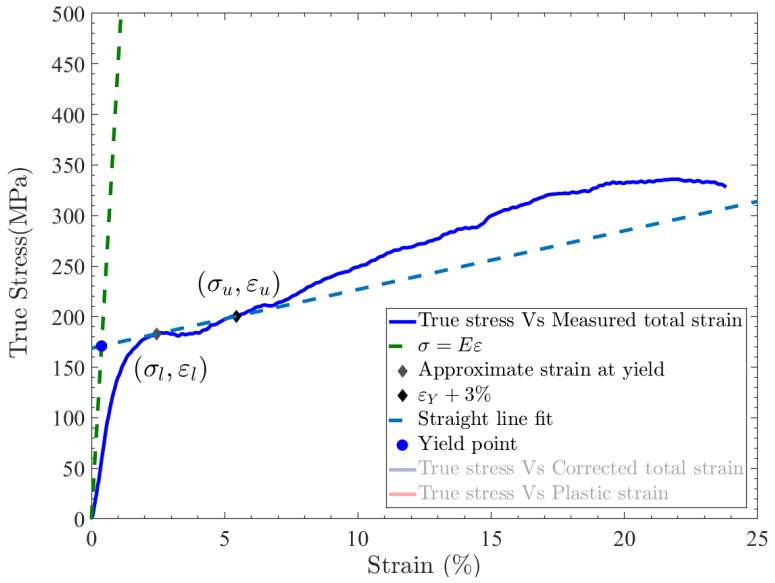

(b) Straight line fit with slope m_h. The blue circle is the corrected yield point.

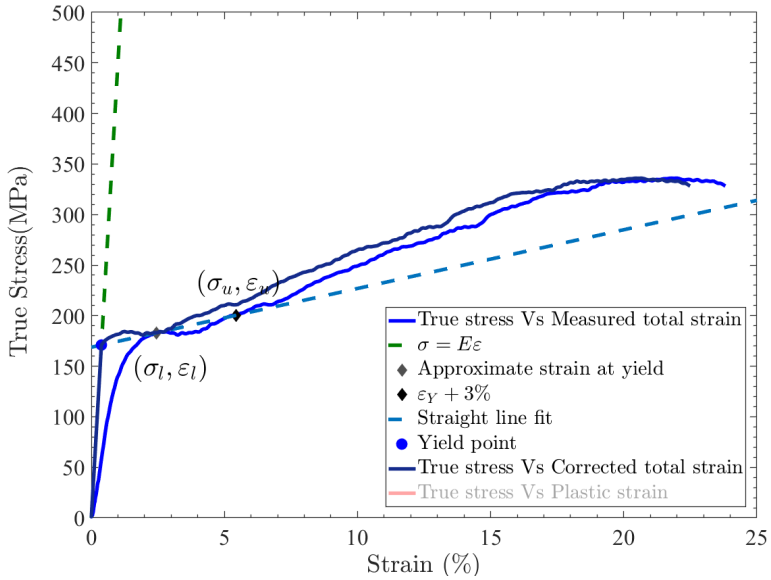

(c) True stress Vs Corrected strain

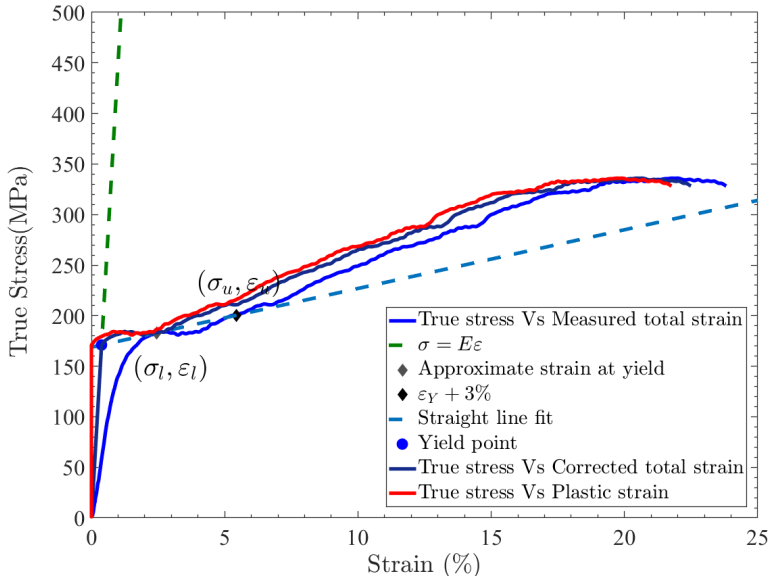

(d) True stress Vs Plastic strain

Figure A.10: Procedure for conversion of true stress-true strain plots to true stress-plastic strain.

intersection of a line with this slope with the elastic curve is defined as the yield stress (Figure A.10b) and is calculated using,

$$\sigma_Y = E\left(\frac{\sigma_m - m_h\varepsilon_m}{E - m_h}\right) \tag{A.3.1}$$

where E is the Young's modulus of the material. $(\sigma_m, \varepsilon_m)$ is any point on the line connecting $(\sigma_l, \varepsilon_l)$ and $(\sigma_u, \varepsilon_u)$. Note that rate effects on Young's modulus were not considered during correction.

- **Step 2: Correcting error in compliance of measured stress-strain curve**

  The compliance in the stress-strain curve due to wave reverberations is corrected using our measure of yield stress (Figure A.10c). A corrected strain (ε_c) measure is calculated using,

$$\varepsilon_c = \begin{cases} \frac{\sigma_m}{E} & , \sigma_m \leq \sigma_Y \\ \varepsilon_m - \varepsilon_l - \frac{\sigma_Y}{E} & , \sigma_m > \sigma_Y \end{cases} \tag{A.3.2}$$

- **Step 3: Extracting plastic strains from corrected strain data** The final step involves using the additive decomposition of total strains into elastic and plastic components.

$$\varepsilon_p = \varepsilon_c - \frac{\sigma}{E} \tag{A.3.3}$$

  Hence a true stress-plastic strain plot can be constructed for reliable comparisons with quasi-static data (Figure A.10d).

A.4 Experimental dataset: Polycrystalline AZ31B alloy

Specimen ID	Strain rate (s^{-1})	Loading Orientation	Recovery (ε_r)
AZ31B_ED_CKB_013	4600	ED	NO
AZ31B_ED_CKB_014	4300	ED	NO
AZ31B_ED_CKB_015	3200	ED	NO
AZ31B_ED_CKB_016	3500	ED	NO
AZ31B_ED_CKB_017	1600	ED	NO
AZ31B_ED_CKB_018	1500	ED	NO
AZ31B_ED_CKB_019	1600	ED	NO
AZ31B_ED_CKB_020	8600	ED	NO
AZ31B_ED_CKB_021	8500	ED	NO
AZ31B_ED_CKB_022	5300	ED	NO
AZ31B_ED_CKB_023	4500	ED	NO
AZ31B_ED_CKB_024	6000	ED	NO
AZ31B_ED_DKB_001	12000	ED	NO
AZ31B_ED_DKB_002	16000	ED	NO
AZ31B_ED_DKB_003	18000	ED	NO
AZ31B_ED_DKB_004	15000	ED	NO

AZ31B_ED_DKB_005	17000	ED	NO
AZ31B_ED_DKB_006	21000	ED	NO
AZ31B_ED_DKB_007	20000	ED	NO
AZ31B_ED_DKB_008	20000	ED	NO
AZ31B_ED_DKB_010	23000	ED	NO
AZ31B_TD_CKB_008	5300	TD	NO
AZ31B_TD_CKB_010	4000	TD	NO
AZ31B_TD_CKB_011	4200	TD	NO
AZ31B_TD_CKB_012	7200	TD	NO
AZ31B_TD_CKB_013	7500	TD	NO
AZ31B_TD_CKB_014	1600	TD	NO
AZ31B_TD_CKB_015	1600	TD	NO
AZ31B_TD_CKB_016	1600	TD	NO
AZ31B_TD_CKB_017	2800	TD	NO
AZ31B_TD_CKB_018	2800	TD	NO
AZ31B_TD_CKB_019	1600	TD	NO
AZ31B_TD_CKB_020	3600	TD	NO
AZ31B_TD_DKB_001	16000	TD	NO
AZ31B_TD_DKB_002	15000	TD	NO
AZ31B_TD_DKB_003	15000	TD	NO
AZ31B_TD_DKB_005	15000	TD	NO

AZ31B_TD_DKB_006	18000	TD	NO
AZ31B_TD_DKB_007	18000	TD	NO
AZ31B_TD_DKB_008	20000	TD	NO
AZ31B_TD_DKB_009	16000	TD	NO
AZ31B_TD_DKB_011	26000	TD	NO
AZ31B_TD_DKB_012	23000	TD	NO
AZ31B_TD_DKB_013	24000	TD	NO
AZ31B_LD_CKB_001	3600	LD	NO
AZ31B_LD_CKB_002	3600	LD	NO
AZ31B_LD_CKB_004	3500	LD	NO
AZ31B_LD_DKB_004	18000	LD	NO
AZ31B_LD_DKB_006	20000	LD	NO
AZ31B_LD_DKB_007	20000	LD	NO
AZ31B_LD_DKB_008	19000	LD	NO
AZ31B_ED_REC_001	∼5000	ED	YES (12%)
AZ31B_ED_REC_002	∼5000	ED	YES (10%)
AZ31B_ED_REC_003	∼5000	ED	YES (10%)
AZ31B_ED_REC_004	∼5000	ED	YES (5%)
AZ31B_ED_REC_005	∼5000	ED	YES (6%)
AZ31B_TD_REC_001	∼4000	TD	YES (5%)
AZ31B_TD_REC_002	∼4000	TD	YES (5%)

AZ31B_TD_REC_003	∼4000	TD	YES (6%)

Table A.1: List of dynamic compression experiments performed on polycrystalline AZ31B (chapter 2)

A.5 Experimental dataset: Single crystal magnesium

Specimen ID	Strain rate (s^{-1})	Recovery (Recovery strain)	Imaging
SCMg001	1700	NO	YES
SCMg002	1700	YES (14%)	YES
SCMg003	1700	YES (3%)	YES
SCMg004	1700	YES (3%)	YES
SCMg005	1500	NO	YES
SCMg006	3000	NO	NO
SCMg007	2500	NO	NO
SCMg008	2700	NO	YES (HIGH MAG)
SCMg009	3000	NO	YES (HIGH MAG)
SCMg010	3000	YES (2.5%)	YES
SCMg011	3000	NO	YES
SCMg012	2100	NO	YES

SCMg013	2000	NO	YES
SCMg014	2000	NO	YES
SCMg015	2000	NO	YES
SCMg016	2000	NO	YES
SCMg017	2000	YES (2.5%)	YES
SCMg018	2000	YES (1.5%)	YES

Table A.2: List of experiments performed on single crystal magnesium. The imaging data for specimen ID's marked in red were not suited for quantitative image processing. Macroscopic data for recovery experiments were not processed due to small recovery strains.

Appendix B

Transformation between laboratory and twin coordinate systems in single crystal magnesium

B.1 Calculation of crystallographic angles in single crystal magnesium

In cubic materials (fcc and bcc) calculation of angles between lattice vectors and reciprocal lattice vectors (or planes) is straightforward as the basis vectors of the unit cell can be directly compared to the laboratory Cartesian coordinate system. However, the basis vectors in the hcp lattice are a little less trivial. The standard and

most convenient Miller index notation for hcp systems is the 4-index notation and the basis vectors in the 4-index and 3-index notation are not parallel to each other. Since most of the material science literature works in the 4-index notation we will continue to use the 4-index notation.

To calculate the angle between lattice vectors a 4-index direct metric tensor ($\mathbf{G}$) was used and to calculate the angles between reciprocal lattice vectors a 4-index reciprocal metric tensor($\mathbf{G}^*$) was used. The metric tensor is simply a transformation tensor whose terms are the dot products of the basis vectors of the unit cell. The dot product between two lattice vectors of some arbitrary basis vector set $a_i : i = 1, 2, 3...$ would be,

$$\mathbf{p}.\mathbf{q} = p_i\mathbf{a_i}.q_j\mathbf{a_j} = p_i\mathbf{a_i}.\mathbf{a_j}q_j = p_iG_{ij}q_j \tag{B.1.1}$$

in Einstein's notation. For a cubic system, the basis vectors $a_i : i = 1, 2, 3$ are orthonormal and the metric tensor becomes an identity tensor. Hence, the dot product reduces to p_iq_i. Since the basis vectors in the hcp lattice are not cartesian in the 4-index notation (Figure 4.6a), the metric tensors are non-trivial. The metric tensor for hcp systems (De Graef [129]) can easily be calculated given the basis vectors. The direct metric tensor (in matrix form) is given as,

$$\mathbf{G} = \frac{a^2}{2}\begin{bmatrix} 2 & -1 & -1 & 0 \\ -1 & 2 & -1 & 0 \\ -1 & -1 & 2 & 0 \\ 0 & 0 & 0 & \frac{2c^2}{a^2} \end{bmatrix} \tag{B.1.2}$$

and the reciprocal metric tensor is given as,

$$\mathbf{G}^* = \frac{2}{9a^2}\begin{bmatrix} 2 & -1 & -1 & 0 \\ -1 & 2 & -1 & 0 \\ -1 & -1 & 2 & 0 \\ 0 & 0 & 0 & \frac{9a^2}{2c^2} \end{bmatrix} \tag{B.1.3}$$

where a and c are the lattice constants. For magnesium $a = 0.317\,nm$ and $c = 0.515\,nm$. Note that the metric tensors depend on lattice parameters as the basis vectors cannot be normalized to become unit vectors.

The dot product between lattice vectors is obtained from Equation B.1.1. For reciprocal lattice vectors the direct metric tensor $\mathbf{G}$ is replaced by the reciprocal metric tensor $\mathbf{G}^*$. Expanding these out, the angle between two lattice vectors $\mathbf{p}$ and $\mathbf{q}$ are given as,

$$\cos\theta = \frac{\mathbf{p}.\mathbf{q}}{|\mathbf{p}||\mathbf{q}|} = \frac{p_i G_{ij} q_j}{\sqrt{p_i G_{ij} p_j}\sqrt{q_i G_{ij} q_j}} \tag{B.1.4}$$

Angle between reciprocal lattice vectors are the same except that G_{ij} is replaced by G^*_{ij}. The angle between a lattice vector ($\mathbf{p}$) and reciprocal lattice vector ($\mathbf{q}$) is given by,

$$\cos\theta = \frac{p_i q_i}{\sqrt{p_i G_{ij} p_j}\sqrt{q_i G^*_{ij} q_j}} \tag{B.1.5}$$

B.2 Transformation between specimen and twin coordinate system

To transform the stress, strain and strain rate tensors between the laboratory coordinate system and the twin coordinate system we use a rotation tensor simply using angles calculated by the method described in section B.1. The basis vectors in the laboratory frame of reference were chosen such that they aligned along the compression direction, imaging direction and the mutually perpendicular direction (pointing towards the top face of the sample) respectively (Figure 4.2). The corresponding basis vectors are denoted using the 4-index notation as,

$$\mathbf{a_1} = [\bar{1}\ \bar{1}\ 2\ 0];\ \mathbf{a_2} = [\bar{1}\ 1\ 0\ 0];\ \mathbf{a_3} = [0\ 0\ 0\ 1] \tag{B.2.1}$$

The basis vectors for the twin frame of reference (Figure 4.6a) were defined as the twin plane normal K_1, the twinning shear direction η_1 and their mutually perpendicular vector. For the twin system (K_1, η_1) marked by the red plane in Figure 4.6a the basis vectors were defined as,

$$\mathbf{a_1'} = \eta_1 = [1\ 0\ \bar{1}\ 1];\ \mathbf{a_3'} = n_{K_1} = \left[\frac{-2}{3a^2}\ 0\ \frac{2}{3a^2}\ \frac{2}{c^2}\right];\ \mathbf{a_2'} = \mathbf{a_3'} \times \mathbf{a_1'} = [1\ \bar{2}\ 1\ 0] \tag{B.2.2}$$

Again here a and c are the lattice constants. Note the normal to the twin plane depends on these constants as the reciprocal basis vectors for a hcp system depend on these parameters. These vectors are known (De Graef [129]) and are simply obtained

as

$$a_i^* = G_{ij}^* a_j \tag{B.2.3}$$

The lattice parameters automatically feature in reciprocal space from Equation B.1.3. Using the two coordinate frames defined with respect to the laboratory and the twin frame of reference a transformation tensor is simply,

$$R_{ij} = \mathbf{a_i^{'}}.\mathbf{a_j} \tag{B.2.4}$$

By this method, the transformation tensor for different twin variants identified from Electron Backscattered Diffraction Microscopy (EBSD) data (chapter 6) can be calculated. Hence stress, strain rate tensors can be transformed to the twin frame of reference based on expected boundary and initial conditions in the laboratory frame of reference.

The rotation matrices hence derived for conjugate (K_1, η_1) is,

$$R_{C1} = \begin{bmatrix} -0.6317 & -0.3647 & 0.6841 \\ 0.5 & -0.866 & 0 \\ 0.5925 & 0.342 & 0.7294 \end{bmatrix} \tag{B.2.5}$$

and for conjugate (K_2, η_2),

$$R_{C2} = \begin{bmatrix} 0.6317 & -0.3647 & 0.6841 \\ 0.5 & 0.866 & 0 \\ -0.5925 & 0.342 & 0.7294 \end{bmatrix} \tag{B.2.6}$$

B.3 Calculation of geometric factor α

The geometric factor α in subsection 4.8.9 was calculated using the rotation matrices derived in section B.2 (equations Equation B.2.5 and Equation B.2.6). For one conjugate, a shear strain of 1 was imposed along the twinning shear direction and transformed to the specimen coordinate system. The strain tensor in the twin coordinate system was,

$$\varepsilon^{'} = \begin{bmatrix} 0 & 0 & 1 \\ 0 & 0 & 0 \\ 1 & 0 & 0 \end{bmatrix} \tag{B.3.1}$$

The basic assumption used here is that at early stages of twinning a bulk of the plastic strain (or strain rate) is concentrated on the twin plane. We perform the inverse transformation corresponding to conjugate (K_1, η_1) i.e. R_{C1} (Equation B.2.5). This results in the strain tensor in the specimen coordinate system,

$$\varepsilon = \begin{bmatrix} -0.75 & -0.43 & -0.06 \\ -0.43 & -0.25 & -0.03 \\ -0.06 & -0.03 & 1 \end{bmatrix} \tag{B.3.2}$$

The geometric factor α is,

$$\alpha = \frac{\varepsilon_{11}}{\varepsilon^{'}_{13}} = 0.75 \tag{B.3.3}$$

Appendix C

Free energy density with strain gradient effects

Following Gurtin [18], we describe visco-plastic free energy functions with strain gradient effects. These models may prove useful near the twin boundary where potential gradients in strain may exist. Since experiments in the past have not focused on this aspect of the twin boundary, we do not know if this additional complication in the defect energy is necessary.

C.1 Constitutive restrictions

In this case, an additional independent variable, $\mathbb{G}^{vp} = \boldsymbol{\nabla F^{vp}}$, is introduced into the constitutive functions (Equation 5.6.9). The new set of constitutive relations are,

$$\Psi = \tilde{\Psi}^{e}(\boldsymbol{E^{e}}, \Theta) + \tilde{\Psi}^{vp}(\boldsymbol{F^{vp}}, \mathbb{G}^{\boldsymbol{vp}}, \{g\}, \{\nu\}) \tag{C.1.1a}$$

$$\boldsymbol{\sigma} = \tilde{\boldsymbol{\sigma}}(\boldsymbol{E^{e}}, \boldsymbol{F^{vp}}, \mathbb{G}^{\boldsymbol{vp}}, \{g\}, \{\nu\}) \tag{C.1.1b}$$

$$\tau^{\alpha} = \boldsymbol{\sigma} : \boldsymbol{s^{\alpha}} \otimes \boldsymbol{m^{\alpha}} = \tilde{\tau}^{\alpha}(\boldsymbol{F^{vp}}, \mathbb{G}^{\boldsymbol{vp}}, \{g\}, \{\nu\}) \tag{C.1.1c}$$

$$\pi^{\alpha} = \tilde{\pi}^{\alpha}(\boldsymbol{F^{vp}}, \mathbb{G}^{\boldsymbol{vp}}, \{g\}, \{\nu\}) \tag{C.1.1d}$$

$$\xi^{\alpha} = \tilde{\xi}^{\alpha}(\boldsymbol{F^{vp}}, \mathbb{G}^{\boldsymbol{vp}}, \{g\}, \{\nu\}) \tag{C.1.1e}$$

$$\dot{\boldsymbol{F}}^{\boldsymbol{vp}} = \sum_{\alpha=1}^{N_s} \nu^{\alpha} \boldsymbol{M^{\alpha}} \tag{C.1.1f}$$

The variational derivative of Ψ is,

$$\dot{\Psi} = \frac{\partial \Psi^{e}}{\partial \boldsymbol{E^{e}}} . \dot{\boldsymbol{E}}^{\boldsymbol{e}} + \frac{\partial \Psi^{e}}{\partial \Theta} . \dot{\Theta} + \frac{\partial \Psi^{vp}}{\partial \boldsymbol{F^{vp}}} . \dot{\boldsymbol{F}}^{\boldsymbol{vp}} + \frac{\partial \Psi^{vp}}{\partial \mathbb{G}^{vp}} \dot{\mathbb{G}}^{vp} + \sum_{\alpha=1}^{N_s} \frac{\partial \Psi^{vp}}{\partial g^{\alpha}} . \dot{g}^{\alpha} \tag{C.1.2}$$

where,

$$\dot{\mathbb{G}}^{vp} = \sum_{\alpha=1}^{N_s} \left[\boldsymbol{\nabla} \nu^{\alpha} \otimes \boldsymbol{M}^{\alpha} + \nu^{\alpha} \boldsymbol{\nabla M^{\alpha}} \right] \tag{C.1.3}$$

Using the two equations above with the dissipation relation Equation 5.5.13,

$$\begin{aligned} \left[\frac{\partial \Psi^{e}}{\partial \boldsymbol{E^{e}}} - \boldsymbol{S} \right] . \dot{\boldsymbol{E}}^{\boldsymbol{e}} + \left[\frac{\partial \Psi^{e}}{\partial \Theta} + \mathcal{N} \right] \dot{\Theta} + \sum_{\alpha=1}^{N_s} \left[\frac{\partial \Psi^{vp}}{\partial \mathbb{G}^{vp}} . \boldsymbol{M^{\alpha}} - \boldsymbol{\xi}^{\alpha} \right] . \boldsymbol{\nabla} \nu^{\alpha} \\ + \sum_{\alpha=1}^{N_s} \left[\frac{\partial \Psi^{vp}}{\partial \boldsymbol{F^{vp}}} . \boldsymbol{M^{\alpha}} + \frac{\partial \Psi^{vp}}{\partial \mathbb{G}^{vp}} . \boldsymbol{\nabla M^{\alpha}} + \left(\sum_{\beta=1}^{N_s} \frac{\partial \Psi^{vp}}{\partial g^{\beta}} h^{\beta\alpha} \right) sgn(\nu^{\alpha}) - \pi^{\alpha} \right] \nu^{\alpha} \\ + \sum_{\alpha=1}^{N_s} \frac{\partial \Psi^{vp}}{\partial \nu^{\alpha}} \dot{\nu}^{\alpha} + \frac{1}{\Theta} \boldsymbol{\nabla} \Theta . \boldsymbol{q} \leq 0 \end{aligned} \tag{C.1.4}$$

This results in the constitutive restrictions,

$$\boldsymbol{S} = \frac{\partial \Psi^e}{\partial \boldsymbol{E^e}} = \mathbb{C} : \boldsymbol{E^e} = \mathbb{C} : \boldsymbol{F^{vp-T}}(\boldsymbol{E} - \boldsymbol{E^{vp}})\boldsymbol{F^{vp-1}} \tag{C.1.5a}$$

$$(\pi^\alpha)^\pm = \frac{\partial \Psi^{vp}}{\partial \boldsymbol{F^{vp}}}.\boldsymbol{M^\alpha} + \frac{\partial \Psi^{vp}}{\partial \mathbb{G}^{vp}}.\boldsymbol{\nabla} \boldsymbol{M^\alpha} \pm \left(\sum_{\beta=1}^{N_s} \frac{\partial \Psi^{vp}}{\partial g^\beta} h^{\beta\alpha} \right) \tag{C.1.5b}$$

$$\boldsymbol{\xi^\alpha} = \frac{\partial \Psi^{vp}}{\partial \mathbb{G}^{vp}}.\boldsymbol{M^\alpha} \tag{C.1.5c}$$

$$\mathcal{N} = -\frac{\partial \Psi^e}{\partial \Theta} \tag{C.1.5d}$$

$$\boldsymbol{q}.\boldsymbol{\nabla}\Theta \leq 0 \tag{C.1.5e}$$

The microscopic force balance (Equation 5.4.1) now includes an additional term as $\boldsymbol{\xi}^\alpha$ is non-zero.

$$\tau^\alpha = (\pi^\alpha)^\pm - \boldsymbol{\nabla} \cdot \boldsymbol{\xi}^\alpha \tag{C.1.6}$$

C.2 Gurtin's free energy density

The total free energy function postulated in Gurtin [18] was,

$$\Psi = \Psi^e(\boldsymbol{E^e}, \Theta) + \Psi^{vp}(\mathbb{G}^{vp}) = \frac{1}{2}(\mathbb{C} : \boldsymbol{E^e} + \beta(\Theta - \Theta_o)) : \boldsymbol{E^e} + \frac{1}{2}\varepsilon|\boldsymbol{\nabla} \boldsymbol{F}^{vp}|^2 \tag{C.2.1}$$

where ε is a proportionality constant that relates the flow stress to the gradient of plastic strain.

Appendix D

Locations of data used in this thesis

All the data used in this thesis has been archived locally on a hard disk drive labeled 'KannanPhD2018Data'. This hard disk will be left behind in the Ramesh lab. Anybody requiring access to this hard disk may contact Prof. K. T. Ramesh at ramesh@jhu.edu. In addition, all the data used for this thesis has been archived online using the Collaborative Research Administration Environment and Data Library (CRAEDL) developed within the Hopkins Extreme Materials Institute (HEMI). The data can be found in the link https://ramesh-lab.craedl.org/directory/4416/.

Specific links for data in each chapter is provided in Table D.1. In each of these links, a 'README.txt' file will provide information about the specific nature of data and locations of data processing codes in the sub-directories. For access to these links, please contact Prof. K. T. Ramesh (ramesh.jhu.edu).

Thesis chapter	Dataset	CRAEDL link
Chapter 2	Conventional Kolsky bar (CKB) data (ECAE AZ31B)	https://ramesh-lab.craedl.org/directory/4430/
	Desktop Kolsky bar (DKB) data (ECAE AZ31B)	https://ramesh-lab.craedl.org/directory/4431/
	LD orientation compression data (both CKB and DKB)	https://ramesh-lab.craedl.org/directory/4446/
	Complete ECAE AZ31B dataset with quasi-static data [36]	https://ramesh-lab.craedl.org/directory/4455/
	Additional datasets for ECAE AZ31B (not used in thesis)	https://ramesh-lab.craedl.org/directory/4448/
Chapter 3	EBSD data (ECAE AZ31B)	https://ramesh-lab.craedl.org/directory/4456/
	High speed imaging (CKB) (ECAE AZ31B)	https://ramesh-lab.craedl.org/directory/4430/
	High speed imaging (DKB) (ECAE AZ31B)	https://ramesh-lab.craedl.org/directory/4431/
Chapter 4	Dynamic compression of single crystal Mg (w/ in-situ images)	https://ramesh-lab.craedl.org/directory/4453/
Chapter 6	Quasi-static stress-strain data (single crystal Mg)	https://ramesh-lab.craedl.org/directory/4458/
	EBSD data (single crystal Mg)	https://ramesh-lab.craedl.org/directory/4457/

Table D.1: Data storage locations

Bibliography

[1] R. Abeyaratne and J. K. Knowles. On the driving traction acting on a surface of strain discontinuity in a continuum. *Journal of the Mechanics and Physics of Solids*, 1990.

[2] Jing Zhang and Shailendra P. Joshi. Phenomenological crystal plasticity modeling and detailed micromechanical investigations of pure magnesium. *Journal of the Mechanics and Physics of Solids*, 60(5):945–972, 2012. ISSN 00225096. doi: 10.1016/j.jmps.2012.01.005. URL http://www.sciencedirect.com/science/article/pii/S0022509612000130.

[3] CE Wehrenberg, David McGonegle, C Bolme, A Higginbotham, A Lazicki, HJ Lee, B Nagler, H-S Park, BA Remington, RE Rudd, et al. In situ x-ray diffraction measurement of shock-wave-driven twinning and lattice dynamics. *Nature*, 550(7677):496, 2017.

[4] P.R Guduru, A.J Rosakis, and G Ravichandran. Dynamic shear bands: an

investigation using high speed optical and infrared diagnostics. *Mechanics of Materials*, 33(7):371–402, jul 2001. doi: 10.1016/s0167-6636(01)00051-5.

[5] JC Gong, LE Malvern, and DA Jenkins. Dispersion investigation in the split Hopkinson pressure bar. *Journal of Engineering Materials and Technology*, 112(3):309–314, 1990. URL http://materialstechnology.asmedigitalcollection.asme.org/article.aspx?articleid=1424435.

[6] Tresa M. Pollock. Weight loss with magnesium alloys. *Science*, 328(5981): 986–987, 2010. ISSN 00368075. doi: 10.1126/science.1182848.

[7] A.A. Luo. Applications: aerospace, automotive and other structural applications of magnesium. In *Fundamentals of Magnesium Alloy Metallurgy*, pages 266–316. Elsevier, 2013. doi: 10.1533/9780857097293.266.

[8] B L Mordike and T Ebert. Magnesium: properties-applications-potential. *Materials Science and Engineering: A*, 302(1):37–45, 2001.

[9] K Eswar Prasad, B Li, N Dixit, M Shaffer, SN Mathaudhu, and KT Ramesh. The dynamic flow and failure behavior of magnesium and magnesium alloys. *Jom*, 66(2):291–304, 2014.

[10] M.F. Ashby. Overview no. 80. *Acta Metallurgica*, 37(5):1273–1293, may 1989. doi: 10.1016/0001-6160(89)90158-2.

[11] J W Christian and S Mahajan. TWINNING. 39:1–157, 1995.

[12] M.R. Barnett. Twinning and the ductility of magnesium alloys. *Materials Science and Engineering: A*, 464(1-2):1–7, aug 2007. doi: 10.1016/j.msea.2006.12.037.

[13] A. Needleman and V. Tvergaard. Analyses of plastic flow localization in metals. *Applied Mechanics Reviews*, 45(3S):S3, 1992. doi: 10.1115/1.3121390.

[14] Marc Andre' Meyers. *Dynamic Behavior of Materials*. 2009. ISBN 9788126547487.

[15] M. H. Yoo and J. K. Lee. Deformation twinning in h.c.p. metals and alloys. *Philosophical Magazine A*, 63(5):987–1000, 1991. ISSN 0141-8610. doi: 10.1080/01418619108213931. URL http://www.tandfonline.com/doi/abs/10.1080/01418619108213931.

[16] J. T. Lloyd and R. Becker. Stress-based crystal analysis of yielding in rolled Mg AZ31B. *Philosophical Magazine*, 96(4):370–386, 2016. ISSN 14786443. doi: 10.1080/14786435.2015.1132854. URL http://www.scopus.com/inward/record.url?eid=2-s2.0-84959543409{&}partnerID=tZOtx3y1.

[17] Phoebus Rosakis and Hungyu Tsai. Dynamic twinning processes in crystals. *International journal of solids and structures*, 32(17-18):2711–2723, 1995.

[18] Morton E Gurtin. On the plasticity of single crystals: free energy, microforces, plastic-strain gradients. *Journal of the Mechanics and Physics of Solids*, 48(5):989–1036, 2000.

[19] W.F.Hosford E.W.Kelley. Plane-strain compression of Magnesium and Magnesium Alloy Crystals. *Trans.AIME*, 242(1):5–13, 1968.

[20] M.R. Barnett. Twinning and the ductility of magnesium alloys. *Materials Science and Engineering: A*, 464(1-2):8–16, aug 2007. doi: 10.1016/j.msea.2007.02.109.

[21] K. Eswar Prasad and K. T. Ramesh. In-situ observations and quantification of twin boundary mobility in polycrystalline magnesium. *Materials Science and Engineering A*, 617:121–126, 2014. ISSN 09215093. doi: 10.1016/j.msea.2014.08.043. URL http://www.sciencedirect.com/science/article/pii/S0921509314010430.

[22] N Dixit, K Y Xie, K J Hemker, and K T Ramesh. Microstructural evolution of pure magnesium under high strain rate loading. *Acta mater.*, 87: 56–67, 2015. URL http://www.sciencedirect.com/science/article/pii/S1359645414009471.

[23] Vignesh Kannan, Kavan Hazeli, and KT Ramesh. The mechanics of dynamic twinning in single crystal magnesium. *Journal of the Mechanics and Physics of Solids*, 2018.

[24] Mark Denis Nave and Matthew Robert Barnett. Microstructures and textures of pure magnesium deformed in plane-strain compression. *Scripta Materialia*, 51(9):881–885, 2004. ISSN 13596462. doi: 10.1016/j.scriptamat.2004.07.002.

[25] Sean R. Agnew and Özgür Duygulu. Plastic anisotropy and the role of non-basal slip in magnesium alloy AZ31B. *International Journal of Plasticity*, 21 (6):1161–1193, 2005. ISSN 07496419. doi: 10.1016/j.ijplas.2004.05.018.

[26] S. B. Yi, C. H.J. Davies, H. G. Brokmeier, R. E. Bolmaro, K. U. Kainer, and J. Homeyer. Deformation and texture evolution in AZ31 magnesium alloy during uniaxial loading. *Acta Materialia*, 54(2):549–562, 2006. ISSN 13596454. doi: 10.1016/j.actamat.2005.09.024.

[27] Christopher S. Meredith, Jeffrey T. Lloyd, and Tomoko Sano. The quasi-static and dynamic response of fine-grained mg alloy AMX602: An experimental and computational study. *Materials Science and Engineering: A*, 673:73–82, sep 2016. doi: 10.1016/j.msea.2016.07.035.

[28] I Ulacia, N V Dudamell, F Gálvez, S Yi, M T Pérez-Prado, and I Hurtado. Mechanical behavior and microstructural evolution of a Mg AZ31 sheet at dynamic strain rates. *Acta Materialia*, 58(8):2988–2998, 2010. ISSN 13596454. doi: 10.1016/j.actamat.2010.01.029.

[29] S. B. Yi, S. Zaefferer, and H. G. Brokmeier. Mechanical behaviour and microstructural evolution of magnesium alloy AZ31 in tension at different temperatures. *Materials Science and Engineering A*, 424(1-2):275–281, 2006. ISSN 09215093. doi: 10.1016/j.msea.2006.03.022.

[30] W J Kim, C W An, Y S Kim, and S I Hong. Scripta Materialia 47 (2002). 2002.

[31] S. R. Agnew, J. A. Horton, T. M. Lillo, and D. W. Brown. Enhanced ductility in strongly textured magnesium produced by equal channel angular processing. *Scripta Materialia*, 50(3):377–381, 2004. ISSN 13596462. doi: 10.1016/j.scriptamat.2003.10.006.

[32] Roberto B. Figueiredo and Terence G. Langdon. Principles of grain refinement and superplastic flow in magnesium alloys processed by ECAP. *Materials Science and Engineering A*, 501(1-2):105–114, 2009. ISSN 09215093. doi: 10.1016/j.msea.2008.09.058.

[33] Xia Yu, Yulong Li, Qiuming Wei, Yazhou Guo, Tao Suo, and Feng Zhao. Microstructure and mechanical behavior of ECAP processed AZ31B over a wide range of loading rates under compression and tension. *Mechanics of Materials*, 86:55–70, 2015. ISSN 01676636. doi: 10.1016/j.mechmat.2015.03.001.

[34] J Koike, T Kobayashi, T Mukai, H Watanabe, M Suzuki, K Maruyama, and K Higashi. The activity of non-basal slip systems and dynamic recovery at room temperature in fine-grained AZ31b magnesium alloys. *Acta Mater*, 51(7): 2055–2065, 2003.

[35] B. Li, S. Joshi, K. Azevedo, E. Ma, K. T. Ramesh, R. B. Figueiredo, and T. G. Langdon. Dynamic testing at high strain rates of an ultrafine-grained magnesium alloy processed by ECAP. *Materials Science and Engineering A*, 517(1-2):24–29, 2009. ISSN 09215093. doi: 10.1016/j.msea.2009.03.032.

[36] N M Krywopusk, L J Kecskes, and T P Weihs. Mechanical behavior of rolled and ECAE processed AZ31B.

[37] Kaliat T. Ramesh. High Rates and Impact Experiments. In *Springer Handbook of Experimental Solid Mechanics*, pages 929–960. Springer, 2008. ISBN 978-0-387-30877-7. doi: 10.1007/978-0-387-30877-7_33. URL http://link.springer.com/10.1007/978-0-387-30877-7{_}33.

[38] Weinong W Chen and Bo Song. *Split Hopkinson (Kolsky) bar: design, testing and applications*. Springer Science & Business Media, 2010.

[39] DA Gorham. A numerical method for the correction of dispersion in pressure bar signals. *Journal of Physics E: Scientific Instruments*, 16(6):477, 1983. URL http://iopscience.iop.org/article/10.1088/0022-3735/16/6/008.

[40] D. Jia and K. T. Ramesh. A rigorous assessment of the benefits of miniaturization in the Kolsky bar system. *Experimental Mechanics*, 44(5):445–454, 2004. ISSN 00144851. doi: 10.1177/0014485104047608.

[41] E. L. Huskins, B. Cao, and K. T. Ramesh. Strengthening mechanisms in an Al-Mg alloy. *Materials Science and Engineering A*, 527(6):1292–1298, 2010. ISSN 09215093. doi: 10.1016/j.msea.2009.11.056.

[42] D. T. Casem, S. E. Grunschel, and B. E. Schuster. Normal and Transverse Displacement Interferometers Applied to Small Diameter Kolsky Bars.

Experimental Mechanics, 52(2):173–184, jul 2012. ISSN 00144851. doi: 10.1007/s11340-011-9524-x.

[43] I Ulacia, S Yi, M T Perez-Prado, N V Dudamell, F Gálvez, D Letzig, and I Hurtado. Texture Evolution of AZ31 Magnesium Alloy Sheet at High Strain Rates. *4th International Conference on High Speed Forming*, 709:189–197, 2010. ISSN 1662-9752. doi: 10.17877/DE290R-8669.

[44] Sanghyun Lee, Hye Jeong Ham, Su Yong Kwon, Sok Won Kim, and Chang Min Suh. Thermal conductivity of magnesium alloys in the temperature range from-125 c to 400 c. *International Journal of Thermophysics*, 34(12):2343–2350, 2013.

[45] Dipankar Ghosh, Owen T Kingstedt, and Guruswami Ravichandran. Plastic work to heat conversion during high-strain rate deformation of mg and mg alloy. *Metallurgical and Materials Transactions A*, 48(1):14–19, 2017.

[46] K. T. Ramesh. Effects of high rates of loading on the deformation behavior and failure mechanisms of hexagonal close-packed metals and alloys. *Metallurgical and Materials Transactions A*, 33(13):927–935, 2002. ISSN 1073-5623. doi: 10.1007/s11661-002-1025-1.

[47] J. R. Rice. Inelastic constitutive relations for solids: An internal variables theory and its application to metal plasticity. *Journal of the Mechanics and Physics of Solids*, 19(6):433–455, 1971. ISSN 0022-5096.

[48] Yingrui Chang and Dennis M. Kochmann. A variational constitutive model for slip-twinning interactions in hcp metals: Application to single- and polycrystalline magnesium. *International Journal of Plasticity*, 73:39–61, 2015. ISSN 07496419. doi: 10.1016/j.ijplas.2015.03.008. URL http://dx.doi.org/10.1016/j.ijplas.2015.03.008.

[49] D. Peirce, R.J. Asaro, and A. Needleman. Material rate dependence and localized deformation in crystalline solids. *Acta Metallurgica*, 31(12):1951–1976, dec 1983. doi: 10.1016/0001-6160(83)90014-7.

[50] UF Kocks. Polyslip in polycrystals. *Acta Metallurgica*, 6(2):85–94, 1958.

[51] R. J. Asaro. Crystal plasticity. *Journal of Applied Mechanics*, 50(4b):921, 1983. doi: 10.1115/1.3167205.

[52] A Marchand and J Duffy. An experimental study of the formation process of adiabatic shear bands in a structural steel. *Journal of the Mechanics and Physics of Solids*, 36(3):251–283, 1988.

[53] M A Meyers, G Subhash, B K Kad, and L Prasad. Evolution of microstructure and shear-band formation in a-hcp titanium. *Mech. Mater.*, 17:175–193, 1994.

[54] Re L Bell and RW Cahn. The dynamics of twinning and the interrelation of slip and twinning in zinc crystals. In *Proceedings of the Royal Society of London A: Mathematical, Physical and Engineering Sciences*, volume 239, pages 494–521. The Royal Society, 1957.

[55] Ming Zhe Bian and Kwang Seon Shin. {1012} Twinning Behavior in Magnesium Single Crystal. *Metals and Materials International*, 19(5):999–1004, 2013. ISSN 15989623. doi: 10.1007/s12540-013-5012-4.

[56] M Zhou, AJ Rosakis, and G Ravichandran. Dynamically propagating shear bands in impact-loaded prenotched plates—i. experimental investigations of temperature signatures and propagation speed. *Journal of the Mechanics and Physics of Solids*, 44(6):981–1006, 1996.

[57] I. Ulacia, N. V. Dudamell, F. Gálvez, S. Yi, M. T. Pérez-Prado, and I. Hurtado. Mechanical behavior and microstructural evolution of a Mg AZ31 sheet at dynamic strain rates. *Acta Materialia*, 58(8):2988–2998, 2010. ISSN 13596454. doi: 10.1016/j.actamat.2010.01.029.

[58] D. R. Chichili, K. T. Ramesh, and K. J. Hemker. The high-strain-rate response of alpha-titanium: Experiments, deformation mechanisms and modeling. *Acta Materialia*, 46(3):1025–1043, jan 1998. ISSN 13596454. doi: 10.1016/S1359-6454(97)00287-5. URL https://www.sciencedirect.com/science/article/pii/S1359645497002875.

[59] D. W. Brown, I. J. Beyerlein, T. A. Sisneros, B. Clausen, and C. N. Tomé. Role of twinning and slip during compressive deformation of beryllium as a function of strain rate. *International Journal of Plasticity*, 29(1):120–135, feb

2012. ISSN 07496419. doi: 10.1016/j.ijplas.2011.08.006. URL https://www.sciencedirect.com/science/article/pii/S074964191100146X.

[60] Mark Denis Nave and Matthew Robert Barnett. Microstructures and textures of pure magnesium deformed in plane-strain compression. *Scripta Materialia*, 51(9):881–885, 2004. ISSN 13596462. doi: 10.1016/j.scriptamat.2004.07.002.

[61] Meng Zhao, Vignesh Kannan, and KT Ramesh. The dynamic plasticity and dynamic failure of a magnesium alloy under multiaxial loading. *Acta Materialia*, 154:124–136, 2018.

[62] MA Meyers, O Vöhringer, and VA Lubarda. The onset of twinning in metals: a constitutive description. *Acta materialia*, 49(19):4025–4039, 2001.

[63] Michael Ortiz and Laurent Stainier. The variational formulation of viscoplastic constitutive updates. *Computer methods in applied mechanics and engineering*, 171(3-4):419–444, 1999.

[64] N. V. Dudamell, I. Ulacia, F. Gálvez, S. Yi, J. Bohlen, D. Letzig, I. Hurtado, and M. T. Pérez-Prado. Twinning and grain subdivision during dynamic deformation of a Mg AZ31 sheet alloy at room temperature. *Acta Materialia*, 59(18):6949–6962, oct 2011. ISSN 13596454. doi: 10.1016/j.actamat.2011.07.047. URL https://www.sciencedirect.com/science/article/pii/S1359645411005337{#}b0275.

[65] NV Dudamell, P Hidalgo-Manrique, A Chakkedath, Z Chen, CJ Boehlert, F Gálvez, S Yi, J Bohlen, D Letzig, and MT Pérez-Prado. Influence of strain rate on the twin and slip activity of a magnesium alloy containing neodymium. *Materials Science and Engineering: A*, 583:220–231, 2013.

[66] Q. Yang and A. K. Ghosh. Deformation behavior of ultrafine-grain (UFG) AZ31B Mg alloy at room temperature. *Acta Materialia*, 54(19):5159–5170, 2006. ISSN 13596454. doi: 10.1016/j.actamat.2006.06.043.

[67] M. R. Barnett, Z. Keshavarz, A. G. Beer, and D. Atwell. Influence of grain size on the compressive deformation of wrought Mg-3Al-1Zn. *Acta Materialia*, 52 (17):5093–5103, 2004. ISSN 13596454. doi: 10.1016/j.actamat.2004.07.015.

[68] M. R. Barnett. A rationale for the strong dependence of mechanical twinning on grain size. *Scripta Materialia*, 59(7):696–698, 2008. ISSN 13596462. doi: 10.1016/j.scriptamat.2008.05.027.

[69] Ramin Aghababaei and Shailendra P. Joshi. Micromechanics of tensile twinning in magnesium gleaned from molecular dynamics simulations. *Acta Materialia*, 69:326–342, 2014. ISSN 13596454. doi: 10.1016/j.actamat.2014.01.014. URL http://dx.doi.org/10.1016/j.actamat.2014.01.014.

[70] Tomoyuki Takeuchi. Dynamic Propagation of Deformation Twins in Iron Single Crystals. 21(12):2616–2622, 1966. ISSN 0031-9015. doi: 10.1143/JPSJ.21.2616.

[71] JN Johnson and RW Rohde. Dynamic Deformation Twinning in Shock-Loaded Iron. *Journal of Applied Physics*, 42(11):4171–4182, 1971.

[72] A Serra, D. J Bacon, and R. C Pond. The crystallography and core structure of twinning dislocations in H.C.P. metals. 36(12):3183–3203, 1988. ISSN 0001-6160. doi: 10.1016/0001-6160(88)90054-5.

[73] R. A. Lebensohn and C. N. Tome. A study of the stress state associated with twin nucleation and propagation in anisotropic materials. 67(1):187–206, 1993. ISSN 0141-8610. doi: 10.1080/01418619308207151.

[74] IJ Beyerlein and CN Tomé. A probabilistic twin nucleation model for hcp polycrystalline metals. In *Proceedings of the Royal Society of London A: Mathematical, Physical and Engineering Sciences*, page rspa20090661. The Royal Society, 2010.

[75] Y. N. Wang and J. C. Huang. The role of twinning and untwinning in yielding behavior in hot-extruded Mg-Al-Zn alloy. *Acta Materialia*, 55(3):897–905, 2007. ISSN 13596454. doi: 10.1016/j.actamat.2006.09.010.

[76] JH Brunton and MPW Wilson. The kinetics of twinning in zinc and tin crystals. In *Proceedings of the Royal Society of London A: Mathematical, Physical and Engineering Sciences*, volume 309, pages 345–361. The Royal Society, 1969.

[77] D.F. Williams and C.M. Reid. A dynamic study of twin-induced brittle fracture. *Acta Metallurgica*, 1971.

[78] Neha Dixit, Lukasz Farbaniec, and KT Ramesh. Twinning in single crystal Mg under microsecond impact along the< a> axis. *Materials Science and Engineering: A*, 693:22–25, 2017.

[79] E. D.H. Davies and S. C. Hunter. The dynamic compression testing of solids by the method of the split Hopkinson pressure bar. *Journal of the Mechanics and Physics of Solids*, 11(3):155–179, 1963. ISSN 00225096. doi: 10.1016/0022-5096(63)90050-4.

[80] Dingyi Sun, Mauricio Ponga, Kaushik Bhattacharya, and Michael Ortiz. Proliferation of twinning in hcp metals: Application to magnesium. *arXiv:1708.01662*, 2017.

[81] N. Dixit. *A Mechanism Based Investigation Of The Dynamic Behavior Of Pure Magnesium*. PhD thesis, Johns Hopkins University, 2015.

[82] L Remy. Kinetics of fcc deformation twinning and its relationship to stress-strain behaviour. *Acta Metallurgica*, 26(3):443–451, 1978.

[83] TE Mitchell and JP Hirth. The shape, configuration and stress field of twins and martensite plates. *Acta metallurgica et materialia*, 39(7):1711–1717, 1991.

[84] M Arul Kumar, AK Kanjarla, SR Niezgoda, RA Lebensohn, and CN Tomé. Numerical study of the stress state of a deformation twin in magnesium. *Acta Materialia*, 84:349–358, 2015.

[85] M Arul Kumar, Irene Jane Beyerlein, and Carlos N Tomé. Effect of local stress fields on twin characteristics in HCP metals. *Acta Materialia*, 116:143–154, 2016.

[86] Jiahao Cheng and Somnath Ghosh. Crystal plasticity finite element modeling of discrete twin evolution in polycrystalline magnesium. *Journal of the Mechanics and Physics of Solids*, 99:512–538, 2017.

[87] NP Daphalapurkar, JW Wilkerson, TW Wright, and KT Ramesh. Kinetics of a fast moving twin boundary in nickel. *Acta Materialia*, 68:82–92, 2014.

[88] E. W. Kelley. *The Plastic Deformation of Magnesium*. PhD thesis, The University of Michigan, College of Engineering, 1967.

[89] A. H. Cottrell and B. A. Bilby. A mechanism for the growth of deformation twins in crystals. 42(329):573–581, 1951. ISSN 1941-5982. doi: 10.1080/14786445108561272.

[90] N Thompson and DJ Millard. Twin formation in cadmium. *The London, Edinburgh, and Dublin Philosophical Magazine and Journal of Science*, 43(339): 422–440, 1952.

[91] J. Wang, I. J. Beyerlein, and C. N. Tomé. An atomic and probabilistic perspective on twin nucleation in Mg. *Scripta Materialia*, 63(7):741–746, 2010. ISSN 13596462. doi: 10.1016/j.scriptamat.2010.01.047.

[92] Melvin Avrami. Kinetics of phase change. I General theory. *The Journal of Chemical Physics*, 7(12):1103–1112, 1939.

[93] G. B. Olson and M Cohen. A perspective on martensitic nucleation. *Annual Rev. Mater. Sci. 11: 1-30*, 1981.

[94] Konstantin D Molodov, Talal Al-Samman, Dmitri A Molodov, and Sandra Korte-Kerzel. On the twinning shear of twins in magnesium–experimental determination and formal description. *Acta Materialia*, 134:267–273, 2017.

[95] Jian Tu and Songquan Zhang. On the twinning growth mechanism in hexagonal close-packed metals. *Materials & Design*, 96:143–149, 2016.

[96] J. F. Nie, Y. M. Zhu, J. Z. Liu, and X. Y. Fang. Periodic segregation of solute atoms in fully coherent twin boundaries. *Science*, 340(6135):957–960, may 2013. doi: 10.1126/science.1229369.

[97] JN Florando, M Rhee, A Arsenlis, MM LeBlanc, and DH Lassila. Calculation of the slip system activity in deformed zinc single crystals using digital 3-d image correlation data. *Philosophical magazine letters*, 86(12):795–805, 2006.

[98] R.W. Klopp, R.J. Clifton, and T.G. Shawki. Pressure-shear impact and the dynamic viscoplastic response of metals. *Mechanics of Materials*, 4(3-4):375–385, dec 1985. doi: 10.1016/0167-6636(85)90033-x.

[99] Ravi Shivaraman, Vignesh Kannan, Todd. C. Hufnagel, and K. T. Ramesh. private communication, 2018.

[100] Rohan Abeyaratne and James K Knowles. *Evolution of phase transitions: a continuum theory*. Cambridge University Press, 2006.

[101] Erastus H Lee. Elastic-plastic deformation at finite strains. ASME, 1969.

[102] Morton E Gurtin, Eliot Fried, and Lallit Anand. *The mechanics and thermodynamics of continua*. Cambridge University Press, 2010.

[103] A Acharya and TG Shawki. The clausius-duhem inequality and the structure of rate-independent plasticity. *International journal of plasticity*, 12(2):229–238, 1996.

[104] R. J. Asaro and A. Needleman. Overview no. 42 texture development and strain hardening in rate dependent polycrystals. 33:923–953, 1985. ISSN 0001-6160. doi: 10.1016/0001-6160(85)90188-9.

[105] Allan F. Bower. Applied mechanics of solids.

[106] P. Rosakis, A.J. Rosakis, G. Ravichandran, and J. Hodowany. A thermodynamic internal variable model for the partition of plastic work into heat and stored energy in metals. *Journal of the Mechanics and Physics of Solids*, 48(3):581–607, mar 2000. doi: 10.1016/s0022-5096(99)00048-4.

[107] D. Peirce, R. J. Asaro, and A. Needleman. An analysis of nonuniform and localized deformation in ductile single crystals. 30:1087–1119, 1982. ISSN 0001-6160. doi: 10.1016/0001-6160(82)90005-0.

[108] Kelvin Y Xie, Zafir Alam, Alexander Caffee, and Kevin J Hemker. Pyramidal {I} slip in c-axis compressed {M}g single crystals. *Scripta Materialia*, 112: 75–78, 2016.

[109] Rohan Abeyaratne and James K. Knowles. On the propagation of maximally dissipative phase boundaries in solids, 1990.

[110] Morton E. Gurtin, Eliot Fried, and Lallit Anand. The mechanics and thermodynamics of continua, 2010.

[111] James Casey. On the derivation of jump conditions in continuum mechanics. *The International Journal of Structural Changes in Solids*, 3(2):61–84, 2011.

[112] Bruce Alexander Bilby and AG Crocker. The theory of the crystallography of deformation twinning. *Proc. R. Soc. Lond. A*, 288(1413):240–255, 1965.

[113] PG Partridge. The crystallography and deformation modes of hexagonal close-packed metals. *Metallurgical reviews*, 12(1):169–194, 1967.

[114] IJ Beyerlein, J Wang, M Barnett, and CN Tome. Double twinning mechanisms in magnesium alloys via dissociation of lattice dislocations. *Proceedings of the Royal Society A*, 468(2141):1496–1520, 2012.

[115] M R Barnett, Z Keshavarz, A G Beer, and X MA. Non-Schmid Behaviour During Scondary Twinning in a Polycrystalline Magnesium Alloy. *Acta Materialia*, 56(1):5–15, 2008.

[116] Neha Dixit, Lukasz Farbaniec, and K. T. Ramesh. Twinning in single crystal mg under microsecond impact along the <a> axis. *Materials Science and Engineering A*, 693:22–25, 2017.

[117] S. R. Agnew, D. W. Brown, and C. N. Tomé. Validating a polycrystal model for the elastoplastic response of magnesium alloy AZ31 using in situ neutron diffraction. *Acta Materialia*, 54(18):4841–4852, 2006. ISSN 13596454. doi: 10.1016/j.actamat.2006.06.020.

[118] P. K. Lambert, C. J. Hustedt, K. S. Vecchio, E. L. Huskins, D. T. Casem, S. M. Gruner, M. W. Tate, H. T. Philipp, A. R. Woll, P. Purohit, J. T. Weiss, V. Kannan, K. T. Ramesh, P. Kenesei, J. S. Okasinski, J. Almer, M. Zhao, A. G. Ananiadis, and T. C. Hufnagel. Time-resolved x-ray diffraction techniques for bulk polycrystalline materials under dynamic loading. 85:093901, 2014. ISSN 0034-6748. doi: 10.1063/1.4893881.

[119] C. J. Hustedt, P. K. Lambert, V. Kannan, E. L. Huskins-Retzlaff, D. T. Casem, M. W. Tate, H. T. Philipp, A. R. Woll, P. Purohit, J. T. Weiss, S. M. Gruner, K. T. Ramesh, and T. C. Hufnagel. In situ time-resolved measurements of

extension twinning during dynamic compression of polycrystalline magnesium. 4:222–230, 2018. ISSN 2199-7446. doi: 10.1007/s40870-018-0152-8.

[120] P. Renganathan, J. M. Winey, and Y. M. Gupta. Shock compression and release of a-axis magnesium single crystals: Anisotropy and time dependent inelastic response. 121:035901, 2017. ISSN 0021-8979. doi: 10.1063/1.4974365.

[121] M. Sliwa, D. McGonegle, C. Wehrenberg, C. A. Bolme, P. G. Heighway, A. Higginbotham, A. Lazicki, H. J. Lee, B. Nagler, H. S. Park, R. E. Rudd, M. J. Suggit, D. Swift, F. Tavella, L. Zepeda-Ruiz, B. A. Remington, and J. S. Wark. Femtosecond x-ray diffraction studies of the reversal of the microstructural effects of plastic deformation during shock release of tantalum. *Phys. Rev. Lett.*, 120:265502, Jun 2018. doi: 10.1103/PhysRevLett.120.265502. URL https://link.aps.org/doi/10.1103/PhysRevLett.120.265502.

[122] J. Duffy, J. D. Campbell, and R. H. Hawley. On the use of a torsional split hopkinson bar to study rate effects in 1100-0 aluminum. 38:83, 1971. ISSN 0021-8936. doi: 10.1115/1.3408771.

[123] J. Duffy, R. H. Hawley, and R. A. Frantz. The deformation of lead in torsion at high strain rates. 39:651, 1972. ISSN 0021-8936. doi: 10.1115/1.3422765.

[124] JT Lloyd. A dislocation-based model for twin growth within and across grains. *Proc. R. Soc. A*, 474(2210):20170709, 2018.

[125] Y.M. Zhu, S.W. Xu, and J.F. Nie. $\{10\bar{1}1\}$ twin boundary structures in a Mg–Gd alloy. *Acta Materialia*, 143:1–12, jan 2018. doi: 10.1016/j.actamat.2017.09.067.

[126] YB Wang, ML Sui, and E Ma. In situ observation of twin boundary migration in copper with nanoscale twins during tensile deformation. *Philosophical Magazine Letters*, 87(12):935–942, 2007.

[127] Dennison Bancroft. The velocity of longitudinal waves in cylindrical bars. *Physical Review*, 59(7):588, 1941. URL http://journals.aps.org/pr/abstract/10.1103/PhysRev.59.588.

[128] Yulong Li and K.T. Ramesh. An optical technique for measurement of material properties in the tension kolsky bar. *International Journal of Impact Engineering*, 34(4):784–798, apr 2007. doi: 10.1016/j.ijimpeng.2005.12.002.

[129] Marc De Graef. *Introduction to conventional transmission electron microscopy*. Cambridge University Press, 2003.

Vita

Vignesh was born in Chennai, India on the 27$^{\text{th}}$ of January, 1991 to Shobha and Baskara Kannan. He attended the National Institute of Technology, Tiruchchirapalli from 2008-2012, graduating first class with distinction with a Bachelor of Technology degree in production engineering. In the fall of 2012, he joined the mechanical engineering masters program at the Johns Hopkins University. He got accepted into the PhD programme the very next summer and began working towards his doctoral dissertation under the mentorship of Prof. K. T. Ramesh. At Hopkins, Vignesh worked on understanding the behavior of magnesium and its alloys under extreme impact loading conditions. He finished the requirements for his doctoral degree on the 7$^{\text{th}}$ of December, 2018. Starting spring 2019, he is all set to begin a post-doctoral position with Prof. Dennis Kochmann at the ETH, Zurich.